THESE

Présentée à

L'Université des Sciences et Technologies de Lille

Pour obtenir le titre de

DOCTEUR EN CHIMIE

Ecole doctorale: Sciences de la Matière, du Rayonnement et de l'Environnement

Discipline: Molécules et Matière Condensée

par

Tong LI

Etude de catalyseurs à base de carbure de molybdène pour le reformage à sec du méthane et la synthèse Fischer-Tropsch

Soutenance le 14 Décembre 2016 devant la commission d'examen:

Rapporteurs

Prof. Pascal FONGARLAND, Professeur, Université Claude-Bernard Lyon 1

Dr. Dominique BEGIN, Directeur de recherche au CNRS, Université de Strasbourg

Examinateur:

Dr. Jean-Marc GIRAUDON, Maitre de conférences, Université des Sciences et Technologies de Lille

Directeur de thèse :

Dr. Andrei KHODAKOV, Directeur de recherche au CNRS, Université des Sciences et Technologies de Lille

Co-directeur de thèse :

Dr. Mirella VIRGINIE, Maitre de conférences, Ecole Nationale Supérieure de Chimie Lille

THESIS

Lille University of Science and Technology

For obtaining a title of

DOCTOR IN CHEMISTRY

Doctoral School: Material, Radiation and Environment Science

Discipline: Molecules and Condensed Matter

by

Tong LI

Study of molybdenum carbide catalysts in dry methane reforming and Fischer-Tropsch synthesis

Defense on 14 December 2016 in front of the examination committee:

Reviewers:

Prof. Pascal FONGARLAND, Professor, Claude Bernard University Lyon 1

Dr. Dominique BEGIN, CNRS Research Director, University of Strasbourg

Examiners:

Dr. Jean-Marc GIRAUDON, Assistant Professor, Lille University of Science and Technology

Ph-D Director:

Dr. Andrei KHODAKOV, CNRS Research Director, Lille University of Science and Technology

Ph-D Co-superviser:

Dr. Mirella VIRGINIE, Assistant Professor, National Graduate School of Engineering Chemistry of Lille

Content

Résumé

Des catalyseurs à base de carbure de molybdène ont été étudiés pour la réaction de reformage du méthane par le CO_2 (RMC) et pour la réaction de synthèse Fischer-Tropsch (SFT). Pour la réaction de RMC, différentes teneurs de Ni en tant que promoteur ont été ajoutées aux catalyseurs Mo_2C/Al_2O_3. Les résultats indiquent que le nickel augmente l'activité et la stabilité des catalyseurs Mo_2C/Al_2O_3. L'addition de nickel provoque la re-carburation des espèces Mo oxycarbures en carbures et conduit à l'augmentation rapide de l'activité lors de la réaction. Les différentes méthodes de préparation ont également une influence notable.

Pour la réaction de SFT, différents supports, mais aussi différents promoteurs, ont été étudiés. Les résultats suggèrent que l'alumine procure une très haute sélectivité vis-à-vis des oléfines légères. L'augmentation de la teneur en potassium diminue les activités d'hydrogénation de CO et inhibe également les réactions de gaz à l'eau. Cependant, il est évident qu'elle augmente également la sélectivité des chaînes oléfines et les propriétés de croissance des chaines carbonée.

Enfin, la réaction RMC sous pression et la réaction de SFT en présence de CH_4 ou de CO_2 ont été étudiées. Les résultats montrent que l'augmentation de la pression conduit à un fort dépôt de carbone sur les catalyseurs à base de carbure de NiMo et l'ajout du CH_4 ou du CO_2 au gaz de synthèse lors de la SFT, contribue à diminuer l'activité d'hydrogénation du CO et influe la distribution des produits.

Mot clé:

Biogaz, Reformage du méthane par le CO_2, Synthèse Fischer-Tropch, Carbure de molybdène, Nickel, Potassium

Abstract

Molybdenum carbide catalysts have been studied in dry methane reforming (DMR) and in Fischer-Tropsch synthesis (FTS). For DMR, different contents of Ni promoted Mo_2C/Al_2O_3 catalysts were investigated. The results indicated that nickel increased the activity and stability of Mo_2C/Al_2O_3 catalysts. The addition of nickel promoted the re-carburization of Mo species from oxycarbide to carbide species and led to the rapid increase in activity during reaction. The different preparation methods also had a significant influence on the nickel promoted Mo_2C/Al_2O_3 catalysts.

For FTS, different supports and different promoters have been investigated for the Mo_2C based catalysts. The results suggested that alumina supported catalyst exhibited higher light olefins selectivity. Increasing the potassium contents led to a decrease in CO hydrogenation activities and also inhibited the water gas shift reaction. However, potassium increased the olefin selectivity and carbon chain growth probability.

Finally, DMR under pressure and FTS in the presence of CH_4 or CO_2 were investigated. The results showed that an increase in pressure led to high carbon deposition over the catalyst surface in DMR and the addition of CH_4 or CO_2 in the syngas decreased the CO hydrogenation activity and affected the products distribution in FTS.

Keywords:

Biogas, Dry methane reforming, Fischer-Tropsch synthesis, Molybdenum carbide, Nickel, Potassium

Preface

The manuscript consists of 6 chapters.

Chapter 1 mainly summarized the development of catalysts for dry methane reforming and Fischer-Tropsch synthesis and the application of molybdenum carbide catalysts in DMR and FTS. Analysis of literature suggested that the combination of dry methane reforming and Fischer-Tropsch synthesis in a single process exhibited obvious advantage due to the saving of energy consumption and facility investment. Molybdenum carbide was a promising catalyst of both DMR and FTS, especially for the combination process.

Chapter 2 introduced the methods of catalyst preparation, characterization and evaluation.

Before the experimental investigations, thermodynamics calculations for both dry methane reforming and Fischer-Tropsch synthesis were performed in chapter 3. Results showed that dry methane reforming was favourable at higher temperature, lower pressure, the increasing of CH_4/CO_2 ratio led to lower CH_4 conversion, higher CO_2 conversion and enhancement of carbon deposition. Besides, Fischer-Tropsch synthesis reactions were kinetically controlled and the products distribution may be dominated by catalysts as well as by reaction conditions. Thermodynamically, the addition of CH_4 and CO_2 on the feedstock slightly decreased the equilibrium conversion.

Oxidation of Mo_2C is the predominant reason for deactivation of Mo_2C catalysts in dry methane reforming. Chapter 4 mainly focused on Mo_2C/Al_2O_3 catalyst promoted with nickel, synthesized by different preparation methods. The results indicated that addition of nickel promoted the re-carburization of Mo from oxycarbide species to carbides species, which resulted in excellent activity and stability. Crystallite size of nickel also played a crucial role over dry methane reforming. At low nickel content (Ni:Mo=1:2), large nickel crystallite size led to well stability in DMR due to better oxidation-recarburization balance. Nevertheless, at high nickel content (Ni:Mo=1:1), large nickel crystallite size resulted in carbon deposition because of the carbon species formation. Besides, the increase in pressure led to heavily carbon deposition over DMR.

Catalytic performance of promoted molybdenum carbide catalysts supported by different materials in Fischer-Tropsch synthesis was studied in chapter 5. The results revealed that all the non-promoted Mo_2C catalysts produced mainly C_1-C_4 light hydrocarbons. Particularly,

alumina supported catalyst, which had higher concentrations of basic acid site, exhibited higher light olefins selectivity. Compared with other promoters, potassium promoted Mo/Al_2O_3 catalyst exhibited higher selectivity to light olefins and better stability from oxidation. Increasing of potassium content decreased the activities of CO hydrogenation and also inhibited the water gas shift reaction. However, it increased the olefin selectivity and carbon chain growth. Furthermore, the addition of CH_4 or CO_2 in the syngas decreased the activity and affected the product selectivity of Fischer-Tropsch synthesis.

Chapter 6 summarized the general conclusion and drew the perspectives of this thesis.

Chapter 1 Literature review

1.1 General Introduction

Energy is the prerequisite for modernized industry system such as agriculture, transport, manufacturing and communication industry. Typically, energy is classified as renewable energy (which are naturally replenished on a human timescale, such as sunlight, wind, tides, hydropower and geothermal heat) and non-renewable energy (which cannot renew itself at a sufficient rate for sustainable economic extraction in meaningful human time-frames such as coal, petroleum, natural gas and nuclear energy) by regeneration capacity [1, 2].

Currently, the fossil energy (includes coal, petroleum, natural gas, flammable ice and shale gas) is the most popular used energy providing about 80% of total energy consumption, and it will remain estimated at 77% until 2030 [3, 4]. As is well known [3-6], the large scale anthropogenic emission of greenhouse gases from the consumption of fossil energy has been considered as the predominant reason for climate change, the most imminent environmental issue in current world. Moreover, the depletion of fossil energy reserves is another severe problem the world is facing today. The development of renewable energy source, instead of fossil energy, became the most important issue during the 21 century.

Renewable energy sources, mainly the utilization of biomass and organic waste materials as a resource of energy, are nowadays attractive substitutes [7-9]. Compared with others renewable energy resources like solar energy and wind energy, the obvious advantage for biomass and organic waste is the continuous power generation capacity. Organic waste materials, such as manure, food waste and farm waste, do not compete with food crops in agricultural land usage [4]. Otherwise, with the worldwide economic development and population growth, the bio-waste is increasingly produced in both developed and developing countries [7]. For example, about 809 million tons of crop straw and 1629 million tons of animal manure are collected every year in China, with a biogas potential of 33.5×10^{10} m^3 (equal to 239.22 million tons of equivalent standard coal) [10, 11]. The production of biogas through anaerobic digestion has been evaluated as one of the most energy-efficient and environmentally friendly technologies for the utilization of organic waste materials.

1.2 Anaerobic digestion

Technologies of biomass and organic waste valorization can be subdivided into thermochemical, biochemical and physicochemical conversion processes. A schematic overview is displayed in Figure 1-1.

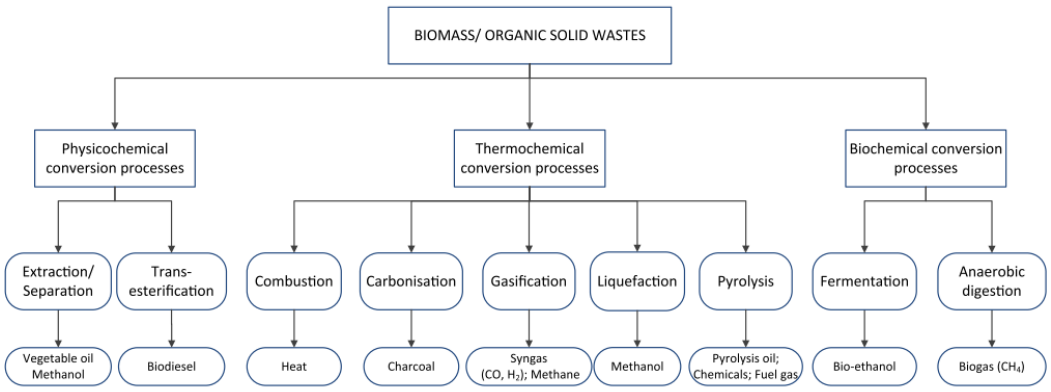

Figure 1-1: Biomass and organic waste conversion technologies [4].

Anaerobic digestion, which is classified as a biochemical conversion process, is the most simple, low cost and widely used process [12]. It is a technology based on the microbial degradation of organic matters under aqueous condition and in the absence of oxygen. The anaerobic digestion process is a dynamic complex system involving four digestion steps: hydrolysis, acidogenesis, acetogenesis and finally methanogenesis [13], which are displayed in Figure 1-2.

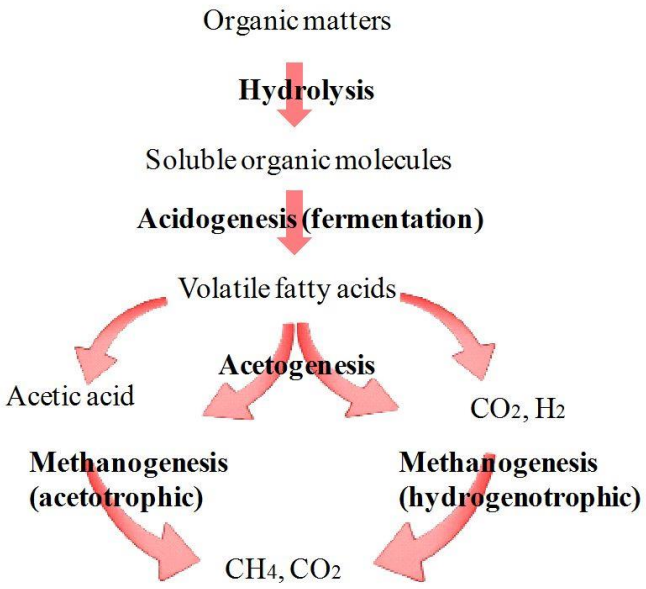

Figure 1-2: Biochemical conversion pathway for anaerobic digestion process [13].

Hydrolysis is a critical rate limiting process which degrades organic matters (such as carbohydrates, lipids, and proteins) to soluble organic molecules (such as sugars, long-chain fatty acids and amino acids) by the hydrolytic bacteria. The generated molecules are further broken into volatile fatty acids, alcohols, CO_2 and H_2 during the acidogenesis step by the acidogenesis bacteria. During the acetogenesis step, these formed volatile fatty acids are

further degraded into acetic acid, CO_2 and H_2. Finally, all these intermediate products are converted mainly into CH_4, CO_2 and water with the digestion of methanogensic bacteria. Three biochemical pathways take place during this latter step:

(I) Acetotrophic methanogenesis:

$$4CH_3COOH=4CO_2+4CH_4 \quad \text{Equation 1-1}$$

(II) Hydrogenotrophic methanogenesis:

$$CO_2+4H_2=2H_2O+CH_4 \quad \text{Equation 1-2}$$

(III) Methylotrophic methanogenesis:

$$4CH_3OH+6H_2=4CH_4+4H_2O \quad \text{Equation 1-3}$$

However, it contains traces of gases such as H_2S, H_2, O_2, and N_2 in the final composition of the biogas.

Compared to the other valorization processes, there are several advantages for anaerobic digestion:

(I) a widespread feedstock: almost every kind of natural organic matters can be proceeded without any pre-treatment. For example, the biomass and organic waste with more than 60% of water can be directly proceeded for anaerobic digestion without pre-treatment, which is undesirable for others methods such as combustion, pyrolysis, gasification and extraction process [4, 14].

(II) Moderate operating conditions: anaerobic digestion is a microbial conversion process in the absence of oxygen, which means it can be processed with microorganism at a gentle temperature (normally 30-60 ℃) [13]. Hence, anaerobic digestion is feasible for both large and small-scale industrial installations [4].

(III) Less pollution: the product of anaerobic digestion (biogas), which consists of methane, carbon dioxide and trace gases such as H_2S, H_2O, H_2, O_2, and N_2, is generally captured as energy sources. It is energy efficient and environmentally friendly because of the low emission of hazardous pollutants [4].

(IV) High value by-product: During anaerobic digestion, about 20–95% of the feedstock organic matter is degraded. Digestate, the residue materials of anaerobic digestion, is nitrogen rich and normally can be used as a nutrient fertilizer [15]. A novel application is to transform

the digestate into biochar, which can be further employed as soil enhancer or adsorbent for purification of wastewater and flue gas [16-18].

1.3 Biogas

1.3.1 Composition of biogas

The composition of biogas strongly depends on the type of the biomass and organic waste as well as the process conditions [19, 20]. The methane content is normally in the range of 50-60% and the carbon dioxide content is approximately of 35-45%, the nitrogen up to 0.5-7%, the hydrogen 5-10% and traces of H_2S and O_2 [21]. The heat value of a biogas containing up to 75% of methane has been calculated to be in the range of 20,100-28,900 kcal.Nm^{-3}.

M. S. Muylaert et al.[21] calculated that 1 m^3 of purified biogas is equivalent to 1.1 L of gasoline or 1.7 L of bioethanol (shown in Table 1-1).

Table 1-1: Energy equivalence of different energy sources with respect to raw and purified biogas [21].

Energy source	Equivalent to 1 m^3 of raw biogas	Equivalent to 1 m^3 of purified biogas
Gasoline	0.63-0.73 L	1.10 L
Ethanol	0.81-1.10 L	1.70 L
Petroleum gas	0.48-0.65L	1.00
Natural gas	0.45-0.61 m^3	0.93 m^3
Wood coal	0.91-1.24 kg	1.90 g
Electric energy	4.6-6.2 kWh	9.4 kWh
Mineral coal	0.60-0.82 kg	1.25 kg

1.3.2 Application of biogas

Biogas can be used for various important commercial applications which can be divided into several aspects regarding the utilization purpose [8, 22, 23].

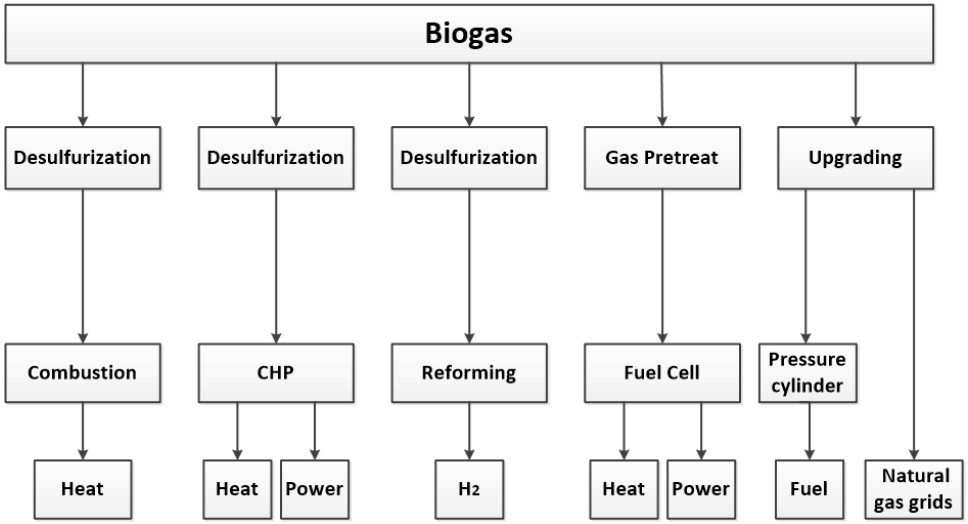

Figure 1-3: Application of biogas [23].

1.3.2.1 Direct combustion

Due to the high content of methane, biogas can be directly used as a combustible gas. The biogas can be directly burned in boilers or burners, which needs low equipment investment. Thus direct combustion is particularly suitable for the utilization of the biogas produced by small family digesters. For example, it has been widely used for household applications such as cooking, heating and lighting on the rural area in China at 1980s. However, the combustion process of biogas to generate heat has low value of utilization efficiency [6, 24].

1.3.2.2 Electricity production with combined heat and power production (CHP)

Electricity production is one of the most common ways for the utilization of natural gas, which can be also designed for the application of biogas. Boilers have the lowest quality requirements of feedstock, while they are rarely used today due to the particularly low energy efficiency. Combined heat and power production (CHP) is a technique widely used for the utilization of biogas in many countries, as it is considered as an efficient way of biogas utilization [25]. This technique leads to a production of about 33-38% of electricity and 62-67% of heat [26]. Valorization of the produced heat is interesting economically because the temperature of exhaust heat is at least 250 ℃, so heat can be used by industry processes, agricultural activities and space heating [27].

1.3.2.3 Upgrading and utilization as vehicle fuel

Biogas can be upgraded to high quality natural gas and used in vehicles. Countries like Sweden, Germany, Switzerland and China have already carried out vehicles that used biogas as fuels [20]. Biogas must fulfil several specifications regarding heating value and impurities. One of the main specifications is that the gas must have a methane content of at least 97% [23]. The process of cleaning the biogas and removing CO_2 is generally referred to an upgrading and afterward, the biogas (biomethane) is considered to have a higher potential as vehicle fuel, even when compared to other biofuels (Shown in Figure 1-4). The advantage of biogas as the vehicles fuels is even much higher if the feedstock is organic waste instead of energy crops [26].

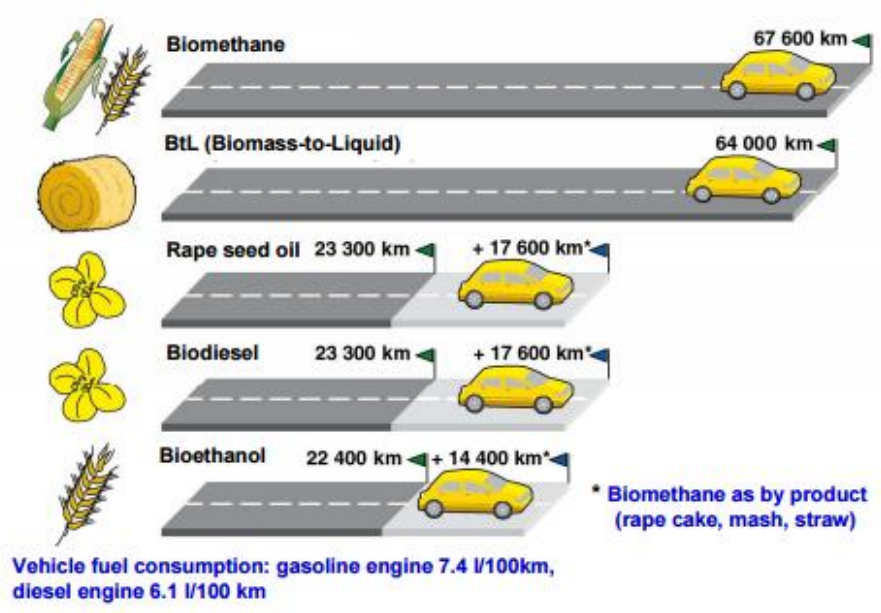

Figure 1-4: Comparison of biofuels: range of a personal car, running on biofuel produced on feedstock/energy crops from on hectare arable land [26].

1.3.2.4 Upgrading and injection in the natural gas grids

An efficient way of integrating the biogas into the energy sector is upgrading of biogas to natural gas quality (biomethane) and injecting it into the existing natural gas grid [26]. Injecting upgraded biogas as biomethane into the natural gas grids widens up the opportunities to transport and utilize biogas in the large energy consumption areas denser in population. Countries like Sweden, Switzerland, Germany and France have standards for injecting biogas into the natural gas grid. The standards, prescribing the limits for components

like sulphur, oxygen, particles and steam, have the aim of avoiding contamination of the gas grid or the end users. The main barriers for biomethane injection are the high costs of upgrading and grid connection. In some cases biogas can be difficult to upgrade to sufficient quality due to large content of nitrogen [23].

1.3.2.5 Fuel for fuel cells

A fuel cell is a device that converts the chemical energy into electricity through a chemical reaction of hydrogen ions with oxygen or another oxidizing agent [28]. The basic physical structure of a fuel cell consists of an electrolyte layer in contact with a porous anode and cathode on both sides (Figure 1-5) [26].

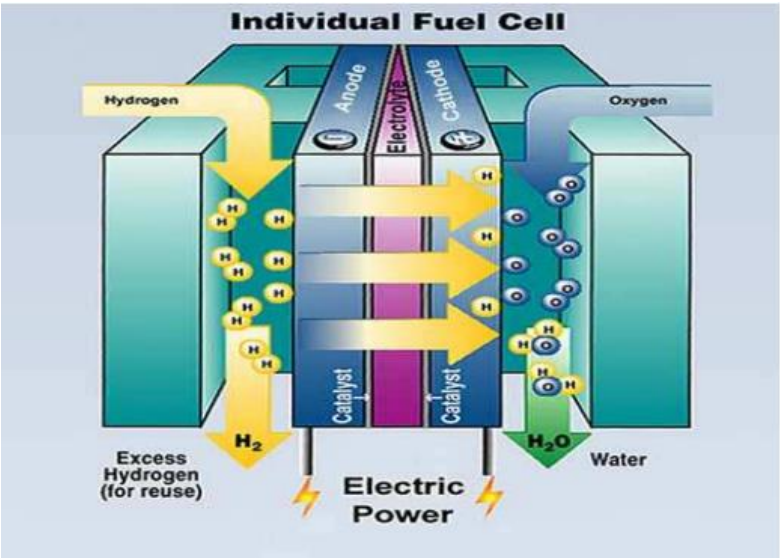

Figure 1-5: Simplified scheme of a fuel cell [26].

In a typical fuel cell, the gaseous fuel (biogas) is feed continuously to the anode (the negative electrode) compartment and an oxidant (oxygen from air) is feed continuously to the cathode (the positive electrode) compartment. An electrochemical reaction takes place at the electrodes, producing an electric current. Fuel cells have high electric efficiency and provide a new pathway for biogas application. The first Molten Carbonate fuel cell for utilization of biogas was built on Germany at 2007 [26]. The catalyst inside the fuel cells is very sensitive to impurities. The investment costs for biogas applications in fuel cells is higher than an application in combined heat and power production [27].

1.3.2.6 Production of hydrogen

Biogas can also be used to produce hydrogen, which is currently recognized as a clean energy. Usually, the production of hydrogen from biogas can occur via these two reactions:

- Dry methane reforming:

$CH_4+CO_2=2H_2+2CO$ Equation 1-4

- Steam methane reforming:

$CH_4+H_2O=3H_2+CO$ Equation 1-5

- Partial oxidation

$CH_4+1/2O_2=CO+2H_2$ Equation 1-6

The utilization of biogas as a feedstock for a reforming process to produce H_2 offers obviously advantages. The production of hydrogen from biogas can help to reduce the emission of both greenhouse gases. Compared with the combustion, it is not necessary for removing CO_2 from biogas. The presence of CO_2 and humidity are advantageous for converting biogas into H_2 via steam and dry reforming reactions. The use of biogas as a renewable resource for producing H_2 has been widely investigated in recent years [6, 29-32].

1.4 Dry methane reforming

Dry reforming of methane, described as $CH_4 + CO_2 = 2H_2 + 2CO$, has been intensively studied since it was reported by Ashcroft [33]. It has two obvious advantages: (1) the reactants of dry methane reforming are two greenhouse gases (CH_4 and CO_2); (2) the produced syngas is suitable for the Fischer-Tropsch synthesis [34, 35] and methanol synthesis.

The average C-H bond energy of methane molecule is 414 kJ/mol, the dissociation energy of CH_3-H is 435 kJ/mol which means that the methane has a high stability. The efficient way to activate and convert methane molecule is a hot topic.

1.4.1 The catalysts for dry methane reforming

High activity and stability catalysts are the key factors for industrialization of dry methane reforming. Nowadays, supported noble metal catalysts (Pt, Rh, Ru, Pd, Ir) and supported transition metal catalysts (Ni, Co, Fe) are mostly investigated.

1.4.1.1 Noble metals catalysts

Abundant studies about the utilization of noble metal catalysts over various supports show their high activity and high stability due to lower carbon deposition sensitivity [36]. Pt is one of the most widely used noble metal catalysts for dry methane reforming. Tomishige et al.[37] compared the catalytic performance of Pt/Al_2O_3 and Ni/Al_2O_3 at different reaction temperatures in dry methane reforming. The result indicated that the CH_4 conversion over Pt/Al_2O_3 was much higher than the conversion over Ni/Al_2O_3 catalysts. O'Connor et al.[38] investigated the mechanism on Pt/ZrO_2 and Pt/Al_2O_3 catalysts in DMR. The results suggested that methane was firstly cracked over the surface of both catalysts; the dissociation of CO_2 over Pt/Al_2O_3 surface needed the assistance of H, while the dissociation of CO_2 over Pt/ZrO_2 surface depends on the surface defects. Bitter et al.[39] compared different supported Pt based catalysts and the results showed better activity in the following order: Pt/ZrO_2 > Pt/TiO_2 > $Pt/\gamma\text{-}A1_2O_3$. For the Pt/TiO_2 and $Pt/\gamma\text{-}A1_2O_3$ samples, carbon deposition covered the active centers, which led to the rapid deactivation. The Pt/ZrO_2 catalyst could keep a high stability during dry methane reforming as no carbon deposition has been observed.

Ru and Rh are also widely used for dry methane reforming [36, 40]. Carrara et al.[40] studied La_2O_3 supported Ru catalyst and the result indicated that the catalysts exhibited good stability for more than 100 h at 550-630 ˚C at CH_4/CO_2=1. Besides, the turnover frequency (TOF), which indicated the reaction rate per unit of metal surface, was constant over a wide dispersion range, there was no influence of properties and structures of support on the reaction rate which depends mainly on the metal surface [41]. Djinovic et al.[36] prepared highly porous and thermally stable 2%Rh-CeO_2 catalysts with a high Rh dispersed metallic particles using structurally ordered KIT-6 SiO_2 by the hard template method. The catalyst exhibited 87% and 93% of CH_4 and CO_2 conversion at 800 ˚C. In addition, a stable average H_2/CO ratio equal to 0.62 was observed at 650 ˚C.

Solymosi et al.[42] investigated Al_2O_3 support for different noble metal (Ru, Pd, Rh, Pt, Ir) catalysts. They demonstrated that the activity order was: Ru > Pd > Rh > Pt > Ir. Ashcroft et al.[33] also compared Al_2O_3 supported different metal (Ni, Pd, Ru, Rh, Ir) catalysts. The results showed that compared to Ru and Pt catalysts, the Ni, Rh and Ir catalysts had excellent catalytic activity. At 770 ˚C, with loading amount of 1wt% of noble metals, they exhibited more than 80% of conversion for both CH_4 and CO_2.

Even though owning high activity, stability and anti-carbon deposition property, the high price and limited reserves on earth restrict the large scale application of noble metal catalysts for the industry, so many researches focus on the non-noble metal catalyst development.

1.4.1.2 Nickel based catalysts

In 1932, Hawk[43] found that Al_2O_3 supported Ni-Co catalysts showed excellent activity over dry methane reforming. Generally, the activity order of dry methane reforming is: Ni > Co >> Cu >> Fe [44, 45]. Nickel is a common catalyst for dry methane reforming. Lemonidou et al. [46] prepared 5wt% Ni on calcium aluminate (molar CaO/Al_2O_3=1/2) catalyst by impregnation method and the CH_4 and CO_2 conversion reached 51.3% and 57.1% at 700 ˚C. Zhang et al.[47] studied composite Sn_2O_3 supported nickel catalysts by sol-gel method. Due to the high dispersion of Ni nano-particles and the interface effect of the support, reaction activity was improved obviously compared with the Ni/CaO and Ni/Sn_2O_3 catalysts.

Nickel is known to have strong capacity for CH_4 decomposition and CO disproportionation (reactions producing carbon deposition) [48-50]. The surface carbon formation is the primary reason for the deactivation of nickel based catalysts.

Addition of promoters is an efficient way to increase the resistance to carbon deposition of nickel based catalysts. Hence bimetallic catalysts prepared by addition of small quantity of noble metals, such as Ni-Pt/γ-Al_2O_3 [51, 52], Ni-Pt/MgO [53] and Ni-Rh/CeO_2-Al_2O_3 [54], have been studied and showed high resistance to carbon deposition. The presence of promoters can help to decrease the particle size of nickel, increasing their dispersion and reaction activity. Compared to Ni catalysts and Pt catalysts, a Ni-Pt bimetallic catalyst exhibits better catalytic performances [55]. Addition of Pt can promote the generation of NiO, which improves the formation of Ni^0 active sites during the reduction process [56].

Promotion by alkali metals can help to decrease CH_4 decomposition and improve the adsorption of CO_2 on the catalyst surface, which is favourable for decreasing the carbon deposition. Juan-Juan et al. [57] studied the effect of adding potassium over Ni/Al_2O_3 catalyst and the result revealed that K could inhibit carbon deposition over the surface and improve the catalyst stability. However, addition of K poisoned Ni species, which led obviously to a decrease in activity. Jeong et al.[58] studied the effects of the addition of Mg, Mn, K, Ca to a Ni/HY catalyst and the results revealed that the promoters participated in the improvement of Ni-based catalyst stability. Ni-Mg/HY catalyst showed the best carbon deposition resistance

capacity and stability. The addition of Mg increased the dispersion of Ni on HY surface. The generated carbonate species over Ni-Mg-HY catalyst also restrained carbon deposition.

Rare earth metals promoters, mainly La and Ce, have been widely studied with nickel based catalysts in dry methane reforming. The promotion of La_2O_3 can increase the dispersion of Ni species and decrease Ni particle size. Moreover, La_2O_3 can help to decrease the migration and aggregation of Ni particle size at high temperature condition. Mo et al.[59] studied La_2O_3 promoted Ni/SiO_2 catalyst, prepared via an in situ self-assembled core–shell precursor route. Nickel species were well dispersed with particle size < 3.0 nm. The addition of La_2O_3 enhanced the interaction between NiO and the silica support to form a more stable nickel silicate. The resulting $Ni–La_2O_3/SiO_2$ catalyst showed excellent catalytic activity and stability without any coking behavior even after 100 hours of reaction on stream. Oemar et al.[60] revealed that La-promoted Ni/SBA-15 catalyst had much higher catalytic activity and stability than the non-promoted Ni/SBA-15 catalyst due to the crucial role of La to simultaneously adsorb the CO_2 and to remove deposited carbon from the metallic Ni surface.

CeO_2 is an important oxygen-storage material that can reserve oxygen at oxygen-rich atmosphere and release it at oxygen-poor atmosphere. This special property can improve the carbon elimination during the reaction and enhance the stability of nickel based catalysts in dry methane reforming. Daza et al.[61] prepared Ce-promoted Ni/Mg–Al catalyst and investigated its catalytic performance in dry methane reforming. The results revealed that the increase in the Ce loading between 1 and 10% caused no considerable effect in the catalytic activity and selectivity but inhibited the coke formation. Akri et al.[62] investigated different Ce loading in a Ni-catalyst supported on illite clay. The results indicated that the addition of Ce increased the surface area and the dispersion of nickel particles. The best catalytic activity and stability were obtained with the catalyst containing 15wt% of Ce apparently attributed to its redox properties and further improvement on the nickel dispersion.

Otherwise, supports such as zeolites [63, 64], transition metal oxides [65, 66] and rare earth metal oxide [67] can improve the dispersion of nickel species, provide strong basic site and have interaction with nickel particles which will improve the activity, restrict carbon deposition and decrease nickel particle sintering. Some special structures such as spinel [68, 69], perovskite [70, 71] and solid solution [72, 73] can efficiently enhance nickel dispersion and decrease sintering of nickel particles.

The promoters of nickel catalysts in literature and their action on dry methane reforming are summarised in Table 1-2.

Table 1-2: summary of promoters for Ni catalyst using in dry methane reforming.

Classifications	Promoters	Catalysts	Promoter content	Action
Noble metals	Pt	Ni-Pt/γ-Al_2O_3 [51]	0.04-0.4%	Increased dispersion and reducibility of Ni, and also enhanced the activity and resistance of carbon deposition
		Ni-Pt/MgO [53]	0.1-0.3%	
	Rh	Ni-Rh/CeO_2-Al_2O_3 [54]	0.5%	Increased Ni reducibility and resistance to carbon deposition
Alkali & alkaline metals	K	KNi/Al_2O_3 [57]	5%	helped to decrease CH_4 decomposition and increase reduction of Ni while decreased activity on DMR
		Ni-K/HY [58]	5%	
	Mg	Ni-Mg/HY [58]	3-10%	Increased the dispersion of nickel, formed carbonate species suppressed carbon deposition
Rare earth metals	La_2O_3	Ni–La_2O_3/SiO_2 [59]	1%	Resulted in stronger interaction between Ni and support, decreased the migration and aggregation of Ni particle size at high temperature; La also actively adsorbed CO_2 and removed the deposited carbon
		Ni-La_2O_3/SBA-15 [60]	1-5%	
	CeO_2	Ce-Ni/Mg–Al [61]	1-10%	CeO_2 is an oxygen-storage material, which can improve the carbon elimination during the reaction and enhance the stability of nickel based catalysts over DMR
		Ce- Ni/Illite clay [62]	5-20%	

1.4.1.3 Molybdenum carbide catalysts

Metal carbides catalysts, especially Mo_2C (molybdenum carbide) and WC (tungsten carbide), have been proven to have excellent activity in dry methane reforming and high resistance to carbon deposition due to their particular structure [74, 75]. The review about molybdenum carbide in dry methane reforming will be particularly described in the section 1.6.2.

1.4.2 The mechanism of dry methane reforming

Two mainly mechanisms for dry methane reforming have been reported. One described that the methane molecule is adsorbed and decomposed on the active surface leading to surface –H and –C whereas, CO_2 molecule directly reacts with –H to generate H_2O without adsorption and decomposition on catalyst surface. The generated H_2O further react with methane to generate syngas. This mechanism insists that it's no obvious different for the mechanisms between dry methane reforming and stream methane reforming due to the existence of H_2O in the dry methane reforming process. Rostrupnielsen et al.[76] investigated CH_4 decomposition on the Ni/MgO catalyst and considered two steps for methane decomposition process:

$$CH_4 + 2* = CH_3^* + H^* \quad \text{Equation 1-7}$$

$$CH_3^* + (3-x)* = CH_{3-x}^* + (3-x)\,H^* \quad \text{Equation 1-8}$$

Osaki et al.[77] studied the surface impulse response over Ni/MgO catalyst, the results insist that the directly generation of H_2 after the adsorption and decomposition of CH_4 on the catalyst surface. Moreover, the decomposition of CH_4 is the rate-determined step for dry methane reforming. CH_4/CD_4 isotope tracer reaction indicates the kinetic isotopic effects for the CH_4 decomposition on the Ni/MgO catalysts surface, and also proves that the rate-determined step for dry methane reforming is CH_4 decomposition.

With the further studies, the mechanism considering the decomposition of CO_2 on the catalysts surface was regarded more reasonable for the dry methane reforming process. Erdohelyi et al.[78] proposed another mechanism:

$$CH_4 = CH_{3(a)} + H_{(a)} \quad \text{Equation 1-9}$$

$$CO_2 + H_{(a)} = CO + OH_{(a)} \quad \text{Equation 1-10}$$

$$CH_4 + O_{(a)} = CH_{3(a)} + OH_{(a)} \quad \text{Equation 1-11}$$

$$CH_3 = CH_{2(a)} + H_{(a)} \quad \text{Equation 1-12}$$

$$CH_2 = CH_{(a)} + H_{(a)} \quad \text{Equation 1-13}$$

$$CH_{x(a)} = C + x\,H_{(a)} \quad \text{Equation 1-14}$$

$$CH_{x(a)} + O_{(a)} = CO + x\,H_{(a)} \quad \text{Equation 1-15}$$

$$CH_{x(a)} + CO_2 = 2\,CO + x\,H_{(a)} \quad \text{Equation 1-16}$$

$$2H_{(a)} = H_2 \quad \text{Equation 1-17}$$

$2\ OH_{(a)} = H_2O + O_{(a)}$ Equation 1-18

This mechanism is more reasonable for the resistance to carbon deposition. The O species which are generated from decomposition of CO_2 can consume the C species generated from CH_4 decomposition and produce CO. There is a competition process between carbon deposition from CH_4 decomposition and consumption of carbon by CO_2. So the enhancement of CO_2 adsorption and decomposition ability of catalysts is a promising way to restrain carbon deposition and to improve the CO selectivity.

1.5 Fischer-Tropsch Synthesis

The Fischer–Tropsch synthesis (FTS) is an industrially useful technology for gas-to-liquid processes which upgrade coal, natural gas or biomass into high quality ultra-clean fuels and other chemical products such as paraffin, olefins and alcohols. Fischer-Tropsch synthesis is a very complex process, the reactions could take place simultaneously between H_2 and CO is as follows:

1. Synthesis of paraffin:

$n\ CO + (2n+1)\ H_2 = C_nH_{2n+2} + n\ H_2O$ Equation 1-19

2. Synthesis of olefins:

$n\ CO + 2n\ H_2 = C_nH_{2n} + n\ H_2O$ Equation 1-20

3. Synthesis of alcohols:

$n\ CO + 2n\ H_2 = C_nH_{2n+1}OH + (n-1)\ H_2O$ Equation 1-21

Syngas has a wide spread source, which can be produced on large-scale by gasification of coal or biomass, reforming of natural gas or biogas [79]. The FTS products are free of sulphur, nitrogen, aromatic compounds and other toxic substances which are clean compared to petroleum products.

Fischer-Tropsch synthesis is successfully applied industrially since the first large-scale FT plant operated in Braunkohle-Benzin in 1936, and the capacity of primary products approached 660 000 tons per year in Germany in 1938 [35]. After the second World War, the Fischer-Tropsch synthesis technology was well developed in South Africa due to the oil embargo, the first coal-based Sasol FT plant was constructed at Sasolburg in 1952 [79, 80]. The oil crisis in 1970s promoted the development of FTS technology to synthesize fuels, low olefins and chemicals in many countries. Sasol built Sasol-II and Sasol-III coal based synthetic oil plants successively in 1980 and 1982 [80]. The first commercial Gas to liquid

(GTL) built by Shell in 1993 in Malaysia, was using a FTS cobalt-based catalyst, with a production capacity of 12 500 barrels per day (bpd). At 2006, Oryx GTL plant based on the Sasol Slurry Phase Distillate (SPD) process with the scale of 34 000 bpd started to on-stream at Qatar. In 2011 Shell has commissioned Pearl the largest FTS plant in the world. In addition, BP Global and Exxon Mobil also kept pay attentions to the FTS process built pilot plants. It can be said that FTS technology has finally come to the stage of full-scale industry and worldwide commercialization [35].

1.5.1 The catalysts for Fischer-Tropsch synthesis

The metals of the group VIII have proven noticeable activity in the Fischer-Tropsch synthesis [35]. Vannice et al. [81] showed that the molecular average weight of hydrocarbons produced by Fischer Tropsch synthesis decreased in the following sequence: Ru > Fe > Co > Rh > Ni > Ir > Pt > Pd.

Ru, Fe and Co are the typical catalysts used for Fischer Tropsch synthesis. Ru is the most active metal for the hydrogenation of carbon monoxide. Whereas, due to the high price and limited reserves, Ru cannot be large-scale used in the industry. Fe and Co catalysts have been widely used in the industry. Moreover, molybdenum carbide, with a catalytic performance similar to those of noble metals as the carbon atoms in Mo_2C molecular can denote their outermost electrons to the D electronic orbit of molybdenum atoms, results in the same electron configuration with noble metals such as palladium and platinum. It has showed excellent catalytic performance in Fischer-Tropsch synthesis, especially for the production of alcohols and light olefins. The advantages of each kind of catalysts are described as follows.

1.5.1.1 Iron based catalysts

The low price is also an important advantage of the widely application for iron based catalysts. Iron based catalysts may show an important light olefins selectivity, which acts as key building blocks for the petrochemical industry [82]. Due to the complex phase change of iron species during reduction step and Fischer-Tropsch synthesis, it is difficult to investigate the relationship between iron species and FTS activity [83]. Riedel et al.[84] investigated Fe-Al-Cu/K_2O catalysts over Fischer-Tropsch synthesis and the results indicate that the Fe_5C_2 phase is the active phase for carbon monoxide hydrogenation; metallic iron exhibits low activity while iron oxide phase is active for water gas shift reaction. Jensen et al.[85]

evidenced 5 different kinds of iron carbides on a Fe-MnO catalyst during Fischer-Tropsch process.

1.5.1.1.1 Effect of promoters on iron based catalyst

The most widely used promoters are alkali metals (K, Na…), Cu, Mn and Mg.

Typically, alkali metals have lower electronegativity compare to iron, which is inclined to donate electron to iron surface. This property of alkali metals promoter can help to increase the electron density of iron, which will promote the dissociative adsorption of CO and enhance the CO conversion. Otherwise, alkali metal promoter such as K can restrict the adsorption of H_2 which will restrict the generation of CH_4 and profit to the carbon chain growth. Ngantsoue-Hoc et al.[86] investigated the promotion of alkali metal over Fe/SiO_2 catalysts, the results indicated that the promotion with K improved the CO hydrogenation as well as the WGS activity. While the addition of Li, Cs and Rb decreased CO conversion. All the alkali metals were inclined to restrict the generation of CH_4.

The addition of Cu can promote the reduction of iron species, which means low temperature of reduction is needed for the iron based catalysts. Zhang et al.[87] investigated the promotion of Cu on the $Fe\text{-}Mn\text{-}K/SiO_2$ catalyst and the results indicated that the addition of Cu could also enhance the carburization rate of iron, while the final extent of carburization was not affected by the promotion of Cu. Due to the increase in the surface basicity from a synergetic effect on the Cu and K co-promoted catalyst ($FeMnCuK/SiO_2$), a decrease in methane and light hydrocarbons as well as an enhancement of heavy hydrocarbons and olefins selectivity were obtained.

Manganese is an excellent promoter for iron catalyst for olefins production by FTS. Wang et al.[88] indicated that the addition of Mn increased the reducing and carburizing abilities of the Fe based catalyst, which led to high CO adsorption/dissociation. As a result, the restriction of hydrogenation on the generated olefins and enhancement of olefins selectivity were obtained.

Pour et al.[89] investigated the promotion of Mg and Ca on a $Fe/Cu/K/SiO_2$ catalyst. The results revealed that Ca and Mg promoters could improve the CO conversion and WGS reaction, suppressed the formation of methane and enhanced the selectivity to olefin and higher chain hydrocarbons.

The promoters of iron catalysts in the literature and their action in Fischer-Tropsch synthesis are summarized in Table 1-3.

Table 1-3: Summary of promoters for iron catalyst using in Fischer-Tropsch synthesis.

Classifications	Promoters	Catalysts	Promoter content	Action
Alkali metals	K	K-Fe/SiO_2 [86]	1%	K improved the activity of CO hydrogenation and WGS reaction, while restricted the generation of CH_4
	Li	Li-Fe/SiO_2 [86]	0.5%	Li decreased CO hydrogenation activity but restricted the generation of CH_4
Transition metals	Cu	Fe-Mn-K/SiO_2 [87]	1%	Cu increased carburization rate of Fe and surface basicity by the interaction with K, shifted products to heavy hydrocarbons and increased olefin/paraffin ratio
	Mn	Mn/Fe [88]	1-25%	Increased the reducing and carburizing abilities of the Fe based catalyst, which lead to high CO adsorption/dissociation and increase olefins selectivity
Alkaline metals	Mg	Mg-Cu/SiO_2 [89]	0.5%	enhanced the catalysts surface basicity while decreased the reducibility of Fe, suppressed the formation of CH_4 and promoted generation of olefin and heavy hydrocarbons
	Ca	Ca-Cu/SiO_2 [89]	1%	Increased surface basicity of catalysts and increased the catalytic activity (FTS and WGS), enhanced selectivity to olefins and heavy hydrocarbons

1.5.1.1.2 Effect of support on iron based catalyst

Support is a very important component of a heterogeneous catalyst. Normally, porous support will provide higher surface area and increase the dispersion of active phase. Otherwise, support will also enhance the thermal stability as well as mechanical strength for heterogeneous catalysts. SiO_2, Al_2O_3 and TiO_2 are typical supports for catalysts and have been widely used in FTS. With the development of material science, different kinds of molecular

sieve and carbon materials with excellent structure have been reported and used as support for FTS catalyst.

Bukur et al.[90] investigated in FTS with a SiO_2 support for a 100Fe/5Cu/4.2K catalyst. The results revealed that SiO_2 suppressed of the reduction and carburization of iron as well as to the decrease in the CO hydrogenation and WGS activity, while the stability increased with the content of SiO_2 support.

Due to its basic and acidic properties, alumina has been widely used for iron catalyst over FTS. Jun et al.[91] revealed that alumina support promotes the dispersion of Cu and K promoters in an iron based catalyst which allows to increase the activity of FTS. Wan et al.[92] revealed a strong Fe-Al_2O_3 interaction on the Fe/Al_2O_3 catalyst. This Fe-Al_2O_3 interaction suppressed the reduction and carburization of iron, the surface basicity of the catalyst and led to a decrease in heavy hydrocarbons selectivity.

With the development of molecular sieves, more and more researchers focus on the application of mesoporous and microporous support structure. Wang et al.[93] investigated various microporous and mesoporous materials supported catalysts over FTS reaction. The result showed that Li^+-exchanged zeolite faujasite support has been proven to be very efficient for producing C_5^+ hydrocarbon fuels. They proposed that the Li^+ cation and the supercage structure of zeolite faujasite, both played important roles in improving the selectivities to C_5^+ hydrocarbons on the Fe catalyst. Cheng et al. [94] studied the effect of pore size on iron based catalysts supported by different kind of molecular supports (MCM-41 and SBA-15 with different pore size) in FTS. The results showed that larger iron oxide crystallites in the large-pore supports were easier carburized than the smaller iron oxide counterparts in small-pore supports. Higher Fischer–Tropsch reaction rates, higher olefin, and C_5^+ selectivities were observed over larger pore iron catalysts. High dispersion of iron oxide in small-pore silica was not favorable for carbon monoxide hydrogenation because of poor iron carburization.

As the graphene layers and tubular morphology structure and the electron-deficient interior and electron-enriched exterior surface, Carbon Nanotubes (CNTs) has been widely studied for an application in catalysis. Guczi et al.[95] studied a Fe/CNT catalyst prepared by impregnation method. They found that the use of CNTs decreased CH_4 selectivity and promoted the generation of olefins and higher C_5^+ hydrocarbons. Chen et al.[96] synthesized iron encapsulated CNT catalysts and investigated its application in FTS. The result indicated

that iron species encapsulated inside CNTs was preferably in a reduced state, leading to high amount of iron carbides under the reaction conditions, which have been recognized to be essential to obtain high FTS activity. The yield of C_5^+ hydrocarbons in presence of the encapsulated iron catalyst was twice over iron catalyst outside CNT and more than 6 times over activated-carbon-supported iron catalyst. Lu et al.[97] investigated a nitrogen doped CNT supported iron catalysts over FTS. The result revealed that nitrogen doping increased the catalyst basicity, which enhanced the dissociative CO adsorption and promoted lower olefin desorption on the catalyst (light olefin selectivity of 46.7%).

1.5.1.2 Cobalt catalysts in Fischer-Tropsch synthesis

Abundant of researches have been investigated for cobalt based catalysts. Compared to iron based catalyst, cobalt based catalyst has a better carbon chain growth capacity (high heavy linear chain hydrocarbon selectivity), a lesser oxygenate production, a better resistance to carbon deposition and lower WGS activity [35]. In this thesis, we mainly summarized the effect of promoters and supports.

1.5.1.2.1 Effect of promoter over cobalt based catalyst

Promoters can improve the reducing capacity and the dispersion of cobalt species. They can as well participate in the increase in the carbon chain growth during FTS. The main investigations of promoters over cobalt based catalysts focused on noble metals (Pt, Pd, Ru, Ir, Rh), Rare earth metal oxides and transition metal oxides.

Noble metals (Pt, Pd, Ru, Ir, Rh) are often used to improve the catalytic performance of cobalt catalysts over FTS. Eschemann et al.[98] found that the catalytic performance of Co/TiO_2 was strongly influenced by the addition of noble metals. The promotion by Ag, Re and high amount of Ru led to increase the activity and the C_5^+ selectivity. Montes et al.[99] investigated the promotion of small amount of Pt on a Co/TiO_2 catalyst prepared by microemulsion method. The results indicated that the presence of Pt improved cobalt reducibility, which led to the enhancement of CO conversion and C_5^+ selectivity.

Rare earth oxides such as CeO_2 and La_2O_3 are also excellent promoters for cobalt based catalysts over FTS. The studies revealed that the interaction of rare earth oxides and cobalt can affect the adsorption properties of H_2 and CO and increase FTS activity and C_5^+ selectivity. Haddad et al.[100] indicated that a Co/SiO_2 catalyst promoted by La^{3+} showed

moderate Co-support interactions which led to enhance the reducibility of the Co species, then to a significant increase in the activity of Fischer–Tropsch synthesis. He et al.[101] investigated the La and Ce promoted cobalt based catalyst over Fischer-Tropsch synthesis. The result revealed that the promotion with both metals led to a better FTS performance compared to the un-promoted catalysts and catalysts promoted with individual rare-earth metals. The CO conversion and the selectivity to long chain hydrocarbons are greatly increased (C_5^+ selectivity was at 80.25%).

The addition of ZrO_2 and MnO_x has been proven to increase the reducing capacity and the dispersion of cobalt species as well as to improve the activity and product distribution. Johnson et al.[102] indicated that Mn promotion increased the abundance of adsorbed CO with weakened C–O bonds. The Lewis acid–base of Mn promoted the cleavage of the C–O bond. Increasing Mn/Co ratio led to a decrease in the ratio of adsorbed H to CO on the surface of the supported Co nanoparticles and decrease in the CH_4 selectivity and an increase in the selectivity to the C_5^+ products. Jongsomjit et al.[103] found the addition of ZrO_2 prevented the interaction between Co and alumina, and increased in the reducibility of Co to the active catalytic metallic phase as well as an increase in the concentration of active Co surface sites.

Table 1-4 summarises the promoters of cobalt catalysts in literature and their action on Fischer-Tropsch synthesis.

Table 1-4: Summary of promoters for cobalt catalyst using in Fischer-Tropsch synthesis.

Classifications	Promoters	Catalysts	Promoter content	Action
Noble metals	Pt	Pt-Co/TiO_2 [99]	0.1-0.25%	Improved cobalt reducibility, enhanced CO conversion and C_5^+ selectivity.
	Re	Co-Re/TiO_2 [98]	0.06-0.24%	The interaction of Re and Co lead to synergistic effects in Co hydrogenation and increased activity of FTS
Rare earth metals	La_2O_3	La^{3+}-Co/SiO_2 [100]	2-18%	La^{3+} promotion increased reducibility of Co and Co^0 concentration on catalyst surface, it increased activity, chain growth capacity and olefin/paraffin ratio significantly.
		Co-La/Silica gel [101]	1-5%	
	CeO_2	Co-Ce/Sillica gel[101]	1-5%	Increased Co reducibility and increased carbon chain growth capacity over FTS

Transition metal oxides	ZrO_2	Zr-Co/γ-Al_2O_3 [103]	2-11%	Decreased the interaction of Co and γ-Al_2O_3, increased the reducibility of Co
	MnO_x	Mn-Co/SiO_2 [102]	1-5%	Increased Lewis acid sites and enhanced adsorption and decomposition of CO, decreased selectivity to CH_4 and increased selectivity to C_5^+

1.5.1.2.2 Support effects in cobalt based catalysts in FTS

The quality of the support can strongly affect the catalytic properties (activity, product distribution and stability) of cobalt based catalysts over Fischer-Tropsch synthesis. The widely used supports for cobalt mainly focused on oxides, molecular sieves and carbon materials.

Traditional oxides supports, such as SiO_2, Al_2O_3, and TiO_2, are widely used for cobalt due to their low price, easy preparation and high mechanical strength. Typically, traditional oxides supports can provide high surface area, large pores channels and then can promote dispersion of cobalt particles. However, the interactions between cobalt and supports may strongly affect the catalytic performance of cobalt based catalyst. Zhang et al. [104] indicated that the abundant presence of silicon hydroxyl on SiO_2 surface led to strong interaction of Co-SiO_2 and resulted in a decrease in Co reducing capacity. The pre-treatment by acetic acid modified the surface properties of silica support, allowing a better dispersion and increased in the reduction degree of supported cobalt. This pre-treated catalyst showed higher CO conversion and lower CH_4 selectivity. The strong interaction between Co and Al_2O_3 and the generated $CoAl_2O_4$ spinel structure led to a decrease in the activity and in the heavy hydrocarbon selectivity [105]. However, the interaction between cobalt and the TiO_2 support may have a positive effect for the reaction activity. Vannice [106] found that Co supported on TiO_2 generated new active sites which lead to higher activity and C_5^+ selectivity.

Due to its high surface area, ordered pore distribution, adjustable pore structure and high thermostability, mesoporous molecular sieves have been widely used as supports for cobalt based catalysts. The ordered pores structure of zeolites promoted the diffusion of reactants and intermediates into the catalyst channels. Moreover, the abundant acidic centers can promote the cracking of the generated heavy hydrocarbons to light hydrocarbons and can also promote isomerization of generated linear hydrocarbons, which leads to the deviation of product distribution from ASF distribution [107]. Yin et al.[108] prepared Hexagonal

Mesoporous Silica (HMS) and MCM-41 molecular sieves supported cobalt catalysts and the results indicated that the HMS supported Co catalyst showed better catalytic activity and C_5^+ selectivity which might be due to its smaller domain size with shorter channels and larger textural mesoporosity. Wang et al.[109] investigated SBA-15 supported cobalt catalysts over Fischer Tropsch synthesis and the result suggested that due to the low cobalt reducing capacity, the Co/SBA-15 catalyst showed a low activity. The Co crystallite size and reducing capacity were strongly affected by the pore size of SBA-15, which affected the FTS activity and product distribution.

1.5.2 The mechanism of Fischer-Tropsch Synthesis

The products of Fischer-Tropsch are very complex as different products can be generated at different reaction conditions. So the mechanism of Fischer-Tropsch synthesis is also very complex.

Reactions including dissociation of adsorbed atoms must take place to transform the CO and H_2 reactants to compounds containing several C-C and C-H bonds. Numerous products are obtained with different carbon chain length and type of functional groups. The functional groups imply different paths and different intermediates. The relative amounts of the products vary in function of the used catalysts, temperature and pressure of FT reaction.

At present, the Fischer-Tropsch synthesis mechanism is still controversial. The universal issues are: dissociative or molecular adsorption of CO on the catalyst surface. Studying the mechanism is beneficial for the studies of the carbon chain initiation, growth, products distribution and kinetic of Fischer-Tropsch synthesis. A lot of mechanistic models have been proposed since Fischer Tropsch synthesis was first reported. Most of the classical mechanisms of Fischer-Tropsch synthesis are described in the following sections.

1.5.2.1 Carbide mechanism

The carbide mechanism was first reported by Fischer and Tropsch in 1926 [110]. This mechanism suggests that the generated metal carbides from CO decomposition over catalysts surface will be hydrogenated to methylene intermediate ($-CH_2-$). Then the methylene intermediate polymerizes and further reacts to generate olefins and paraffin (shown in Scheme 1-1). This is the first mechanism for Fischer-Tropsch synthesis. Craxford and Rideal [111] confirmed this mechanism through kinetic investigation. Experiments with ^{14}C tracer, in

which a metal carbide layer containing ^{14}C was formed on the catalyst and then reacted with syngas, have been investigated. The carbide mechanism can explain only a minority part of the product distribution [112]. However, some metals such as ruthenium (which is particularly efficient in the generation of C-C bonds in Fischer Tropsch synthesis [113]), does not form stable carbides. The carbide mechanism can well explain the generation of linear hydrocarbons obviously, meanwhile, it cannot explain the formation of branched hydrocarbons and oxy-compounds [114]. Moreover, the reaction rate of the generation for the surface carbides from CO is lower than the generation of liquid hydrocarbons, which is also inconsistent for the carbide mechanism.

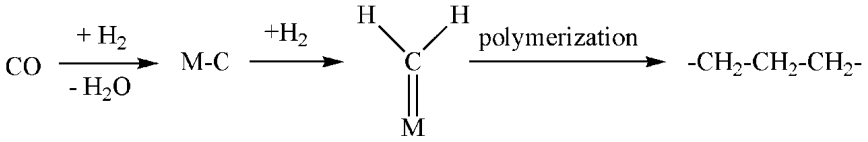

Scheme 1-1: carbide mechanism.

1.5.2.2 Oxygenate (enol) mechanism

Due to the shortcoming of carbide mechanism, Anderson [115] proposed an oxygenate mechanism which can explain the product distribution of Fischer-Tropsch synthesis. According to him, chemisorbed CO reacts with adsorbed H_2 to form oxygenate intermediate HCOH (shown in Scheme 1-2). Chain initiation starts by the generation of C_2 species from the condensation and water elimination of HCOH species. The chain grows from the terminal hydroxyl group and generates oxy-compounds such as alcohols. Hydrocarbons can be formed from the dehydration of alcohols or from the cracking of adsorbed intermediate species. This mechanism can explain well the generation of linear hydrocarbons and oxy-compounds. Emmett [116-119] provided strong support for this mechanism by the ^{14}C tracer technology. ^{14}C labelled as alcohol or alkene, was added with syngas for Fischer Tropsch synthesis. The results indicated that the addition of alkene or alcohol was able to initiate the chain growth. There was no obvious evidence for the existence of intermediates such as HCOH and oxy-compound species during FTS process.

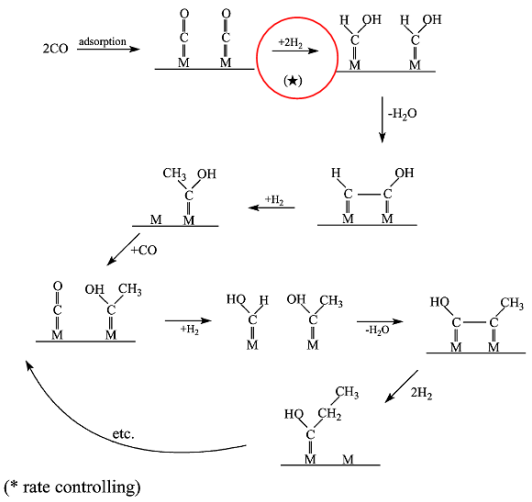

Scheme 1-2: Oxygenate (enol) mechanism [120].

1.5.2.3 CO insertion mechanism

Based on the homogeneous phase organic-metal catalysts mechanism, Pichler [120, 121] proposed the chain initiation from the insertion of CO over metal-hydrogen bond. The hydrogenation of CO on the catalyst surface to generate formyl species, which can be further hydrogenated to hydroxy-methylene species, was hypothesized. The generated hydroxy-methylene can be further hydrogenated leading to carbene or methyl. Carbon chain grows with repeated CO insertion and hydrogenation (shown in Scheme 1-3). This mechanism can well explain the details for the formation of linear products, as well as the generation of hydroxy-compounds, whereas, it cannot explain the generation of branched hydrocarbons.

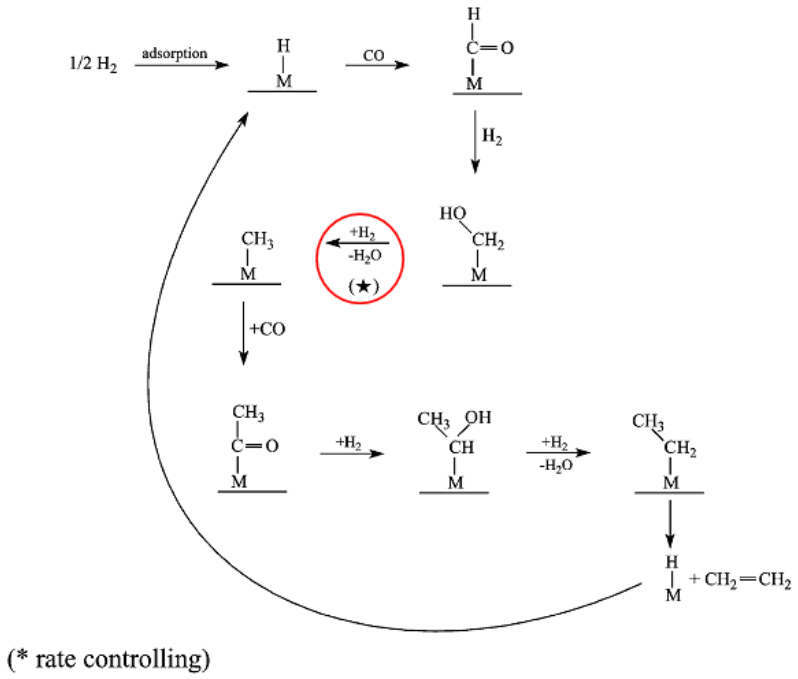

Scheme 1-3: CO insertion mechanism [120].

1.5.2.4 Carbene mechanism

With the development of the surface science instrumentation, abundant of carbides on the catalyst surface can be observed [122-124]. This mechanism (shown in Scheme 1-4) can be described by the CO decomposition on the surface to generate oxygen (O_{suface}) and carbon ($C_{surface}$) species on the catalysts surface. Hence, $O_{surface}$ can further react with syngas to generate H_2O and CO_2, whereas, $C_{surface}$ is hydrogenated to produce methylene then hydrocarbons by the insertion of carbene and reaction with methylene. This mechanism can well explain the generation of branched hydrocarbons and oxy-compounds. But it cannot well explain the deviation of Anderson-Schulz-Flory (ASF) distribution over C_2 species, the slight generation of isomerization products is not coincident with the carbene mechanism [125].

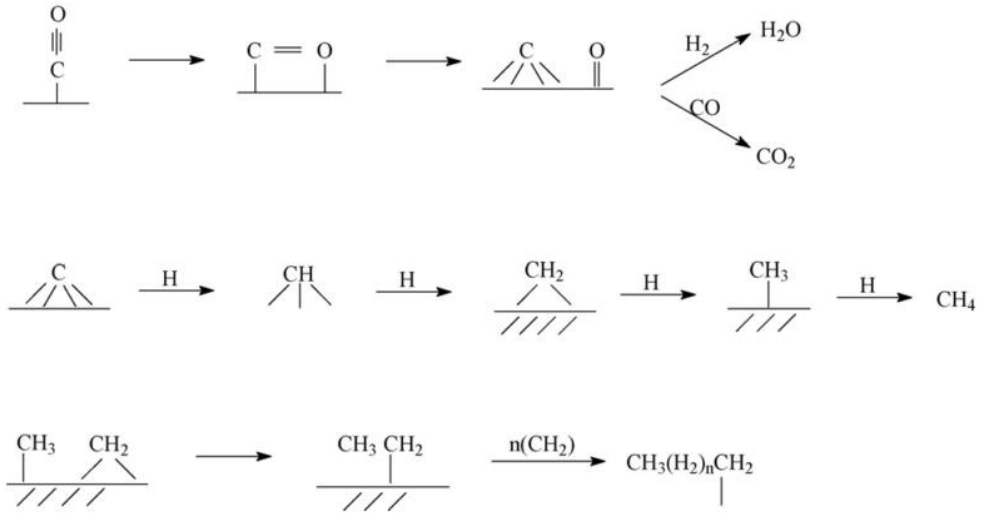

Scheme 1-4: Carbine mechanism [125].

A lot of mechanisms have been proposed for Fischer Tropsch synthesis process. Each of these mechanisms has evidence to support it, whereas, contradictory data also exist for all of them [113]. Hence, Fischer Tropsch synthesis system could not be controlled by only single mechanism (the product distribution may be controlled by several mechanisms). Moreover, the investigations of present mechanisms were mainly based on the catalyst surface reaction or macroscopical performances for the Fischer Tropsch synthesis.

1.6 Molybdenum carbide catalysts

Transition metal carbides have been paid attention since Levy and Boudart[126] reported that tungsten carbide exhibited catalytic properties approaching those of platinum catalysts. Molybdenum carbide catalysts have received special attention because they are easily prepared with high surface areas using the temperature programmed reduction method described by Boudart et al [127]. The metal carbides have similar performances as noble metals which may be due to their similar electronic structure.

1.6.1 Preparation methods of molybdenum carbides

The traditional methods for the preparation of molybdenum carbide involved directly carburization of metallic molybdenum with graphitic carbon at high temperature (normally > 1000 ℃), which is unsuitable for catalysts due to the very low surface area of generated molybdenum carbide product [128]. Different preparation methods have been used for the synthesis of high surface area molybdenum carbide materials.

1.6.1.1 Temperature-programmed reduction method (TPR)

Temperature-programmed reduction method has been established by Volpe and Boudart [129] in 1980s and it has been widely used to synthetize molybdenum carbide with high surface area. Typically, the molybdenum oxide precursor is treated under hydrocarbon/H_2 atmosphere in a temperature programmed process. The oxide precursor is reduced and carburized with the increasing temperature to generate molybdenum carbide. MoO_3, MoO_2 or even molybdenum salt can be used as precursor and the carburization gas can be CH_4, C_2H_6, C_3H_8 as well as CO. This method is easy to operate and can be used for both bulk and supported molybdenum carbide.

Claridge et al. [75] prepared bulk Mo_2C with BET surface area of 30 m^2/g with TPR method under CH_4/H_2 mixtures at 727 ℃. Frank et al. [130] prepared Mo_2C/CNT by impregnation method with CH_4/H_2 and C_2H_6/H_2 gases mixtures. The results revealed that MoO_3 was reduced to MoO_2 in a temperature range of 400-500 ℃, the partial carburization of MoO_2 to MoO_xC_y occurred at 500-600 ℃, while the complete transformation of MoO_xC_y to Mo_2C occurred at the end of the carburization process after 1 h at 700 ℃.

1.6.1.2 Pyrolysis method

Pyrolysis method involves the thermo-decomposition of special molybdenum compound (such as molybdenum hexacarbonyl) under inert gaseous atmosphere and high temperature, which is a simple method for the synthesis of molybdenum carbides catalysts. This raw material for Mo_2C is not easy to get and the insolubility of molybdenum hexacarbonyl limits the application of supported catalysts for pyrolysis method.

Giraudon et al.[131] prepared successfully molybdenum carbides using dimolybdenum alkyne complex by pyrolysis method under hydrogen at low temperatures (550 ℃). However, organic impurities have been detected in the generated Mo_2C samples. Li et al. [132] synthetized composite microtubes shape Mo_2C/MoCO by thermal decomposition of $Mo(CO)_6$ under well-controlled conditions, at about 600 ℃ under argon flow.

1.6.1.3 Direct thermal solid carburization method

Thermal solid carburization is a preparation method that converts molybdenum compounds with carbon or carbon-containing materials at high temperature into Mo_2C.

Generally, molybdenum oxides and molybdenum salts react with specific organics compounds to generate molybdenum-organic complexes, and then increase temperature under inert or reducing gases atmosphere to produce molybdenum carbide. Mo_2C prepared by thermal solid carburization method usually owns high surface area. Liang et al.[133] impregnated ammonium heptamolybdate on an ultra-high surface area carbon material (BET surface >3000m^2/g) and then increased the temperature up to 700 ℃ under an H_2 flow. A β-Mo_2C supported on activated carbon support with a BET surface area of 2180 m^2/g was successfully produced. Wang et al. [128] pretreated ammonium heptamolybdate with hexamethylenetetramine (HMT) to generate a molybdenum HMT complex, and then the complex was calcined in argon atmosphere at 700 ℃ to produce a bulk β-Mo_2C with a BET surface area of 31.9 m^2/g.

When compared with the TPR method, this thermal solid carburization method is simple, does not require gas flow of alkane (CH_4 or C_2H_6), and slow ramp rate is not required. However, this method is not optimized to get supported carbide catalysts or can only be used to get carbon material supported carbide catalysts.

1.6.1.4 Chemical vapor deposition method (CVD)

Chemical vapor deposition method is a very important method for catalyst preparation which has been used for production of molybdenum carbide. Typically, molybdenum compound and activated carbon mixture are heated up to high temperature (800 ℃) under inert gases atmosphere. Molybdenum compound sublimates into a gas phase and is adsorbed into activated pores, and then when increasing the temperature up to 1300 ℃, further reactions to get molybdenum carbide occur. Miyao et al.[134] synthesized successfully an alumina-supported Mo carbide catalyst using a chemical vapor deposition (CVD) technique.

The obvious defect for the chemical vapor deposition is the difficulty to control the operating process and limited production capacity.

1.6.2 Applications of molybdenum carbide

Since Levy and Boudart[126] reported that tungsten carbide exhibits catalytic properties approaching those of platinum, more and more [researches focus on metal carbides. It has been widely used in hydrodesulfurization (HDS) and hydrodenitrogenation (HDN) processes

and also exhibits high activity for dry reforming, alkane isomerization, and CO hydrogenation [135-137]. Many works in the literature reveal that molybdenum carbide materials are effective catalysts for dry methane reforming. This thesis mainly describes the application of molybdenum carbides in dry methane reforming and Fischer-Tropsch synthesis.

1.6.2.1 Application of molybdenum carbides in DMR

In 1997, York A. P. E. [74] reported that molybdenum carbide catalysts are active for methane activation in steam reforming and CO_2 reforming. Mo_2C have a high selectivity towards CO and H_2. No carbon deposition was observed over molybdenum carbide catalyst during the reactions. J. B. Claridge [75] used high-surface-area molybdenum catalysts, which were prepared by the temperature programming reduction method with methane. The results showed that both DMR activity and CO yield were very high.

Even through the metal carbide catalysts have high activity and good resistance of carbon deposition, the oxidation of those materials at atmospheric pressure is the primary reason for their deactivation. A. R. S. Darujati et al.[138] investigated the oxidation process and the effect of CO co-feed with CH_4 and CO_2 on a molybdenum carbide catalyst using dynamically XRD system (DXRD). The result shows that CO_2 is a strong oxidizing agent and the high temperature oxidation cannot be totally prevented by CO at the high concentration employed in this study. The oxidation process may be as the following equation:

$$Mo_2C + 5\ CO_2 \leftrightarrow 2\ MoO_2 + 6\ CO \qquad \text{Equation 1-22}$$

The oxidation of Mo_2C by CO_2 to form MoO_2 was hypothesized to be faster than the carburization of MoO_2 with CH_4 to form Mo_2C. It is the reason of deactivation of metal carbides. Many works study the stability of metal carbides during methane dry reforming.

Pressure is a significant factor for the catalyst stability. J. B. Claridge et al.[74] investigated the lifetime of β-Mo_2C for the dry methane reforming reaction at different pressure and temperature. When the dry reforming reaction was carried out at elevated pressure, high activity was maintained during more than 72 h with no observable deterioration in activity. This suggests that the increase in pressure can be a good way to keep an excellent stability of metal carbides during dry methane reforming.

1.6.2.1.1 Effect of support for Mo_2C catalysts on dry methane reforming

Support can improve the dispersion of molybdenum species, provide strong basic sites and strong interaction with molybdenum particles. This could affect the catalytic performance and stability of Mo_2C catalysts over dry methane reforming. Darujati et al.[139] investigated the stability of Mo_2C in dry methane reforming over Al_2O_3, ZrO_2 and MgO supports in the presence of Ce, K and Zr promoters. The alumina appeared to be superior compared to other supports due to its high surface area and high thermal stability, and Mo_2C/γ-Al_2O_3 had a higher activity than a bulk Mo_2C catalyst. Du et al.[140] studied the Mo_2C supported on ZrO_2 catalysts over dry methane reforming. Due to the Lewis acid and basic active sites on the surface of ZrO_2 and enhancement of Mo species dispersion, the supported Mo_2C catalysts exhibited a higher conversion than the corresponding low surface area bulk Mo_2C catalyst. Huang et al.[141, 142] investigated the SBA-15 supported Mo_2C catalysts over dry methane reforming. The result indicated that the Ni/Mo_2C/SBA-15 catalyst exhibited a better catalytic and anti-coking performance due to smaller metal particles, higher metal dispersion, and better ordered pore distribution compared with Mo_2C catalysts. The surface carbon of nickel migrated to molybdenum carbide, which prevented the oxidation of molybdenum carbide and coke deposition.

1.6.2.1.2 Effect of promoters for Mo_2C catalysts on dry methane reforming

Promoters are often used to improve the activity and to enhance the stability of molybdenum carbide catalysts over dry methane reforming.

Rare earth metals promoters, mainly La and Ce, have been widely studied on nickel based catalysts over dry methane reforming; it is also been studied on the promotion of molybdenum carbide catalysts. France et al.[143] investigated the effect of La promotion over Al_2O_3 supported Co-Mo carbide catalysts over dry methane reforming. The addition of lanthanum at low loading level (1 wt%) results in smaller carbide crystallite sizes compared to catalysts containing either no lanthanum or higher lanthanum loading levels and possessed superior catalytic properties for dry methane reforming and was stable for 100 h.

Ce was found to act as an active site for strong CO_2 adsorption; a redox cycle was also proposed which accounted for CO_2 and CO interactions with the Ce^{3+} and Ce^{4+} oxides. It was employed as a promoter for molybdenum carbide catalysts in the study of Darujati et al.[139] The results revealed the promotion of Ce dramatically improved the stability of the Mo_2C/Al_2O_3 catalysts. Characterizations indicated that the Ce prevent oxidation of Mo_2C by CO_2 during reaction.

Transition metals like Ni and Co are known to own a well CH_4 decomposition capacity, which is beneficial for resistance to molybdenum carbides oxidation of during dry methane reforming. France et al.[143] found that cobalt inserts into the Mo_2C lattice, which significant enhanced the conversion yield and stability of the catalysts. Increasing the Co loading in the mixed metal carbides was seen to enhance the resistance of the catalyst to the reverse water gas shift reaction.

Chaktong A.[144-146] explored a series of Ni modified Mo_2C catalysts. The results showed that the synergistic effect between nickel and molybdenum clearly improved the stability. For Ni: Mo=1:2, the Ni–Mo_2C catalyst shows high conversion and stability over a run of 20 h. Not like the single molybdenum catalyst, the Ni promoted catalysts could even be carburized in a flow of CH_4/CO_2. On the other hand, rapid decline of performance was observed over Ni:Mo is 1:3 and 1:1. The CO_2-TPO and XRD investigation indicated that on the case of Ni: Mo=1:1, the reason of catalyst deactivation was coking rather than oxidation, while on the case of Ni: Mo=1:3, the deactivation is mainly due to oxidation. They mentioned that when at a proper Ni/Mo molar ratio that an "oxidation–recarburization" cycle could be established and a stable DRM activity could be maintained as demonstrated in the case of Ni:Mo=1:2 (as is shown in Figure 1-6) .

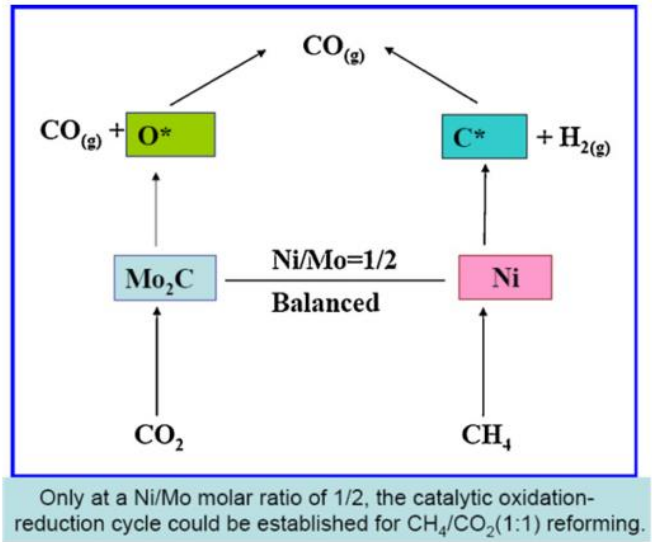

Figure 1-6: Catalytic oxidation–recarburization cycle over Ni–Mo_2C catalyst.

1.6.2.2 Applications of molybdenum carbide in FTS

Noble metal Ru has been proven excellent performance on Fischer-Tropsch synthesis, which is the most active metal for the hydrogenation of carbon monoxide [135]. High price

and limited reserves on the earth restrict the large scale application of Ru catalysts on the industry. Molybdenum carbide (Mo_2C), which shows strong similarity in the catalytic performances with those of more expensive noble metals, has been received increasing attention during the past several decades [147]. Particularly, Molybdenum carbide has become an attractive and promising catalyst for replacement of traditional Fischer–Tropsch (FT) catalysts for hydrocarbon production due to its resistance for carbon deposition. The studies of molybdenum carbides over Fischer-Tropsch synthesis mainly focus on the synthesis of alcohols and olefins.

1.6.2.2.1 Use of molybdenum carbide catalysts for alcohol synthesis from syngas

The catalytic process of mixed alcohol synthesis (MAS) from coal or natural gas derived from syngas is one of the challenging and attractive subjects in the field of C1 chemistry [148]. Individual molybdenum carbide catalyst has been revealed to mainly generate light alkanes [149, 150]. Addition of different promoters may therefore lead to the modification of molybdenum carbides structure, electronic properties and reactivity of active sites. The FTS products selectivities on molybdenum carbide catalysts can be also affected by the promotion.

Alkali metal promoters, which can increase the electron density of iron and promote the dissociated adsorption of CO and enhance the CO conversion, have been widely studied for the iron based catalysts over FTS. The addition of alkali metals promoter to molybdenum carbides based catalysts was also studied by many researchers. Woo et al.[149] studied the K_2CO_3 promotion in the bulk molybdenum carbide catalysts. The result revealed that un-promoted molybdenum carbide produced mainly hydrocarbons of C1-C7. The K_2CO_3-promoted molybdenum carbide catalysts were shown to produce C1-C7 linear alcohols from synthesis gas with fairly high selectivity for C_2^+OH. Al-Megren [151] explored the K promotion over supported molybdenum carbide catalysts. The result indicated potassium content has a significant effect on the catalyst performance. The addition of K improved Mo_2C dispersion on support. Shou et al.[152] indicated addition of Rb_2CO_3 to Mo_2C/MgO substantially improved the selectivity to alcohols at the expense of hydrocarbons. Higher alcohol synthesis was favoured at high syngas pressure and low CO conversion.

Transition metals, especially Fe, Co and Ni, have good catalytic performance for FTS, and also been studied as promoters for molybdenum carbide catalysts in alcohols synthesis over FTS. Griboval-Constant et al.[153] investigated Co dispersed on Mo_2C over Fischer–Tropsch reaction and compared to bulk Mo_2C. It was found that bulk Mo_2C gave light

hydrocarbons, alcohols and CO_2. Noteworthy activity increases with the promotion with cobalt. The addition of Co increased the formation of heavy hydrocarbons. Xiang et al. [135-137, 150, 154, 155] prepared a serial of different transition metals promoted K/β-Mo_2C catalysts: K/Fe/β-Mo_2C, K/Co/β-Mo_2C, and K/Ni/β-Mo_2C. The addition of Ni and Co were shown to result in highly active and selective catalysts towards the synthesis of mixed alcohols, especially for the C_2^+OH production, but addition of Fe caused a slight increase for methanol and decrease for C_2-C_4 alcohols. The presence of Co increased the selectivity to both higher alcohols and hydrocarbons obviously. A strong synergistic interaction between Co and Mo was proven. The formed new phases "Co_3Mo_3C" and "Co_2C" over Co promoted K/β-Mo_2C catalysts might be responsible for the high activity. The addition of nickel also enhanced higher alcohols synthesis. The characterization suggested a synergistic effect of potassium and nickel on β-Mo_2C, which favoured the alcohols synthesis. The production of alcohols appeared to be relevant to the presence of Mo^{4+} species, whereas the formation of hydrocarbons was closely associated with Mo^{2+} and/or Mo^0 species on the surface of β-Mo_2C-based catalyst. The promotion effects of Fischer-Tropsch synthesis were followed the sequence: Ni >> Co > Fe for the activity and Ni > Co > Fe for the C_2^+ alcohol selectivity.

1.6.2.2.2 Synthesis of olefins over molybdenum carbide catalysts

As an important part of Fischer-Tropsch synthesis products, light olefins, includes ethylene, propylene, and butylene, acts as key building blocks for the petrochemical industry due to their widely used in variety of reactions [82]. Some studies focus on the synthesis of light olefins over molybdenum carbides catalysts. Kim et al.[156] studied supported and unsupported molybdenum and molybdenum carbides over FTS at atmospheric pressure. A large amount of CO_2 was produced and a high paraffin/olefin ratio reflected high activities of these catalysts for hydrogenation. As individual molybdenum carbides catalysts mainly generated light alkanes, the studies for molybdenum carbide catalysts main concentrate on the promoted catalysts.

Park et al. [157] investigated unsupported molybdenum carbides and the addition of K_2CO_3 at atmospheric pressure, they found the molybdenum carbides catalysts produced mostly C_1-C_5 paraffin. The promotion of the catalyst with 20w% K_2CO_3 yielded C_2-C_5 hydrocarbons consisting of 80-100% olefins and reduced methane selectivity. The selectivity of C_2-C_5 olefins among all hydrocarbon products was 50-70 wt% at CO conversions up to 70%.

Dai-Viet N et al. [158-166] investigated different metals promoted molybdenum carbide catalyst. All catalysts were investigated at atmosphere pressure in Fischer-Tropsch Synthesis. The result showed that Fischer–Tropsch specific reaction rate decreased in the order; MoC_{1-x}/TiO_2 > MoC_{1-x}/SiO_2 > MoC_{1-x}/ZrO_2 > MoC_{1-x}/Al_2O_3 parallel to the trend for Mo carbide production rate. Different promoters K, Na, Co, and Ce have been added to modify the catalysts performance. The result showed that F-T activity improved with promoter addition in the order; K–MoC_{1-x}/Al_2O_3 > Na–MoC_{1-x}/Al_2O_3 > Ce–MoC_{1-x}/Al_2O_3 > Co–MoC_{1-x}/Al_2O_3 > MoC_{1-x}/Al_2O_3 while chain growth probability varied with feed composition and was enhanced by all promoters.

1.7 Hypothesized industry process for utilization of biogas by dry methane reforming and Fischer-Tropsch synthesis analysis

As shown in the previous sections, the product of dry methane reforming is syngas, which is at the same time a feedstock for Fischer-Tropsch synthesis. Hence, the generated syngas from dry methane reforming can be used for the Fischer-Tropsch synthesis. The hypothesized industry process could be summarized and is displayed in Figure 1-7.

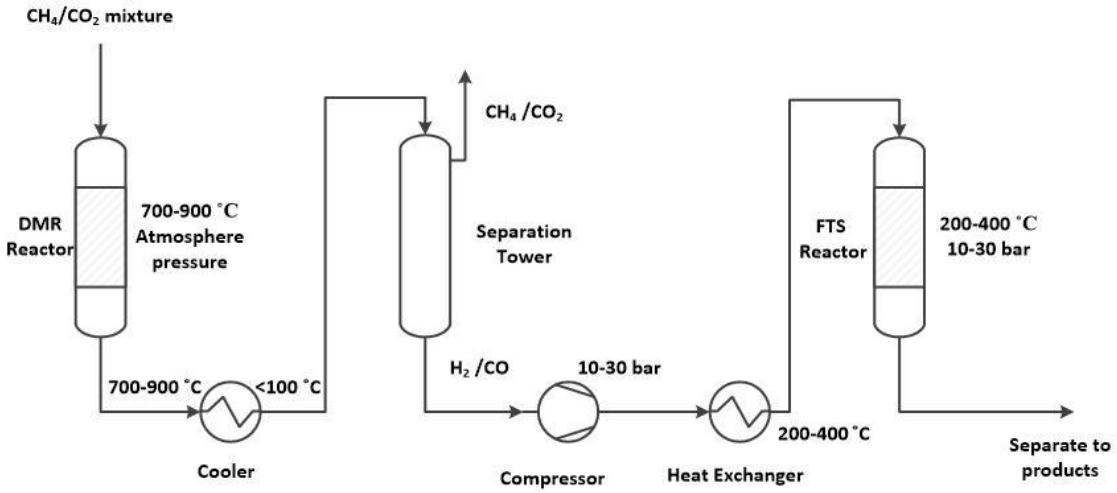

Figure 1-7: Schematic for hypothesized industry process of dry methane reforming and Fischer-Tropsch synthesis.

Dry methane reforming process is known as an endothermic reaction, which indicates that higher temperature is advantageous for the syngas production. However, high temperature obviously increases the cost and energy consumption. Thus, the reforming of methane is generally operated at 700 – 900 ˚C based on the balance of reactant conversion and manipulation cost.

Generally, the generated syngas from DMR contains unreacted CH_4 and CO_2. Separation of CH_4 and CO_2 is necessary for syngas proceed to Fischer-Tropsch synthesis. Furthermore, the process for Fischer-Tropsch synthesis is generally operated at elevated pressure (10-30 bar) [35]. Thus, a compressor is required for compressing the feed gas before Fischer-Tropsch synthesis reactor (shown in Figure 1-7).

Pressure Swing Adsorption (PSA) and membrane separation, which are two common technologies for CH_4 and CO_2 separation, are known to be operated at low temperature [167-169]. Besides, the inlet temperature for a compressor is limited to 100 ˚C (higher gas temperature will lead to lower compressor efficiency). Thus, the product gas owning high temperature (normally 700-900 ˚C) from dry methane reforming process has to be cooled down to low temperature through a cooler.

1.8 The objectives of this thesis

Dry methane reforming and Fischer-Tropsch synthesis can also be proposed to be combined in a sequential process. The industry process for sequential dry methane reforming and Fisher-Tropsch synthesis is proposed and shown in the Figure 1-8.

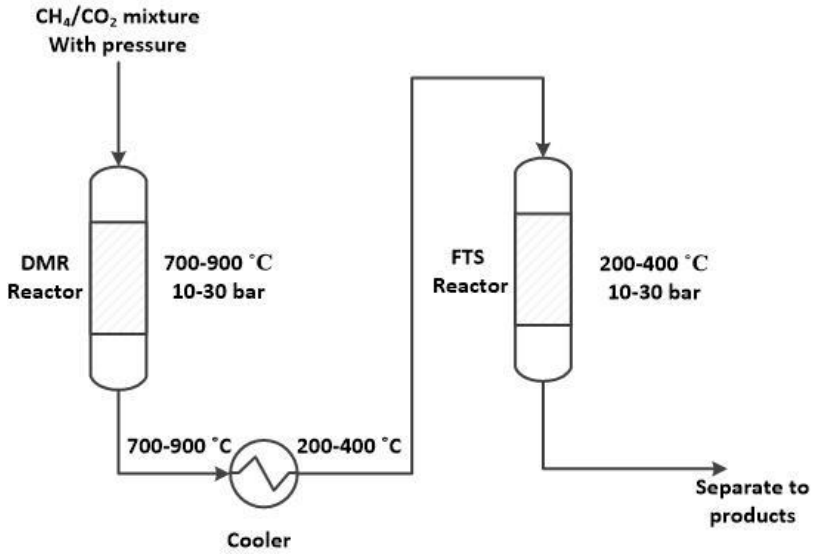

Figure 1-8: Schematic for industry process of sequential dry methane reforming and Fischer-Tropsch synthesis in a single process.

In the sequential process, dry methane reforming and Fischer-Tropsch synthesis could be performed at same pressure. Separation, compressing and additional heat exchange procedure are then not needed. The sequential DMR and FTS process exhibits obviously advantage due to the evident saving of energy consumption and facility investment.

Catalyst plays a crucial role for this proposed process. Owning similar structure with noble metals, molybdenum carbide has been proven good performances in dry methane reforming and an excellent capacity for resistance toward carbon deposition. Molybdenum carbide has been also used in Fischer-Tropsch synthesis. Molybdenum carbide ensures high Water-Gas Shift reaction activity. This indicates that Mo_2C is efficient in the case of low H_2/CO ratio syngas, which is particularly applicable for the syngas generated from DMR. Furthermore, molybdenum carbide exhibits sulphur tolerance property [170], which is a distinct advantage as biogas always contains traces of H_2S.

Additionally, using the same catalysts for both reactions of DMR and FTS is advantageous and reduces the process cost (catalyst synthesis, activation, regeneration, recycling).

Thus, the general goal of this thesis is to investigate the feasibility of combining dry methane reforming and Fischer-Tropsch synthesis in a single process by developing molybdenum carbide catalysts that can be used for both DMR and FTS.

Thus, the specific goals for dry methane reforming of this thesis are to:

- Investigate the structure, the chemical properties and the DMR catalytic performances of nickel promoted Mo_2C catalysts, supported on alumina;
- Study the interaction between Mo and alumina support as well as the catalytic performance in DMR with the different preparation methods;
- Study the catalytic behaviours of molybdenum carbide catalysts in DMR at elevated pressure.

The specific goals for FTS of this thesis are to:

- Study the support influence on the structure, the chemical properties and the FTS catalytic performances of non-promoted molybdenum carbides catalysts;
- Study the effect of promoters (K, Na, Fe and Ni) on the structure, chemical properties and FTS catalytic performance of the supported molybdenum carbides catalysts;
- Optimize the promoter content;
- Investigate the influence of CH_4 and CO_2 containing syngas on Fischer-Tropsch synthesis.

1.9 References

[1] O. Tahvonen, S. Salo, Economic growth and transitions between renewable and nonrenewable energy resources, European Economic Review, 45 (2001) 1379-1398.

[2] O. Ellabban, H. Abu-Rub, F. Blaabjerg, Renewable energy resources: Current status, future prospects and their enabling technology, Renewable and Sustainable Energy Reviews, 39 (2014) 748-764.

[3] O. Hijazi, S. Munro, B. Zerhusen, M. Effenberger, Review of life cycle assessment for biogas production in Europe, Renewable and Sustainable Energy Reviews, 54 (2016) 1291-1300.

[4] L. Appels, J. Lauwers, J. Degrève, L. Helsen, B. Lievens, K. Willems, J. Van Impe, R. Dewil, Anaerobic digestion in global bio-energy production: Potential and research challenges, Renewable and Sustainable Energy Reviews, 15 (2011) 4295-4301.

[5] A. Colmenar-Santos, G. Zarzuelo-Puch, D. Borge-Diez, C. García-Diéguez, Thermodynamic and exergoeconomic analysis of energy recovery system of biogas from a wastewater treatment plant and use in a Stirling engine, Renewable Energy, 88 (2016) 171-184.

[6] N. Hajjaji, S. Martinez, E. Trably, J.-P. Steyer, A. Helias, Life cycle assessment of hydrogen production from biogas reforming, International Journal of Hydrogen Energy, 41 (2016) 6064-6075.

[7] C. Zhang, H. Su, J. Baeyens, T. Tan, Reviewing the anaerobic digestion of food waste for biogas production, Renewable and Sustainable Energy Reviews, 38 (2014) 383-392.

[8] J.B. Holm-Nielsen, T. Al Seadi, P. Oleskowicz-Popiel, The future of anaerobic digestion and biogas utilization, Bioresource Technology, 100 (2009) 5478-5484.

[9] A. Hublin, D.R. Schneider, J. Džodan, Utilization of biogas produced by anaerobic digestion of agro-industrial waste: Energy, economic and environmental effects, Waste Management & Research, (2014) 0734242X14539789.

[10] X. Wang, X. Lu, G. Yang, Y. Feng, G. Ren, X. Han, Development process and probable future transformations of rural biogas in China, Renewable and Sustainable Energy Reviews, 55 (2016) 703-712.

[11] T. Zhang, Y. Yang, D. Xie, Insights into the production potential and trends of China's rural biogas, International Journal of Energy Research, 39 (2015) 1068-1082.

[12] V. Massaro, S. Digiesi, G. Mossa, L. Ranieri, The sustainability of anaerobic digestion plants: a win–win strategy for public and private bodies, Journal of Cleaner Production, 104 (2015) 445-459.

[13] H. Cheng, L. Wang, Lignocelluloses Feedstock Biorefinery as Petrorefinery Substitutes, (2013).

[14] A.J. Ward, P.J. Hobbs, P.J. Holliman, D.L. Jones, Optimisation of the anaerobic digestion of agricultural resources, Bioresource technology, 99 (2008) 7928-7940.

[15] F. Tambone, P. Genevini, G. D'Imporzano, F. Adani, Assessing amendment properties of digestate by studying the organic matter composition and the degree of biological stability during the anaerobic digestion of the organic fraction of MSW,

Bioresource Technology, 100 (2009) 3140-3142.

[16] M. Inyang, B. Gao, P. Pullammanappallil, W. Ding, A.R. Zimmerman, Biochar from anaerobically digested sugarcane bagasse, Bioresource Technology, 101 (2010) 8868-8872.

[17] Y. Yao, B. Gao, M. Inyang, A.R. Zimmerman, X. Cao, P. Pullammanappallil, L. Yang, Biochar derived from anaerobically digested sugar beet tailings: Characterization and phosphate removal potential, Bioresource Technology, 102 (2011) 6273-6278.

[18] M. Inyang, B. Gao, Y. Yao, Y. Xue, A.R. Zimmerman, P. Pullammanappallil, X. Cao, Removal of heavy metals from aqueous solution by biochars derived from anaerobically digested biomass, Bioresource Technology, 110 (2012) 50-56.

[19] C. Chen, W. Guo, H.H. Ngo, D.-J. Lee, K.-L. Tung, P. Jin, J. Wang, Y. Wu, Challenges in biogas production from anaerobic membrane bioreactors, Renewable Energy.

[20] W. Papacz, Biogas as vehicle fuel, Journal of KONES, 18 (2011) 403-410.

[21] L.C. Martins das Neves, A. Converti, T.C. Vessoni Penna, Biogas production: new trends for alternative energy sources in rural and urban zones, Chemical engineering & technology, 32 (2009) 1147-1153.

[22] E. Theofanous, N. Kythreotou, G. Panayiotou, G. Florides, I. Vyrides, Energy production from piggery waste using anaerobic digestion: Current status and potential in Cyprus, Renewable Energy, 71 (2014) 263-270.

[23] M. Persson, O. Jönsson, A. Wellinger, Biogas upgrading to vehicle fuel standards and grid injection, in: IEA Bioenergy task, 2006.

[24] M.R. Hamedi, A. Tsolakis, C.S. Lau, Biogas upgrading for on-board hydrogen production: Reforming process CFD modelling, International Journal of Hydrogen Energy, 39 (2014) 12532-12540.

[25] M. Pöschl, S. Ward, P. Owende, Evaluation of energy efficiency of various biogas production and utilization pathways, Applied Energy, 87 (2010) 3305-3321.

[26] Teodorita Al Seadi, Dominik Rutz, Heinz Prassl, Michael Köttner, Tobias Finsterwalder, Silke Volk, R. Janssen, Biogas Handbook, in, 2008.

[27] P. Weiland, Biogas production: current state and perspectives, Applied Microbiology and Biotechnology, 85 (2009) 849-860.

[28] H. Zhang, P.K. Shen, Recent development of polymer electrolyte membranes for fuel cells, Chemical Reviews, 112 (2012) 2780-2832.

[29] S.G. Gopaul, A. Dutta, Dry reforming of multiple biogas types for syngas production simulated using Aspen Plus: The use of partial oxidation and hydrogen combustion to achieve thermo-neutrality, International Journal of Hydrogen Energy, 40 (2015) 6307-6318.

[30] K.-H. Lin, H.-F. Chang, A.C.C. Chang, Biogas reforming for hydrogen production over mesoporous Ni2xCe1−xO2 catalysts, International Journal of Hydrogen Energy, 37 (2012) 15696-15703.

[31] S. Appari, V.M. Janardhanan, R. Bauri, S. Jayanti, Deactivation and regeneration of Ni catalyst during steam reforming of model biogas: An experimental investigation, International Journal of Hydrogen Energy, 39 (2014) 297-304.

[32] M. Kaewpanha, G. Guan, Y. Ma, X. Hao, Z. Zhang, P. Reubroychareon, K. Kusakabe, A. Abudula, Hydrogen production by steam reforming of biomass tar over biomass char supported molybdenum carbide catalyst, International Journal of Hydrogen Energy, 40 (2015) 7974-7982.

[33] A. Ashcroft, A. Cheetham, M. Green, Partial oxidation of methane to synthesis gas using carbon dioxide, Nature, 352 (1991) 225-226.

[34] Y. Cui, H. Zhang, H. Xu, W. Li, Kinetic study of the catalytic reforming of CH4 with CO2 to syngas over Ni/α-Al2O3 catalyst: The effect of temperature on the reforming mechanism, Applied Catalysis A: General, 318 (2007) 79-88.

[35] A.Y. Khodakov, W. Chu, P. Fongarland, Advances in the development of novel cobalt Fischer-Tropsch catalysts for synthesis of long-chain hydrocarbons and clean fuels, Chemical Reviews, 107 (2007) 1692-1744.

[36] P. Djinović, J. Batista, A. Pintar, Efficient catalytic abatement of greenhouse gases: Methane reforming with CO2 using a novel and thermally stable Rh–CeO2 catalyst, International Journal of Hydrogen Energy, 37 (2012) 2699-2707.

[37] K. Tomishige, S. Kanazawa, K. Suzuki, M. Asadullah, M. Sato, K. Ikushima, K. Kunimori, Effective heat supply from combustion to reforming in methane reforming with CO2 and O2: comparison between Ni and Pt catalysts, Applied Catalysis A: General, 233 (2002) 35-44.

[38] A.M. O'Connor, Y. Schuurman, J.R. Ross, C. Mirodatos, Transient studies of carbon dioxide reforming of methane over Pt/ZrO2 and Pt/Al2O3, Catalysis today, 115 (2006) 191-198.

[39] J. Bitter, W. Hally, K. Seshan, J. Van Ommen, J. Lercher, The role of the oxidic support on the deactivation of Pt catalysts during the CO2 reforming of methane, Catalysis today, 29 (1996) 349-353.

[40] C. Carrara, J. Munera, E. Lombardo, L. Cornaglia, Kinetic and stability studies of Ru/La2O3 used in the dry reforming of methane, Topics in Catalysis, 51 (2008) 98-106.

[41] M.F. Mark, W.F. Maier, CO2-Reforming of Methane on Supported Rh and Ir Catalysts, Journal of Catalysis, 164 (1996) 122-130.

[42] F. Solymosi, G. Kutsan, A. Erdöhelyi, Catalytic reaction of CH4 with CO2 over alumina-supported Pt metals, Catalysis letters, 11 (1991) 149-156.

[43] C.O. Hawk, P.L. Golden, H. Storch, A. Fieldner, Conversion of Methane to Carbon Monoxide and Hydrogen, Industrial & Engineering Chemistry, 24 (1932) 23-27.

[44] O. Tokunaga, S. Ogasawara, Reduction of carbon dioxide with methane over Ni-catalyst, Reaction Kinetics and Catalysis Letters, 39 (1989) 69-74.

[45] X. Hengyong, S. Xixian, F. Yemei, X. Guolin, L. Jinxiang, Y. Wenge, Z. Peiheng, Studies of Reforming Methane with Carbon Dioxide to Produce Synthesis Gas I. Catalyst and Its Catalytic Property, Petrochemical Technology, 3 (1992) 001.

[46] A. Lemonidou, M. Goula, I. Vasalos, Carbon dioxide reforming of methane over 5wt.% nickel calcium aluminate catalysts – effect of preparation method, Catalysis today, 46 (1998) 175-183.

[47] W. Zhang, B. Liu, Y. Tian, CO2 reforming of methane over Ni/Sm2O3–CaO

catalyst prepared by a sol–gel technique, Catalysis Communications, 8 (2007) 661-667.

[48] M. Usman, W.M.A. Wan Daud, H.F. Abbas, Dry reforming of methane: Influence of process parameters—A review, Renewable and Sustainable Energy Reviews, 45 (2015) 710-744.

[49] J. Deng, M. Cai, W. Sun, X. Liao, W. Chu, X.S. Zhao, Oxidative Methane Reforming with an Intelligent Catalyst: Sintering‐Tolerant Supported Nickel Nanoparticles, ChemSusChem, 6 (2013) 2061-2065.

[50] Z. Xu, N. Wang, W. Chu, J. Deng, S. Luo, In situ controllable assembly of layered-double-hydroxide-based nickel nanocatalysts for carbon dioxide reforming of methane, Catalysis Science & Technology, 5 (2015) 1588-1597.

[51] M. García-Diéguez, E. Finocchio, M.Á. Larrubia, L.J. Alemany, G. Busca, Characterization of alumina-supported Pt, Ni and PtNi alloy catalysts for the dry reforming of methane, Journal of Catalysis, 274 (2010) 11-20.

[52] M. García-Diéguez, I.S. Pieta, M.C. Herrera, M.A. Larrubia, L.J. Alemany, Nanostructured Pt- and Ni-based catalysts for CO2-reforming of methane, Journal of Catalysis, 270 (2010) 136-145.

[53] F. Meshkani, M. Rezaei, Nanocrystalline MgO supported nickel-based bimetallic catalysts for carbon dioxide reforming of methane, International Journal of Hydrogen Energy, 35 (2010) 10295-10301.

[54] M. Ocsachoque, F. Pompeo, G. Gonzalez, Rh–Ni/CeO2–Al2O3 catalysts for methane dry reforming, Catalysis Today, 172 (2011) 226-231.

[55] Ş. Özkara-Aydınoğlu, A.E. Aksoylu, CO2 reforming of methane over Pt–Ni/Al2O3 catalysts: Effects of catalyst composition, and water and oxygen addition to the feed, International Journal of Hydrogen Energy, 36 (2011) 2950-2959.

[56] B. Christian Enger, R. Lødeng, A. Holmen, A review of catalytic partial oxidation of methane to synthesis gas with emphasis on reaction mechanisms over transition metal catalysts, Applied Catalysis A: General, 346 (2008) 1-27.

[57] J. Juan-Juan, M. Román-Martínez, M. Illán-Gómez, Catalytic activity and characterization of Ni/Al2O3 and NiK/Al2O3 catalysts for CO2 methane reforming, Applied Catalysis A: General, 264 (2004) 169-174.

[58] H. Jeong, K.I. Kim, D. Kim, I.K. Song, Effect of promoters in the methane reforming with carbon dioxide to synthesis gas over Ni/HY catalysts, Journal of Molecular Catalysis A: Chemical, 246 (2006) 43-48.

[59] L. Mo, K.K.M. Leong, S. Kawi, A highly dispersed and anti-coking Ni-La2O3/SiO2 catalyst for syngas production from dry carbon dioxide reforming of methane, Catalysis Science & Technology, 4 (2014) 2107-2114.

[60] U. Oemar, Y. Kathiraser, L. Mo, X.K. Ho, S. Kawi, CO2 reforming of methane over highly active La-promoted Ni supported on SBA-15 catalysts: mechanism and kinetic modelling, Catalysis Science & Technology, 6 (2016) 1173-1186.

[61] C.E. Daza, J. Gallego, F. Mondragón, S. Moreno, R. Molina, High stability of Ce-promoted Ni/Mg–Al catalysts derived from hydrotalcites in dry reforming of methane, Fuel, 89 (2010) 592-603.

[62] M. Akri, T. Chafik, P. Granger, P. Ayrault, C. Batiot-Dupeyrat, Novel nickel promoted illite clay based catalyst for autothermal dry reforming of methane, Fuel, 178 (2016) 139-147.

[63] N. Wang, K. Shen, L. Huang, X. Yu, W. Qian, W. Chu, Facile Route for Synthesizing Ordered Mesoporous Ni–Ce–Al Oxide Materials and Their Catalytic Performance for Methane Dry Reforming to Hydrogen and Syngas, ACS Catalysis, 3 (2013) 1638-1651.

[64] N. Wang, W. Chu, T. Zhang, X.S. Zhao, Synthesis, characterization and catalytic performances of Ce-SBA-15 supported nickel catalysts for methane dry reforming to hydrogen and syngas, International Journal of Hydrogen Energy, 37 (2012) 19-30.

[65] Z.L. Zhang, V.A. Tsipouriari, A.M. Efstathiou, X.E. Verykios, Reforming of Methane with Carbon Dioxide to Synthesis Gas over Supported Rhodium Catalysts: I. Effects of Support and Metal Crystallite Size on Reaction Activity and Deactivation Characteristics, Journal of Catalysis, 158 (1996) 51-63.

[66] E. Ruckenstein, Y.H. Hu, Carbon dioxide reforming of methane over nickel/alkaline earth metal oxide catalysts, Applied Catalysis A: General, 133 (1995) 149-161.

[67] Z. Zhang, X.E. Verykios, S.M. MacDonald, S. Affrossman, Comparative study of carbon dioxide reforming of methane to synthesis gas over Ni/La2O3 and conventional nickel-based catalysts, The Journal of Physical Chemistry, 100 (1996) 744-754.

[68] F.F. de Sousa, H.S. de Sousa, A.C. Oliveira, M.C. Junior, A.P. Ayala, E.B. Barros, B.C. Viana, A.C. Oliveira, Nanostructured Ni-containing spinel oxides for the dry reforming of methane: effect of the presence of cobalt and nickel on the deactivation behaviour of catalysts, International Journal of Hydrogen Energy, 37 (2012) 3201-3212.

[69] Z. Boukha, C. Jiménez-González, B. de Rivas, J.R. González-Velasco, J.I. Gutiérrez-Ortiz, R. López-Fonseca, Synthesis, characterisation and performance evaluation of spinel-derived Ni/Al2O3 catalysts for various methane reforming reactions, Applied Catalysis B: Environmental, 158–159 (2014) 190-201.

[70] N. Wang, X. Yu, Y. Wang, W. Chu, M. Liu, A comparison study on methane dry reforming with carbon dioxide over LaNiO3 perovskite catalysts supported on mesoporous SBA-15, MCM-41 and silica carrier, Catalysis Today, 212 (2013) 98-107.

[71] E.-h. Yang, Y.-s. Noh, S. Ramesh, S.S. Lim, D.J. Moon, The effect of promoters in La0.9M0.1Ni0.5Fe0.5O3 (M = Sr, Ca) perovskite catalysts on dry reforming of methane, Fuel Processing Technology, 134 (2015) 404-413.

[72] R. Zanganeh, M. Rezaei, A. Zamaniyan, Dry reforming of methane to synthesis gas on NiO–MgO nanocrystalline solid solution catalysts, International Journal of Hydrogen Energy, 38 (2013) 3012-3018.

[73] M. Jafarbegloo, A. Tarlani, A.W. Mesbah, J. Muzart, S. Sahebdelfar, NiO–MgO Solid Solution Prepared by Sol–Gel Method as Precursor for Ni/MgO Methane Dry Reforming Catalyst: Effect of Calcination Temperature on Catalytic Performance, Catalysis Letters, 146 (2016) 238-248.

[74] A.E. York, J. Claridge, A. Brungs, S. Tsang, M.H. Green, Molybdenum and tungsten carbides as catalysts for the conversion of methane to synthesis gas using stoichiometric feedstocks, Chemical Communications, (1997) 39-40.

[75] J.B. Claridge, A.P. York, A.J. Brungs, C. Marquez-Alvarez, J. Sloan, S.C. Tsang, M.L. Green, New catalysts for the conversion of methane to synthesis gas: molybdenum and tungsten carbide, Journal of Catalysis, 180 (1998) 85-100.

[76] J. Rostrupnielsen, J.B. Hansen, CO2-Reforming of Methane over Transition Metals, Journal of Catalysis, 144 (1993) 38-49.

[77] T. Osaki, H. Masuda, T. Mori, Intermediate hydrocarbon species for the CO2-CH4 reaction on supported Ni catalysts, Catalysis letters, 29 (1994) 33-37.

[78] A. Erdöhelyi, J. Cserenyi, E. Papp, F. Solymosi, Catalytic reaction of methane with carbon dioxide over supported palladium, Applied Catalysis A: General, 108 (1994) 205-219.

[79] H. Jahangiri, J. Bennett, P. Mahjoubi, K. Wilson, S. Gu, A review of advanced catalyst development for Fischer–Tropsch synthesis of hydrocarbons from biomass derived syngas, Catalysis Science & Technology, 4 (2014).

[80] D. Leckel, Diesel production from Fischer−Tropsch: the past, the present, and new concepts, Energy & Fuels, 23 (2009) 2342-2358.

[81] M.A. Vannice, The catalytic synthesis of hydrocarbons from H2CO mixtures over the group VIII metals, Journal of Catalysis, 37 (1975) 449-461.

[82] H.M. Torres Galvis, K.P. de Jong, Catalysts for Production of Lower Olefins from Synthesis Gas: A Review, ACS Catalysis, 3 (2013) 2130-2149.

[83] M. DING, Y. YANG, H. XIANG, Y. LI, Relationship between Iron Phase and Activity of Iron-Based Fischer-Tropsch Synthesis Catalyst, Chinese Journal of Catalysis, 31 (2010).

[84] T. Riedel, H. Schulz, G. Schaub, K.-W. Jun, J.-S. Hwang, K.-W. Lee, Fischer–Tropsch on Iron with H2/CO and H2/CO2 as Synthesis Gases: The Episodes of Formation of the Fischer–Tropsch Regime and Construction of the Catalyst, Topics in Catalysis, 26 (2003) 41-54.

[85] K. Jensen, F. Massoth, Studies on iron-manganese oxide carbon monoxide catalysts: I. Structure of reduced catalyst, Journal of Catalysis, 92 (1985) 98-108.

[86] W. Ngantsoue-Hoc, Y. Zhang, R.J. O'Brien, M. Luo, B.H. Davis, Fischer− Tropsch synthesis: activity and selectivity for Group I alkali promoted iron-based catalysts, Applied Catalysis A: General, 236 (2002) 77-89.

[87] C.-H. Zhang, Y. Yang, B.-T. Teng, T.-Z. Li, H.-Y. Zheng, H.-W. Xiang, Y.-W. Li, Study of an iron-manganese Fischer–Tropsch synthesis catalyst promoted with copper, Journal of Catalysis, 237 (2006) 405-415.

[88] C. Wang, Q. Wang, X. Sun, L. Xu, CO Hydrogenation to Light Alkenes Over Mn/Fe CatalystsPrepared by Coprecipitation and Sol-gel Methods, Catalysis Letters, 105 (2005) 93-101.

[89] A. Nakhaei Pour, S.M.K. Shahri, H.R. Bozorgzadeh, Y. Zamani, A. Tavasoli, M.A. Marvast, Effect of Mg, La and Ca promoters on the structure and catalytic behavior of iron-based catalysts in Fischer–Tropsch synthesis, Applied Catalysis A: General, 348 (2008) 201-208.

[90] D.B. Bukur, X. Lang, D. Mukesh, W.H. Zimmerman, M.P. Rosynek, C. Li, Binder/support effects on the activity and selectivity of iron catalysts in the Fischer-Tropsch

synthesis, Industrial & engineering chemistry research, 29 (1990) 1588-1599.

[91] K.-W. Jun, H.-S. Roh, K.-S. Kim, J.-S. Ryu, K.-W. Lee, Catalytic investigation for Fischer–Tropsch synthesis from bio-mass derived syngas, Applied Catalysis A: General, 259 (2004) 221-226.

[92] H.-J. Wan, B.-S. Wu, C.-H. Zhang, H.-W. Xiang, Y.-W. Li, B.-F. Xu, F. Yi, Study on Fe–Al2O3 interaction over precipitated iron catalyst for Fischer–Tropsch synthesis, Catalysis Communications, 8 (2007) 1538-1545.

[93] P. Wang, J. Kang, Q. Zhang, Y. Wang, Lithium ion-exchanged zeolite faujasite as support of iron catalyst for Fischer-Tropsch synthesis, Catalysis letters, 114 (2007) 178-184.

[94] K. Cheng, M. Virginie, V.V. Ordomsky, C. Cordier, P.A. Chernavskii, M.I. Ivantsov, S. Paul, Y. Wang, A.Y. Khodakov, Pore size effects in high-temperature Fischer–Tropsch synthesis over supported iron catalysts, Journal of Catalysis, 328 (2015) 139-150.

[95] L. Guczi, G. Stefler, O. Geszti, Z. Koppány, Z. Kónya, É. Molnár, M. Urbán, I. Kiricsi, CO hydrogenation over cobalt and iron catalysts supported over multiwall carbon nanotubes: Effect of preparation, Journal of Catalysis, 244 (2006) 24-32.

[96] W. Chen, Z. Fan, X. Pan, X. Bao, Effect of Confinement in Carbon Nanotubes on the Activity of Fischer−Tropsch Iron Catalyst, Journal of the American Chemical Society, 130 (2008) 9414-9419.

[97] J. Lu, L. Yang, B. Xu, Q. Wu, D. Zhang, S. Yuan, Y. Zhai, X. Wang, Y. Fan, Z. Hu, Promotion Effects of Nitrogen Doping into Carbon Nanotubes on Supported Iron Fischer-Tropsch Catalysts for Lower Olefins, ACS Catalysis, (2014).

[98] T.O. Eschemann, J. Oenema, K.P. de Jong, Effects of noble metal promotion for Co/TiO2 Fischer-Tropsch catalysts, Catalysis Today, 261 (2016) 60-66.

[99] V. Montes, M. Boutonnet, S. Järås, M. Lualdi, A. Marinas, J.M. Marinas, F.J. Urbano, M. Mora, Preparation and characterization of Pt-modified Co-based catalysts through the microemulsion technique: Preliminary results on the Fischer–Tropsch synthesis, Catalysis Today, 223 (2014) 66-75.

[100] G.J. Haddad, B. Chen, J.J.G. Goodwin, Effect of La3+Promotion of Co/SiO2on CO Hydrogenation, Journal of Catalysis, 161 (1996) 274-281.

[101] L. He, BotaoTeng, Y. Zhang, M. Fan, Development of composited rare-earth promoted cobalt-based Fischer–Tropsch synthesis catalysts with high activity and selectivity, Applied Catalysis A: General, 505 (2015) 276-283.

[102] G.R. Johnson, S. Werner, A.T. Bell, An Investigation into the Effects of Mn Promotion on the Activity and Selectivity of Co/SiO2 for Fischer–Tropsch Synthesis: Evidence for Enhanced CO Adsorption and Dissociation, ACS Catalysis, 5 (2015) 5888-5903.

[103] B. Jongsomjit, J. Panpranot, J.G. Goodwin Jr, Effect of zirconia-modified alumina on the properties of Co/γ-Al2O3 catalysts, Journal of Catalysis, 215 (2003) 66-77.

[104] Y. Zhang, K. Hanayama, N. Tsubaki, The surface modification effects of silica support by organic solvents for Fischer–Tropsch synthesis catalysts, Catalysis Communications, 7 (2006) 251-254.

[105] J. Zhang, J. Chen, J. Ren, Y. Li, Y. Sun, Support effect of Co/Al2O3 catalysts for Fischer–Tropsch synthesis☆, Fuel, 82 (2003) 581-586.

[106] M.A. Vannice, Hydrogenation of co and carbonyl functional groups, Catalysis Today, 12 (1992) 255-267.

[107] L. Guczi, I. Kiricsi, Zeolite supported mono-and bimetallic systems: structure and performance as CO hydrogenation catalysts, Applied Catalysis A: General, 186 (1999) 375-394.

[108] D. Yin, W. Li, W. Yang, H. Xiang, Y. Sun, B. Zhong, S. Peng, Mesoporous HMS molecular sieves supported cobalt catalysts for Fischer–Tropsch synthesis, Microporous and Mesoporous Materials, 47 (2001) 15-24.

[109] Y. Wang, M. Noguchi, Y. Takahashi, Y. Ohtsuka, Synthesis of SBA-15 with different pore sizes and the utilization as supports of high loading of cobalt catalysts, Catalysis Today, 68 (2001) 3-9.

[110] F. Fischer, H. Tropsch, Synthesis of petroleum at atmospheric pressure from gasification products of coal, 7 (1926) 97-104.

[111] S.R. Craxford, E.K. Rideal, The mechanism of the synthesis of hydrocarbons from water gas, Journal of the Chemical Society (Resumed), (1939) 1604-1614.

[112] J.T. Kummer, T.W. DeWitt, P.H. Emmett, Some Mechanism Studies on the Fischer-Tropsch Synthesis Using C14, Journal of the American Chemical Society, 70 (1948) 3632-3643.

[113] C.K. Rofer-DePoorter, A comprehensive mechanism for the Fischer-Tropsch synthesis, Chemical Reviews, 81 (1981) 447-474.

[114] O.C. Elvins, A.W. Nash, The Reduction of Carbon Monoxide, Nature, 118 (1926) 154.

[115] H.H. Storch, R.A. Anderson, N. Golumbic, The Fischer-Tropsch and related syntheses, Wiley New York, 1951.

[116] J.T. Kummer, H.H. Podgurski, W.B. Spencer, P.H. Emmett, Mechanism Studies of the Fischer—Tropsch Synthesis. The Addition of Radioactive Alcohol, Journal of the American Chemical Society, 73 (1951) 564-569.

[117] J.T. Kummer, P.H. Emmett, Fischer—Tropsch Synthesis Mechanism Studies. The Addition of Radioactive Alcohols to the Synthesis Gas, Journal of the American Chemical Society, 75 (1953) 5177-5183.

[118] W.K. Hall, R.J. Kokes, P.H. Emmett, Mechanism Studies of the Fischer-Tropsch Synthesis. The Addition of Radioactive Methanol, Carbon Dioxide and Gaseous Formaldehyde, Journal of the American Chemical Society, 79 (1957) 2983-2989.

[119] W.K. Hall, R.J. Kokes, P.H. Emmett, Mechanism Studies of the Fischer-Tropsch Synthesis: The Incorporation of Radioactive Ethylene, Propionaldehyde and Propanol, Journal of the American Chemical Society, 82 (1960) 1027-1037.

[120] B.H. Davis, Fischer–Tropsch synthesis: current mechanism and futuristic needs, Fuel processing technology, 71 (2001) 157-166.

[121] v.H. Pichler, H. Schulz, Neuere Erkenntnisse auf dem Gebiet der Synthese von Kohlenwasserstoffen aus CO und H2, Chemie Ingenieur Technik, 42 (1970) 1162-1174.

[122] R.W. Joyner, Mechanism of hydrocarbon synthesis from carbon monoxide and

hydrogen, Journal of Catalysis, 50 (1977) 176-180.

[123] R.C. Brady, R. Pettit, Reactions of diazomethane on transition-metal surfaces and their relationship to the mechanism of the Fischer-Tropsch reaction, Journal of the American Chemical Society, 102 (1980) 6181-6182.

[124] R.C. Brady, R. Pettit, Mechanism of the Fischer-Tropsch reaction. The chain propagation step, Journal of the American Chemical Society, 103 (1981) 1287-1289.

[125] B.H. Davis, Fischer–Tropsch Synthesis: Reaction mechanisms for iron catalysts, Catalysis Today, 141 (2009) 25-33.

[126] R. Levy, M. Boudart, Platinum-like behavior of tungsten carbide in surface catalysis, science, 181 (1973) 547-549.

[127] M. Boudart, S.T. Oyama, L. Volpe, High specific surface area carbides and nitrides, in, Google Patents, 1985.

[128] H.-M. Wang, X.-H. Wang, M.-H. Zhang, X.-Y. Du, W. Li, K.-Y. Tao, Synthesis of Bulk and Supported Molybdenum Carbide by a Single-Step Thermal Carburization Method, Chemistry of Materials, 19 (2007) 1801-1807.

[129] L. Volpe, M. Boudart, Compounds of molybdenum and tungsten with high specific surface area, Journal of Solid State Chemistry, 59 (1985) 348-356.

[130] B. Frank, K. Friedel, F. Girgsdies, X. Huang, R. Schlögl, A. Trunschke, CNT‐Supported MoxC Catalysts: Effect of Loading and Carburization Parameters, ChemCatChem, (2013).

[131] J.-M. Giraudon, L. Leclercq, G. Leclercq, A. Lofberg, A. Frennet, Organometallic route to dimolybdenum carbide via a low-temperature pyrolysis of a dimolybdenum alkyne complex, Journal of Materials Science, 28 (1993) 2449-2454.

[132] X.-L. Li, Y.-D. Li, Synthesis of Scroll-Type Composite Microtubes of Mo2C/MoCO by Controlled Pyrolysis of Mo(CO)6, Chemistry – A European Journal, 10 (2004) 433-439.

[133] C. Liang, P. Ying, C. Li, Nanostructured β-Mo2C Prepared by Carbothermal Hydrogen Reduction on Ultrahigh Surface Area Carbon Material, Chemistry of Materials, 14 (2002) 3148-3151.

[134] T. Miyao, I. Shishikura, M. Matsuoka, M. Nagai, CVD Synthesis of Alumina-supported Molybdenum Carbide Catalyst, Chemistry Letters, (1996) 561-562.

[135] K. Fang, D. Li, M. Lin, M. Xiang, W. Wei, Y. Sun, A short review of heterogeneous catalytic process for mixed alcohols synthesis via syngas, Catalysis Today, 147 (2009) 133-138.

[136] M. Xiang, D. Li, H. Xiao, J. Zhang, W. Li, B. Zhong, Y. Sun, K/Ni/β-Mo2C: A highly active and selective catalyst for higher alcohols synthesis from CO hydrogenation, Catalysis Today, 131 (2008) 489-495.

[137] M. Xiang, J. Zou, CO Hydrogenation over Transition Metals (Fe, Co, or Ni) Modified K/Mo 2 C Catalysts, Journal of Catalysts, 2013 (2013).

[138] A.R. Darujati, D.C. LaMont, W.J. Thomson, Oxidation stability of Mo< sub> 2</sub> C catalysts under fuel reforming conditions, Applied Catalysis A: General, 253 (2003)

397-407.

[139] A.R. Darujati, W.J. Thomson, Stability of supported and promoted-molybdenum carbide catalysts in dry-methane reforming, Applied Catalysis A: General, 296 (2005) 139-147.

[140] X. Du, L. France, V. Kuznetsov, T. Xiao, P. Edwards, H. AlMegren, A. Bagabas, Dry reforming of methane over ZrO2-supported Co–Mo carbide catalyst, Applied Petrochemical Research, 4 (2014) 137-144.

[141] T. Huang, W. Huang, J. Huang, P. Ji, Methane reforming reaction with carbon dioxide over SBA-15 supported Ni–Mo bimetallic catalysts, Fuel Processing Technology, 92 (2011) 1868-1875.

[142] J. Huang, T. Huang, L. Liu, W. Huang, R. Ma, Mo2C/SBA-15 Modified by Ni for the Dry Reforming of Methane, Energy Sources, Part A: Recovery, Utilization, and Environmental Effects, 33 (2011) 2249-2256.

[143] L.J. France, X. Du, N. Almuqati, V.L. Kuznetsov, Y. Zhao, J. Zheng, T. Xiao, A. Bagabas, H. Almegren, P.P. Edwards, The effect of lanthanum addition on the catalytic activity of γ-alumina supported bimetallic Co–Mo carbides for dry methane reforming, Applied Petrochemical Research, 4 (2014) 145-156.

[144] C. Shi, A. Zhang, X. Li, S. Zhang, A. Zhu, Y. Ma, C. Au, Ni-modified Mo2C catalysts for methane dry reforming, Applied Catalysis A: General, 431 (2012) 164-170.

[145] A. Zhang, A. Zhu, B. Chen, S. Zhang, C. Au, C. Shi, In-situ synthesis of nickel modified molybdenum carbide catalyst for dry reforming of methane, Catalysis Communications, 12 (2011) 803-807.

[146] C. Shi, S. Zhang, X. Li, A. Zhang, M. Shi, Y. Zhu, J. Qiu, C. Au, Synergism in NiMoOx precursors essential for CH4/CO2 dry reforming, Catalysis Today, 233 (2014) 46-52.

[147] M. Nagai, K. Matsuda, Low-temperature water–gas shift reaction over cobalt–molybdenum carbide catalyst, Journal of Catalysis, 238 (2006) 489-496.

[148] V. Subramani, S.K. Gangwal, A Review of Recent Literature to Search for an Efficient Catalytic Process for the Conversion of Syngas to Ethanol, Energy & Fuels, 22 (2008) 814-839.

[149] H.C. Woo, K.Y. Park, Y.G. Kim, J.S. Lee, Mixed alcohol synthesis from carbon monoxide and dihydrogen over potassium-promoted molybdenum carbide catalysts, Applied catalysis, 75 (1991) 267-280.

[150] M. Xiang, D. Li, H. Xiao, J. Zhang, H. Qi, W. Li, B. Zhong, Y. Sun, Synthesis of higher alcohols from syngas over Fischer–Tropsch elements modified K/β-Mo< sub> 2</sub> C catalysts, Fuel, 87 (2008) 599-603.

[151] H. Al-Megren, T. Xiao, M. AlKinany, S. Aldree, Y. Huang, H. Chen, P.P. Edwards, V. Kuznetsov, High alcohol synthesis (HAS) from syngas over supported molybdenum carbide catalysts, Applied Petrochemical Research, 3 (2013) 71-77.

[152] H. Shou, R.J. Davis, Reactivity and in situ X-ray absorption spectroscopy of Rb-promoted Mo2C/MgO catalysts for higher alcohol synthesis, Journal of Catalysis, 282 (2011) 83-93.

[153] A. Griboval-Constant, J.-M. Giraudon, G. Leclercq, L. Leclercq, Catalytic behaviour of cobalt or ruthenium supported molybdenum carbide catalysts for FT reaction, Applied Catalysis A: General, 260 (2004) 35-45.

[154] M. Xiang, D. Li, W. Li, B. Zhong, Y. Sun, K/Fe/β-Mo2C: A novel catalyst for mixed alcohols synthesis from carbon monoxide hydrogenation, Catalysis Communications, 8 (2007) 88-90.

[155] M. Xiang, D. Li, W. Li, B. Zhong, Y. Sun, Synthesis of higher alcohols from syngas over K/Co/β-Mo2C catalysts, Catalysis Communications, 8 (2007) 503-507.

[156] H.-G. Kim, K.H. Lee, J.S. Lee, Carbon monoxide hydrogenation over molybdenum carbide catalysts, Research on Chemical Intermediates, 26 (2000) 427-443.

[157] K.Y. Park, W.K. Seo, J.S. Lee, Selective synthesis of light olefins from syngas over potassium-promoted molybdenum carbide catalysts, Catalysis letters, 11 (1991) 349-356.

[158] D.-V.N. Vo, T.-H. Nguyen, E.M. Kennedy, B.Z. Dlugogorski, A.A. Adesina, Fischer–Tropsch synthesis: Effect of promoter type on alumina-supported Mo carbide catalysts, Catalysis Today, 175 (2011) 450-459.

[159] D.-V.N. Vo, C.G. Cooper, T.-H. Nguyen, A.A. Adesina, D.B. Bukur, Evaluation of alumina-supported Mo carbide produced via propane carburization for the Fischer–Tropsch synthesis, Fuel, 93 (2012) 105-116.

[160] D.-V.N. Vo, V. Arcotumapathy, B. Abdullah, A.A. Adesina, Non-linear ASF product distribution over alkaline-earth promoted molybdenum carbide catalysts for hydrocarbon synthesis, Catalysis Today, 214 (2013) 42-49.

[161] D.-V.N. Vo, A.A. Adesina, Fischer–Tropsch synthesis over alumina-supported molybdenum carbide catalyst, Applied Catalysis A: General, 399 (2011) 221-232.

[162] D.-V.N. Vo, A.A. Adesina, Kinetics of the carbothermal synthesis of Mo carbide catalyst supported on various semiconductor oxides, Fuel Processing Technology, 92 (2011) 1249-1260.

[163] D.V.N. Vo, V. Arcotumapathy, B. Abdullah, A.A. Adesina, Evaluation of Ba‐promoted Mo carbide catalyst for Fischer‐Tropsch synthesis, Journal of Chemical Technology and Biotechnology, (2012).

[164] D.V.N. Vo, V. Arcotumapathy, B. Abdullah, A.A. Adesina, Evaluation of Ba‐promoted Mo carbide catalyst for Fischer‐Tropsch synthesis, Journal of Chemical Technology and Biotechnology, 88 (2013) 1358-1363.

[165] A. Siahvashi, D. Chesterfield, F. Alenazey, A.A. Adesina, Syngas Production via C3H8 Dry Reforming: Effect of Co and Mo Addition on Ni/Al2O3 Catalyst, Applied Catalysis B: Environmental, (2013).

[166] A. Siahvashi, D. Chesterfield, A.A. Adesina, Propane CO2 (Dry) reforming over bimetallic Mo-Ni/Al2O3 catalyst, Chemical Engineering Science, (2013).

[167] J. Schell, N. Casas, D. Marx, M. Mazzotti, Precombustion CO2 Capture by Pressure Swing Adsorption (PSA): Comparison of Laboratory PSA Experiments and Simulations, Industrial & Engineering Chemistry Research, 52 (2013) 8311-8322.

[168] L. Riboldi, O. Bolland, Evaluating Pressure Swing Adsorption as a CO2 separation

technique in coal-fired power plants, International Journal of Greenhouse Gas Control, 39 (2015) 1-16.

[169] J.K. Adewole, A.L. Ahmad, S. Ismail, C.P. Leo, Current challenges in membrane separation of CO2 from natural gas: A review, International Journal of Greenhouse Gas Control, 17 (2013) 46-65.

[170] M.L. Pritchard, R.L. McCauley, B.N. Gallaher, W.J. Thomson, The effects of sulfur and oxygen on the catalytic activity of molybdenum carbide during dry methane reforming, Applied Catalysis A: General, 275 (2004) 213-220.

Chapter 2 Experimental part

2.1 Introduction

This chapter describes all the materials and equipments involved in the experiments as well as the catalyst preparation methods, characterization techniques and catalytic performance measurement methods for dry methane reforming and Fischer-Tropsch synthesis. A series of different content nickel supported molybdenum catalysts promoted with different elements (Ni, Fe, Na and K) were prepared by different methods. The catalysts were characterized by various characterization techniques to study their physical and chemical properties. The molybdenum-nickel promoted catalysts were tested with fixed-bed reactor to evaluate their catalytic performance in dry methane reforming. The catalysts Ni-, Fe-, Na- and K-promoted catalysts were evaluated in a fixed-bed reactor to study the catalytic performance in Fischer-Tropsch synthesis.

2.2 Catalysts Preparation

2.2.1 Preparation of nickel promoted molybdenum carbide catalysts for dry methane reforming reaction

Nickel promoted Mo_2C catalysts were mainly prepared by 3 methods: Incipient wetness impregnation, mechanical mixing method and impregnation & precipitation method. The preparation process is as follows.

2.2.1.1 Incipient wetness impregnation

Incipient wetness impregnation is a commonly used technique for the synthesis of heterogeneous catalysts [1]. Typically, the active metal precursor is dissolved in an aqueous or organic solution. Then the metal-containing solution is added to a catalyst support containing the same pore volume as the volume of the solution that was added. Capillary action draws the solution into the pores. The catalyst can then be dried and calcined, depositing the metal on the catalyst surface. The maximum loading is limited by the solubility of the precursor in the solution. The concentration profile of the impregnated compound depends on the mass transfer conditions within the pores during impregnation and drying.

Molybdenum was added to alumina support with an aqueous solution of $(NH_4)_6Mo_7O_{24}\cdot 4H_2O$ (Sigma-Aldrich), which is a common precursor for Mo_2C. The gamma alumina (PURALOX NWa155, SASOL Germany) was thermally pretreated at 700 ˚C in air

for 6 h to ensure thermal stability. An aqueous solution of precursors was prepared firstly. Ni precursor $Ni(NO_3)_2$ $6H_2O$ (Sigma-Aldrich) was added on the catalyst by co-impregnation method. Nickel-molybdenum precipitation would be generated in 10 minutes after adding nickel in the solution.

Chelating agents are known to have the properties of increasing the solubility and the stability of the metal precursors for the preparation of supported catalysts [2, 3]. Hence, citric acid was employed as the chelating agent to avoid the nickel-molybdenum precipitation [4].

The water absorption volume was 0.75 ml water per gram alumina measured visually. The molybdenum solution was added in the alumina support drop by drop with stirring glass rod by hand. The powders were matured for 2 hours, to make sure of the completed impregnation. The impregnated catalysts were dried at 110 ˚C overnight, and then the samples were calcined at 450 ˚C in the air with a heating rate of 1 ˚C/min for 6 h. At this temperature, ammonium molybdate can be thermally decomposed to molybdenum trioxide and nickel nitric can be thermally decomposed to nickel oxide.

$$(NH_4)_6Mo_7O_{24}\cdot 4H_2O = 7\ MoO_3 + 6\ NH_4 + 7\ H_2O \qquad \text{Equation 2-1}$$

$$Ni(NO_3)_2\cdot 6H_2O = NiO + 2\ N_2O_5 + 6\ H_2O \qquad \text{Equation 2-2}$$

Then molybdenum oxide were carburized to molybdenum carbide in-situ in the reactor by CH_4/H_2 = 1/4 gas mixture, meanwhile, nickel oxide would be reduced to metal nickel.

2.2.1.2 Mechanical mixing method

Mechanical mixing method is a second common method for the preparation of heterogeneous solid catalysts. Typically, several active metal precursors are mixed mechanically with supports. The catalysts can be calcined to decompose the metal to oxide phase. The purpose for the mixture is to get uniformed distribution of the active phase. Solvent free, low energy cost, easy to manipulate are the main advantages that make this method interesting for solid catalyst preparation in the industry.

The Mo and Ni precursors ($(NH_4)_6Mo_7O_{24}$ $4H_2O$ and $Ni(NO_3)_2$ $6H_2O$) with an optimal ratio were added into deionized water to prepare a green aqueous solution. As discussed previously NiMo precipitation was generated in 10 minutes with the equation:

$$(NH_4)_6Mo_7O_{24} + 3\ Ni(NO_3)_2 = Ni_3Mo_7O_{24}\downarrow + 6\ NH_4NO_3 \qquad \text{Equation 2-3}$$

To improve the interaction between Mo and Ni, the precipitate was aged overnight. Then the generated liquid-solid mixture was dried at 100 ˚C for 12 hours to remove the water. The generated green powder was mechanically mixed with alumina support (which has been thermally pretreated at 700 ˚C in air for 6 h) with an agate mortar. And then the samples were calcined at 450 ˚C in the air with a heating rate of 1 ˚C/min for 6 h. The catalyst was tableted with a tableting machine for 1 minute. The pills generated from tableting were grinded and sieved to 50-150 μm.

2.2.1.3 Impregnation & precipitation method

For the Impregnation & precipitation method, no citric acid was employed. The Mo ($(NH_4)_6Mo_7O_{24}\cdot 4H_2O$) and Ni precursor ($Ni(NO_3)_2\ 6H_2O$) with optimal ratio were added into deionized water to prepare an aqueous solution. The aqueous solution was impregnated into alumina support before the generation of NiMo precipitation, within the 10 minutes. After dying at 110 ˚C overnight, the samples were calcined at 450 ˚C in the air with a heating rate of 1 ˚C/min for 6 h.

The catalyst nomenclature, method of preparation and nickel contents are listed in Table 2-1.

Table 2-1: Catalysts contents of nickel promoted molybdenum carbides catalysts

Catalysts	Preparation method	Catalysts contents (wt%)		Ni/Mo Ratio(mol)
		Ni	Mo	
Mo/Al_2O_3	Incipient wetness impregnation	0	10	-
$NiMo/Al_2O_3$-1:2	Incipient wetness impregnation	3.2	10	1:2
$NiMo/Al_2O_3$-1:1	Incipient wetness impregnation	6.4	10	1:1
Ni/Al_2O_3	Incipient wetness impregnation	6.4	0	-
$NiMo/Al_2O_3$-1:2-M	Mechanical mixture	3.2	10	1:2
$NiMo/Al_2O_3$-1:1-M	Mechanical mixture	6.4	10	1:1
$NiMo/Al_2O_3$-1:2-IP	Impregnation & precipitation	3.2	10	1:2
$NiMo/Al_2O_3$-1:1-IP	Impregnation & precipitation	6.4	10	1:1

2.2.2 Preparation of molybdenum carbide catalysts for Fischer-Tropsch synthesis reaction

2.2.2.1 Preparation of SBA-15 support

SBA-15 was obtained using block copolymer (P123) poly (ethylene glycol)-block-poly (pro-pylene glycol)-block-poly (ethylene glycol), average M_n ca. 5800 (Aldrich, 43546-5) as a template. Firstly, 6 g of P123 copolymer was dispersed in 45 g of water and 180 g of 2 M HCl under stirring. After complete dissolving of P123, 12.75 g of tetraethylorthosilicate (TEOS) were added to the solution. The mixture was kept at 40 ˚C under stirring for 24 h to obtain a uniform solution. Then the solution was transferred into a hermetically closed polypropylene flask and kept in an oven at 100 ˚C for 48 h. The gel was washed with deionized water, dried at 100 ˚C for 12 h, and calcined with flow air at 550 ˚C for 6 h with the temperature ramping of 1 ˚C /min.

2.2.2.2 Preparation of CMK-3 support

The synthesis of CMK-3 was carried out according to the procedure reported in literature [5]. Briefly, 5 g of above-mentioned SBA-15 was added to a solution obtained by dissolving 6.25 g of sucrose and 0.7 g of H_2SO_4 in 25 g of H_2O. The mixture was transferred to a drying oven for 6 h at 100 ˚C, and followed by increasing the oven temperature to 160 ˚C for 6 h. After dissolving additional 4 g of sucrose, 0.45 g of H_2SO_4 and 25 g of H_2O, the mixture was treated again at 100 ˚C and 160 ˚C using the same drying oven. The carburization was completed by pyrolysis with heating to typically 900 ˚C under N_2. The obtained carbon-silica composite was washed with 1 M NaOH solution twice at 95 ˚C to remove the silica template. The template-free carbon material was filtered, washed with deionized water, and dried at 120 ˚C overnight. The synthesized CMK-3-Na was treated with 1 M nitric acid solution at 50 ˚C for 2 h to eliminate the residual Na and introduce some hydrophilic oxygenated functional groups in order to facilitate penetration of the molybdenum precursors into the mesopores [6].

2.2.2.3 Preparation of CNTs support

Carbon nanotubes (Hydroxyl muti-wall carbon nanotubes, MFG Code: MH508-0728, Chengdu Organic Chemicals Co. Ltd., Chinese Academy of Sciences purity ≥ 95%,outer diameter 20-30 nm) were treated with 65% nitric acid at 80 ˚C for 16 h.

2.2.2.4 Preparation of activated carbon support

Activated carbon (CECA S. A.) was washed with 5% nitric acid at 60 ˚C for 4 h to remove the ashes and impurities and then washed with deionized water and dried in the oven at 100 ˚C over night.

2.2.2.5 Preparation of supported molybdenum catalysts

The non-promoted molybdenum catalysts were prepared by incipient wetness impregnation on support by an aqueous solution of ammonium molybdate tetrahydrate ($(NH_4)_6Mo_7O_{24}.4H_2O$, Sigma-Aldrich). After being dried at 100˚C overnight, the samples were calcined at 450˚C under air flow for 6 h. Particularly, the carbon materials supported sample were calcined under N_2 flow to avoid oxidation of carbon at high temperature.

The Ni and Fe promoted Mo/Al_2O_3 catalysts were prepared with the incipient wetness co-impregnation method, citric acid was employed as the chelating agent avoid precipitation. K and Na were added in the catalyst by a mechanical mixture method. The calcined Mo/Al_2O_3 samples were milled mechanically with K_2CO_3 (Sigma-Aldrich) or Na_2CO_3 (Sigma-Aldrich) precursors in different ratio with an agate mortar, and then re-calcined at 450 ˚C for 6 h. The catalyst nomenclature and contents are listed in Table 2-2.

Table 2-2: Catalysts contents of molybdenum carbides catalysts for FTS

Catalysts	**Contents (wt%)**					**promoter/Mo Ratio (mol)**
	promoter				Mo	
	K	Na	Fe	Ni		
Mo/AC	-	-	-	-	10	-
Mo/SBA-15	-	-	-	-	10	-
Mo/CNTs	-	-	-	-	10	-
Mo/CMK-3	-	-	-	-	10	-
Mo/Al_2O_3	-	-	-	-	10	-
$NiMo/Al_2O_3$-1:5	-	-	-	1.2	10	1:5
$FeMo/Al_2O_3$-1:5	-	-	1.2	-	10	1:5
$NaMo/Al_2O_3$-1:5	-	0.5	-	-	10	1:5
KMo/Al_2O_3-1:5	0.8	-	-	-	10	1:5
KMo/Al_2O_3-1:2	2.1	-	-	-	10	1:2
KMo/Al_2O_3-1:1	4.2	-	-	-	10	1:1

2.3 Evaluation of catalytic performance

2.3.1 Equipment for evaluation of dry methane reforming

Dry Methane Reforming reaction was tested with a fixed-bed setup (shown in Figure 2-1). Typically, 0.6 g catalyst was loaded in a quartz tubular reactor (2 cm inner diameter). Prior to the catalytic tests, the molybdenum catalysts were carburized in situ at 700 ˚C for 2 h with a ramp of 5 ˚C/min under CH_4/H_2 mix gas flow (flow rate = 50 ml/min CH_4/H_2 = 1:4). Then the reactor was cooled down to 25 ˚C and purged with N_2 flow for 1 h. Mixed feedstock gas with a molar ratio of $CH_4/CO_2/N_2$ = 1/1/1 was switched into the catalyst bed. Nitrogen was employed as an internal standard for calculating carbon monoxide conversion. The temperature was increased up to 700 ˚C at 5 ˚C /min from 25 ˚C to reaction temperature. The gaseous hourly space velocity (GHSV) was fixed at 6 000 $mL.h^{-1}.gcat^{-1}$. The effluent gases from the reactor were analyzed on-line using a GC-1690 micro gas chromatograph equipped with a Molecular sieve column, a PLOT U column and thermal conductivity detectors (TCD). Activity was evaluated every 50 ℃ in the temperature range of 700–850 ℃ and stability was measured every 20 minutes.

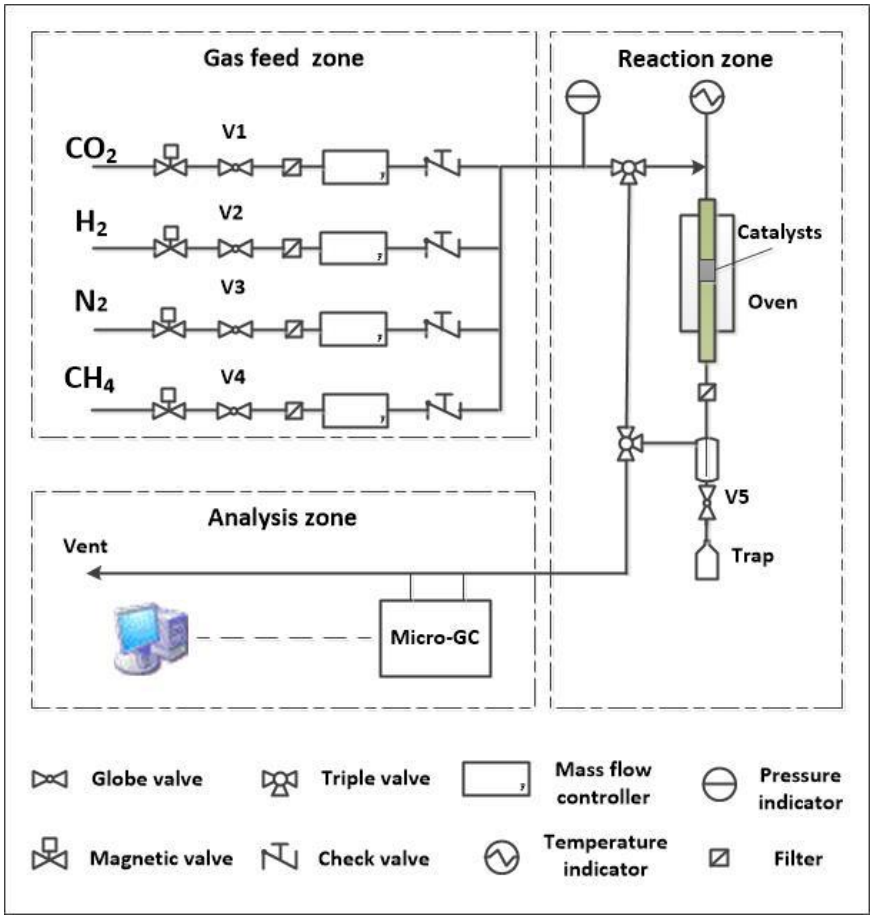

Figure 2-1: schematic diagram of setup for dry methane reforming test.

The Conversion of CH_4 (X_{CH4}) and CO_2 (X_{CO2}), the selectivity of H_2 (S_{H2}), and syngas ratios were calculated by using equations as follows:

$$X_{CH4} = \frac{F_{CH4,in} - F_{CH4,out}}{F_{CH4,in}} \times 100\% \quad \text{Equation 2-4}$$

$$X_{CO2} = \frac{F_{CO2,in} - F_{CO2,out}}{F_{CO2,in}} \times 100\% \quad \text{Equation 2-5}$$

$$S_{H2} = \frac{F_{H2,out}}{2(F_{CH4,in} - F_{CH4,out})} \times 100\% \quad \text{Equation 2-6}$$

$$Ratio\ of\ \frac{H_2}{CO} = \frac{F_{H2,out}}{F_{CO,out}} \quad \text{Equation 2-7}$$

The inlet flow rate of internal standard gas N_2 is controlled by mass flow controller (MFC), so the flow rate of CH_4, CO_2, H_2 and CO on the outlet can be calculated by followed equations.

$$F_{CH4,out} = F_{N2,in} \times \frac{A_{CH4,out}}{A_{N2},out} \times \frac{f_{CH4}}{f_{N2}} \quad \text{Equation 2-8}$$

$$F_{CO2,out} = F_{N2,in} \times \frac{A_{CO2,out}}{A_{N2},out} \times \frac{f_{CO2}}{f_{N2}} \quad \text{Equation 2-9}$$

$$F_{H2,out} = F_{N2,in} \times \frac{A_{H2,out}}{A_{N2},out} \times \frac{f_{H2}}{f_{N2}} \quad \text{Equation 2-10}$$

$$F_{CO,out} = F_{N2,in} \times \frac{A_{CO,out}}{A_{N2},out} \times \frac{f_{CO}}{f_{N2}} \quad \text{Equation 2-11}$$

Where:

A: Peaks area exported from GC;

f : Calibration factor;

F: Flow rate

Therein, calibration factor *f* of each component was obtained by the measurement of a standard gas on the same GC-1690 micro gas chromatograph.

2.3.2 Catalytic test for Fischer-Tropsch synthesis

Carbon monoxide hydrogenation reaction was tested in a fixed-bed setup (shown in Figure 2-2). Typically, 0.3 g catalyst was loaded in the middle of a fixed-bed stainless steel tubular reactor (2 cm inner diameter) between quartz wool plugs. As Fischer-Tropsch synthesis is strong exothermic reaction, silicon carbide were filled into the reactor space (shown in Figure 2-3) to increase the heat transfer. Moreover, a thermocouple was installed inside of the reactor in order to control the reaction temperature accurately.

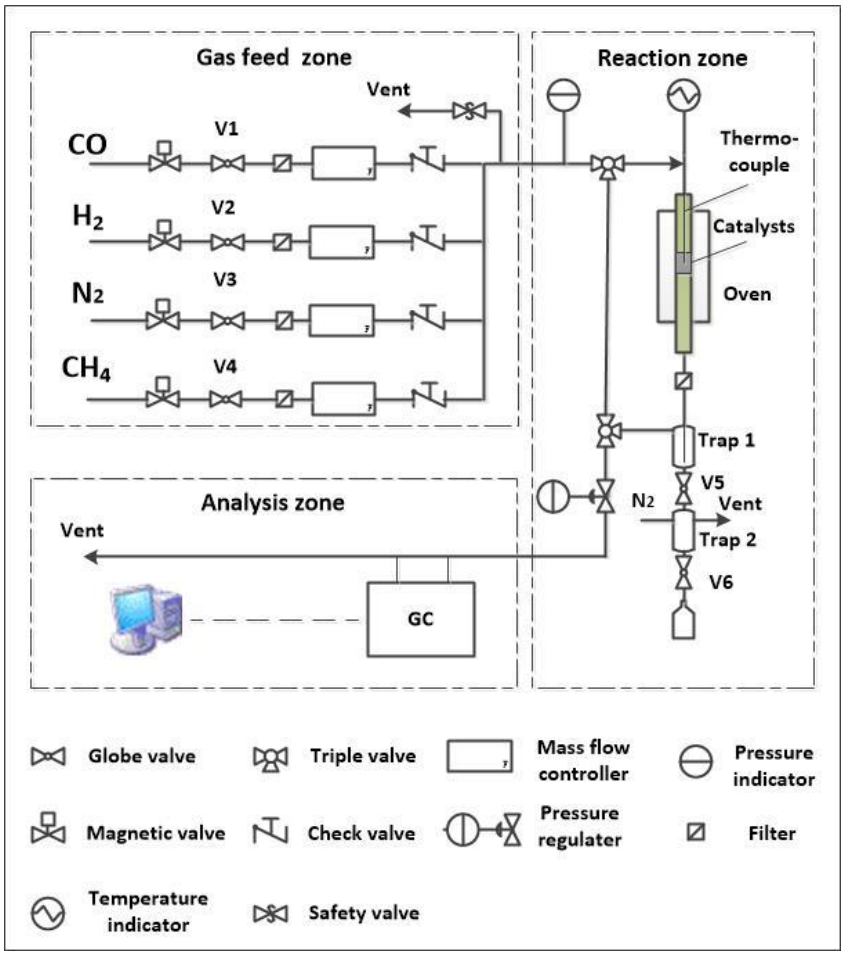

Figure 2-2: schematic diagram of setup for dry methane reforming test.

Prior to the catalytic tests, the molybdenum catalysts were carburized in situ at 700 ˚C for 2 h with a ramp of 5 ˚C/min under CH_4/H_2 mix gas flow (flow rate = 50 ml/min CH_4/H_2=1:4). Then the reactor was cooled down to 25 ˚C and purged with N_2 flow for 1 h. A syngas with a molar ratio of H_2/CO = 2 was switched through the reactor and the total pressure was regulated to 10 bars. Nitrogen was employed as an internal standard for calculating carbon monoxide conversion. The temperature was increased up to 300 ˚C at 1 ˚C/min to reaction temperature. The gaseous hourly space velocity (GHSV) was 12000 $mL.h^{-1}.g\ cat^{-1}$.

The effluent gases from the reactor were analyzed by on-line gas chromatography. Analysis of N_2, CO, CO_2, and CH_4 was performed using a packed CTR-1 column and a TCD detector. Gaseous hydrocarbons (C_1–C_4) and alcohols were separated in a capillary Rt-Q PLOT column and analyzed by a Flame ionization detector (FID). The liquid products (oil and water phases) were collected in the traps kept at 20 ˚C and analyzed off-line by gas chromatography.

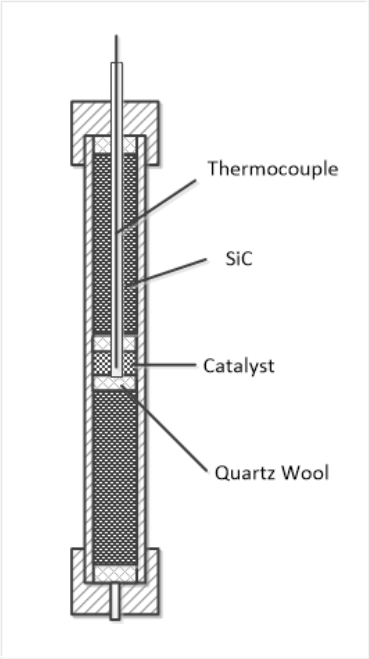

Figure 2-3: schematic diagram of fixed-bed reactor of Fischer-Tropsch synthesis.

The CO conversion can be calculated by the equation:

$$X_{CO} = \frac{F_{CO,in} - F_{CO,out}}{F_{CO,in}} \times 100\% \quad \text{Equation 2-12}$$

$$S_{CO2} = \frac{F_{CO2,out}}{F_{CO,in} - F_{CO,out}} \times 100\% \quad \text{Equation 2-13}$$

$$S_{CH4} = \frac{F_{CH4,out}}{F_{CO,in} - F_{CO,out}} \times 100\% \quad \text{Equation 2-14}$$

Similarly, the flow rate of CO, CO_2 and CH_4 can be calculated based on inlet flow rate of internal standard gas N_2 by the followed equations.

$$F_{CO,out} = F_{N2,in} \times \frac{A_{CO,out}}{A_{N2},out} \times \frac{f_{CO}}{f_{N2}} \quad \text{Equation 2-11}$$

$$F_{CH4,out} = F_{N2,in} \times \frac{A_{CH4,out}}{A_{N2},out} \times \frac{f_{CH4}}{f_{N2}} \quad \text{Equation 2-8}$$

$$F_{CO2,out} = F_{N2,in} \times \frac{A_{CO2,out}}{A_{N2},out} \times \frac{f_{CO2}}{f_{N2}} \quad \text{Equation 2-9}$$

The operation of the FID is based on the detection of ions formed during combustion of organic compounds in a hydrogen flame. Hydrocarbons generally have molar response factors that are proportional to number of carbon atoms in their molecule, while oxygenates and other species that contain heteroatoms tend to have a lower response factor [7], so selectivity of olefins and paraffin can be calculated correlated with CH_4 as shown in Equation 2-15 and Equation 2-16.

$$F_{Cj} = \frac{A_{Cj}}{A_{CH_4}} \times F_{CH_4}$$ Equation 2-15

$$S_{Cj} = \frac{F_{Cj}}{F_{CO,in} - F_{CO,out}}$$ Equation 2-16

j: the carbon number of generated hydrocarbon

Herein, the selectivity is based on the carbon atom moles.

Moreover, alcohols calibration factors were obtained by the use of a standard solution, which contains methanol, ethanol and hexane, on the GC-450 gas chromatograph. Thus, the selectivity of alcohols can be calculated with the CH_4 correlation through the relative calibration factors of hexane.

$$F_{C_i-OH} = \frac{A_{C_i-OH}}{A_{CH_4}} \times \frac{i \times f_{C_i-OH}}{6 \times f_{CH4}} \times F_{CH_4}$$ Equation 2-17

$$S'_{Ci-OH} = \frac{F_{Ci-OH}}{F_{CO,in} - F_{CO,out}}$$ Equation 2-18

i: the carbon numbers for generated alcohol.

Generally, for the sake of clarity, CO_2 is excluded from the organic product selectivity, the CO_2 free selectivity can be obtained by Equation 2-19and Equation 2-20.

$$S_{Cj} = \frac{S'_{Cj}}{1 - S_{CO2}}$$ Equation 2-19

$$S_{Ci-OH} = \frac{S'_{Ci-OH}}{1 - S_{CO2}}$$ Equation 2-20

2.4 Catalyst Characterizations

Different characterization techniques were employed to investigate the physical and chemical properties of catalysts. Please note that for characterization, after carburization with a mixture of H_2/CH_4 = 4:1 for 2 h at 700 ℃, the catalysts were passivated and removed from the reactor. A very small amount of O_2 was introduced in the flowing N_2 (1% O_2 in N_2) for passivation of the samples at room temperature.

2.4.1 Textural characteristics

Textural characteristics, which can provide the specific surface area, pore volume and pore size of a catalyst, were measured using N_2 adsorption-desorption experiment at -196 ℃. Before the measurement, the catalyst was outgassed at 200 ℃. The isotherms were measured using a Micrometrics ASAP 2010 system. Surface area was calculated by BET equation. The pore size distribution was calculated from the desorption branches of the isotherms using Barrett-Joyner-Halenda (BJH) formula.

2.4.2 X-ray diffraction

X-ray diffraction (XRD) can analyse the existed crystallite phases on catalysts and probably calculate the size of the crystallite. The X-ray diffraction patterns were recorded by a Bruker D8 Advance diffractometer using Cu (Kα) radiation at room temperature from 10° to 80 ° with 0.02 ° step size and 2 s step time. Crystallite phases were determined by comparing the diffraction patterns with those in the standard powder XRD files (JCPDS) published by the International Center for Diffraction Data. The average crystallite size of MoO_2, Mo_2C and metallic Ni were calculated according to the Scherrer equation.

$$D = \frac{0.89\gamma}{\beta \cos\theta} \qquad \text{Equation 2-21}$$

Where D is the average crystallite diameter, λ is the X-ray wavelength, β: the line broadening at half the maximum intensity (FWHM), θ is the Bragg angle.

2.4.3 Hydrogen temperature-programmed reduction

Hydrogen temperature-programmed reduction (H_2-TPR) is used to study the reducibility of active phase on the catalysts and determine different phases through temperature of reduction. The H_2-TPR was carried out on AutoChem II 2920 apparatus from Micromeritics using 0.1 g of the sample under 5 vol% H_2 diluted in Ar stream (50 ml/min). The temperature was increased from room temperature up to 900 ℃ with a rate of 10 ℃/min. The effluent gas was analysed with a thermal conductivity detector (TCD).

2.4.4 Temperature-programmed desorption of CO_2

Temperature-programmed desorption of CO_2 (CO_2-TPD) can characterize the basic sites and determine quantitatively basicity of the catalysts. The CO_2-TPD curves were carried out on a NH_3/CO_2–TPD equipment (shown in Figure 2-4). 0.05 g of catalyst was loaded in a fixed-bed quartz tubular reactor (0.5 cm inner diameter) between quartz wool plugs. The samples were pretreated under a flow of an inert carrier gas (He) at 150 ℃ for 2 h to remove the water adsorbed on the catalyst surface. The process of CO_2 adsorption was carried out by the injection of CO_2 gas using a 6-port valve with 10 times injections in order to get CO_2 saturation. The CO_2 desorption process was measured throughout heating the catalyst up to 700 ℃ (15 ℃/min) under a flow of He. The effluent gases at the outlet of the reactor were analyzed by a thermal conductivity detector (TCD).

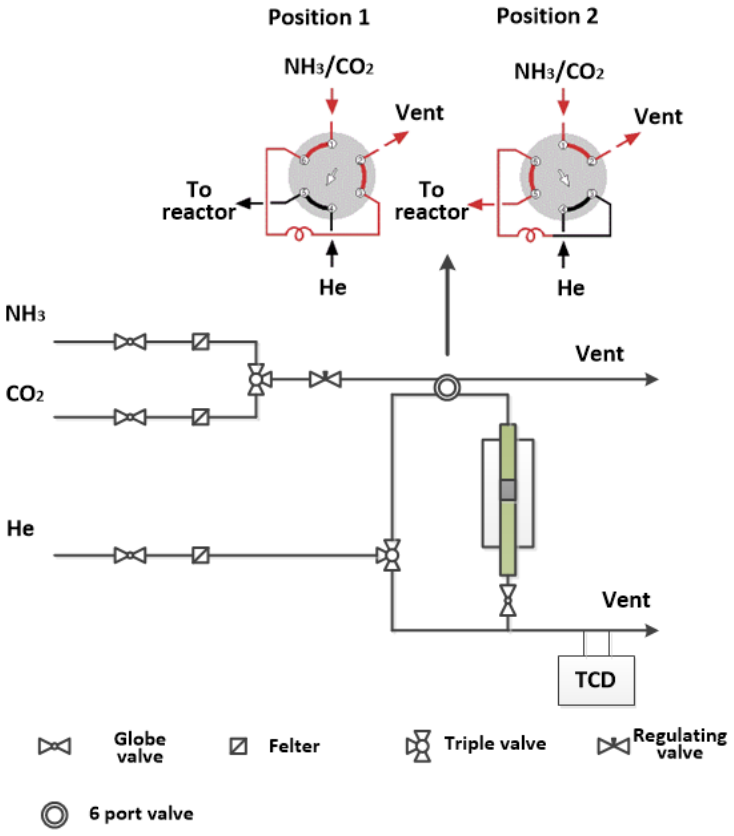

Figure 2-4: schematic diagram for the equipment of NH_3/CO_2-TPD.

2.4.5 Laser Raman spectroscopy

Raman spectroscopy provides information about molecular vibrations that can be used for sample phases identification. The Laser Raman spectra of the oxidized Mo-based catalysts were run on a Dilor XY800 spectrometer with a Krypton ion laser (Spectra Physics model

Beamlok). A laser wavelength of 532 nm and a filter with diameter of 0.6 were employed. The dispersed radiation is received by the CCD (Charge Coupled Device) detector cooled with liquid nitrogen. The *LabSpec* software allows acquisition and data processing.

2.4.6 X-ray photoelectron spectroscopy

X-ray photoelectron spectroscopy (XPS) can determine quantitatively the elemental composition and chemical state of the elements that exist on the surface of a catalyst. The XPS spectra were recorded with a VG ESCALAB 220 XL spectrometer equipped with a monochromatic Al Kα (E = 1486.6 eV) X-ray source. The binding energies (BE) of Mo3d, O1s, C1s Ni2p and K2p were determined by computer fitting of the measured spectra and referred to the Al 2p peak of the support at 74.6 eV, using Casa XPS software. The binding energies were estimated within ± 0.2 eV.

2.4.7 Transmission electron microscopy (TEM)

Transmission electron microscopy (TEM) can observe objects with a few angstroms, which is used to observe the microstructure of catalysts and to measure diameter of nanoparticles. TEM measurements were performed using a TECNA microscope, operating at a voltage of 200 kV. The sample powder was ultrasonically dispersed in ethanol and deposited on a copper grid recovered by a carbon membrane prior to the measurements. The particle size was measured using more than 300 particles by the software *Nano Measurer*.

2.4.8 Temperature programmed surface reaction

Temperature programmed surface reaction (TPSR) is able to provides information of active phase through the initial activation temperature. The TPSR of CH_4/CO_2 was measured in a fixed bed reactor. Before the TPSR experiment, the catalyst was carburized with mixture gas H_2/CH_4 (H_2/CH_4 = 4:1, 50 ml/min) for 2 h at 700 ˚C. After cooling down to 25 ˚C under a N_2 flow, the temperature of the reactor was raised to 850 ˚C at the uniform ramp of 5 ˚C/min with the mixed gas with a molar ratio of $CH_4/CO_2/N_2$ = 1. The products of CH_4/CO_2-TPSR were analyzed on line every 3 minutes (15 ˚C) by a GC-1690 micro gas chromatograph equipped with a Molecular sieve column and a PLOT U column and thermal conductivity detectors (TCD).

2.4.9 SEM-EDS

Scanning electron microscopy (SEM-EDS) is used to observe surface properties of a catalyst with well three-dimensional images and analyze qualitatively and quantitatively the elementals on a catalyst surface. SEM-EDS measurements were performed using a Quanta 200 microscope with an applied voltage of 15 KV. Energy-dispersive X-ray spectroscopy measurements (EDS) were recorded by QuanTax QX2, ROENTEC with an applied voltage of 15 KV.

2.4.10 Thermo-gravimetric analyses

Thermo-gravimetric analysis is used to analyse the chemical state of the element and the carbon deposition on a catalysts through the decomposition or oxidation temperature and mass change. Thermo-gravimetric analyses were measured with thermogravimetric analyzer (TA instruments SDT 2960 simultaneous DSC-TGA). 10 mg of the sample was heated under air atmosphere from room temperature to 850 ℃ at a rate of 10 ℃/min and kept at 850 ℃ for 30 minutes.

2.5 Reference

[1] J.A. Schwarz, C. Contescu, A. Contescu, Methods for preparation of catalytic materials, Chemical Reviews, 95 (1995) 477-510.

[2] D. Valencia, T. Klimova, Kinetic study of NiMo/SBA-15 catalysts prepared with citric acid in hydrodesulfurization of dibenzothiophene, Catalysis Communications, 21 (2012) 77-81.

[3] T.E. Klimova, D. Valencia, J.A. Mendoza-Nieto, P. Hernández-Hipólito, Behavior of NiMo/SBA-15 catalysts prepared with citric acid in simultaneous hydrodesulfurization of dibenzothiophene and 4,6-dimethyldibenzothiophene, Journal of Catalysis, 304 (2013) 29-46.

[4] W. Lai, W. Song, L. Pang, Z. Wu, N. Zheng, J. Li, J. Zheng, X. Yi, W. Fang, The effect of starch addition on combustion synthesis of NiMo–Al2O3 catalysts for hydrodesulfurization, Journal of Catalysis, 303 (2013) 80-91.

[5] S. Jun, S.H. Joo, R. Ryoo, M. Kruk, M. Jaroniec, Z. Liu, T. Ohsuna, O. Terasaki, Synthesis of new, nanoporous carbon with hexagonally ordered mesostructure, Journal of the American Chemical Society, 122 (2000) 10712-10713.

[6] K.-S. Ha, G. Kwak, K.-W. Jun, J. Hwang, J. Lee, Ordered mesoporous carbon nanochannel reactors for high-performance Fischer–Tropsch synthesis, Chemical Communications, 49 (2013) 5141-5143.

[7] T. Holm, Aspects of the mechanism of the flame ionization detector, Journal of Chromatography A, 842 (1999) 221-227.

Chapter 3 Thermodynamics analysis for dry methane reforming & Fischer-Tropsch synthesis

3.1 Introduction

Biogas, which come from anaerobic digestion of organic matters, such as farm waste, animal mature and household garbage, is one of the most promising renewable resources [1-3]. Generally, the biogas composition contains 50-65% of methane and 35-50% of carbon dioxide, which are strong greenhouse gases that have a great influence on the global weather [1, 4]. The development and the use of biogas are not only about recycling of resources, but can help to decrease the greenhouse effect.

The dry methane reforming (DMR) into syngas, received lately much attention as both CH_4 and CO_2 are consumed [5-9]. The generated syngas, with an hydrogen to carbon monoxide ratio close to 1:1, make it suitable for the synthesis of valuable products by Fischer-Tropsch synthesis (FTS) [10, 11]. Also, FTS is an industrially useful technology for gas-to-liquid processes which upgrade coal, natural gas or biomass into high quality ultra-clean fuels and other chemical products such as paraffin, olefins and alcohols. It has become one of the most important routes of energy instead of petroleum products.

Combined DMR and FTS in a single process can be proposed as syngas is both the product of DMR and the reactant of FTS. As is well known [12, 13], separation processes require high energy consumption, which occupies a considerable proportion of devices and operating cost on an industry process.

Hence, in this proposed work, the separation of unreacted CH_4 and CO_2 from DMR product is not needed for a combined dry methane reforming and Fischer–Tropsch synthesis process. This exhibits obviously some advantages due to the reduced energy consumption and devices cost. Generally, the Fischer-Tropsch synthesis is performed at elevated pressure (generally 10-30 bar) [11]. There are two ways to achieve high pressure for syngas [14]. The first method is to perform syngas production at high pressure. The second method is to compress the syngas after it is produced. Generally, the inlet temperature for a compressor should be below 100 ˚C and a higher inlet gas temperature will lead to lower the compressor efficiency. This implies that the outlet gas, owning high temperature (normally 700-900 ˚C) from dry methane reforming process, has to be cooled down to low temperature. Additional heat exchange procedure is needed, which obviously increases cost and heat consumption. Thus, it should be more interesting to perform dry methane reforming under high temperature to produce syngas.

Thermodynamic analysis of a reaction can provide a basis for experimental and computational studies. Moreover, it can be useful in understanding the limits and constrains of a reaction process [15].

In this chapter, the thermodynamics calculations for dry methane reforming and Fischer-Tropsch synthesis were studied under the same conditions of the experiments. The thermodynamics effect of carbon deposition, pressure, CH_4/CO_2 feed ratio and the presence of N_2 inert gas over dry methane reforming were also studied. In addition, as the FTS feedstock of the sequential process, which is a product of DMR, consists of unreacted CH_4 and CO_2, thermodynamics effect of the presence of methane and carbon dioxide was also investigated on Fischer-Tropsch synthesis.

3.2 Thermodynamics analysis on the literature

3.2.1 The thermodynamics of dry methane reforming

Dry methane reforming is a complex process, the main reaction is described as:

$CH_4 + CO_2 = 2\,H_2 + 2\,CO \qquad \Delta H_{298}^0 = 247\ \mathrm{kJ/mol}$ Equation 3-1

$\Delta G^0 = 61770 - 67.32T$ [16]

This reaction is particularly endothermic. High temperature and low pressure are required.

Reverse Water Gas Shift reaction (RWGS) occurs simultaneously as aside reaction:

$H_2 + CO_2 = CO + H_2O \qquad \Delta H_{298}^0 = -41\ \mathrm{kJ/mol}$ Equation 3-2

$\Delta G^0 = -8545 + 7.84T$

The reaction balance of dry methane reforming is affected by the reverse Water-Gas Shift reaction which leads to low H_2/CO ratio.

Under conditions of stoichiometric dry methane reforming, there also exist other reactions:

Methane decomposition:

$CH_4 = C + 2\,H_2 \qquad \Delta H_{298}^0 = 75\mathrm{kJ/mol}$ Equation 3-3

CO disproportionation (Boudouard reaction) which are considered as the main reasons of carbon deposition on the catalysts [17].

$2\,CO = C + CO_2 \quad \Delta H_{298}^0 = -172 kJ/mol$ Equation 3-4

And CO/CO_2 hydrogenation reaction

$CO + H_2 = C + H_2O \quad \Delta H_{298}^0 = -175 kJ/mol$ Equation 3-5

$CO_2 + 2\,H_2 = C + 2\,H_2O \quad \Delta H_{298}^0 = -134 kJ/mol$ Equation 3-6

Temperature is the most important factor for dry methane reforming. Wang et al.[16] calculated the lowest reaction temperatures of the dry methane reforming, methane decomposition and CO disproportionation and the result is shown in Table 3-1. Dry methane reforming takes place at 640 ˚C accompanied by methane decomposition reaction, while above 820 ˚C reverse water gas shift reaction and CO disproportionation reaction cannot occur. In the temperature range of 557-700 ˚C carbon deposition occured from methane decomposition or CO disproportionation reaction.

Table 3-1: Limiting temperature for different reactions of DMR

Reaction	Temperature/˚C	
Dry methane reforming	Lower temperature	640
Methane decomposition		557
CO disproportionation	Higher temperature	700
Reverse water gas shift		820

Bradford and Vannice [18] reported that dry methane reforming reaction was favored thermodynamically at temperature higher than 727 ˚C. Zhang [19] also found that methane decomposition and CO disproportionation were the direct source for carbon deposition. When the temperature rises from 527˚C to 627˚C, carbon deposition increased obviously.

As shown in Equation 3-1, dry methane reforming is a volume expansion reaction, low pressure, which can promote the reaction balance shift to right side, is beneficial to the reaction. Wang et al.[16] investigated the equilibrium conversion at total pressure of 0.01-0.1 atm with CO_2/CH_4 = 1, and the results indicated that conversions at lower pressure are higher than those at higher pressure. Jafarbegloo et al.[15] investigated the effect of pressure on methane and carbon dioxide conversions at stoichiometric feed composition at 800 ℃. Increasing the pressure led to decrease in the conversion of methane and CO_2 reaction which is reasonable for a volume expansion reaction.

CH_4/CO_2 feeding ratio is also an important factor which greatly affects dry methane reforming reaction. Nakamura and Uchijima [20] insisted that excessed CO_2 among raw materials could avoid carbon deposition at atmospheric pressure. Jafarbegloo et al. [15] calculated the equilibrium conversion versus CH_4/CO_2 molar ratio. Increasing CO_2 fraction allows shifting the dry methane reforming toward the production of H_2 and CO, then methane conversion increases. A rapid drop in conversion of carbon dioxide is observed when CO_2/CH_4 ratio is bigger than the stoichiometric feed ratio, because the excess CO_2 cannot undergo appreciable chemical transformation due to its high stability under the reaction conditions.

Chein et al.[14] investigated the carbon deposition of dry methane reforming at different CO_2/CH_4 ratio and pressure. The colorful surface (shown in Figure 3-1) represents the critical point of carbon formation. Above the surface is a carbon-free zone while the carbon formation zone is below the surface. At a given CO_2/CH_4 ratio, the temperature limit for carbon formation increases as the pressure increases. In addition, at the same pressure, temperature limit increases as the CO_2/CH_4 ratio decreases. This means that using excess CO_2 can avoid carbon formation at lower temperatures. Higher temperature is required to achieving carbon-free operation at the lower CO_2/CH_4 ratio and higher pressure condition.

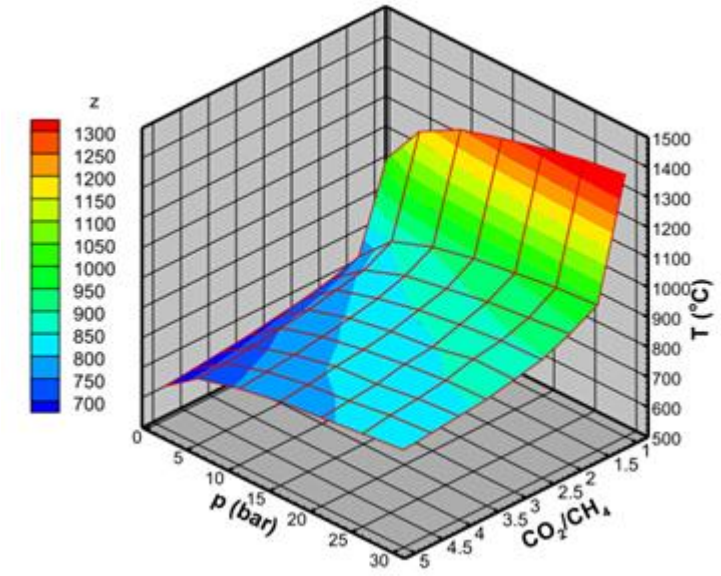

Figure 3-1: Temperature limit for carbon deposition as functions of pressure and CO_2/CH_4 [14].

As a brief summary, dry methane reforming is a strong endothermic reaction, the equilibrium constant increases rapidly with the increase in temperature. High temperature is beneficial for DMR activity. CO disproportionation and reverse carbon gasification reaction

are exothermic reactions, high temperature is not suitable. Higher temperature is more advantageous for increasing equilibrium conversion of dry methane reforming. Elevated pressure is disadvantageous for dry methane reforming and leads to a decrease in CH_4 and CO_2 conversion and increase in carbon deposition and water generation. Excess of CO_2 among feedstock inhibits carbon deposition during dry methane reforming.

3.2.2 The thermodynamics analysis for Fischer Tropsch synthesis

Besides, Fischer-Tropsch synthesis is a very complex process, and the reactions can take place simultaneously between H_2 and CO:

Synthesis of paraffins:

$$n\,CO + (2n+1)\,H_2 = C_nH_{2n+2} + n\,H_2O \qquad \text{Equation 3-7}$$

Synthesis of olefins:

$$nCO + 2n\,H_2 = C_nH_{2n} + nH_2O \qquad \text{Equation 3-8}$$

Synthesis of alcohols:

$$n\,CO + 2n\,H_2 = C_nH_{2n+1}OH + (n-1)\,H_2O \qquad \text{Equation 3-9}$$

Moreover, water gas shift reaction may also occur in the Fischer-Tropsch process:

$$H_2O + CO = CO_2 + H_2 \qquad \text{Equation 3-10}$$

In order to calculate the probability of product formation, Keim [21] simplified the Fischer Tropsch synthesis system by the assumption that the reactions are independent of each other. Calculations of Gibbs free energy on the basis of Equations (Equation 3-7 to Equation 3-10), which can indicate the spontaneity of a reaction, are shown in Figure 3-2. The results reveal that the formation of methane is favored in a temperature range of 50-350 ℃. The probability of product formation decreases in the order: CH_4 >> paraffins > olefins > oxygenated. A syngas rich in hydrogen favors the formation of paraffin, whereas a syngas rich in carbon monoxide leads to an increased formation of olefins and aldehydes without consideration of carbon deposition [22].

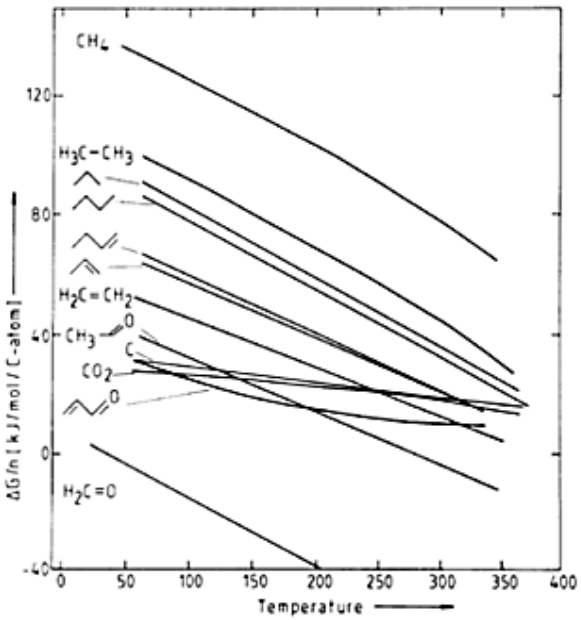

Figure 3-2: temperature influence on the Gibbs free energy of FTS products [21].

Dry [23] indicated that the main products of Fischer-Tropsch synthesis should be CH_4, CO_2 and graphite at 1 bar of pressure, the calculated amounts of higher hydrocarbon were negligible. Whereas in practice, the CH_4 selectivity is lower, carbon is negligible and the heavy hydrocarbon is higher. Christoffel [24] compared the typical selectivity obtained over iron catalysts at 327 ℃, 16 bar pressure and H_2/CO of 2. It is clearly indicated that the significant difference between the Fischer Tropsch synthesis result and the thermodynamic distribution, estimated in the same conditions, is strongly controlled by the kinetics and the product distribution may be dominated by the type of catalyst as well as by reaction conditions.

3.3 Modelling and simulation methodology

The Gibbs free energy (also referred to as G) is the thermodynamic potential that is minimized when a system reaches chemical equilibrium at constant pressure and temperature [12]. The equilibrium composition of dry methane reforming is obtained by the minimization of Gibbs free energy with the following equation:

$$\Delta G_{total} = \sum_{i-1}^{n} n_i \, G_i \qquad \text{Equation 3-11}$$

The equilibrium component was calculated by *HSC Chemistry 6.0* software. For the thermodynamics calculation of dry methane reforming, 6 possible compounds are considered: CH_4, CO_2, H_2, CO, H_2O, and carbon formation (amorphous and graphitic carbon).

To calculate the equilibrium composition of the FTS reaction, the products was simplified. So 27 possible compounds are considered during the simulations, including n-alkanes and n-olefins (in the C_2-C_{10} range), lower alcohol (in the C_1-C_3 range), CO, CO_2, CH_4, H_2 and H_2O [11, 25].

3.4 Thermodynamics calculations of dry methane reforming

3.4.1 Carbon formation in DMR

As is reported in the literature [26-28], carbon formation is a common phenomenon due to the reaction 1-3 to 1-6. It is interesting to investigate the influence of carbon formation on the dry methane reforming. Figure 3-3 displays the equilibrium results of dry methane reforming at $CH_4/CO_2/N_2$=1:1:1 and atmosphere pressure, with and without carbon formation consideration.

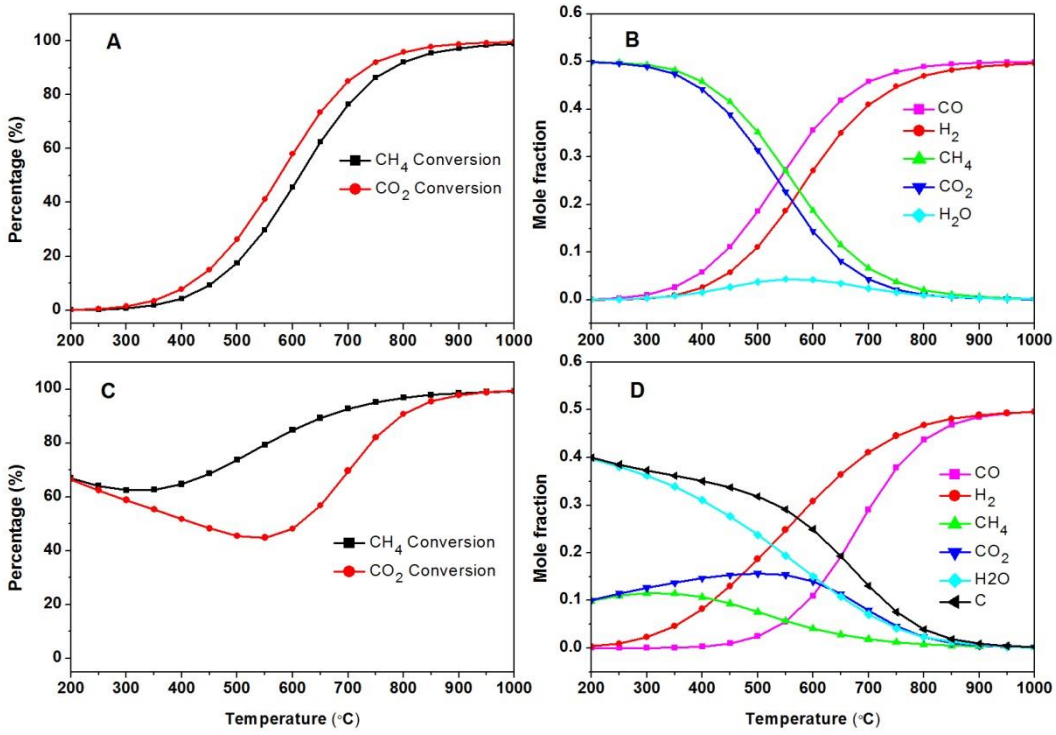

Figure 3-3: The influence of carbon formation on equilibrium species for dry methane reforming at atmosphere pressure, $CH_4/CO_2/N_2$=1:1:1. **(A):** equilibrium conversion of CH_4 and CO_2 without considering carbon formation; **(B):** equilibrium mole fraction without considering carbon formation; **(C):** equilibrium conversion of CH_4 and CO_2 considering carbon formation; **(D):** equilibrium mole fraction considering carbon formation.

As is shown in Figure 3-3, high reaction temperature is thermodynamically advantageous for the dry methane reforming. Due to the reverse water gas shift reaction, the conversion of CO_2 is always greater than the one of CH_4. The CH_4 and CO_2 equilibrium curves clearly display that at higher temperature (> 800 ℃) the CO2 and CH4 conversions are closer and generate higher H_2/CO ratio. The formation of H_2O is close to zero at temperature above 850 ˚C.

The CH_4 and CO_2 conversions curves displayed different behaviors when carbon deposition is taking in consideration (shown in Figure 3-3 (B)). CO_2 produced reactions like water gas shift reaction (Reverse Equation 3-2) and CO disproportionation reaction (Equation 3-4) are exothermic reactions and thermodynamically favored at low temperature. In contrast, regarding methane, reactions such as dry methane reforming and methane decomposition are endothermic and enhanced monotonically with the increase in temperature. The overall effect is a higher methane conversion compared to carbon dioxide in the range of 250 to 850 ℃. The equilibrium components of the reacting species for dry methane reforming are presented in Figure 3-3 (D). Upon increasing the temperature, the composition shifts to the production of CO and H_2. The coke and other components constituents approaches zero at temperature higher than 850 ℃. The H_2/CO ratio decreases with increasing the temperature and approaches to the stoichiometric 1:1 ratio.

3.4.2 Influence of Pressure on DMR

The influence of pressure on the equilibrium composition of dry methane reforming was investigated and the result is shown in Figure 3-4. The increasing in pressure leads to a decrease in both CH_4 and CO_2 conversion, indicating dry methane reforming is unfavorable at high pressure. This is reasonable for a reaction with an increase in moles (volume expansion). Moreover, the influence of pressure is obvious at pressure from 1 bar to 5 bar and inclined to limiting values at increasing pressure from 5 bar to 20 bar.

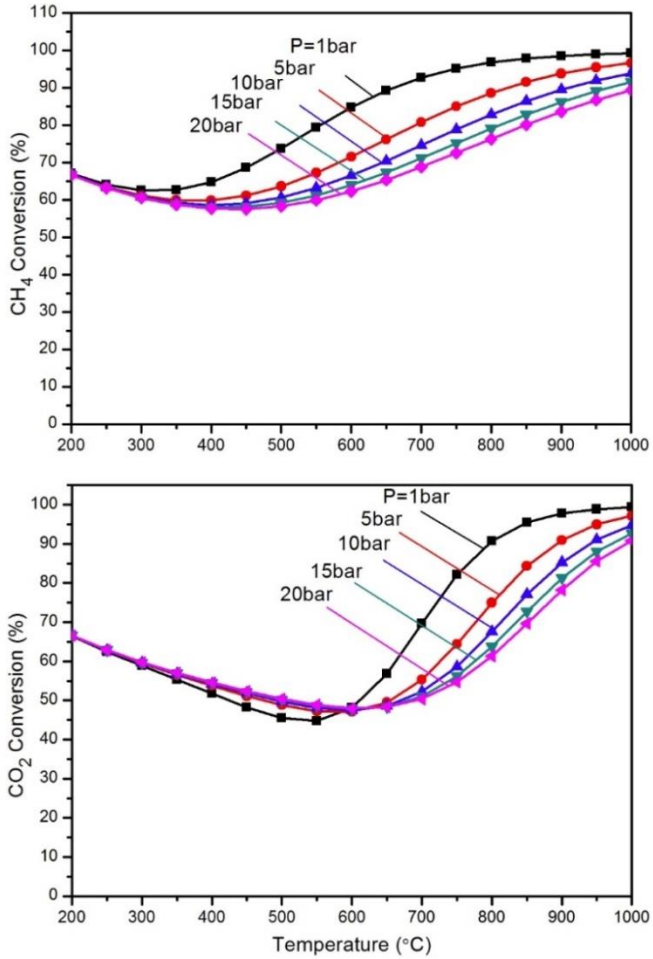

Figure 3-4: Influence of the pressure on the equilibrium conversions of CH_4 and CO_2 at $CH_4/CO_2/N_2$=1:1:1, considering carbon deposition.

The corresponding equilibrium yields of H_2, CO, carbon and H_2O are displayed in Figure 3-5. It is clearly indicated that the pressure has a strong influence on the equilibrium product distribution. The H_2 and CO production decreases with the increase in pressure, the pressure influence is more visible at the range of 600-900 ˚C, which is the common investigation temperature range. Carbon formation is more important at high pressure as the carbon generating reactions (Equation 3-4, Equation 3-5 and Equation 3-6) are generally volume decreasing reactions, which are thermodynamically favorable at high pressure. At the same temperature, water formation is higher with the increase in pressure. This may be due to greater CO_2 mole fraction at higher pressure which is advantage for the CO_2 consumed reactions such as reverse water gas shift reaction and CO_2 hydrogenation (shown in Equation 3-2 and Equation 3-6), which are also H_2O produced reactions.

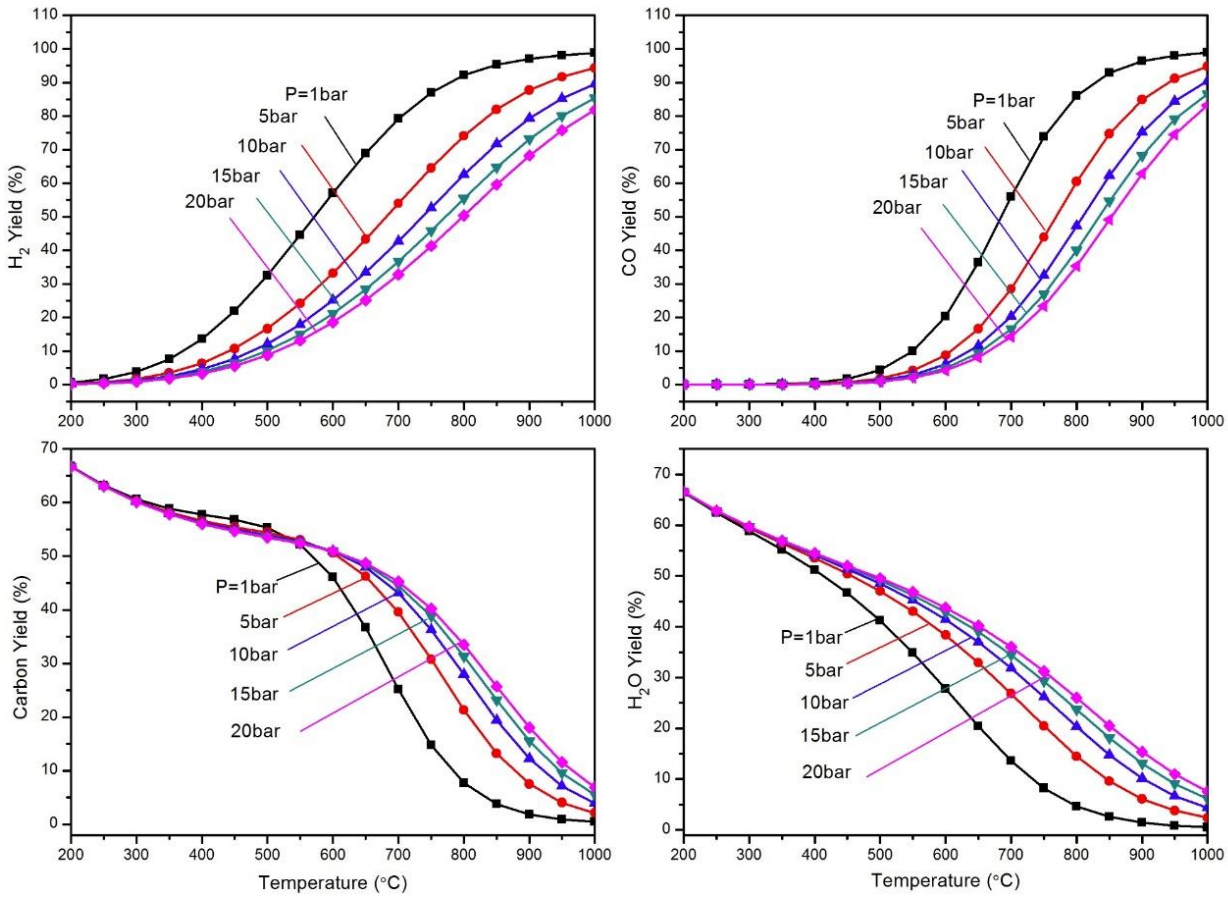

Figure 3-5: Pressure influence on **(a)** equilibrium yield of H_2; **(b)** equilibrium yield of CO; **(c)** equilibrium carbon yield; **(d)** equilibrium yield of H_2O at $CH_4/CO_2/N_2$=1:1:1, considering carbon deposition.

3.4.3 Influence of CH_4/CO_2 ratio on DMR

As already reported [3, 4], the composition of biogas strongly depends on the type of the biomass, the organic waste as well as the process conditions. The content of methane is normally in the range of 50-60%, carbon dioxide 35-45%. So it is interesting to study the effect of CH_4/CO_2 ratio for the dry methane reforming. Different CH_4/CO_2 ratios over the equilibrium composition were investigated. Figure 3-6 displays the equilibrium conversion of CH_4 and CO_2 at 10 bar and $(CH_4+CO_2)/N_2$ = 2:1.

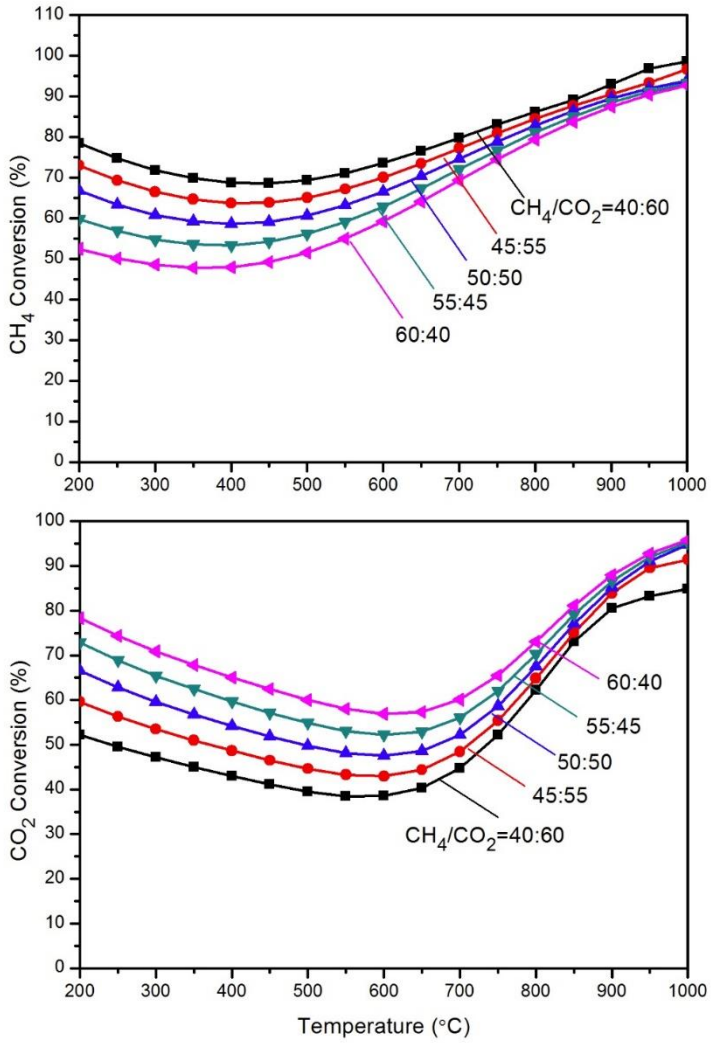

Figure 3-6: The influence of CH_4/CO_2 ratio on the equilibrium conversion of CH_4 and CO_2 at $(CH_4+CO_2)/N_2$ = 2:1 and pressure =10 bar.

It is clearly shown in Figure 3-6 that CH_4 conversion decreases with the increase in CH_4/CO_2 ratio, while CO_2 conversion increases with the rise of CH_4/CO_2 ratio. It is worth to point out that the influence of CH_4/CO_2 ratio is obvious at low temperature while it becomes inconspicuous at the temperature range of 600-900 ˚C.

Figure 3-7 shows the equilibrium yield of H_2, CO, H_2O and carbon formation at different CH_4/CO_2 ratio. There is a slight influence on the H_2 yield over different CH_4/CO_2 ratio at our research scope, specifically at elevated temperature (more than 900 ℃). In contrary, the CO, H_2O yield and carbon formation are strongly affected by the CH_4/CO_2 ratio.

The CO yield decreases with the increase in CH_4/CO_2 ratio. Dry methane reforming and reverse carbon gasification reactions are not in favor to CO production. At this high CH_4/CO_2 ratio, reaction of methane decomposition is predominant which explains the increase in

carbon formation at high CH_4/CO_2 ratio. H_2O yield is prevented by the excess of CH_4 and is promoted by the excess of CO_2 as this later species participates in the reverse water gas shift reaction, CO_2 methanation and CO_2 hydrogenation. Moreover, at low CH_4/CO_2 ratio, excess CO_2 prevents the carbon formation by its oxidation property.

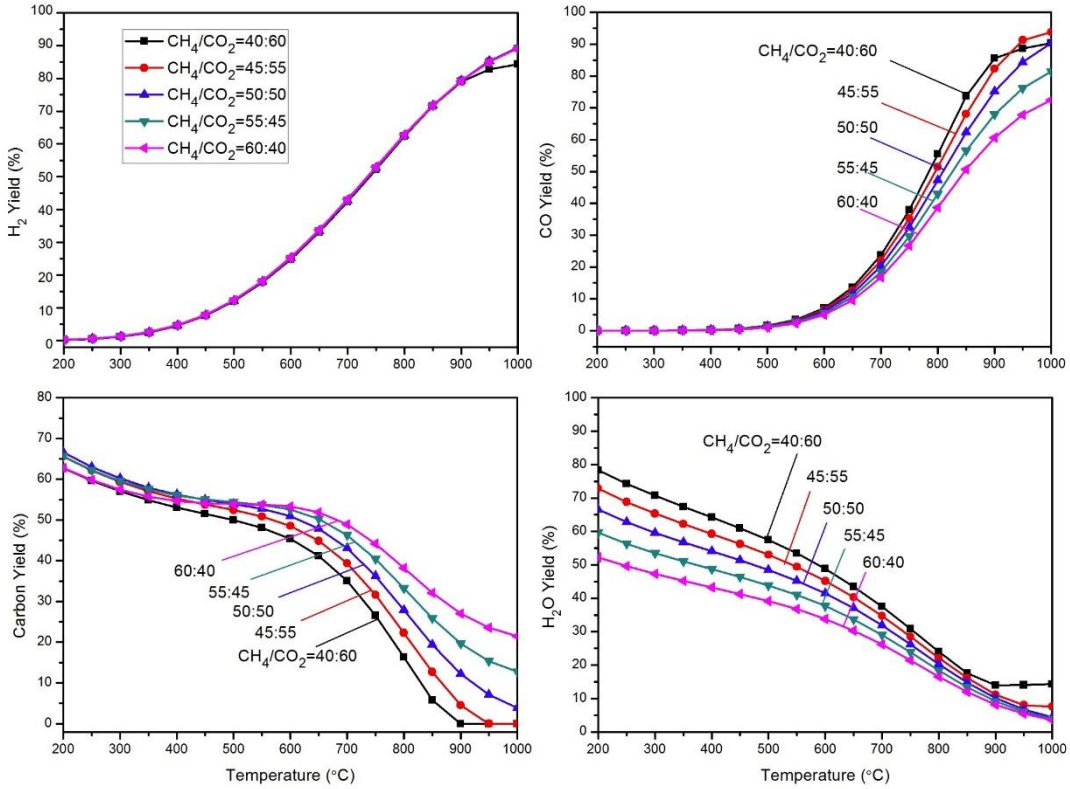

Figure 3-7: The influence of CH_4/CO_2 ratio on **(a)** the equilibrium yield of H_2; **(b)** equilibrium yield of CO; **(c)** equilibrium carbon yield; **(d)** equilibrium yield of H_2O at $(CH_4+CO_2)/N_2$=2:1 and pressure =10 bar.

3.4.4 Influence of the dilution with N_2 on DMR

Generally, the biogas contains 0.5-7% of nitrogen [1]. In addition, in order to calculate the composition of the outlet gas after dry methane reforming, N_2 was normally employed as an internal standard gas. So it is necessary to study the effect of the presence of this inert gas on the dry methane reforming. Different content of N_2 was investigated over the dry methane reforming equilibrium.

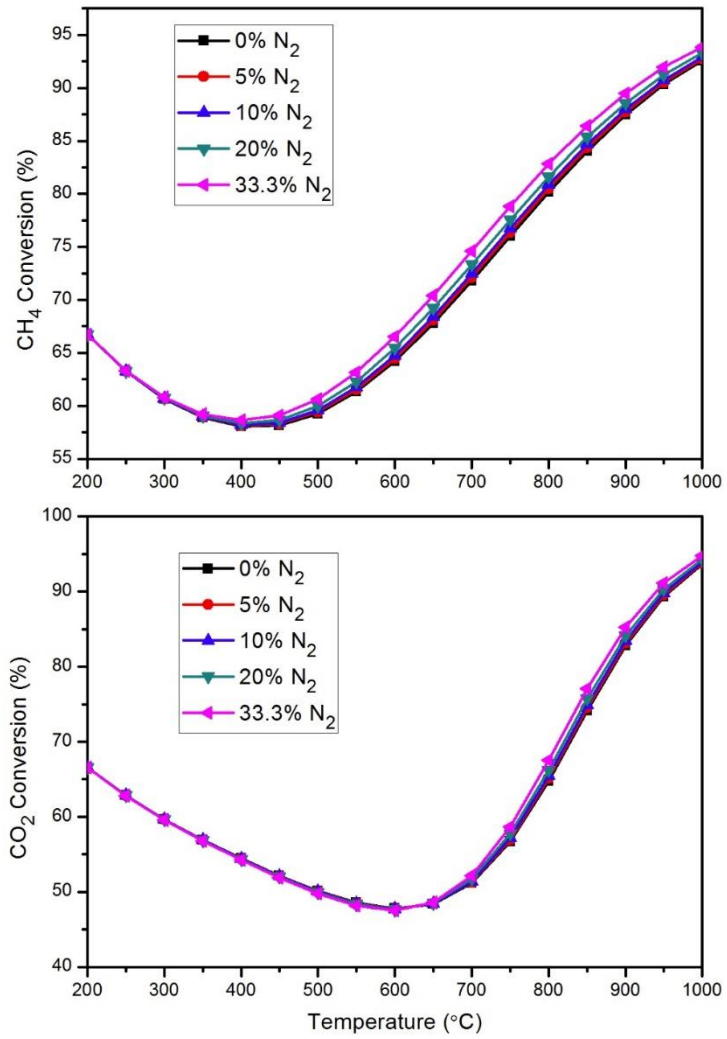

Figure 3-8: Influence of the presence of N_2 on the equilibrium conversion of CH_4 and CO_2 at CH_4/CO_2=1:1 and pressure=10 bar.

Based on the result in Figure 3-8 and Figure 3-9, N_2 has a positive effect on DMR resulting in a slight increase in CH_4 and CO_2 conversions. The addition of inert gas decreases the partial pressure of CH_4 and CO_2. The influence of the dilution with nitrogen on the production of hydrogen, carbon monoxide, carbon and water was negligible.

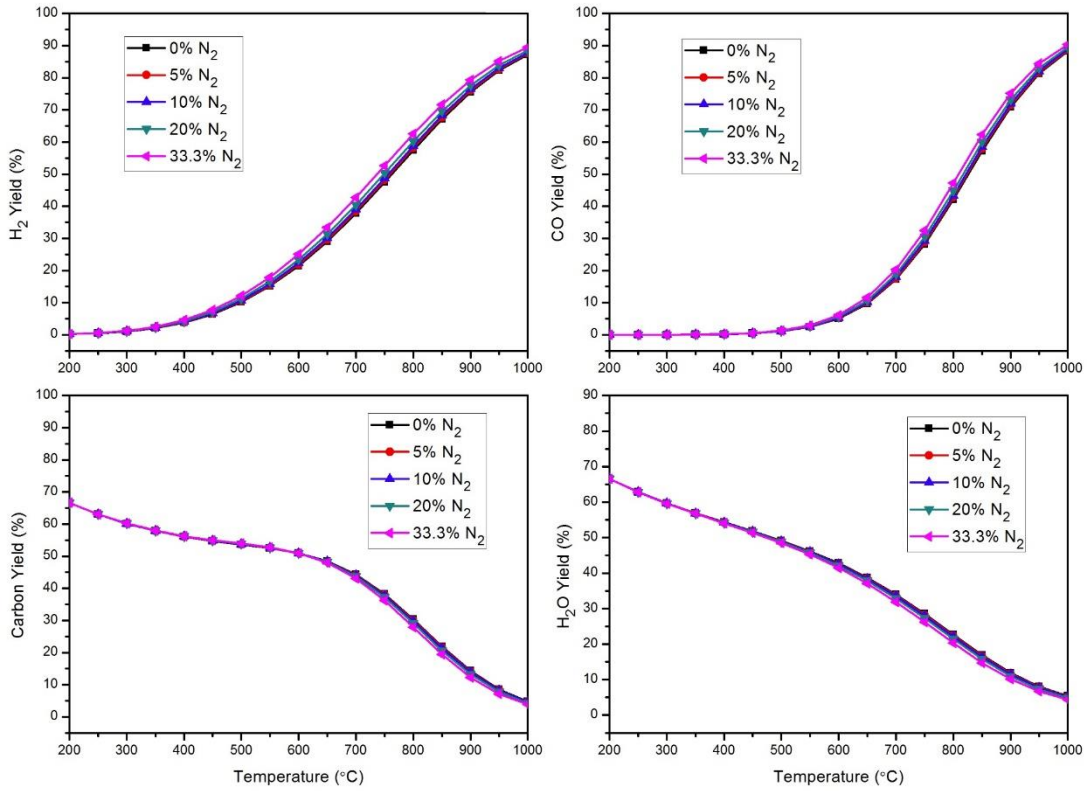

Figure 3-9: The influence of the presence of N_2 on **(a)** the equilibrium yield of H_2; **(b)** equilibrium yield of CO; **(c)** equilibrium carbon yield; **(d)** equilibrium yield of H_2O at $CH_4/CO_2/N_2$=1:1:1 and pressure = 10 bar.

3.5 Thermodynamic calculation of Fischer-Tropsch synthesis

3.5.1 Products distribution

As is shown in the Table 3-2, the equilibrium conversions of CO and H_2 approach 100% at 300 ˚C and 20 bar. Thermodynamically, the main products are CO_2 and CH_4 (25.3% and 74.7% respectively), while the selectivities of longer chain products (the C_2^+ products) and alcohols are negligible, which is concordant with some results in the literature [25, 29].

In practice, the CH_4 selectivity is lower, and higher selectivities of longer chain products and alcohols products are observed. Besides, the product distribution strongly depends on the catalysts. It is clearly indicated the significant difference between actual Fischer-Tropsch synthesis results and the distribution estimated by thermodynamic consideration. This strongly implies that Fischer Tropsch synthesis reactions are kinetically controlled and the product distribution is dominated by catalysts [21].

Table 3-2: Comparison between thermodynamic calculation and actual selectivity of Fischer-Tropsch synthesis product.

	Compound	Calculation result/%	Experiment results in bibliographies/ %	
			$FeSiO_2$ [30]	$KMoS_2/Al_2O_3$ [31]
conversion	CO	100	76.9	21.3
	H_2	99.5	51.6	-
Selectivity	CO_2	25.3	32.1	33.2
	CH_4	74.7	17.7	18.9
	C_2-C_4	2.89×10^{-3}	12.9	15.9
	$C_2^{=}$-$C_4^{=}$	2.74×10^{-8}	18.3	10.7
	C_5^{+}	1.61×10^{-14}	18.8	6.3
	C-OH	9.68×10^{-8}	0	15.1

Calculation condition: $H_2/CO/N_2$=40:20:1; Temperature=300 ˚C; pressure=20 bar; Reaction condition: $H_2/CO/N_2$=40:20:1; Temperature=300 ˚C; pressure=20 bar.

3.5.2 Influence of the presence of CH_4 and CO_2

The influence the presence of CH_4 and CO_2 is investigated and the equilibrium conversion is presented in Figure 3-10. It is clearly indicated that the conversion of CO and H_2 slightly decrease with the presence of CH_4 and CO_2. This results suggests that thermodynamically, the small amount of CH_4 and CO_2 (that could come from a non-conversion of a part a those reactants during the DMR reaction) in the feed gas scarcely affect the reaction equilibrium on the Fischer-Tropsch synthesis.

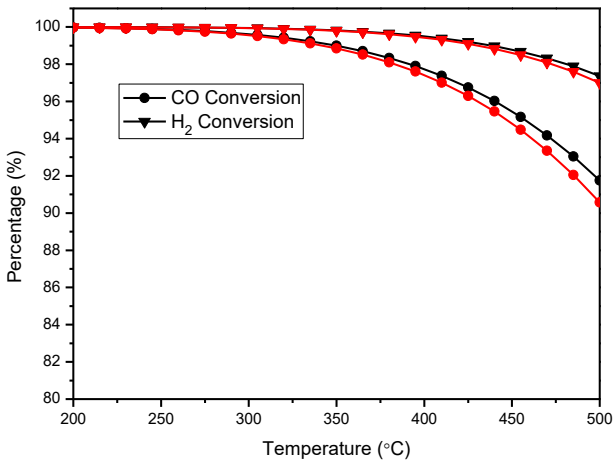

Figure 3-10: Equilibrium conversions of H_2 and CO at different temperature (**Black line:** pure syngas, **Red line** syngas with 5% CH_4 and 5% CO_2) at pressure = 10 bar and H_2/CO = 1.

3.6 Conclusion

Thermodynamic analysis of dry methane reforming via Gibbs free energy minimization method was employed to evaluate the effect of temperature, pressure, CH_4/CO_2 ratio and the presence of N_2. Based on the calculation results, the following conclusions are given:

- Carbon and H_2O formation are not favored at high temperature: the increase in temperature promotes the dry methane reforming reaction and the reverse water gas shift reaction, CO disproportionation and CO/CO_2 hydrogenation. Thus the generation of carbon and water formation is limited, leading to a ratio of H_2/CO approaching to the stoichiometric ratio of the DMR reaction.

- Increase in pressure is not favorable for dry methane reforming reaction. A decrease in methane and carbon dioxide conversion as well as the H_2 and CO selectivity along with the increase in water and carbon formation are observed with the pressure increase.

- Increasing CH_4/CO_2 ratio leads to lower CH_4 conversion and higher CO_2 conversion. The high CH_4/CO_2 ratio is inclined to restrict the RWGS reaction, leading to a decrease in H_2O production, to increase the carbon formation and affect scarcely the H_2 generation.

- Inert gas decreases the partial pressure of the reacting components, while no effect was observed on the thermodynamics of dry methane reforming.

Thermodynamic analysis of Fischer-Tropsch synthesis via Gibbs free energy minimization method was employed to estimate the products distribution and was applied for comparison with experimental results performed in the same condition of temperature and pressure. The calculation results indicated the Fischer-Tropsch synthesis reactions are kinetically controlled and the products distribution may be dominated by catalysts as well as by reaction conditions. Thermodynamically, the addition of CH_4 and CO_2 on the feedstock slightly decreases the equilibrium conversion especially at higher temperatures.

3.7 Reference

[1] L.C. Martins das Neves, A. Converti, T.C. Vessoni Penna, Biogas production: new trends for alternative energy sources in rural and urban zones, Chemical engineering & technology, 32 (2009) 1147-1153.

[2] E. Theofanous, N. Kythreotou, G. Panayiotou, G. Florides, I. Vyrides, Energy production from piggery waste using anaerobic digestion: Current status and potential in Cyprus, Renewable Energy, 71 (2014) 263-270.

[3] C. Chen, W. Guo, H.H. Ngo, D.-J. Lee, K.-L. Tung, P. Jin, J. Wang, Y. Wu, Challenges in biogas production from anaerobic membrane bioreactors, Renewable Energy.

[4] W. Papacz, Biogas as vehicle fuel, Journal of KONES, 18 (2011) 403-410.

[5] S.G. Gopaul, A. Dutta, Dry reforming of multiple biogas types for syngas production simulated using Aspen Plus: The use of partial oxidation and hydrogen combustion to achieve thermo-neutrality, International Journal of Hydrogen Energy, 40 (2015) 6307-6318.

[6] K.-H. Lin, H.-F. Chang, A.C.C. Chang, Biogas reforming for hydrogen production over mesoporous Ni2xCe1−xO2 catalysts, International Journal of Hydrogen Energy, 37 (2012) 15696-15703.

[7] S. Appari, V.M. Janardhanan, R. Bauri, S. Jayanti, Deactivation and regeneration of Ni catalyst during steam reforming of model biogas: An experimental investigation, International Journal of Hydrogen Energy, 39 (2014) 297-304.

[8] M. Kaewpanha, G. Guan, Y. Ma, X. Hao, Z. Zhang, P. Reubroychareon, K. Kusakabe, A. Abudula, Hydrogen production by steam reforming of biomass tar over biomass char supported molybdenum carbide catalyst, International Journal of Hydrogen Energy, 40 (2015) 7974-7982.

[9] N. Hajjaji, S. Martinez, E. Trably, J.-P. Steyer, A. Helias, Life cycle assessment of hydrogen production from biogas reforming, International Journal of Hydrogen Energy, 41 (2016) 6064-6075.

[10] Y. Cui, H. Zhang, H. Xu, W. Li, Kinetic study of the catalytic reforming of CH4 with CO2 to syngas over Ni/α-Al2O3 catalyst: The effect of temperature on the reforming mechanism, Applied Catalysis A: General, 318 (2007) 79-88.

[11] A.Y. Khodakov, W. Chu, P. Fongarland, Advances in the development of novel cobalt Fischer-Tropsch catalysts for synthesis of long-chain hydrocarbons and clean fuels, Chemical Reviews, 107 (2007) 1692-1744.

[12] R.H. Perry, D.W. Green, Perry's chemical engineers' handbook, McGraw-Hill Professional, 1999.

[13] P.C. Wankat, Separation Process Engineering: Includes Mass Transfer Analysis, Pearson Education, 2012.

[14] R.Y. Chein, Y.C. Chen, C.T. Yu, J.N. Chung, Thermodynamic analysis of dry reforming of CH4 with CO2 at high pressures, Journal of Natural Gas Science and Engineering, 26 (2015) 617-629.

[15] M. Jafarbegloo, A. Tarlani, A.W. Mesbah, S. Sahebdelfar, Thermodynamic analysis of carbon dioxide reforming of methane and its practical relevance, International Journal of Hydrogen Energy, 40 (2015) 2445-2451.

[16] S. Wang, G. Lu, G.J. Millar, Carbon dioxide reforming of methane to produce synthesis gas over metal-supported catalysts: state of the art, Energy & Fuels, 10 (1996) 896-904.

[17] J. Rostrupnielsen, J.B. Hansen, CO2-Reforming of Methane over Transition Metals, Journal of Catalysis, 144 (1993) 38-49.

[18] M. Bradford, M. Vannice, CO2 reforming of CH4, Catalysis Reviews, 41 (1999) 1-42.

[19] J. Zhang, H. Wang, A.K. Dalai, Development of stable bimetallic catalysts for carbon dioxide reforming of methane, Journal of Catalysis, 249 (2007) 300-310.

[20] J. Nakamura, K. Kubushiro, T. Uchijima, Behavior of surface oxygen on a Rh/Si02 catalyst in oxidation of methane, in: K.F.T.U. T. lnui, M. Masai (Eds.) Studies in Surface Science and Catalysis, Elsevier, 1993, pp. 373-376.

[21] W. Keim, Catalysis in C1 chemistry, Springer Science & Business Media, 2012.

[22] I. Romey, P.F.M. Paul, Synthetic Fuels from Coal: Status of the Technology, Springer Science & Business Media, 1987.

[23] J.R. Anderson, M. Boudart, Catalysis: science and technology volume Springer Science & Business Media, 1981.

[24] E.G. Christoffel, Laboratory reactors and heterogeneous catalytic processes, Catalysis Reviews Science and Engineering, 24 (1982) 159-232.

[25] Antonio C.D. Freitas, R. Guirardello, Thermodynamic Characterization of Hydrocarbon Synthesis from Syngas using Fischer-Tropsch Type Reaction chemical engineering transactions, 43 (2015) 6.

[26] Z. Xu, N. Wang, W. Chu, J. Deng, S. Luo, In situ controllable assembly of layered-double-hydroxide-based nickel nanocatalysts for carbon dioxide reforming of methane, Catalysis Science & Technology, 5 (2015) 1588-1597.

[27] N. Wang, W. Chu, T. Zhang, X.S. Zhao, Synthesis, characterization and catalytic performances of Ce-SBA-15 supported nickel catalysts for methane dry reforming to hydrogen and syngas, International Journal of Hydrogen Energy, 37 (2012) 19-30.

[28] M. Usman, W.M.A. Wan Daud, H.F. Abbas, Dry reforming of methane: Influence of process parameters—A review, Renewable and Sustainable Energy Reviews, 45 (2015) 710-744.

[29] M. Bell, Thermodynamically controlled catalysis: equilibria in Fischer-Tropsch synthesis, Canadian metallurgical quarterly, 34 (1995) 331-341.

[30] K. Cheng, M. Virginie, V.V. Ordomsky, C. Cordier, P.A. Chernavskii, M.I. Ivantsov, S. Paul, Y. Wang, A.Y. Khodakov, Pore size effects in high-temperature Fischer–Tropsch synthesis over supported iron catalysts, Journal of Catalysis, 328 (2015) 139-150.

[31] C. Liu, M. Virginie, A. Griboval-Constant, A. Khodakov, Impact of potassium content on the structure of molybdenum nanophases in alumina supported catalysts and their performance in carbon monoxide hydrogenation, Applied Catalysis A: General, 504 (2015) 565-575.

Chapter 4 Impact of nickel promotion for Mo_2C/Al_2O_3 catalysts and their performances in dry methane reforming

4.1 Introduction

Dry methane reforming, which consumes two strong greenhouse gases CH_4 and CO_2 and produces important chemicals H_2 and CO, has been intensively studied [1].

Catalysts play a crucial role in dry methane reforming process. Noble metals, such as Ru, Rh, Pd, Pt and Ir, display excellent catalytic performances and good stability for the dry methane reforming, whereas, their limited resources and high cost restrict their utilization at the industrial scales. Transition metals, such as Fe, Cu, Co especially Ni have been proven to be efficient catalysts for dry methane reforming [2, 3]. However, carbon deposition over transition metals is a crucial problem which is the main restriction for their application in the industry [4].

Molybdenum carbide, which has similar electronic structure with noble metals, has been widely used as catalyst for many reactions [5-7]. Particularly, it is becoming an attractive and promising catalyst for replacement of traditional dry methane reforming catalysts due to its excellent resistance for carbon deposition. However, in previous works [8-10], molybdenum carbide catalysts exhibited stable activity only at elevated pressure. Nevertheless, at atmospheric pressure, molybdenum carbide is easily oxidized by CO_2 during the dry methane reforming reaction and generates inactive phase such as MoO_2, which leads to rapid deactivation of the catalyst:

$$Mo_2C + 5\ CO_2 = 2\ MoO_2 + 6\ CO \qquad \text{Equation 4-1}$$

Otherwise, MoO_2 can be re-carburized by CH_4 to Mo_2C phase, which can be described as:

$$6\ MoO_2 + 5\ CH_4 = 3\ Mo_2C + 2\ CO + 10\ H_2O \qquad \text{Equation 4-2}$$

An oxidation-recarburization balance between MoO_2 and Mo_2C phase exists in the case of Mo_2C based catalyst. CO_2 dissociation on the catalysts is usually faster than that of CH_4, particularly at the atmosphere pressure condition [11].

As is reported in the literature [12-17], Ni promotion can help to keep bulk Mo_2C catalyst from the oxidation during reaction. Many publications focus on bulk molybdenum carbides [10, 14, 16, 17], while very few reports have been addressed so far to supported molybdenum carbide catalysts. Besides, the preparation method is crucial as it strongly affects the microstructure of the catalysts (such as the crystallite size of active phase) and/or the

interaction between active phase and support (which may has a strong impact on the catalytic behaviors).

This chapter particularly focuses on the influence of nickel promotion over alumina supported molybdenum carbide catalysts prepared by different methods: incipient wetness impregnation, impregnation & precipitation and mechanical mixture method. The catalyst nomenclatures, methods of preparation and nickel contents are listed in Table 4-1.

Table 4-1: Catalysts contents of nickel promoted molybdenum carbides catalysts.

Catalysts	Preparation method	Catalysts contents (wt%)		Ni/Mo Ratio(Atomic)
		Ni	Mo	
Mo/Al_2O_3	Incipient wetness impregnation	0	10	-
$NiMo/Al_2O_3$-1:2	Incipient wetness impregnation	3.2	10	1:2
$NiMo/Al_2O_3$-1:1	Incipient wetness impregnation	6.4	10	1:1
Ni/Al_2O_3	Incipient wetness impregnation	6.4	0	-
$NiMo/Al_2O_3$-1:2-M	Mechanical mixing	3.2	10	1:2
$NiMo/Al_2O_3$-1:1-M	Mechanical mixing	6.4	10	1:1
$NiMo/Al_2O_3$-1:2-IP	Impregnation & precipitation	3.2	10	1:2
$NiMo/Al_2O_3$-1:1-IP	Impregnation & precipitation	6.4	10	1:1

The different catalysts were characterized by nitrogen adsorption, X-ray diffraction (XRD), X-ray Photoelectron spectroscopy (XPS), Temperature Programmed Reduction of Hydrogen (H_2-TPR), Temperature Programmed Surface Reaction (TPSR), Scanning Electron Microscopy (SEM) and Thermo Gravimetric Analysis (TGA). The catalytic performances were evaluated in a fixed bed reactor at atmospheric pressure. Particularly dry methane reforming under pressure was also investigated in this chapter.

4.2 Characterizations of fresh nickel promoted Mo/Al_2O_3 catalysts

4.2.1 Textural structure

The specific surface area is an important catalyst characteristic. The textural properties of the alumina support, calcined and carburized Mo-based catalysts and those of the Ni promoted Mo-based catalysts are displayed in Table 4-2.

The surface area, average pore volume and diameter decreased after alumina impregnation with molybdenum. This decrease is probably partially due to both the “dilution”

effect of the support with molybdenum and the partial pore blockage of alumina by molybdenum species [18]. In addition, the promotion by nickel resulted in a further decrease in the catalyst surface area.

Table 4-2: the Physical properties of Mo carbides catalysts.

Sample		S_{BET} m^2/g	V_{total} cm^3/g	D_{meso} nm
Calcined samples	Al_2O_3	138.7	0.42	6.0
	Mo/Al_2O_3	123.4	0.33	5.4
	$NiMo/Al_2O_3$-1:1	115.2	0.31	5.1
Carburized samples	Mo/Al_2O_3	119.7	0.34	5.7
	$NiMo/Al_2O_3$-1:1	106.6	0.31	5.3
	$NiMo/Al_2O_3$-1:1-M	104.8	0.32	5.3
	$NiMo/Al_2O_3$-1:1-IP	101.3	0.30	5.8

The BET surface area also decreased after carburization (123.4 m^2/g before and 119.7 m^2/g after carburization for Mo/Al_2O_3 catalyst; 115.2 m^2/g before and 104.8 m^2/g after carburization for $NiMo/Al_2O_3$-1:1 catalyst). This decrease is probably attributed to the partial pore blockage of alumina support caused by the carbon formation during carburization process [19].

Beside, despite the preparation method of catalyst (mechanical mixing, impregnation & precipitation or incipient wetness impregnation), the textural properties (surface area, average pore volume and diameter) of the carburized samples remains similar. This is in accordance to previous reports [18].

4.2.2 X-ray diffraction for oxide catalysts

X-ray diffraction patterns for calcined nickel promoted Mo/Al_2O_3 catalysts are shown in Figure 4-1. The diffraction peaks at 2θ of 23.3 °, 25.7 ° and 27.3 ° for the non-promoted Mo/Al_2O_3 catalyst are attributed to the crystallographic planes of the orthorhombic MoO_3 phase (JCPDS 35-0609). The XRD peaks broadening indicates higher dispersion of molybdenum species on the alumina support [20].

After nickel promotion by incipient wetness impregnation, no characteristic peaks of MoO_2 or MoO_3 were detected on the diffractograms (Figure 4-1 b and c). This suggests that the molybdenum species were better dispersed on the alumina support, the crystallite sizes

should be below the detection limits of X-ray diffraction [21]. The addition of nickel promotes the dispersion of molybdenum species on the alumina support. No new diffraction peaks corresponding to nickel-containing crystalline phases are observed.

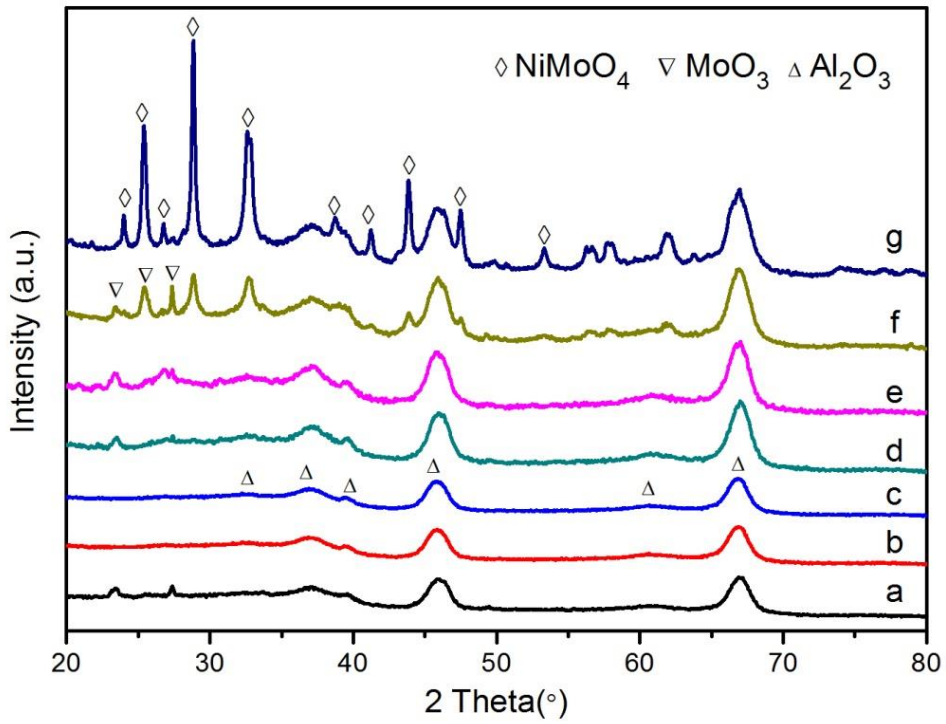

Figure 4-1: XRD patterns of calcined nickel promoted Mo/Al_2O_3 catalysts (**a**) Mo/Al_2O_3; (**b**) $NiMo/Al_2O_3$-1:2; (**c**) $NiMo/Al_2O_3$-1:1; (**d**) $NiMo/Al_2O_3$-1:2-IP; (**e**) $NiMo/Al_2O_3$-1:1-IP; (**f**) $NiMo/Al_2O_3$-1:2-M; (**g**) $NiMo/Al_2O_3$-1:1-M.

The XRD patterns for nickel promoted Mo/Al_2O_3 catalysts prepared by other methods were also investigated. For the mechanical mixture $NiMo/Al_2O_3$-1:1-M catalyst (Figure 4-1 g), the peaks at 2θ of 24.0 °, 25.3 °, 28.8 °, 32.3 °, 38.6 °, 41.2 °, 43.9 °, 47.4 °, and 53.4 ° can be attributed to the crystallographic planes of the monoclinic $NiMoO_4$ phase (JCPDS 35-0948). The shape and evident intensity indicated the presence of considerable crystallite size for the $NiMoO_4$ phase. Moreover, the same characteristic peaks of both $NiMoO_4$ and MoO_3 are evidenced over $NiMoO_3/Al_2O_3$-1:2-M catalyst (Figure 4-1 f) with lower intensity, which may be due to the less nickel content compared with the stoichiometric catalyst. The characteristic peaks of MoO_3 are visible over both catalysts prepared by impregnation & precipitation method: $NiMo/Al_2O_3$-1:1-IP and $NiMo/Al_2O_3$-1:2-IP (Figure 4-1 e and d). This indicates the presence of greater MoO_3 crystallite size compared with their counterparts prepared by incipient wetness impregnation. The crystallite size of molybdenum species increases

following the preparation method order of: mechanical mixture > impregnation & precipitation > incipient wetness impregnation.

4.2.3 X-ray diffraction for carburized catalysts

X-ray diffraction patterns for carburized NiMo/Al_2O_3-1:1 catalysts prepared by the three different methods were investigated and the results are shown in Figure 4-2. No characteristic peaks for MoO_2 or MoO_3 were detected for the carburized NiMo/Al_2O_3-1:1 (incipient wetness impregnation) and NiMo/Al_2O_3-1:1-IP (impregnation & precipitation) catalysts. It is difficult to characterize Mo_2C/Al_2O_3 because some of the characteristic peaks of β-Mo_2C overlapped with the characteristic peaks of alumina phase. However, the other characteristic peaks of β-Mo_2C at 2θ = 52.3 °, 61.9 °, 74.6 °, and 75.5 ° were not detected. No characteristic peaks for metallic nickel or nickel oxide have been observed, which allowed to conclude that the molybdenum carbide and nickel were highly dispersed on the alumina support, the crystallite sizes being below the detection limits of X-ray diffraction [21].

In the catalyst prepared by mechanical mixture, the width of the XRD peaks suggests that this catalyst presents larger crystallite size compared to the other two catalysts. Intense peaks were detected at 2θ of 34.4 °, 38.0 °, 39.4 °, 52.3 °, 61.9 °, 74.6 °, and 75.5 ° and can be attributed to molybdenum carbide. Other peaks at 2θ of 44.3 °, 51.7 ° and 76.1 ° are visible and can be attributed to metallic nickel. No characteristic peaks of molybdenum oxide or nickel oxide were observed, which indicated that the molybdenum species were completely converted to carbides phase during the carburization process.

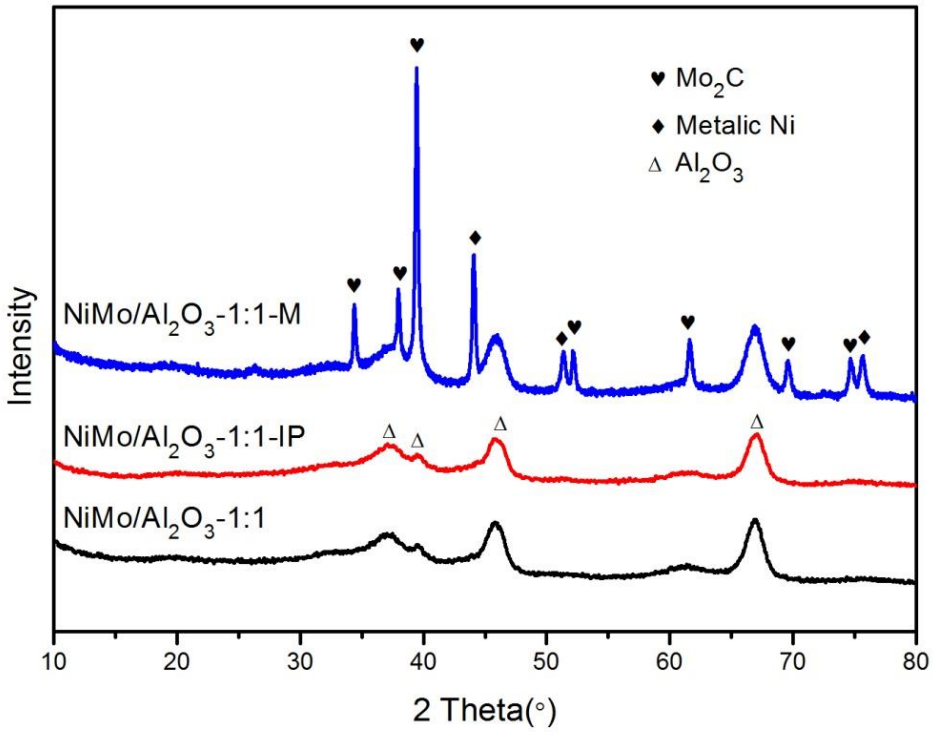

Figure 4-2: XRD patterns of carburized $NiMo/Al_2O_3$-1:1 catalyst prepared by different methods.

4.2.4 H_2-TPR for oxide catalysts

To investigate the interaction between Ni, Mo species and alumina support of the calcined catalysts, H_2-TPR experiments were employed and the results are shown in Figure 4-3.

Unsupported bulk NiO is known to be reduced to metallic Ni^0 in the 200 - 450 ℃ [14, 22, 23]. However, as is shown in Figure 4-3, the reduction peak of nickel (6.4 wt%, same content of Ni with $NiMo/Al_2O_3$-1:1 catalyst) supported on alumina is shifted to the 450-750 ℃ temperature range, which may due to the strong interaction between NiO and the alumina support. These strong $NiO\text{-}Al_2O_3$ interactions are caused by the dissolution and incorporation of Al^{3+} ions in NiO crystallites [23, 24].

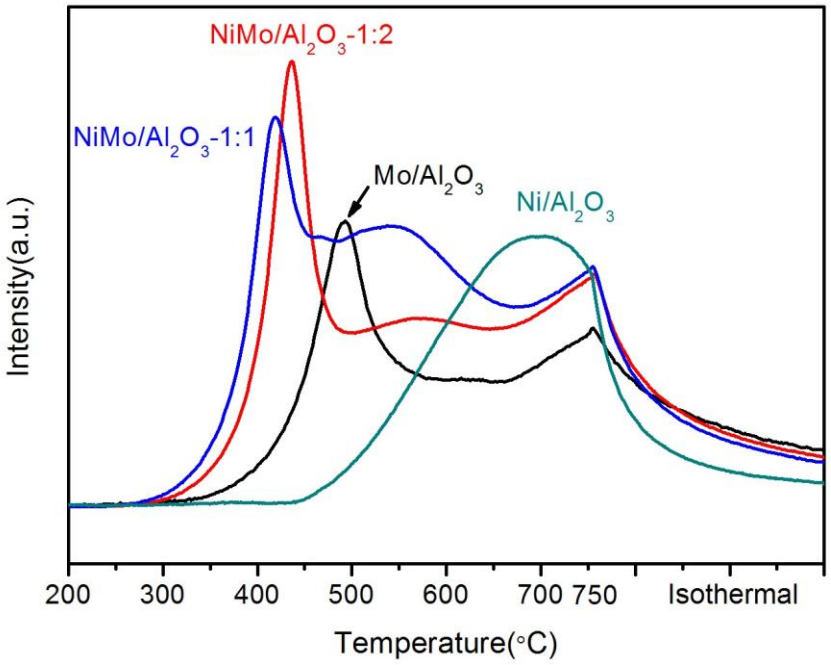

Figure 4-3: H_2-TPR of calcined molybdenum based catalyst, nickel based catalyst and nickel promoted molybdenum catalysts.

Two reduction peaks are distinguished for the calcined Mo/Al_2O_3 catalyst. The low temperature peak at around 490 ℃ can be attributed to the partial reduction of polymolybdate or MoO_3 from Mo^{6+} to Mo^{4+} [20, 25-27]. Whereas the high temperature broad peak at approximately 750 ℃ may be due to further progress in the reduction of partially reduced molybdenum species to metallic Mo species (Mo^{4+} to Mo^0), together with the reduction of tetrahedrally coordinated Mo species, which were difficult to reduce due to their strong interaction with alumina support [20, 26, 28, 29].

Similarly, nickel promoted Mo/Al_2O_3 catalysts also exhibited the low temperature H_2 consumption peak at the range of 400 to 450 ℃ which can be attributed to the partial reduction of polymolybdate from Mo^{6+} to Mo^{4+} and high temperature peak at approximately 750 ℃ that corresponding to second H_2 consumption peak of non-promoted Mo/Al_2O_3 catalyst. An obvious shift to lower temperature for the first peak is observed with the addition of nickel. This may indicate that the promotion of nickel weakens the interaction between molybdenum and alumina support.

Particularly, a new peak at around 550 ℃ is observed, which intensity varies with the increase in the amount of nickel. This peak can be attributed to the reduction of $NiMoO_4$ species [12, 16, 29, 30].

4.2.5 H_2-TPR for carburized catalysts

The H_2-TPR curves of carburized $NiMo/Al_2O_3$-1:1 catalysts prepared by the three different methods are shown in Figure 4-4. For the carburized $NiMo/Al_2O_3$-1:1 sample, the TCD signal indicates the presence of an intense hydrogen consumption peak between 250 - 375 ℃, a smaller hydrogen consumption peak between 425-600 ℃ and a broad hydrogen consumption peak between 650-900 ℃. Note that some peaks can be attributed to production of methane during the TPR experiments. Previous reports [19, 31-33] suggested that several layers of carbon could be formed on the surface of an ideal Mo_2C phase. The first peak can be attributed to the reaction of hydrogen with oxygen (as the catalysts have been passivated before the TPR experiment) and/or to the reduction of surface carbidic carbon. The second peak can be attributed to the reduction of a sublayer of carbon, producing methane. The third broad H_2 consumption peak can be attributed to the reduction of Mo_2C phase [31, 33] along with the reduction of graphitic carbon [34].

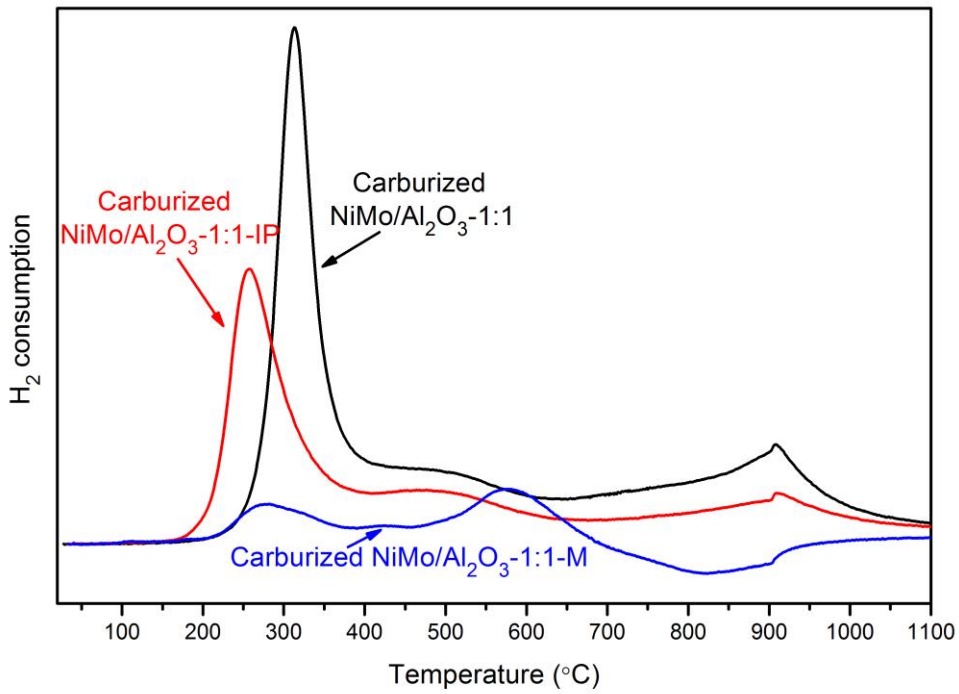

Figure 4-4: H_2-TPR of carburized $NiMo/Al_2O_3$-1:1 catalyst prepared by different methods.

Impregnation & precipitation method prepared sample ($NiMo/Al_2O_3$-1:1-IP) showed similar H_2 consumption curve with its counterpart prepared by incipient wetness impregnation. However, a shift to lower temperature of the first peak and a decrease in intensity was observed for the catalyst prepared by impregnation & precipitation method ($NiMo/Al_2O_3$-1:1-IP). This shift is probably due to the weaker interaction between Mo species and alumina support prepared by impregnation & precipitation method.

Catalyst prepared by mechanical mixture method ($NiMo/Al_2O_3$-1:1-M) displayed a significant different trend for the H_2-TPR. Three hydrogen consumption peaks at the range of 200-400 ℃, 375-475 ℃ and 500-700 ℃ as well as a slight hydrogen generation peak (negative peak) at the temperature range of 700 to 900 ℃ were observed. The previous two peaks can be attributed to the reduction of Mo oxide phase generated during the passivation step and reduction of surface carbidic carbon, respectively. The third peak may be attributed to the gradual reduction of Mo_2C phase, which is similar to molybdenum bulk carbides catalysts reported in the literature [32, 35]. Compared with the other 2 samples, a slight shift to lower temperature was observed, which may be due to the weak interaction between molybdenum and alumina support prepared by mechanical mixture method.

The following peak of H_2 generation may be assigned to the hydrogen spillover [36, 37], which is a common phenomenon for noble metals such as Pt [38, 39]. Hydrogen molecules can be adsorbed and dissociated by noble metal catalyst and migrated into nonmetal support which served as a hydrogen “reservoir”. With increasing the temperature, the hydrogen is desorbed. As the molybdenum carbides catalyst is said to have similar structure with noble metal, the observation of hydrogen spillover phenomena over molybdenum carbide has been proved [36, 37, 40, 41]. It occurred during the carburization process under CH_4/H_2 flow, with the increase in temperature and the reduction of Mo_2C.

4.2.6 X-ray Photoelectron spectroscopy for carburized catalysts

XPS technology was employed to investigate chemical states of the elements in the carburized nickel promoted Mo_2C catalysts. Before the measurements, the catalysts have been passivated in order to be transferred from the quart reactor to the XPS cell. The results are displayed in Figure 4-5, Table 4-3 and Figure 4-6.

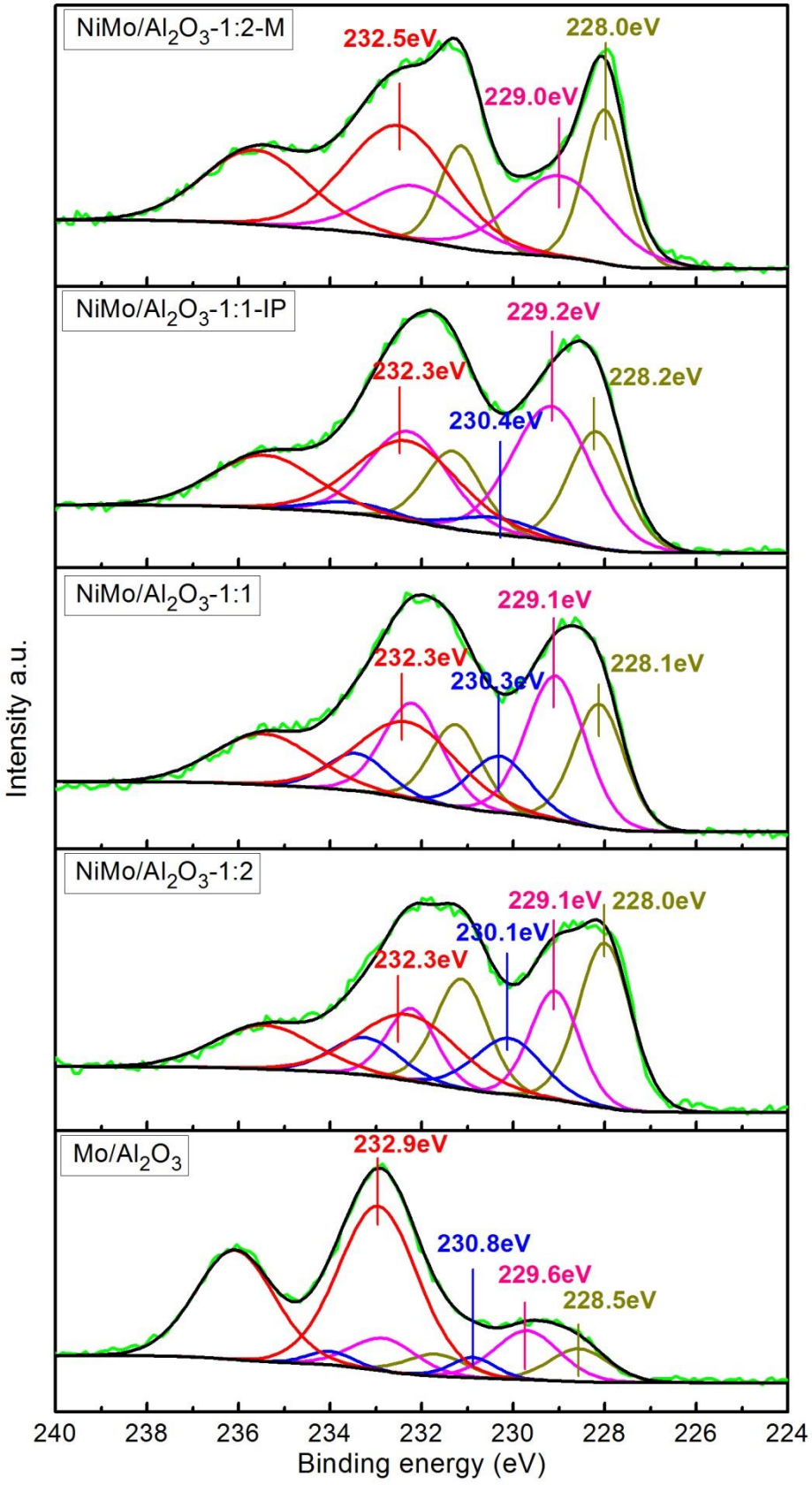

Figure 4-5: Mo 3d XPS spectra of carburized nickel promoted Mo/Al_2O_3 catalysts prepared by different methods.

The Mo 3d XPS spectrum of carburized Mo/Al_2O_3 catalyst is illustrated in Figure 4-5. The broad envelop of the Mo 3d signal can be decomposed in several separate overlapping doublets indicating that Mo exist on different oxidation state:

- The peak at binding energy (BE) of 228.5 eV can be attributed to Mo^{2+} species which may be involved in Mo carbide [42-45].
- The peak at binding energy of 229.6 eV can be attributed to Mo^{4+} species which can probably be associated to the MoO_2 species [46-48] .
- The peak at binding energy of 230.8 eV can be identified to $Mo^{\delta+}$ ($4 < \delta < 6$) which may be involved in Mo oxycarbide species [14, 46, 49].
- The one at binding energy of 232.9 eV can be attributed to Mo^{6+} species which may be involved in MoO_3 species [14, 46].

The presence of those two later species can be explained by the passivation step which oxidized the surface Mo carbide. However, it cannot be totally excluded that the presence of oxides can be due to incomplete carburization.

As is shown in Figure 4-5, similar XPS spectra were observed for the carburized nickel promoted Mo/Al_2O_3 catalysts. All the catalysts displayed intense peaks of Mo^{2+}, $Mo^{\delta+}$, and Mo^{6+} species. The presence of Mo^{2+} species strongly implied the existence of Mo_2C phase on the carburized catalysts. No characteristic peak of metallic molybdenum was detected for all the catalysts. Particularly, no characteristic peak of Mo^{4+} species was observed for $NiMo/Al_2O_3$-1:2-M sample.

Table 4-3 displays the molybdenum species distribution obtained by XPS. The result indicated that a considerable percentage of Mo^{6+} species (68.1%) and a low percentage of Mo^{2+} species (10.3%) on the unprompted Mo/Al_2O_3 catalyst. The addition of nickel promoter increased the Mo^{2+} species and decreased Mo^{6+} species, which were obviously observed on the carburized $NiMo/Al_2O_3$-1:2 and $NiMo/Al_2O_3$-1:1 catalysts. This may imply that the promotion of nickel improves the carburization capacity of Mo/Al_2O_3 catalyst.

The considerable percentage of Mo^{2+} species suggests the presence of Mo_2C phase over carburized $NiMo/Al_2O_3$-1:1-IP and $NiMo/Al_2O_3$-1:2-M catalysts.

Table 4-3: Mo species distribution (Mo^{X+}/Mo ratio) of carburized nickel promoted Mo/Al_2O_3 catalysts prepared by different methods.

Catalysts		Mo species distribution (%)			
		Mo^{2+}	Mo^{4+}	$Mo^{\delta+}$	Mo^{6+}
Mo/Al_2O_3	Position/eV	228.5	229.7	230.8	232.9
	Species distribution	10.3	16.8	4.8	68.1
$NiMo/Al_2O_3$-1:2	Position/eV	228	229.1	230.1	232.3
	Species distribution	35.5	21.8	15.6	27.1
$NiMo/Al_2O_3$-1:1	Position/eV	228.1	229.1	230.3	232.3
	Species distribution	24.2	32.9	13.3	29.6
$NiMo/Al_2O_3$-1:1-IP	Position/eV	228.2	229.2	230.4	232.3
	Species distribution	27.1	44.4	5.6	22.9
$NiMo/Al_2O_3$-1:2-M	Position/eV	228	229	230.2	232.5
	Species distribution	25.0	30.0	0	45.0

Figure 4-6 shows the C1s XPS spectra of carburized Mo/Al_2O_3 and Ni promoted Mo/Al_2O_3 catalysts, after deconvolution of the broad envelop of the C 1s signal, 4 carbon peaks are observed:

- The first peak at a binding energy of 282.9 eV can be attributed to the carbidic carbon which may be characteristic of the molybdenum carbide phase [42, 44, 45, 50];

- The peak at a binding energy about 284.8 eV can be associated to C-C bond from free carbon (such as graphitic carbon) [44, 45]. This carbon may be due to the carbon deposition that is usually found on the surface of molybdenum carbide samples;

- The peak at a binding energy of 286.3 eV can be attributed to the C-O bond [45, 50];

- The last peak at a binding energy of 288.7 eV can be associated to the C=O bond. Those two later species may be due to the surface oxidation during passivation or the carbon of oxycarbides species [42, 44, 45].

As is clearly displayed in the Figure 4-6, all catalysts showed evident carbon peaks for free carbon (Binding energy = 284.8 eV) and oxidized carbon (Binding energy at 286.3 eV and 288.7 eV). Besides, except the $NiMo/Al_2O_3$-1:1 catalyst, characteristic peaks attributed to

carbidic carbon were observed over all the other samples, which further proves the presence of molybdenum oxycarbides. It needs to point out that the intensity of carbidic carbon peak was very low. The absence of carbidic carbon peak in the $NiMo/Al_2O_3$-1:1 catalyst or the low intensity is probably due to the surface oxidation during passivation step.

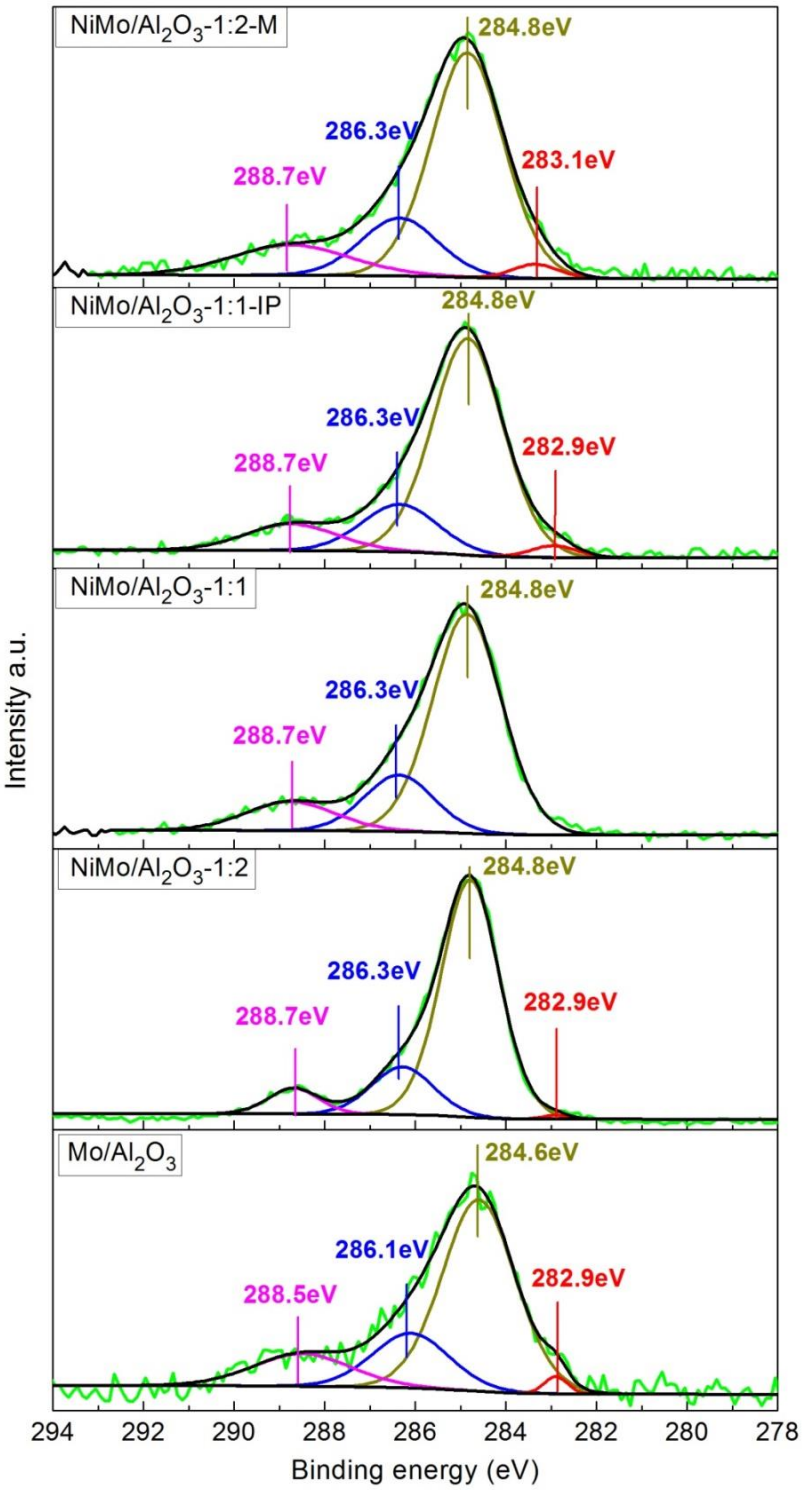

Figure 4-6: C 1s XPS spectra of carburized Mo/Al_2O_3 and nickel promoted Mo/Al_2O_3 catalysts prepared by different methods.

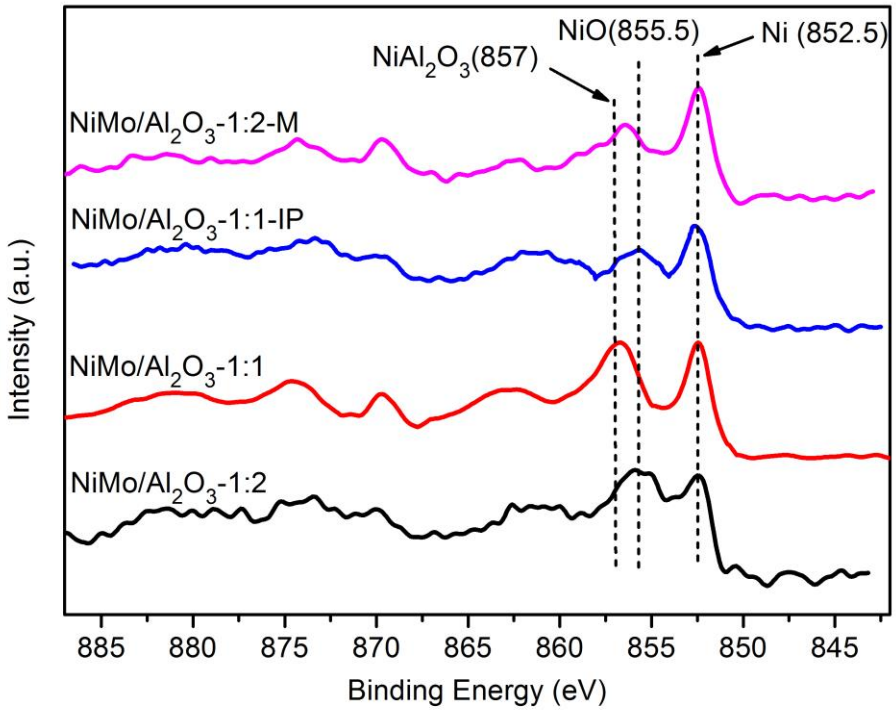

Figure 4-7: Nickel 2p XPS spectra of carburized nickel promoted Mo/Al_2O_3 catalysts prepared by different methods.

Figure 4-7 shows the nickel 2p XPS spectra of carburized nickel promoted Mo/Al_2O_3 catalysts prepared by different methods. Different nickel species were detected by the XPS spectra:

- The peaks at binding energy of 852.5 eV can be attributed to metallic nickel phase Ni^0 [51, 52];
- The peaks at binding energy of 855.5 eV can be attributed to Ni^{2+} species which can be involved in NiO phase [52, 53];
- The peak at binding energy of 857 eV can be attributed to Ni–Al spinel ($NiAl_2O_3$) phase [51, 53, 54] due to the interaction between nickel species and alumina support.

As is clearly displayed in Figure 4-7, all the samples showed peaks of metallic nickel for the nickel promoted Mo/Al_2O_3 catalysts after carburization. Characteristic peaks attributed to NiO and Ni–Al spinel were also detected for all the samples. This may suggest incomplete reduction of nickel due to the strong interaction between nickel species and alumina support as well due to the carburization process.

4.2.7 (CH_4/CO_2)-Temperature programmed surface reaction (TPSR)

Figure 4-8 shows the (CO_2-CH_4)-TPSR profiles obtained over carburized Ni/Al_2O_3 catalyst, Mo/Al_2O_3 catalyst and with different amount of nickel promotion.

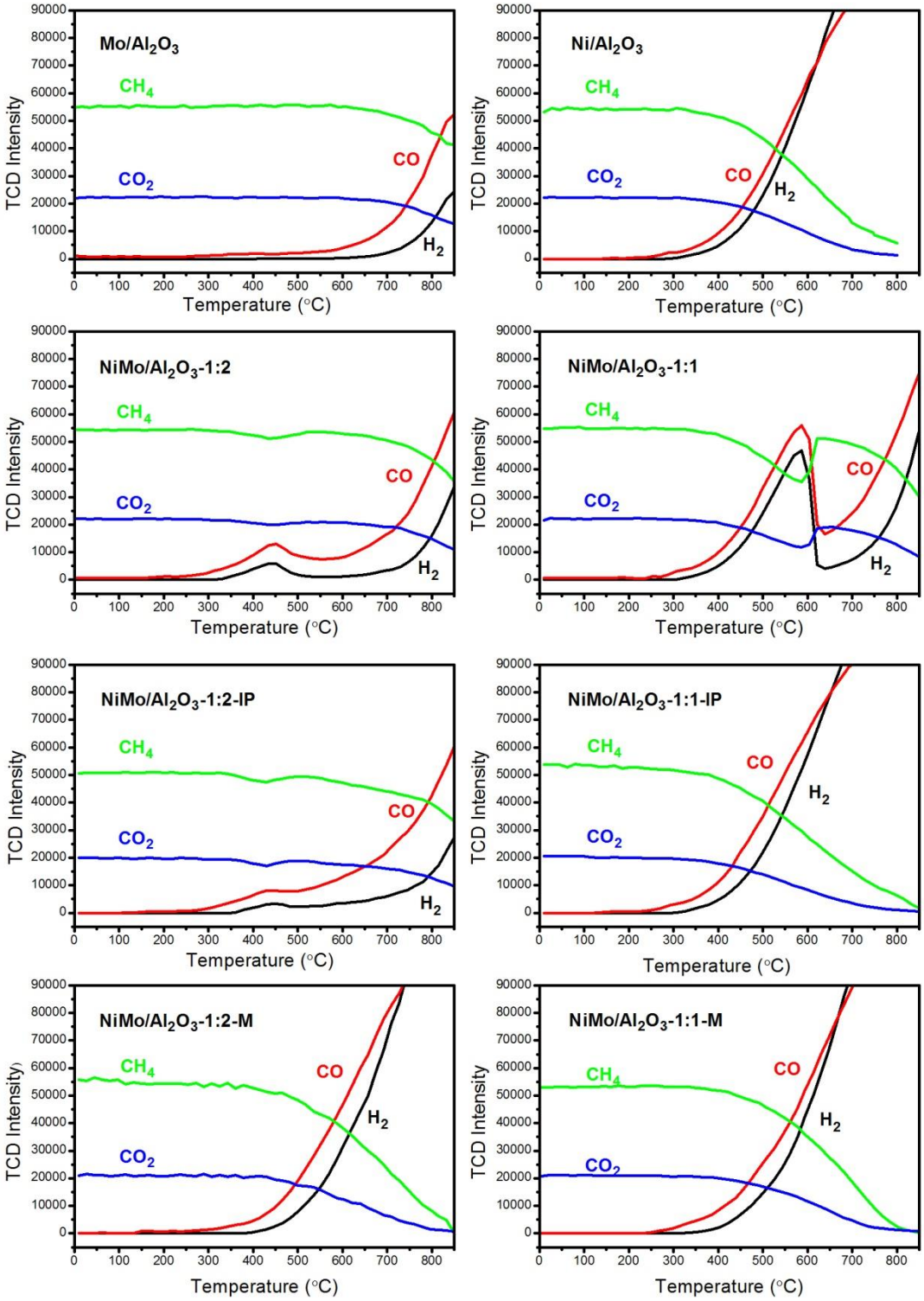

Figure 4-8: (CO_2-CH_4)-Temperature programmed surface reaction (TPSR) over carburized molybdenum based catalyst, nickel based catalyst and Ni promoted Mo/Al_2O_3 catalysts.

As it is obviously shown in Figure 4-8, the initial activation temperature of methane and carbon dioxide is about 620 ℃ for the non-promoted molybdenum carbide catalyst, whereas, methane and carbon dioxide are activated at lower temperature (300 ℃) over the reference nickel catalyst.

Preparation methods have a significant influence on the TPSR curves over dry methane reforming. For the catalyst prepared by incipient wetness impregnation, with the addition of nickel at a Ni:Mo ratio 1:2, a slight activity is observed at 300 ℃, which coincides with the activation temperature of nickel species. This suggests the presence of metallic nickel phase. The CH_4 and CO_2 conversions increased when the ratio Ni:Mo is raised to 1:1 at this same temperature of 300 ℃. Afterward, the reaction was activated again at about 620 ℃ which coincide with the activation temperature of molybdenum carbide species.

The $NiMo/Al_2O_3$-1:2-IP catalyst exhibited similar trend with its counterpart $NiMo/Al_2O_3$-1:2 catalyst. However, different curves were observed for the $NiMo/Al_2O_3$-1:1-IP catalyst compared with the $NiMo/Al_2O_3$-1:1 catalyst by incipient wetness impregnation method. The curves are similar to the TPSR curves of Ni supported on alumina catalyst, with a reforming activity starting at about 300 ℃. No activity decrease was detected after reaction activated at 300 ℃.

For the two samples prepared using mechanical mixing, $NiMo/Al_2O_3$-1:2-M and $NiMo/Al_2O_3$-1:1-M catalysts, the reaction was activated at 300 ℃ and the activity increased with increasing the temperature. Their TPSR profiles are similar to those of the reference Ni/Al_2O_3 catalyst.

This implies that the dry methane reforming over the Mo_2C catalysts strongly depends on the Ni promotion, particle size and the interaction between Mo and support.

4.3 Catalytic performance over dry methane reforming

4.3.1 Catalytic performance at different temperature

The catalytic performance of different amount of nickel promoted Mo/Al_2O_3 catalyst was measured in a fixed-bed tubular quartz reactor. Before the reaction, all the samples were carburized in-situ with CH_4/H_2 at 700 ℃ for 2 h. The activity was evaluated every 50 ℃ over the temperature range of 700–850 ℃ and stability was measured for the catalyst with the greatest conversion at 850 ℃. The catalytic performances are shown in Figure 4-9.

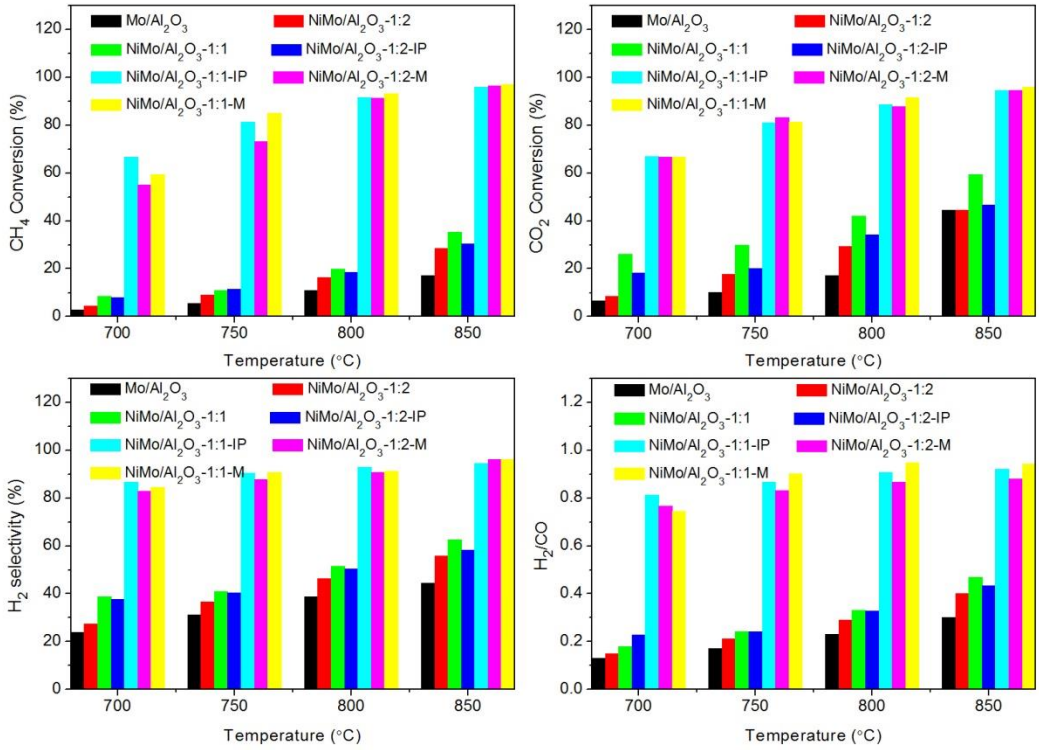

Figure 4-9: Effect of Ni over Mo_2C/Al_2O_3 catalysts at different reaction temperature over GHSV = 6000 $ml.g^{-1}.h^{-1}$, time on stream = 1h and atmosphere pressure.

As is shown in Figure 4-9, non-promoted molybdenum carbide catalyst showed low activity in dry methane reforming. The methane and carbon dioxide conversion are as low as 2.9% and 6.7% respectively at 700 ℃. The higher conversion of CO_2 than methane may be due to the simultaneous occurrence of the reverse water gas shift reaction ($CO_2 + H_2 = H_2O + CO$) [54, 55], which is also the reason for low H_2/CO ratio. As expected, increasing temperature increased dry methane reforming activity. The methane conversion and CO_2 conversion reached 17.2% and 44.6% respectively at 850 ℃. Furthermore, the H_2/CO ratio also increased obviously with the increase in temperature, which is in agreement with the thermodynamic analysis [55, 56].

The results indicated that catalyst activity and H_2 selectivity are dependent on Ni/Mo ratio [10]. Let us first discuss about the performance of the 3 catalysts prepared by impregnation method. Compared to the non-promoted molybdenum carbides catalyst, the addition of nickel increased the dry methane reforming activity

Different catalytic performances were observed for the catalysts prepared by different methods in dry methane reforming. Compared with the incipient wetness impregnation prepared counterpart $NiMo/Al_2O_3$-1:2, higher activity and H_2 selectivity were observed in the $NiMo/Al_2O_3$-1:2-IP samples prepared by impregnation & precipitation method. Significant

influences were obtained with the increasing of nickel content over dry methane reforming. $NiMo/Al_2O_3$-1:1-IP catalyst exhibited excellent activity and H_2 selectivity. The CH_4 and CO_2 conversion reached 96.0% and 95.1% along with 94.6% of H_2 selectivity and a H_2/CO ratio of 0.92 at 850 ℃. Different to the other samples, all catalysts prepared by the mechanical mixture displayed excellent catalytic performance in dry methane reforming.

4.3.2 Stability of Ni promoted Mo/Al_2O_3 catalysts in dry methane reforming

For the further study, the stability of nickel promoted molybdenum carbide catalysts was investigated at GHSV = 6000 $ml.g^{-1}.h^{-1}$, at 850 ℃. The stability performances were shown in Figure 4-10.

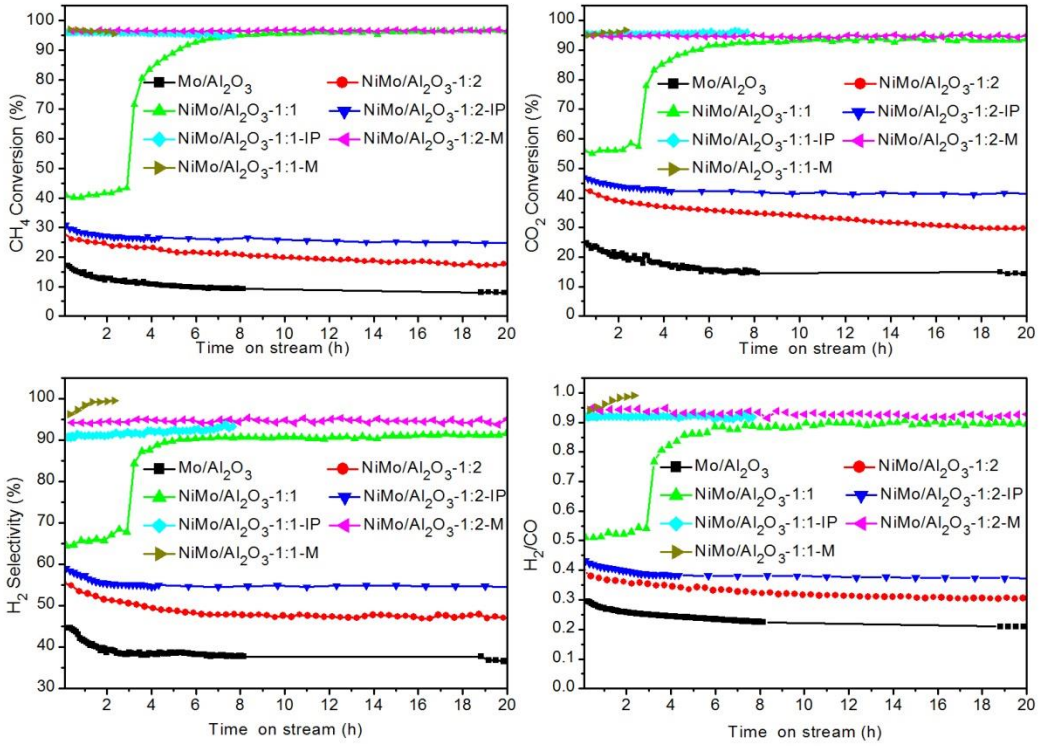

Figure 4-10: Lifetime of nickel promoted molybdenum carbide catalysts over dry methane reforming at temperature of 850 ℃ and GHSV = 6000 $ml.g^{-1}.h^{-1}$.

As is shown in Figure 4-10, for the non-prompted molybdenum carbide catalyst, a rapid decline of dry methane reforming activity and H_2 selectivity was observed within the 4 hours of time on stream. Then the activity remains stable around 10% conversion of CH_4 and 15% conversion of CO_2.

The addition of nickel leads to an increase in the catalysts stability. At a Ni:Mo ratio of 1:2, the NiMo/Al_2O_3-1:2 catalyst still exhibited a slight and slow decrease in activity. With a Ni:Mo ratio of 1:1, the NiMo/Al_2O_3-1:1 catalyst showed a rapid increase in activity after about 3 hours of reaction. The same test was repeated in the same condition and an identical result was obtained. The methane and carbon dioxide conversion increased from 41% up to 96.5% and from 55% up to 93.4%, H_2 selectivity reached 91.3%, and the H_2/CO ratio attained 0.89. It is worth pointing out that no obvious decrease in activity was observed during the 20 hours after the rapid increase. The catalytic performance means that some new phase may be generated during the dry methane reforming test over the NiMo/Al_2O_3-1:1 catalyst.

Preparation methods also have a significant influence on the stability. The NiMo/Al_2O_3-1:2-IP catalyst exhibited similar conversions and a slightly better stability than the counterpart catalyst prepared by incipient wetness impregnation method (NiMo/Al_2O_3-1:2). The NiMo/Al_2O_3-1:2-M catalyst prepared by mechanical mixture displayed excellent stability and product selectivities from the first hours of test and during the 20 hours of time on stream.

Both previous catalysts prepared by impregnation & precipitation and by mechanical mixing, when the Ni:Mo ratio increases to 1:1, showed high activity in CH_4 and CO_2 conversion since the beginning of the test. A blockage of the reactor was observed after 7 h time on stream for NiMo/Al_2O_3-1:1-IP and after 3 h for NiMo/Al_2O_3-1:1-M, which may be due to high carbon deposition on these two catalysts during the dry methane reforming.

4.4 Characterizations of spent NiMo/Al_2O_3 catalysts

4.4.1 CH_4/CO_2-TPSR for spent NiMo/Al_2O_3-1:1 catalyst

As the activity changed significantly over NiMo/Al_2O_3-1:1 during dry methane reforming process, it is necessary to investigate the (CO_2-CH_4)-TPSR for the spent catalyst (Figure 4-11). As is obviously shown in Figure 4-11, the (CO_2-CH_4)-TPSR profiles of spent catalysts have shown different tendency compared with the fresh catalyst. The initial activation temperature of methane and carbon dioxide was about 520 ℃, which is between the initial activation temperature of molybdenum carbide species and nickel species. This implies that during dry methane reforming process at high temperature, a new nickel-molybdenum mixed phase has been generated *in-situ*. This seems to have a beneficial influence on the activity and stability for dry methane reforming.

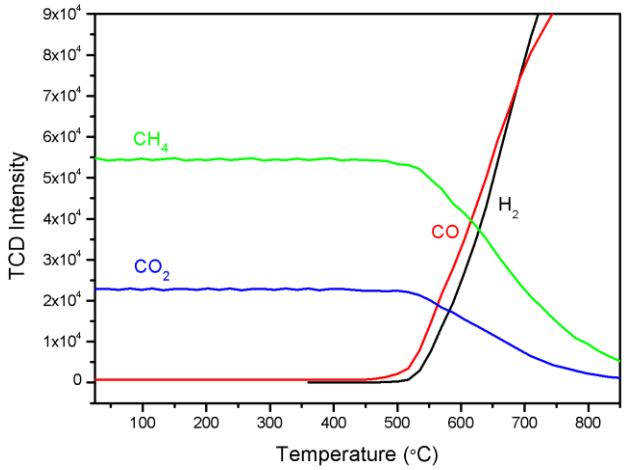

Figure 4-11: *In-situ* (CO_2-CH_4)-temperature programmed surface reaction (TPSR) of spent $NiMo/Al_2O_3$-1:1 catalyst.

4.4.2 X-ray diffraction for spent catalysts

The XRD patterns of spent nickel promoted Mo/Al_2O_3 catalysts were investigated and the results were shown in Figure 4-12 and Table 4-4. Differently to the carburized molybdenum carbide sample, all the spent samples exhibited evident peaks of molybdenum or nickel.

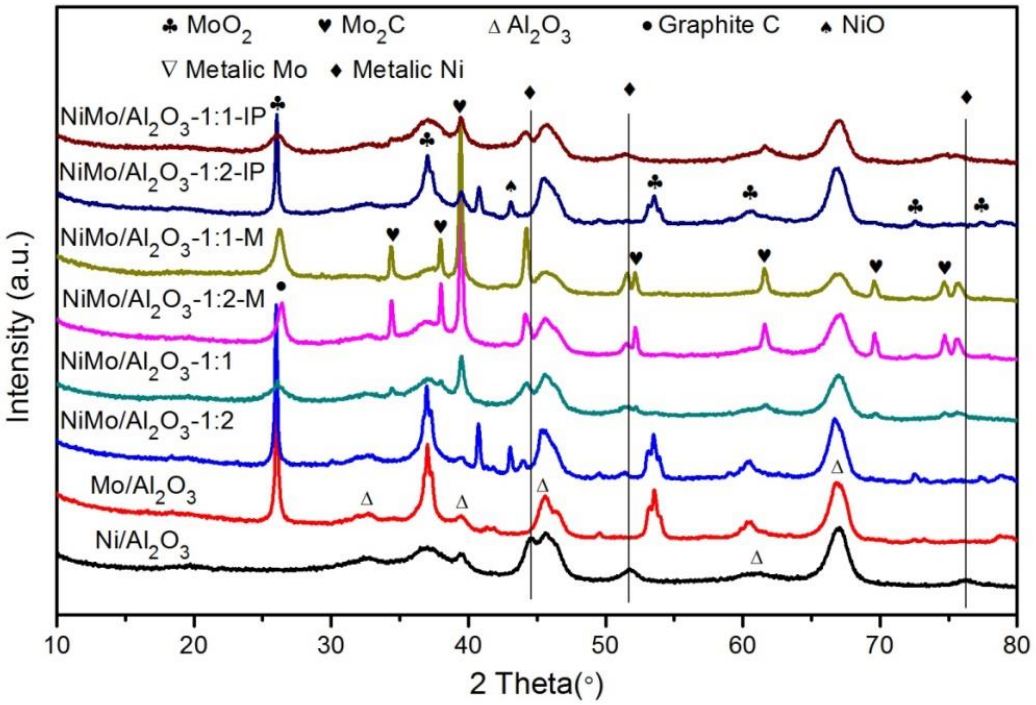

Figure 4-12: XRD pattern for spent nickel promoted Mo/Al_2O_3 catalysts at 850 ℃ for 20 hours (Particularly, $NiMo/Al_2O_3$-1:1-IP after 7 hour test and $NiMo/Al_2O_3$-1:1-M after 3 hour test due to the blockage of reactor).

The promotion of nickel has significant impact on the XRD patterns for the spent catalysts. The catalysts prepared by impregnation method indicated the growth of the crystallite size during dry methane reforming reaction at 850 ℃. The presence of characteristic peaks of MoO_2 for both the spent Mo/Al_2O_3 and $NiMo/Al_2O_3$-1:2 catalysts was observed. This indicated that the oxidation of molybdenum carbides takes place during methane reforming process. The oxidation of Mo_2C phase should be the reason for the deactivation [9, 10]. A peak corresponding at 2θ of 43.1 ° for the nickel oxide was also detected. This suggests that Ni oxidation also occurred during the reaction.

For the spent $NiMo/Al_2O_3$-1:1 sample, no visible peaks for molybdenum oxide and evident peaks for β-Mo_2C were detected. This suggests that molybdenum carbide phase was stable during dry methane reforming reaction at this NiMo ratio of 1:1. It's worth pointing out that there was an apparent shift to lower angle for the Ni peaks over the spent $NiMo/Al_2O_3$-1:1 samples, which indicates the insertion of molybdenum into nickel lattice [57]. This result confirms the existence of a NiMo mixed phase.

Different XRD patterns were obtained over the spent catalysts prepared by different methods. For samples prepared by the impregnation & precipitation methods, important oxidation of Mo and Ni were observed. MoO_2 and NiO were observed in the low nickel content sample ($NiMo/Al_2O_3$-1:2-IP). This is similar to the $NiMo/Al_2O_3$-1:2 prepared by impregnation method. Analogous result was obtained for $NiMo/Al_2O_3$-1:1-IP comparing to the $NiMo/Al_2O_3$-1:1 catalyst.

Stable molybdenum carbide was obtained in both samples prepared by mechanical mixture method. This was evidenced by the absence of molybdenum oxide peak and high peaks intensity for β-Mo_2C detected from XRD. For those prepared samples, it’s worth pointing out also a shift to lower angle of XRD peaks of metallic Ni peaks which indicates the insertion of molybdenum into nickel lattice.

The crystallite sizes estimation (from XRD measurement) for catalysts with a NiMo ratio of 1:1 prepared by different method is displayed in Table 4-4. Both metal nickel and molybdenum carbides exhibited different crystallite sizes among the three different catalysts. Lower Ni crystallite sizes were obtained for the catalyst prepared by incipient wetness impregnation (9.4 nm) followed by the catalysts prepared by impregnation & precipitation method (13.9 nm) then by mechanical mixture. A different trend was observed for the Mo_2C crystallite size.

Table 4-4: Crystallite size of spent $NiMo/Al_2O_3$-1:1 catalysts prepared by different methods.

Catalysts	Crystallite size /nm	
	Size of **Ni** at 44.2 °	Size of Mo_2C at 39.5 °
Spent $NiMo/Al_2O_3$-1:1	**9.4**	20.5
Spent $NiMo/Al_2O_3$-1:1-IP	**13.9**	15.3
Spent $NiMo/Al_2O_3$-1:1-M	**25.3**	32.1

Smaller Mo_2C crystallite size was observed for catalyst prepared by the impregnation & precipitation method (15.3 nm) and may be due to the shorter time on stream. Higher Mo_2C crystallite size was observed for the catalyst prepared by mechanical mixing.

4.4.3 X-ray Photoelectron spectroscopy for spent catalysts

XPS was employed to investigate the element chemical states of the spent $MoAl_2O_3$ and nickel promoted $MoAl_2O_3$ catalysts. Our goal was to investigate the reason of the rapid increase in activity during dry methane reforming process of $NiMo/Al_2O_3$-1:1 catalyst, XPS has been performed to observe the catalyst surface at different stages of reaction: before the increase in the activity (a test was stopped at 2 hours of time on steam), after the increase in the activity (a test was stopped at 6 hours of time on steam) and after 20 hours test at 850 ℃. The results are displayed in Figure 4-13, Table 4-5 and Figure 4-14.

For the spent Mo/Al_2O_3, the molybdenum species mainly exist with Mo^{6+}, Mo^{4+} and $Mo^{\delta+}$, no Mo^{2+} belonged to molybdenum carbides was detected, which confirmed oxidation of molybdenum during dry methane reforming. This result coincides with XRD patterns.

For the $NiMo/Al_2O_3$-1:1 catalyst, before the increase in activity ($NiMo/Al_2O_3$-1:1-2h), a low intensity peak for Mo^{2+} was detected over Mo 3d spectrum, which may strongly suggest the oxidation of molybdenum in dry methane reforming. While after the increase in activity, for the spent catalysts (($NiMo/Al_2O_3$-1:1-6h and $NiMo/Al_2O_3$-1:1-20h), significant intensity of the peak belonging to Mo^{2+} was observed.

For the $NiMo/Al_2O_3$-1:1-IP catalyst, intense peaks attributed to Mo^{6+}, $Mo^{\delta+}$, Mo^{4+}, and Mo^{2+} were obtained in the Mo 3d XPS spectrum. The significant peak for Mo^{2+} confirmed the presence of molybdenum carbide phase.

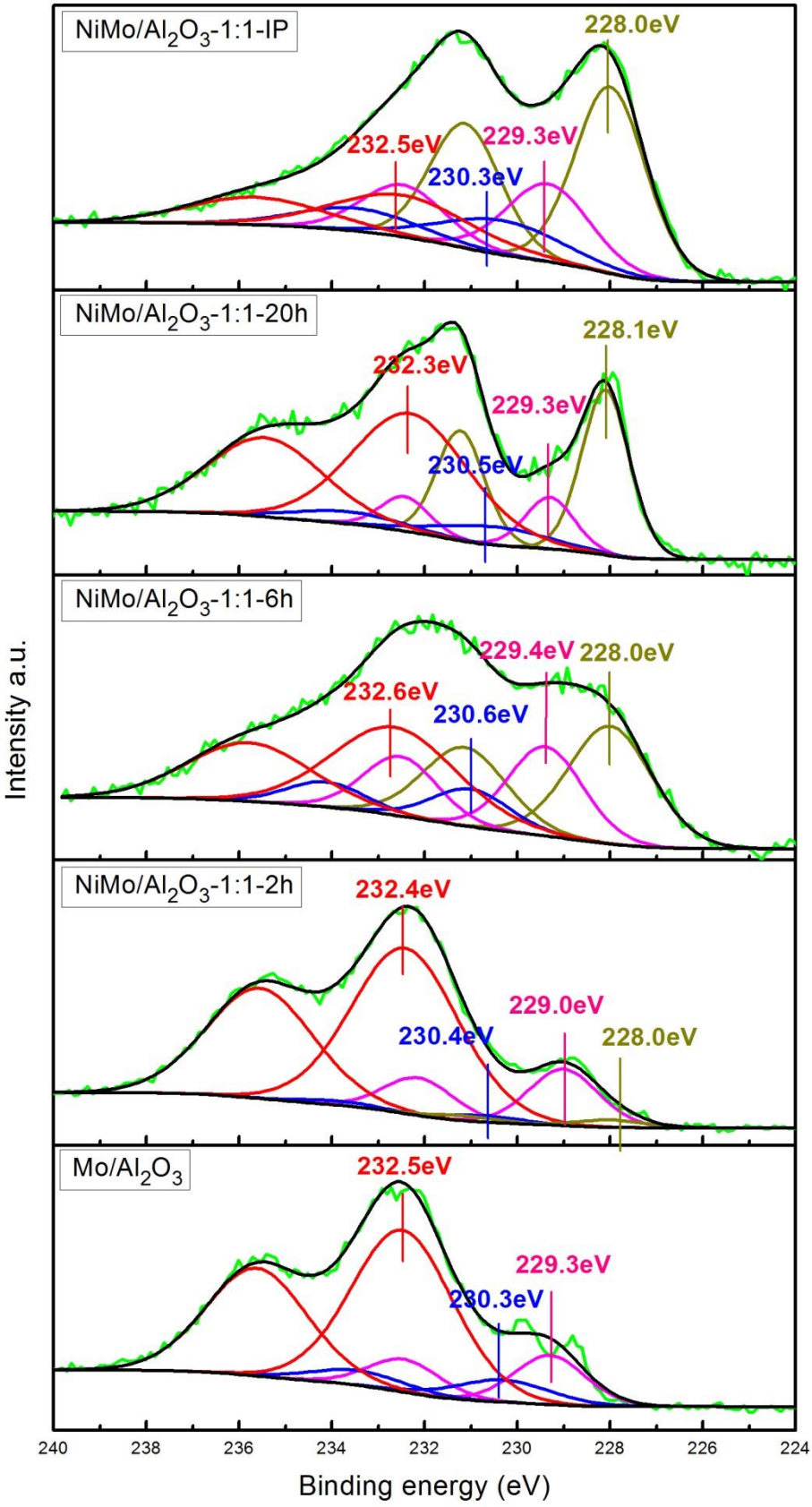

Figure 4-13: Mo 3d XPS spectra of spent catalysts at different stage of reaction 850 ℃.

The molybdenum species distribution for spent catalysts obtained by XPS is shown in Table 4-5. Compared to the catalyst surface before the increase in activity, a significant enhancement of molybdenum carbide phase has been observed in $NiMo/Al_2O_3$-1:1 after 20 hours of time on stream (from 2.2% to 30.4% and 30.1%, respectively). This result may suggest that molybdenum oxide phase and oxycarbide phase have been "re-carburized" into Mo_2C phase by CH_4 during the dry methane reforming [10]. The increase in Mo_2C phase in the spent catalysts may be the dominant reason for the increase in activity during the dry methane reforming test. The results also further suggest that the addition of Ni promotes "re-carburization" of the Mo from oxycarbide species to carbides species during the DMR.

Table 4-5: Mo species distribution (Mo^{X+}/Mo ratio) of spent catalysts prepared by different methods and $NiMo/Al_2O_3$-1:1 catalyst different stages of reaction at 850 ℃.

Catalysts		**Mo species distribution (%)**			
		Mo^{2+}	**Mo^{4+}**	**$Mo^{\delta+}$**	**Mo^{6+}**
Mo/Al_2O_3	Position/eV	—	229.3	230.3	232.5
	Species distribution	**0**	**16.1**	**9.5**	**74.4**
$NiMo/Al_2O_3$-1:1-2h	Position/eV	228	229	230.7	232.4
	Species distribution	**2.2**	**17.4**	**2.1**	**78.2**
$NiMo/Al_2O_3$-1:1-6h	Position/eV	228	229.4	230.4	232.6
	Species distribution	**30.4**	**20.7**	**15.0**	**33.9**
$NiMo/Al_2O_3$-1:1-20h	Position/eV	228.1	229.3	230.5	232.3
	Species distribution	**30.1**	**9.7**	**7.5**	**52.6**
$NiMo/Al_2O_3$-1:1-IP	Position/eV	228	229.3	230.3	232.5
	Species distribution	**44.7**	**21.9**	**14.1**	**19.3**

Figure 4-14 shows the C1s XPS spectra of spent catalysts at different stages of reaction at 850 ℃. No carbidic carbon was detected, which further confirmed the absence of Mo_2C phase.

Compared to the catalyst surface before the increase in activity, the peak of carbidic carbon was observed over the catalyst surface after 20 hours of time on stream. This result coincides with the Mo 3d spectra, which proves the significant enhancement of Mo_2C phase.

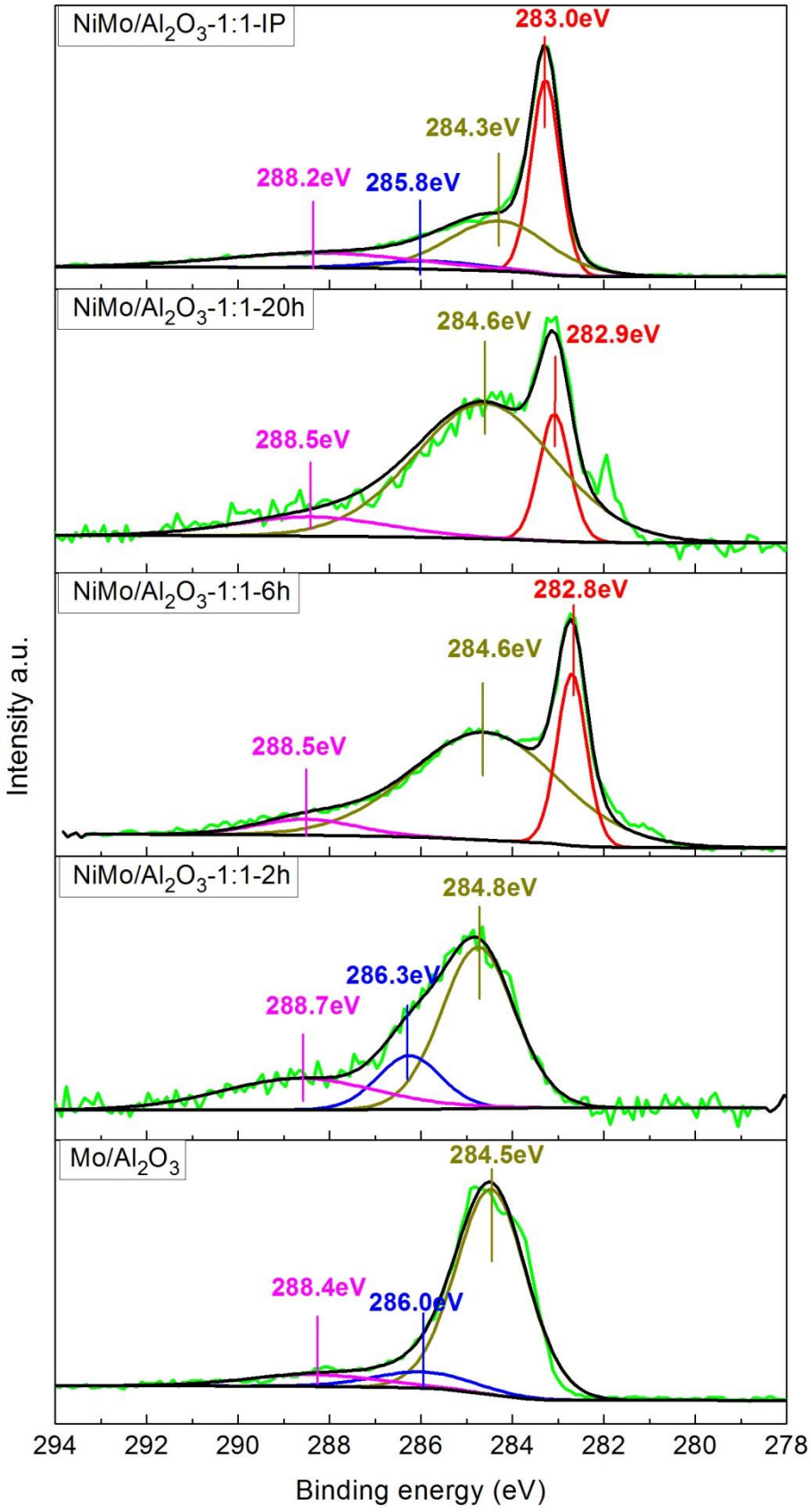

Figure 4-14: C 1s XPS spectra of spent catalysts different stages of reaction at 850 ℃.

Intense peaks of carbidic carbon were confirmed from C 1s spectra for spent NiMo/Al_2O_3-1:1-IP catalysts, which are consistent with the Mo 3d spectra and XRD patterns.

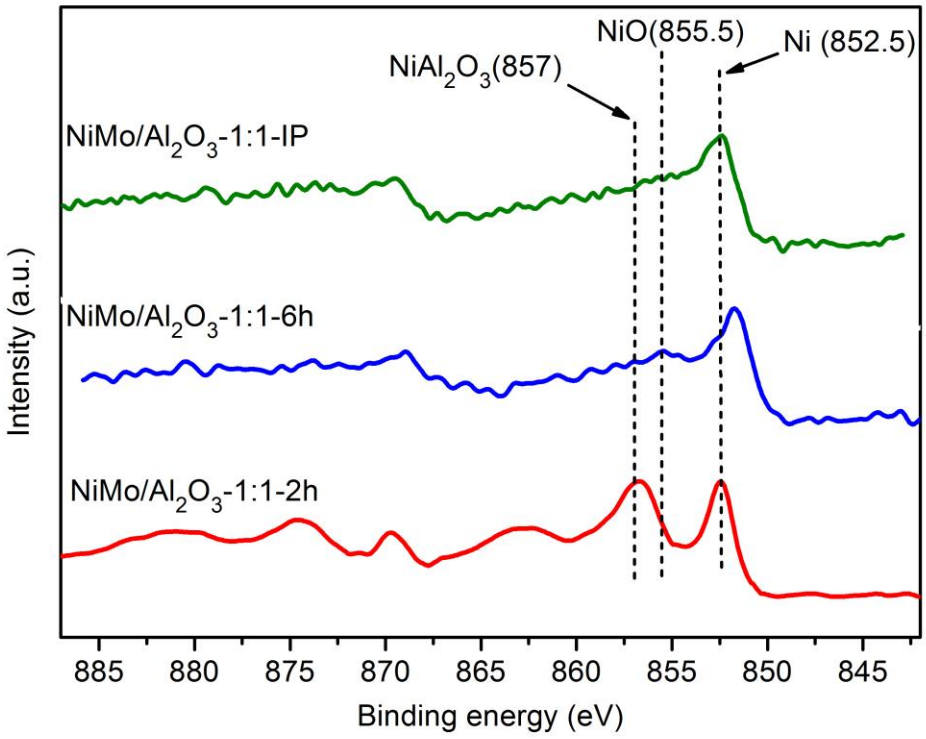

Figure 4-15: Normalized Ni 2p XPS spectra of spent catalysts different stages of reaction at 850 ℃.

Figure 4-15 shows the Ni 2p spectra of spent nickel promoted Mo/Al_2O_3 catalysts in different stages of reaction. For the NiMo/Al_2O_3-1:1 catalyst, compared to the fresh catalyst, the relative peaks intensity of metallic nickel increased with the reaction time, which suggests the increase of nickel reducibility during the reaction, more nickel was reduced into metallic phase.

This same tendency was also observed for the spent NiMo/Al_2O_3-1:1-IP catalyst as after test, on the spectra the main peak is representative of metallic nickel peak. The result suggests the increase of nickel reducibility during the dry methane reforming reaction at high temperature.

4.4.4 Thermo-gravimetric analysis

Thermo-gravimetric analysis of carburized and spent nickel promoted Mo_2C catalysts has been performed. With the increase in temperature under air, it is possible to get the mass

loss due to the carbon combustion (Equation 4-3) and the mass increase due to the oxidation of molybdenum carbides and metallic nickel (Equation 4-4, Equation 4-5 and Equation 4-6):

$C(s) + O_2(g) = CO_2(g)$ ΔH_{298} = -94.1kcal/mol Equation 4-3

$Mo_2C(s) + 4\ O_2(g) = 2\ MoO_3(s) + CO_2(g)$ ΔH_{298} = -438.1kcal/mol Equation 4-4

$2\ MoO_2(s) + O_2(g) = 2\ MoO_3(s)$ ΔH_{298} = -74.9kcal/mol Equation 4-5

$2Ni(s) + O_2(g) = 2\ NiO(s)$ ΔH_{298} = -114.6kcal/mol Equation 4-6

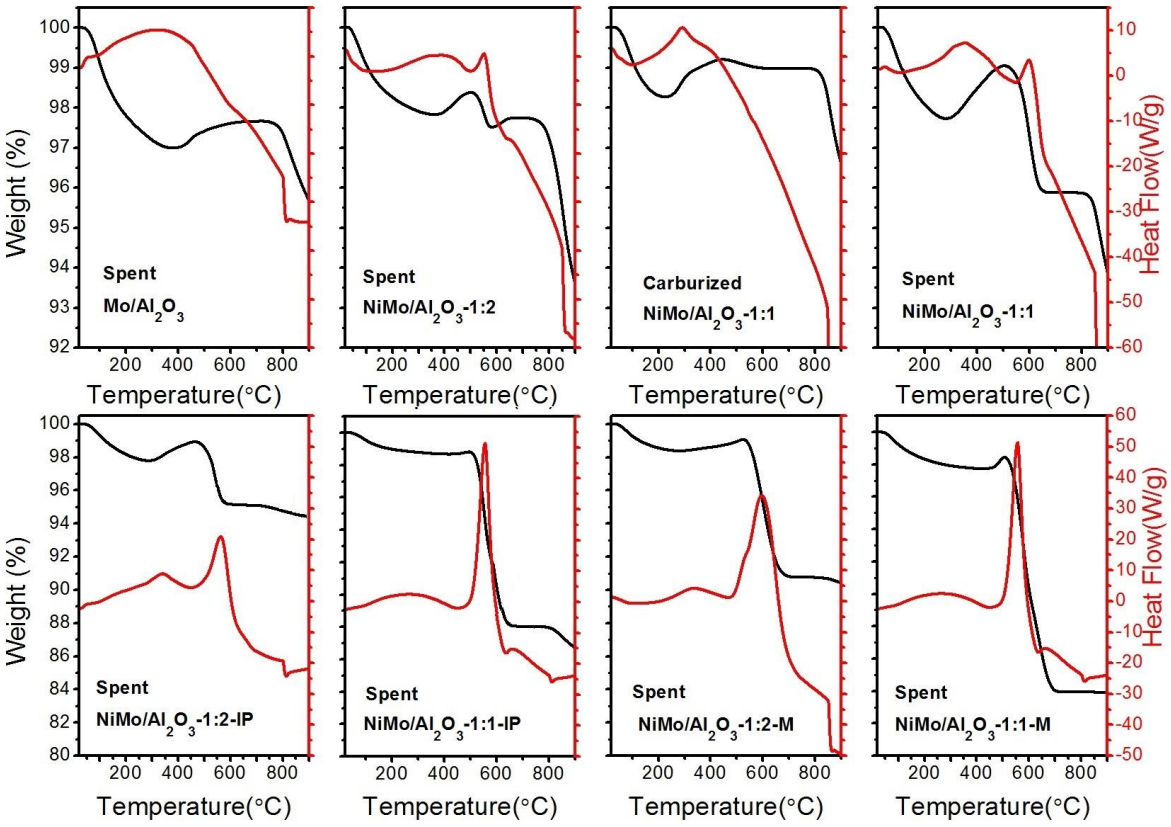

Figure 4-16: TG/DTG profiles of spent catalysts after 20 hour reaction (particularly, $NiMo/Al_2O_3$-1:1-IP after 7 hour test and $NiMo/Al_2O_3$-1:1-M after 3 hour test due to the blockage of reactor).

The thermo gravimetric analysis results for spent Ni promoted molybdenum carbide catalysts after 20 hours of reaction are displayed in the Figure 4-16. It can be seen that all the samples exhibited a series of mass changes.

The weight loss below 100 ℃ can be attributed to the desorption of water so the mass loss for carbon deposition need to be calculated from 110 ℃ [58].

As published in the literature, the mass loss between 110 ℃ until 375 ℃ along with the heat release can be attributed to the oxidation of surface carbidic carbon [59]. It is observed for all samples. The weight gain from about 300 ℃ until 550 ℃ can be attributed to the oxidation of molybdenum carbides phase to molybdenum oxide phase [60] along with the

oxidation of MoO_2 phase [61] to MoO_3 in the presence of oxygen. At higher temperature, between 500 ℃ to 690 ℃, a significant mass loss is observed accompanied by an exothermal peak, which can be attributed to the oxidation of graphitic carbon [59, 62]. The significant mass loss around 800 ℃ accompanied with the rapid endothermic process was observed for all samples and can be attributed to the sublimation of MoO_3 [63, 64].

Let us discuss the influence of nickel content. The carburized NiMo/Al_2O_3-1:1 catalyst presents a mass loss at range of 110 ℃ to 375 ℃ and a mass gain at range of 300 ℃ until 550 ℃, which indicated the existence of molybdenum carbides. The small mass loss due to the oxidation of the graphitic carbon at the range of 500 ℃ to 690 ℃ revealed that only small amount of carbon was generated during carburization under the CH_4/H_2 flow in the NiMo/Al_2O_3-1:1 catalyst.

The spent catalysts, NiMo/Al_2O_3-1:1 catalyst exhibited higher mass gain compared to the spent non promoted Mo/Al_2O_3 and NiMo/Al_2O_3-1:2 catalysts at temperature from about 300 ℃ until 550 ℃. This indicates the presence of higher concentrations of carbides phase. This result is in agreement with the XRD result. The greater mass loss in the range of 500 ℃ - 690 ℃ also indicated the presence of graphitic carbon in the spent NiMo/Al_2O_3-1:1 catalyst. Note that in the later temperature range, no mass loss corresponding to graphitic carbon was observed in the spent non promoted Mo/Al_2O_3.

A small mass gain at 580 ℃ to 670 ℃ along with a slowdown of heat decrease was observed in the spent of NiMo/Al_2O_3-1:2 catalyst and can be attributed to the oxidation of metallic nickel [65]. This was not observed for the NiMo/Al_2O_3-1:1 catalyst, due probably to the abundant presence of graphitic carbon on this later catalyst. The mass loss from graphitic carbon combustion overlapped the mass increase from the oxidation of metallic nickel.

The catalyst preparation method also significantly impacts the TGA curves of the nickel promoted molybdenum carbide catalysts. The spent NiMo/Al_2O_3-1:2-IP catalyst exhibited similar TGA curves to the spent NiMo/Al_2O_3-1:2 but a higher mass loss due to the graphitic carbon combustion.

The amount of carbon deposition is in the order of NiMo/Al_2O_3-1:2 (0.94%) < NiMo/Al_2O_3-1:2-IP (4.2%) < NiMo/Al_2O_3-1:2-M (8.4%) and NiMo/Al_2O_3-1:1 (3.2 %) < NiMo/Al_2O_3-1:1-IP (10.2%) < NiMo/Al_2O_3-1:1-M (14.4%).

It is interesting to note that the carbon deposition coincides with the nickel crystallite size variation (Mechanical Mixture > Impregnation & precipitation > Impregnation). This

may imply that the carbon deposition may strongly depend on the catalysts metallic nickel crystallite size [53, 66, 67].

4.4.5 SEM-EDS

The carburized and spent nickel promoted molybdenum carbide catalysts were characterised by SEM and EDS-mapping (shown in Figure 4-17 and Figure 4-18).

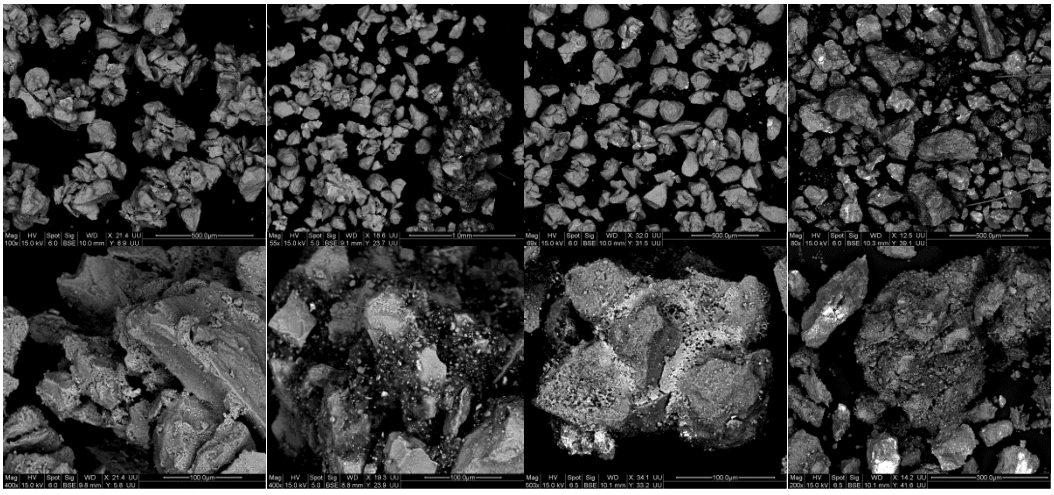

Carburized NiMo/Al_2O_3-1:1 | Spent NiMo/Al_2O_3-1:1 | Spent NiMo/Al_2O_3-1:2 | Spent NiMo/Al_2O_3-1:2-M

Figure 4-17: SEM of of Ni promoted Mo/Al_2O_3 catalysts.

The presence of carbon was not observed for the carburized NiMo/Al_2O_3-1:1 sample, which is in agreement with the XRD and TGA results. Besides, SEM mapping indicated the high dispersion of nickel and molybdenum species on the alumina support surface. This is consistent to the absence of nickel and molybdenum characteristic peaks over XRD.

Few carbons were observed on the spent NiMo/Al_2O_3-1:2 sample from the SEM mapping images, whereas carbon species was observed on the surface of both spent NiMo/Al_2O_3-1:1 and spent NiMo/Al_2O_3-1:2-M catalysts. Those catalysts exhibited excellent catalytic performance in dry methane reforming.

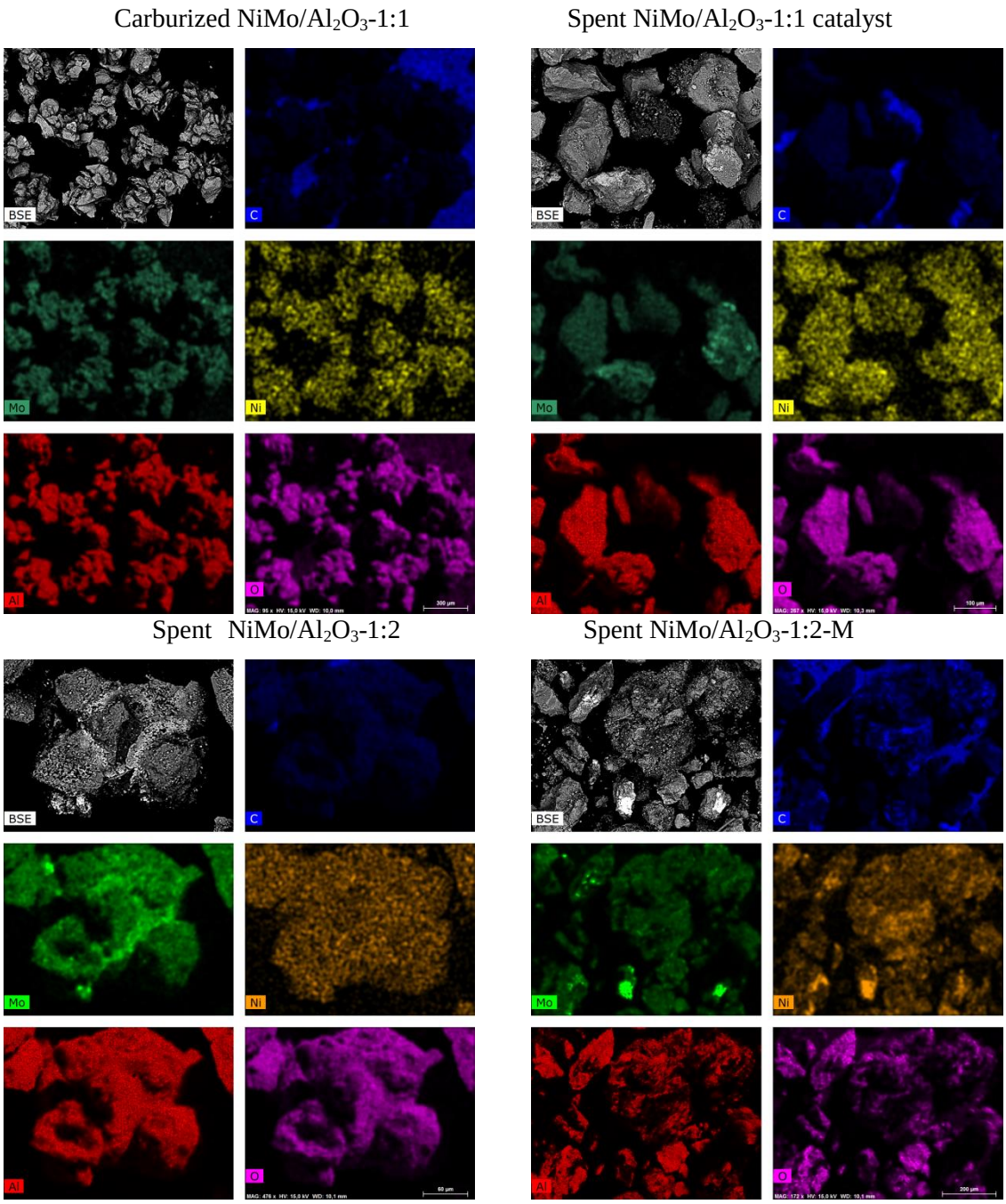

Figure 4-18: SEM mapping of Ni promoted Mo/Al_2O_3 catalyst.

The aggregation of molybdenum species and nickel species were observed from the SEM mapping images for all the spent samples, indicating the growth of crystallite aggregation during dry methane reforming at high temperature, which was also proven by the XRD results.

4.5 Dry methane reforming under pressure

As shown in previous results, $NiMo/Al_2O_3$-1:2-M catalyst displays excellent catalytic performance and stability. This catalyst was used in a fixed-bed tubular stainless steel reactor

for dry methane reforming under pressure. Similarly, before the reaction, the sample was carburized in-situ with CH_4/H_2 at 700 ℃ for 2 h. The results of the catalytic tests under pressure are shown in Table 4-6. Particularly, in order to excluded the influence of carbon deposition, the catalytic data was calculated at the time on stream of 1 hour.

Table 4-6: Catalytic performance for dry methane reforming over $NiMo/Al_2O_3$-1:2-M catalyst Temperature=750 ℃, CH_4/CO_2=1.

Pressure	Temperature / ℃	CH_4 Conv. /%	CO_2 Conv. /%	CO Selec. /%
1 bar	750	69.5	73.7	97.5
	700	61.9	73.0	93.9
5bar	750	44.4	57.6	87.5
	700	37.6	46.4	78.4
10bar	750	39.4	48.7	73.7
	700	32.9	38.9	70.3

As obviously shown in Table 4-6, the $NiMo/Al_2O_3$-1:2-M catalyst displays interesting catalytic performance at atmosphere pressure. The CH_4 and CO_2 conversion reached 61.9% and 73.0% at 700 ℃ as well as 69.5% and 73.7% at 750 ℃. The high CO selectivity (93.9% at 700 ℃ and 97.5% at 750 ℃) indicated the negligible carbon formation during the dry methane reforming process at this pressure.

The pressure rise significantly affects the catalytic performance. A decrease in both CH_4 and CO_2 conversion were observed, which is agreement with the thermodynamics calculation in the chapter 3. The decrease in CO selectivity implied also the enhancement of carbon formation on the catalyst surface during the dry methane reforming at high pressure.

The stability of $NiMo/Al_2O_3$-1:2-M catalyst at 5 and 10 bar is displayed in Figure 4-19. A continuous decline of methane and CO_2 conversion as well as the decline of CO selectivity was observed. Note that the increase in pressure during the DMR reaction (from originally 5 bar to 12 bar and from originally 10 bar to 13 bar) was observed. This is attributed to the formation of high amount of coke that led to the blockage of reactor, since the enhancement of the pressure.

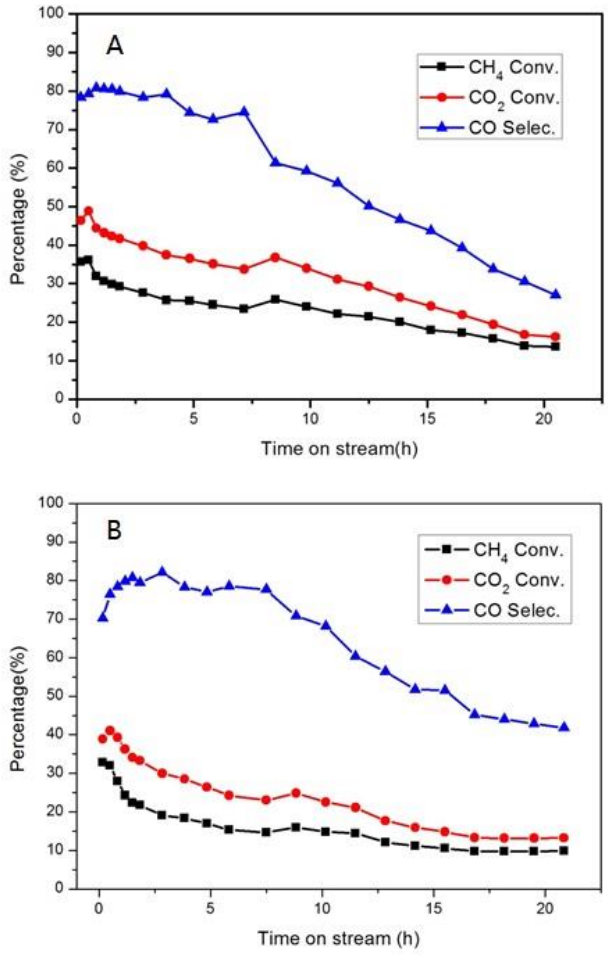

Figure 4-19: Lifetime of NiMo/Al_2O_3-1:2-M over dry methane reforming at 700 ℃ (A: pressure = 5 bar, B: pressure = 10bar).

4.6 Discussion

It is known that molybdenum carbide presents similar electronic configuration to noble metals, especially to Pt, and shows excellent catalytic performance for dry methane reforming. Nevertheless, oxidation of Mo_2C to MoO_2 phase during dry methane reforming process at atmosphere pressure leads to deactivation. Previous reports indicated that the nickel promotion helped to improve the stability of bulk molybdenum carbide catalysts. In this work, we mainly focus on the promotion with different nickel contents of alumina supported molybdenum carbide catalysts and the preparation methods.

Let us first discuss the impact of nickel content on the alumina supported molybdenum carbide catalysts prepared by incipient wetness impregnation method. The obtained results revealed an evident influence of nickel content on the catalyst structure and the catalytic performances in dry methane reforming. XRD suggests that, due to the peak broadening for

molybdenum species, molybdenum phase is highly dispersed on the alumina surface support after calcination. The carburization at 700 ℃ did not lead to an enhancement of the molybdenum and nickel crystallite size, which was also confirmed by Ni and Mo element distribution from SEM mapping. H_2-TPR highlighted strong interaction between molybdenum and alumina support for non-promoted samples after calcination. The addition of nickel is supposed to weaken this interaction between Mo and alumina support. However, a strong interaction between Ni, Mo and alumina for calcined samples has also been confirmed by the H_2-TPR.

In contrast with the literature [8, 11, 68], the catalytic data demonstrated that the non-promoted Mo/Al_2O_3 catalyst showed particularly low activity in dry methane reforming. As expected, it also displayed bad stability. XRD data of the spent non-promoted Mo/Al_2O_3 sample revealed the apparent enhancement of molybdenum crystallite size and existence of MoO_2, which has been regarded as the predominant reason for the low activity. Addition of nickel leads to the increase in activity on dry methane reforming. Note that for the $NiMo/Al_2O_3$-1:2 catalyst, decrease in activity can be still observed.

The catalytic performance evolves with time on stream. A rapid increase in activity was observed over $NiMo/Al_2O_3$-1:1 after about 3 hours of reaction, which is rarely reported in the literature. The XRD did not detect the presence of molybdenum oxide phase in the spent sample. Otherwise, XPS analysis indicates significant enhancement of molybdenum carbides species. This implies the re-carburization of molybdenum species during dry methane reforming over $NiMo/Al_2O_3$-1:1 catalyst. Besides, XPS spectra also confirm the increase of reducibility for nickel species due to the enhancement of metallic nickel phase. Sintering of molybdenum species and nickel species was also observed for the spent samples as the increase in crystallite size detected by XRD, SEM as well as H_2-TPR. Sintering increases the reducibility of nickel species and produce more metallic nickel. The addition of nickel and sintering of Ni and Mo species inclined the balance of carburization/oxidation to re-carburization side [10, 46]. Carbon deposition has been certified on the surface of the spent $NiMo/Al_2O_3$-1:1 catalyst by many characterization techniques such as XRD, SEM and TGA due to a faster CH_4 decomposition rate than the CO_2 decomposition.

Preparation methods also have significant influence on the structure and catalytic performance of the nickel promoted molybdenum carbides catalysts in dry methane reforming. XRD revealed that the crystallite size for molybdenum species followed the order of

mechanical mixture > impregnation & precipitation > incipient wetness impregnation for the calcined catalysts.

Catalytic data suggest the evident impact of preparation methods on the nickel promoted molybdenum carbide catalysts. In the case of Ni:Mo = 1:2, the dry methane reforming activity and stability followed the order: mechanical mixture > impregnation & precipitation > incipient wetness impregnation, which coincide with the order of the calcined catalysts crystallite size. Beside, in the case of sufficient nickel content (Ni:Mo=1:1), excellent activity for dry methane reforming was obtained for all the three catalysts. A blockage of reactor was observed for the catalysts prepared by impregnation & precipitation and mechanical mixture method due to the carbon deposition, which was confirmed by XRD and TGA results.

The carbon deposition is related to the stability of these catalysts and particularly coincides with the crystallite size of the metallic nickel. It suggests that the carbon deposition over dry methane reforming process strongly depends on the crystallite size for the metallic nickel. It can be concluded that the metallic nickel crystallite size strongly affects the catalytic performance and carbon deposition. Nickel is known as one of the most effective metal to increase CH_4 dissociation to H_2 and carbon species [54, 69, 70]. It has been proven that the carbon formation from CH_4 dissociation is strongly affected by the nickel crystallite size [53, 66].

For the dry methane reforming process, a possible redox mechanism was hypothesized by J.B. Claridge [11]. the CO_2 dissociates to O* after adsorbed on the molybdenum carbides surface, O* species which adsorbed on the molybdenum carbides surface, may further react with Mo_2C to oxycarbide species. Otherwise, methane can dissociates to C* as well as H_2 after adsorbed on the Mo_2C surface. The molybdenum oxycarbide species will further react with C* species which come from CH_4 dissociation and generate to CO.

$$CO_2 = CO + O^* \qquad \text{Equation 4-7}$$

$$2\ CO_2 + Mo_2C = 2\ MoOC + 2\ CO \qquad \text{Equation 4-8}$$

$$CH_4 = C^* + 2\ H_2 \qquad \text{Equation 4-9}$$

$$2\ MoOC + C^* = Mo_2C + 2\ CO \qquad \text{Equation 4-10}$$

However, the molybdenum oxycarbide species may also further react with O* species formed from CO_2 dissociation, to generate to MoO_2, which is the reason for the molybdenum carbide oxidation.

$MoOC + 2\ O^* = MoO_2 + CO$ Equation 4-11

The existence of oxycarbide species in $NiMo/Al_2O_3$-1:1 catalyst before its sharp increase in activity is proven by XPS spectra. The presence of MoO_2 phase in the spent non-promoted Mo_2C catalysts is also consistent with this hypothesis.

4.7 Conclusion

The Mo/Al_2O_3 catalyst containing different nickel contents prepared by different methods and their catalytic behaviours in dry methane reforming were investigated in this chapter. Non-promoted Mo_2C catalysts showed low stability due to the oxidation of molybdenum carbides during dry methane reforming. The addition of nickel has significant influence on the catalytic performance on the molybdenum carbide catalysts. Rapid increase in activity was observed during dry methane reforming process over $NiMo/Al_2O_3$-1:1 catalyst. Characterizations indicated that the addition of nickel and sintering of Ni species resulted in the re-carburization for the Mo to carbides phase and the activity increase during dry methane reforming.

Preparation methods also have significant influence on the structure and catalytic performance of the nickel promoted molybdenum carbides catalysts in dry methane reforming. The catalytic performance for $NiMo/Al_2O_3$ catalysts prepared by different methods is summarized in Table 4-7. In the case of Ni/Mo=1:2 composition, the catalyst prepared by mechanical mixture exhibited particularly high activity and stability.

Table 4-7: Summary of catalytic performance for $NiMo/Al_2O_3$ catalysts prepared by different method.

Ni:Mo Ratio		**Preparation method**		
		Incipient wetness impregnation	Impregnation & precipitation	Mechanical mixture
1:2	Crystallite size	Small	Medium	Large
	Activity	bad	bad	Good
	Stability	Oxidation	Oxidation	Good
1:1	Crystallite size	Small	Medium	Large
	Activity	Good	Good	Good
	Stability	Good	Carbon deposition	Carbon deposition

The order of the amount for carbon deposition is particularly in agreement with the order of crystallite size for the metallic nickel. It suggests that the crystallite size for the metallic nickel strongly affect the catalytic performance in dry methane reforming and carbon formation capacity. At low nickel content, large nickel crystallite size results in better oxidation-recarburization balance, which leads to good stability. Nevertheless, large nickel crystallite size also leads to fast carbon species formation and results in significant carbon deposition on the catalysts surface.

As last, the increase in pressure decreases the dry methane reforming activity and leads to severe carbon deposition over NiMo/Al_2O_3-1:2-M catalyst.

4.8 Reference

[1] A. Ashcroft, A. Cheetham, M. Green, Partial oxidation of methane to synthesis gas using carbon dioxide, Nature, 352 (1991) 225-226.

[2] O. Tokunaga, S. Ogasawara, Reduction of carbon dioxide with methane over Ni-catalyst, Reaction Kinetics and Catalysis Letters, 39 (1989) 69-74.

[3] X. Hengyong, S. Xixian, F. Yemei, X. Guolin, L. Jinxiang, Y. Wenge, Z. Peiheng, Studies of Reforming Methane with Carbon Dioxide to Produce Synthesis Gas I. Catalyst and Its Catalytic Property, Petrochemical Technology, 3 (1992) 001.

[4] N. Wang, K. Shen, L. Huang, X. Yu, W. Qian, W. Chu, Facile Route for Synthesizing Ordered Mesoporous Ni–Ce–Al Oxide Materials and Their Catalytic Performance for Methane Dry Reforming to Hydrogen and Syngas, ACS Catalysis, 3 (2013) 1638-1651.

[5] K. Fang, D. Li, M. Lin, M. Xiang, W. Wei, Y. Sun, A short review of heterogeneous catalytic process for mixed alcohols synthesis via syngas, Catalysis Today, 147 (2009) 133-138.

[6] M. Xiang, D. Li, H. Xiao, J. Zhang, W. Li, B. Zhong, Y. Sun, K/Ni/β-Mo2C: A highly active and selective catalyst for higher alcohols synthesis from CO hydrogenation, Catalysis Today, 131 (2008) 489-495.

[7] M. Xiang, J. Zou, CO Hydrogenation over Transition Metals (Fe, Co, or Ni) Modified K/Mo 2 C Catalysts, Journal of Catalysts, 2013 (2013).

[8] A.J. Brungs, A.P. York, M.L. Green, Comparison of the group V and VI transition metal carbides for methane dry reforming and thermodynamic prediction of their relative stabilities, Catalysis letters, 57 (1999) 65-69.

[9] J. Sehested, C. Jacobsen, S. Rokni, J. Rostrup-Nielsen, Activity and Stability of Molybdenum Carbide as a Catalyst for CO2 Reforming, Journal of Catalysis, 201 (2001) 206-212.

[10] C. Shi, A. Zhang, X. Li, S. Zhang, A. Zhu, Y. Ma, C. Au, Ni-modified Mo2C catalysts for methane dry reforming, Applied Catalysis A: General, 431 (2012) 164-170.

[11] J.B. Claridge, A.P. York, A.J. Brungs, C. Marquez-Alvarez, J. Sloan, S.C. Tsang, M.L. Green, New catalysts for the conversion of methane to synthesis gas: molybdenum and tungsten carbide, Journal of Catalysis, 180 (1998) 85-100.

[12] C. Shi, S. Zhang, X. Li, A. Zhang, M. Shi, Y. Zhu, J. Qiu, C. Au, Synergism in NiMoOx precursors essential for CH4/CO2 dry reforming, Catalysis Today, (2013).

[13] T.E. Klimova, D. Valencia, J.A. Mendoza-Nieto, P. Hernández-Hipólito, Behavior of NiMo/SBA-15 catalysts prepared with citric acid in simultaneous hydrodesulfurization of dibenzothiophene and 4,6-dimethyldibenzothiophene, Journal of Catalysis, 304 (2013) 29-46.

[14] C. Shi, S. Zhang, X. Li, A. Zhang, M. Shi, Y. Zhu, J. Qiu, C. Au, Synergism in NiMoOx precursors essential for CH4/CO2 dry reforming, Catalysis Today, 233 (2014) 46-52.

[15] D. Valencia, T. Klimova, Kinetic study of NiMo/SBA-15 catalysts prepared with citric acid in hydrodesulfurization of dibenzothiophene, Catalysis Communications, 21 (2012) 77-81.

[16] A. Zhang, A. Zhu, B. Chen, S. Zhang, C. Au, C. Shi, In-situ synthesis of nickel modified molybdenum carbide catalyst for dry reforming of methane, Catalysis Communications, 12 (2011) 803-807.

[17] S. Zhang, C. Shi, B. Chen, Y. Zhang, Y. Zhu, J. Qiu, C. Au, Catalytic role of-Mo2C in DRM catalysts that contain Ni and Mo, (2015).

[18] C. Liu, M. Virginie, A. Griboval-Constant, A. Khodakov, Impact of potassium content on the structure of molybdenum nanophases in alumina supported catalysts and their performance in carbon monoxide hydrogenation, Applied Catalysis A: General, 504 (2015) 565-575.

[19] W. Wu, Z. Wu, C. Liang, X. Chen, P. Ying, C. Li, In situ FT-IR spectroscopic studies of CO adsorption on fresh Mo2C/Al2O3 catalyst, The Journal of Physical Chemistry B, 107 (2003) 7088-7094.

[20] F. El Kady, S. Shaban, A.A. El Naga, Catalytic dehydrogenation of cyclohexene over MoO3/γ-Al2O3 catalysts, Transition Metal Chemistry, 36 (2011) 237-244.

[21] G. Wang, J.A. Schaidle, M.B. Katz, Y. Li, X. Pan, L.T. Thompson, Alumina supported Pt–Mo2C catalysts for the water–gas shift reaction, Journal of Catalysis, 304 (2013) 92-99.

[22] J.C. Escritori, S.C. Dantas, R.R. Soares, C.E. Hori, Methane autothermal reforming on nickel–ceria–zirconia based catalysts, Catalysis Communications, 10 (2009) 1090-1094.

[23] M.H. Youn, J.G. Seo, P. Kim, I.K. Song, Role and effect of molybdenum on the performance of Ni-Mo/γ-Al2O3 catalysts in the hydrogen production by auto-thermal reforming of ethanol, Journal of Molecular Catalysis A: Chemical, 261 (2007) 276-281.

[24] Z.O. Malaibari, E. Croiset, A. Amin, W. Epling, Effect of interactions between Ni and Mo on catalytic properties of a bimetallic Ni-Mo/Al2O3 propane reforming catalyst, Applied Catalysis A: General, 490 (2015) 80-92.

[25] S. Rajagopal, H.J. Marini, J.A. Marzari, R. Miranda, Silica-Alumina-Supported Acidic Molybdenum Catalysts - TPR and XRD Characterization, Journal of Catalysis, 147 (1994) 417-428.

[26] S.L. González-Cortés, T.-C. Xiao, T.-W. Lin, M.L.H. Green, Influence of double promotion on HDS catalysts prepared by urea-matrix combustion synthesis, Applied Catalysis A: General, 302 (2006) 264-273.

[27] S. Damyanova, L. Petrov, M.A. Centeno, P. Grange, Characterization of molybdenum hydrodesulfurization catalysts supported on ZrO2-Al2O3 and ZrO2-SiO2 carriers, Applied Catalysis A: General, 224 (2002) 271-284.

[28] W. Lai, W. Song, L. Pang, Z. Wu, N. Zheng, J. Li, J. Zheng, X. Yi, W. Fang, The effect of starch addition on combustion synthesis of NiMo–Al2O3 catalysts for hydrodesulfurization, Journal of Catalysis, 303 (2013) 80-91.

[29] W. Lai, L. Pang, J. Zheng, J. Li, Z. Wu, X. Yi, W. Fang, L. Jia, Efficient one pot synthesis of mesoporous NiMo–Al2O3 catalysts for dibenzothiophene hydrodesulfurization, Fuel Processing Technology, 110 (2013) 8-16.

[30] S.A. Ali, S. Ahmed, K.W. Ahmed, M.A. Al-Saleh, Simultaneous hydrodesulfurization of dibenzothiophene and substituted dibenzothiophenes over phosphorus

modified CoMo/Al2O3 catalysts, Fuel Processing Technology, 98 (2012) 39-44.

[31] J.S. Lee, S.T. Oyama, M. Boudart, Molybdenum carbide catalysts, Journal of Catalysis, 106 (1987) 125-133.

[32] K.J. Leary, J.N. Michaels, A.M. Stacy, Carbon and oxygen atom mobility during activation of Mo2C catalysts, Journal of Catalysis, 101 (1986) 301-313.

[33] G. Leclercq, M. Kamal, J.F. Lamonier, L. Feigenbaum, P. Malfoy, L. Leclercq, Treatment of bulk group VI transition metal carbides with hydrogen and oxygen, Applied Catalysis A: General, 121 (1995) 169-190.

[34] K. Oshikawa, M. Nagai, S. Omi, Characterization of molybdenum carbides for methane reforming by TPR, XRD, and XPS, The Journal of Physical Chemistry B, 105 (2001) 9124-9131.

[35] K.J. Leary, J.N. Michaels, A.M. Stacy, The use of TPD and TPR to study subsurface mobility: Diffusion of oxygen in Mo2C, Journal of Catalysis, 107 (1987) 393-406.

[36] R. Del Toro, M. Minichini, J.L. Brito, P. Betancourt, Unsupported Molybdenum Carbide and Nitride Catalysts for Polychlorinated Biphenyls Hydrodechlorination, Catalysis Letters, 143 (2013) 1145-1152.

[37] R.R. Oliveira Jr, A.S. Rocha, V. Teixeira da Silva, A.B. Rocha, Investigation of hydrogen occlusion by molybdenum carbide, Applied Catalysis A: General, 469 (2014) 139-145.

[38] L.-Q. Dou, Y.-S. Tan, D.-S. Lu*, Coated silica as support for platinum catalyst, Applied Catalysis, 66 (1990) 235-246.

[39] R. Prins, Hydrogen Spillover. Facts and Fiction, Chemical Reviews, 112 (2012) 2714-2738.

[40] A.-M. Alexander, J.S. Hargreaves, Alternative catalytic materials: carbides, nitrides, phosphides and amorphous boron alloys, Chemical Society Reviews, 39 (2010) 4388-4401.

[41] X. Liu, K.J. Smith, Acidity and deactivation of Mo2C/HY catalysts used for the hydrogenation and ring opening of naphthalene, Applied Catalysis A: General, 335 (2008) 230-240.

[42] A. Griboval-Constant, J.-M. Giraudon, G. Leclercq, L. Leclercq, Catalytic behaviour of cobalt or ruthenium supported molybdenum carbide catalysts for FT reaction, Applied Catalysis A: General, 260 (2004) 35-45.

[43] M. Xiang, D. Li, W. Li, B. Zhong, Y. Sun, Synthesis of higher alcohols from syngas over K/Co/β-Mo2C catalysts, Catalysis Communications, 8 (2007) 503-507.

[44] G. Vitale, H. Guzmán, M.L. Frauwallner, C.E. Scott, P. Pereira-Almao, Synthesis of nanocrystalline molybdenum carbide materials and their characterization, Catalysis Today, 250 (2015) 123-133.

[45] N. Perret, X. Wang, L. Delannoy, C. Potvin, C. Louis, M.A. Keane, Enhanced selective nitroarene hydrogenation over Au supported on β-Mo2C and β-Mo2C/Al2O3, Journal of Catalysis, 286 (2012) 172-183.

[46] Z. Yao, J. Jiang, Y. Zhao, F. Luan, J. Zhu, Y. Shi, H. Gao, H. Wang, Insights into the deactivation mechanism of metal carbide catalysts for dry reforming of methane via

comparison of nickel-modified molybdenum and tungsten carbides, RSC Advances, 6 (2016) 19944-19951.

[47] Y. Zhao, Z. Yao, Y. Shi, X. Qiao, G. Wang, H. Wang, J. Yin, F. Peng, A novel approach to the synthesis of bulk and supported [small beta]-Mo2C using dimethyl ether as a carbon source, New Journal of Chemistry, 39 (2015) 4901-4908.

[48] Y. Ma, G. Guan, P. Phanthong, X. Hao, W. Huang, A. Tsutsumi, K. Kusakabe, A. Abudula, Catalytic Activity and Stability of Nickel-Modified Molybdenum Carbide Catalysts for Steam Reforming of Methanol, The Journal of Physical Chemistry C, 118 (2014) 9485-9496.

[49] Y. Ma, G. Guan, X. Hao, Z. Zuo, W. Huang, P. Phanthong, K. Kusakabe, A. Abudula, Highly-efficient steam reforming of methanol over copper modified molybdenum carbide, RSC Advances, 4 (2014) 44175-44184.

[50] A.C. Lausche, J.A. Schaidle, L.T. Thompson, Understanding the effects of sulfur on Mo2C and Pt/Mo2C catalysts: Methanol steam reforming, Applied Catalysis A: General, 401 (2011) 29-36.

[51] D.J. Suh, T.-J. Park, S.-H. Lee, K.-L. Kim, Nickel–alumina composite aerogels as liquid-phase hydrogenation catalysts, Journal of Non-Crystalline Solids, 285 (2001) 309-316.

[52] Ş. Özkara-Aydınoğlu, A.E. Aksoylu, CO2 reforming of methane over Pt–Ni/Al2O3 catalysts: Effects of catalyst composition, and water and oxygen addition to the feed, International Journal of Hydrogen Energy, 36 (2011) 2950-2959.

[53] M. Tan, X. Wang, Y. Hu, X. Shang, L. Zhang, X. Zou, W. Ding, X. Lu, Influence of nickel content on structural and surface properties, reducibility and catalytic behavior of mesoporous [gamma]-alumina-supported Ni-Mg oxides for pre-reforming of liquefied petroleum gas, Catalysis Science & Technology, 6 (2016) 3049-3063.

[54] Z. Xu, N. Wang, W. Chu, J. Deng, S. Luo, In situ controllable assembly of layered-double-hydroxide-based nickel nanocatalysts for carbon dioxide reforming of methane, Catalysis Science & Technology, 5 (2015) 1588-1597.

[55] M. Bradford, M. Vannice, CO2 reforming of CH4, Catalysis Reviews, 41 (1999) 1-42.

[56] M. Jafarbegloo, A. Tarlani, A.W. Mesbah, S. Sahebdelfar, Thermodynamic analysis of carbon dioxide reforming of methane and its practical relevance, International Journal of Hydrogen Energy, 40 (2015) 2445-2451.

[57] S. Shah, O.G. Marin-Flores, M.G. Norton, S. Ha, Molybdenum carbide supported nickel–molybdenum alloys for synthesis gas production via partial oxidation of surrogate biodiesel, Journal of Power Sources, 294 (2015) 530-536.

[58] Z. Hou, T. Yashima, Meso-porous Ni/Mg/Al catalysts for methane reforming with CO2, Applied Catalysis A: General, 261 (2004) 205-209.

[59] D. Liu, X.Y. Quek, W.N.E. Cheo, R. Lau, A. Borgna, Y. Yang, MCM-41 supported nickel-based bimetallic catalysts with superior stability during carbon dioxide reforming of methane: Effect of strong metal–support interaction, Journal of Catalysis, 266 (2009) 380-390.

[60] L.J. France, X. Du, N. Almuqati, V.L. Kuznetsov, Y. Zhao, J. Zheng, T. Xiao, A.

Bagabas, H. Almegren, P.P. Edwards, The effect of lanthanum addition on the catalytic activity of γ-alumina supported bimetallic Co–Mo carbides for dry methane reforming, Applied Petrochemical Research, 4 (2014) 145-156.

[61] C.-h. Guo, G.-j. Zhang, Z.-r. Shen, P.-c. Sun, Z.-y. Yuan, Q.-h. Jin, B.-h. Li, D.-t. Ding, T.-h. Chen, Hydrothermal synthesis and formation mechanism of micrometer-sized MoO2 hollow spheres, Chinese Journal of Chemical Physics, 19 (2006) 543-548.

[62] A.E. Galetti, M.F. Gomez, L.A. Arrúa, M.C. Abello, Hydrogen production by ethanol reforming over NiZnAl catalysts: Influence of Ce addition on carbon deposition, Applied Catalysis A: General, 348 (2008) 94-102.

[63] X. Du, L. France, V. Kuznetsov, T. Xiao, P. Edwards, H. AlMegren, A. Bagabas, Dry reforming of methane over ZrO2-supported Co–Mo carbide catalyst, Applied Petrochemical Research, 4 (2014) 137-144.

[64] S.A. Halawy, M.A. Mohamed, G.C. Bond, Characterization of unsupported molybdenum oxide—cobalt oxide catalysts, Journal of Chemical Technology and Biotechnology, 58 (1993) 237-245.

[65] R.V. Mambrini, T.L. Fonseca, A. Dias, L.C.A. Oliveira, M.H. Araujo, F.C.C. Moura, Magnetic composites based on metallic nickel and molybdenum carbide: A potential material for pollutants removal, Journal of Hazardous Materials, 241–242 (2012) 73-81.

[66] D. Chen, R. Lødeng, A. Anundskås, O. Olsvik, A. Holmen, Deactivation during carbon dioxide reforming of methane over Ni catalyst: microkinetic analysis, Chemical Engineering Science, 56 (2001) 1371-1379.

[67] J.-H. Kim, D.J. Suh, T.-J. Park, K.-L. Kim, Effect of metal particle size on coking during CO2 reforming of CH4 over Ni–alumina aerogel catalysts, Applied Catalysis A: General, 197 (2000) 191-200.

[68] A.J. Brungs, A.P. York, J.B. Claridge, C. Márquez-Alvarez, M.L. Green, Dry reforming of methane to synthesis gas over supported molybdenum carbide catalysts, Catalysis Letters, 70 (2000) 117-122.

[69] M. Usman, W.M.A. Wan Daud, H.F. Abbas, Dry reforming of methane: Influence of process parameters—A review, Renewable and Sustainable Energy Reviews, 45 (2015) 710-744.

[70] J. Deng, M. Cai, W. Sun, X. Liao, W. Chu, X.S. Zhao, Oxidative Methane Reforming with an Intelligent Catalyst: Sintering‐Tolerant Supported Nickel Nanoparticles, ChemSusChem, 6 (2013) 2061-2065.

Chapter 5 Fischer-Tropsch synthesis over promoted Mo_2C based catalysts

5.1 Introduction

Depletion of crude oil resources has led to the growing interest in the alternative feedstocks in recent years [1, 2]. Fischer-Tropsch synthesis, which aims at converting syngas into biofuels, is considered as one of most promising routes for renewable, clean fuels and also chemicals [3]. Syngas can be obtained by gasification of renewable sources such as biomass and organic waste. It can be also obtained by dry/steam reforming or partial oxidation of natural gas and from coal gasification [4].

Light olefins (ethylene, propylene, and butylene) act as key building blocks for the petrochemical industry [5]. Therein, ethylene has been regarded as one of the most important indicators of the development of petrochemical industry. Light olefins are obtained in the industry either by naphta steam cracking, ethane cracking or by methanol conversion to olefins process (MTO). In the naphta steam cracking, the olefins are by-side products and the selectivity to specific olefins is rather low. Ethane cracking produces only ethylene. The MTO technology involves a number of technological steps which reduce the overall conversion efficiency. In addition, the catalyst undergoes obvious deactivation. Thus, Fischer-Tropsch synthesis provides a new and clean route for generation of light olefins.

Molybdenum carbide (Mo_2C) has catalytic performances comparable to expensive noble metals (Pt and Ru). This molybdenum carbide phase has been widely used in hydrodesulfurization (HDS)[6, 7] and hydrodenitrogenation (HDN) processes [8]. It also exhibits high activity for dry reforming, alkane isomerization, and CO hydrogenation [9-11]. Molybdenum carbide has received growing attention during the past decades as a catalyst for carbon monoxide hydrogenation [12]. One of the major advantages of the molybdenum carbide catalyst is its resistance to carbon deposition compared to more conventional cobalt and iron catalysts [13, 14]. Molybdenum carbide does not contain sulfur. Differently to the molybdenum sulfide catalysts [15], no sulfur can be found in the reaction products over molybdenum carbide. Sulfur content can be a problem especially for production of fuels with very strict sulfur specifications.

Selectivity however remains a major challenge of molybdenum carbide systems. The molybdenum carbide phase mainly generates light alkanes [16, 17]. Addition of different promoters may lead however to the modification of molybdenum carbide structure and its electronic properties, thus influencing the reactivity.

Previous reports [16-20] indicated that the promotion of Mo_2C-based catalysts by potassium significantly enhanced their selectivity towards alcohols, in particular under high pressures reaction conditions. The potassium promoted molybdenum carbides catalysts also exhibit high activity for water–gas shift (WGS) reaction. Other alkali metal and transition metal promoters were also used [15, 21-23]. Many publications focused on the bulk molybdenum carbides [9-11, 17, 24, 25], while very few reports have been addressed so far to supported molybdenum carbide catalysts. High dispersion of the active phase, mechanical and thermal stability are the major advantages of supported catalysts. In addition, the support can modify the chemical and electronic structures of the active sites and thus affect the catalytic performances.

This chapter particularly focuses on the effect of different supports and promoters as well as the operating conditions on the structure and catalytic performance of supported molybdenum carbide catalysts. At different preparation stages, the catalysts were characterized by nitrogen adsorption, X-ray diffraction (XRD), Raman spectroscopy, X-ray Photoelectron spectroscopy (XPS), temperature program reduction of hydrogen (H_2-TPR), temperature desorption of CO_2 and Transmission Electron Microscope (TEM). The catalytic performance was evaluated in a fixed bed reactor.

5.2 Impact of different supports on the Mo_2C based catalysts

5.2.1 Catalytic performance of different supported Mo carbide catalysts

Support plays a very important role on the catalytic performance in Fischer-Tropsch synthesis. Firstly, the impact of different supports was investigated on the activity of molybdenum carbide catalysts.

Carbon monoxide hydrogenation was conducted at 300 ℃ and with a H_2/CO ratio of 2. Before the reaction, all the samples were carburized in-situ with CH_4/H_2 at 700 ℃ for 2 h. The CO conversion and product selectivities were obtained at the steady state and at iso-GHSV (12000 $cm^3.g^{-1}.h^{-1}$). Methane, light olefins and paraffin, alcohols, heavy hydrocarbons and carbon dioxide were the major products of the FT reaction whatever the materials used as support of molybdenum carbide catalysts. For the sake of clarity, carbon dioxide was included in the total selectivity calculations, but is excluded from the hydrocarbon selectivity. The results obtained with different supported molybdenum carbide catalysts are given in Table 5-1.

Table 5-1: Catalysis performance of different supported Mo carbide catalysts (Catalysts were diluted with SiC (1:5), H_2/CO= 2.0, Temperature= 300 ℃, Time on stream= 40 h, GHSV= 12,000 ml $g^{-1}h^{-1}$).

Catalysts	Pressure/ bar	X_{CO} (%)	CH distribution (% C mol)					CO_2 selectivity
			CH_4	$C_2^=$-$C_4^=$	**C_2-C_4**	C_5^+	C-OH	
10Mo/Al_2O_3	20	29.4	43.5	3.2	41.8	9.1	2.4	45.2
	10	14.4	40.0	9.0	41.7	6.7	2.5	45.8
10Mo/SBA-15	20	18.5	46.3	1.6	41.6	10.6	0	38.6
	10	10.1	47.6	1.9	40.1	10.4	0	40.0
10Mo/CMK	20	23.9	53.1	0.4	33.8	12.7	0	41.5
	10	14.5	52.3	1.5	34.5	11.7	0	42.9
Mo/AC	10	17.9	47.2	1.4	40.2	11.2	0	49.5
Mo/CNTs	10	29.7	48.8	1.0	43.2	8.0	0	41.2

As is shown in Table 5-1, all the non-promoted Mo_2C catalysts produced mainly C_1-C_4 light hydrocarbons, and the selectivity to heavy hydrocarbons was negligible, which is in agreement with previous reports [26, 27]. Due to the strong water gas shift reaction activity of molybdenum carbide, considerable CO_2 selectivity was obtained with all the samples.

The reduction of pressure from 20 bar to 10 bar contributes to the decrease in CO conversion, whereas, no significant influence on the hydrocarbons and CO_2 selectivities was observed.

However, it is possible to observe that over alumina support, higher light olefins selectivity was obtained with the decrease in pressure. The alumina supported molybdenum carbide catalyst also generated alcohols with a selectivity of 2.5%, which was not detected for the other supported samples.

5.2.2 Textural properties for different supported Mo based catalysts

The textural properties of the different catalysts are displayed in Table 5-2. Due to the rich internal porous structure of commercial gamma alumina, the Al_2O_3 supported molybdenum catalyst exhibits high surface area (123.4 m^2/g). Besides, the average pore size is about 5.4 nm and the pore volume is as high as 0.33 cm^3/g. SBA-15 is known to own a particular high surface area [28]. The SBA-15 supported catalyst exhibits a surface area of 1068.1 m^2/g, a pore volume of 1.07 cm^3/g and about 7.8 nm of pores diameter. In SBA-15

the hexagonal cylindrical pores are connected to each other by small micropores in their walls. These textural parameters are consistent with the literature [29]. The CMK-3 support was prepared by filling the mesopores of SBA-15 by a template with sucrose, then the subsequent removal of the template. The latter support consists of a network of carbon rods and has a surface very similar to the one of SBA-15 [29]. The size of the CMK-3 pores is smaller (3.2 nm) in comparison to SBA-15 [30]. Activated carbon (AC) supported catalyst has a relatively large surface area (522 m^2/g), pore volume (0.41cm^3/g) and an average pores size similar to the alumina supported catalyst. The acid treated CNTs have uniform diameters of about 9.0 nm and relatively high surface area (78.6 cm^2/g).

Table 5-2**:** Physical properties of Mo-based catalysts.

Sample	S_{BET} m^2/g	V_{total} cm^3/g	D_{meso} nm
10Mo/Al_2O_3	123.4	0.33	5.4
10Mo/SBA-15	1068.1	1.07	7.8
10Mo/CMK-3	1215.3	1.12	3.2
10Mo/AC	522.7	0.41	5.2
10Mo/CNTs	78.6	0.32	9.0

5.2.3 XRD for different supported Mo based catalysts

The calcined molybdenum catalysts were also characterized by X-ray diffraction and the XRD patterns are shown in Figure 5-1. It is needed to point out that the catalysts supported by alumina and SBA-15 were calcined under an air flow, while the catalysts supported by carbon materials were calcined under nitrogen flow in order to avoid the oxidation of carbon materials at high temperature.

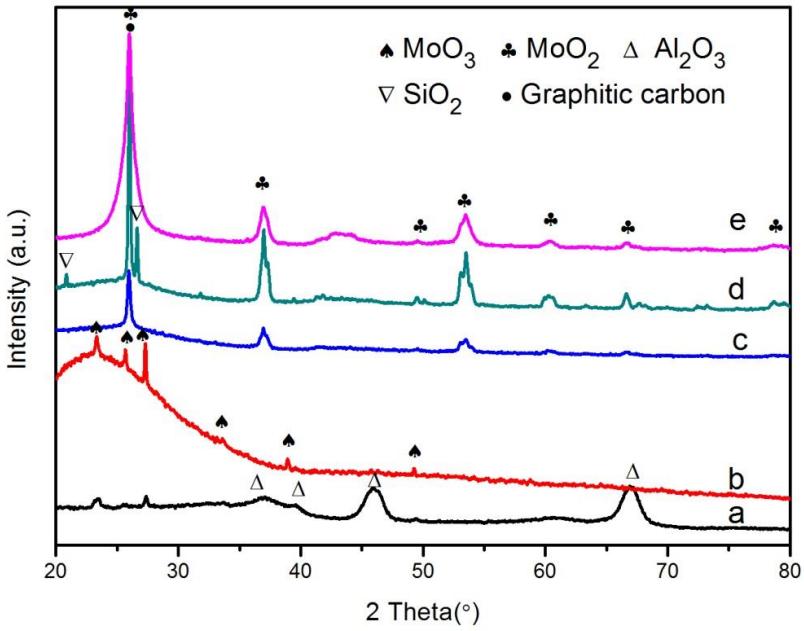

Figure 5-1: XRD patterns for calcined different supported molybdenum carbides catalyst **(a)** Mo/Al_2O_3; **(b)** Mo/SBA-15; **(c)** Mo/CMK-3; **(d)** Mo/AC; **(e)** Mo/CNTs.

As is shown in Figure 5-1, the diffraction peaks at 2θ of 23.3°, 25.7° and 27.3° for the Mo/Al_2O_3 catalyst are attributed to the crystallographic planes of the orthorhombic MoO_3 phase (JCPDS 35-0609). The broadening of the peaks indicates a good dispersion of molybdenum species on the alumina support [31]. Besides, characteristic peaks of orthorhombic MoO_3 phase (at 2θ of 23.3°, 25.7°, 27.3°, 33.7, 39.0° and 49.2°) are observed for the calcined Mo/SBA-15 catalyst. The relative sharp shape suggests larger crystallite size of MoO_3 compared to those present in the alumina supported catalysts.

Narrow peaks at 2θ of 20.9° and 26.6° for Mo/AC catalyst are attributed to the presence of traces of quartz in the activated carbon support. The peaks at 2θ of 26.0° for Mo/CNTs are attributed to the graphitic carbon of CNTs. No characteristic peaks of MoO_3 phase were detected over the three catalysts supported by carbon materials. However, the peaks at 2θ of 26.0°, 36.9°, 49.5°, 53.1°, 53.5°, 60.2°, 66.5° and 79.3°, which are attributed to the MoO_2 phase (JCPDS 32-0671), were observed for all the three carbon materials supported catalysts. This result strongly implies that ammonium molybdate decomposes only into MoO_2 instead of MoO_3 on these carbon materials under the inert atmosphere.

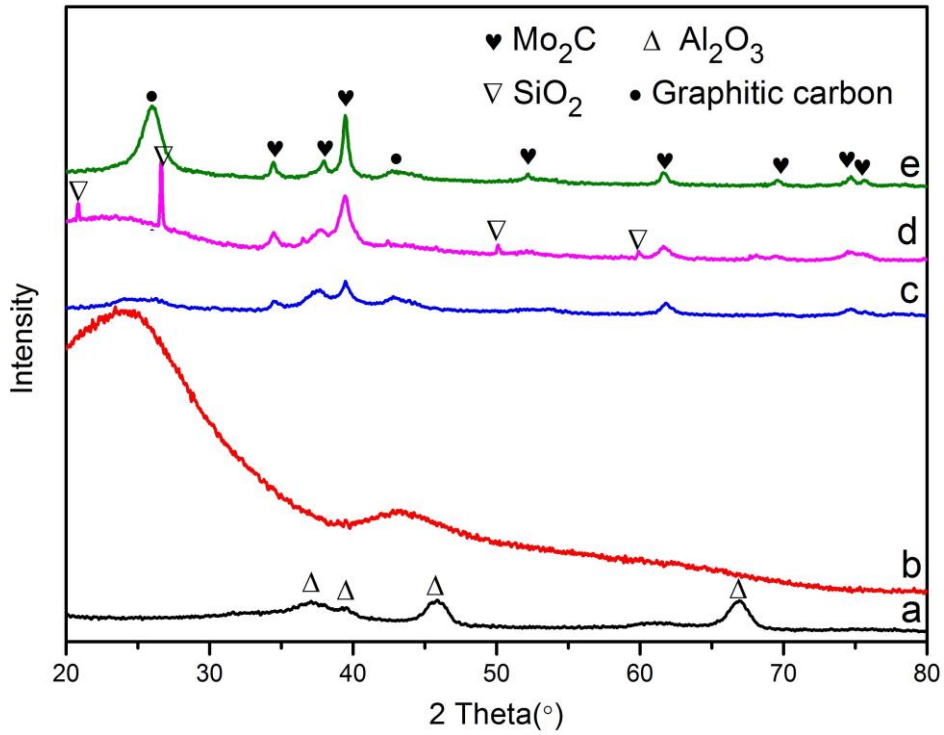

Figure 5-2: XRD patterns for carburized different supported molybdenum carbides catalyst (a) Mo/Al_2O_3; (b) Mo/SBA-15; (c) Mo/CMK-3; (d) Mo/AC; (e) Mo/CNTs.

The carburized molybdenum catalysts were also characterized by X-ray diffraction. Figure 5-2 shows the XRD patterns for the carburized molybdenum on different supports. After the carburization, no characteristic peaks of MoO_2 or MoO_3 were detected on the XRD patterns for all catalysts. This suggests that the molybdenum oxide species were completely converted in molybdenum carbide phase.

Note, however, that it is not obvious to confirm the presence of carbide in the Mo/Al_2O_3 and in the Mo/SBA-15 catalysts by X-ray diffraction. Some of the β-Mo_2C peaks are overlapped with the characteristic peaks of alumina. The absence of characteristic peaks of carbide phase could be also explained by finely dispersed molybdenum carbides on alumina and SBA-15. The crystallite sizes could be below the detection limit of X-ray diffraction [32].

For the carburized carbon materials supported catalysts (Mo/CMK-3, Mo/AC and Mo/CNTs), the peaks at 2θ = 34.5 °, 38.0 °, 39.6 °, 52.3 °, 61.9 °, 69.8 ° and 75.0 ° and 76.0 ° are attributed to molybdenum carbide phase. This confirms that the molybdenum oxide species were completely converted into carbide.

5.2.4 CO_2-TPD for different supported Mo based catalysts

CO_2 temperature programmed desorption is a common technique to quantitatively characterize the basic sites of solid catalysts [33]. However, it is difficult to characterize the carbon support materials due to the decomposition of the abundant surface oxygen complexes over carbon materials with the release of CO_2 or CO at high temperature [33-35], which also contributes to the CO_2 signal and leads to incorrect results. Thus, CO_2-TPD was employed only to characterize Mo/Al_2O_3 and Mo/SBA-15 catalysts.

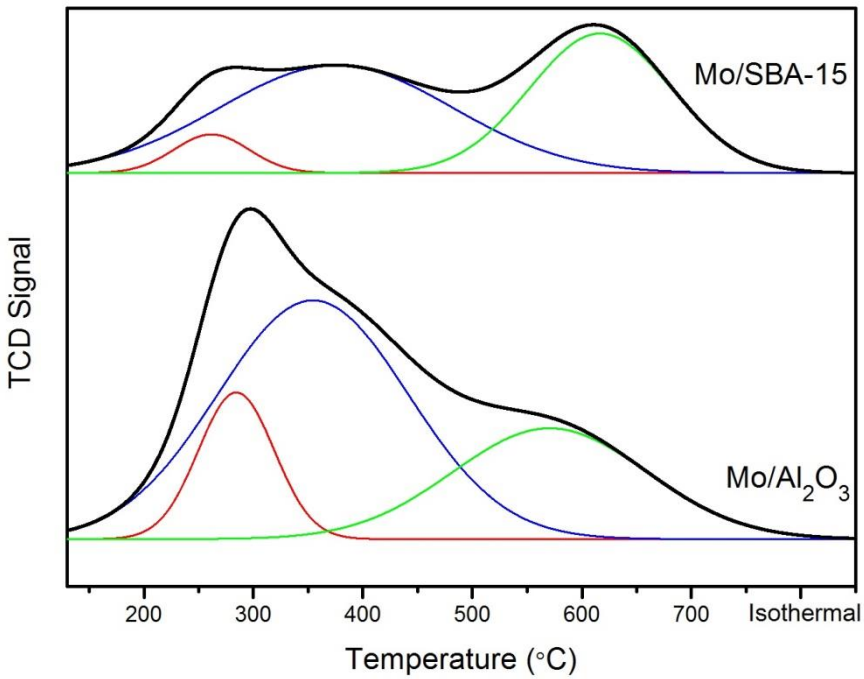

Figure 5-3: CO_2-TPD curves for carburized molybdenum carbides catalysts.

The results of the basicity of the molybdenum carbide catalysts are shown in Figure 5-3. Both samples showed broad CO_2 desorption peaks from 150 ℃ to 700 ℃. Those peaks can be decomposed into 3 peaks after fitting by the Gauss function. The peak located in the temperature range of 150 - 350 ℃ is assigned to weak basic sites; the peak between 200 - 550 ℃ is assigned to moderate basic sites; the peak in the range of 400 - 700 ℃ is attributed to strong basic sites. The average amounts of CO_2 adsorption for the sites with different basicity are displayed in Table 5-3.

Table 5-3: CO_2 desorption amount of different material supported Mo_2C catalysts in mmol/g.

Samples	CO_2 desorption (mmol/g)			
	Weak basic site	Moderate basic site	Strong basic site	total
Mo/Al_2O_3	0.014	0.065	0.032	0.111
Mo/SBA-15	0.004	0.036	0.028	0.068

The Mo/Al_2O_3 catalyst exhibits higher CO_2 adsorption amount, especially for weak and moderate basic sites. The basic sites are known to have a beneficial influence on the generation of olefins in CO hydrogenation [36]. This result is in agreement with the FT results, for which the Mo/Al_2O_3 catalyst showed higher selectivity to olefins at 20 bar and even much higher at 10 bar.

5.2.5 XPS for different supported Mo based catalysts

The carburized Mo/Al_2O_3, Mo/CNTs and Mo/AC catalysts have been characterized by XPS. The resulting Mo 3d spectra are shown in Figure 5-4.

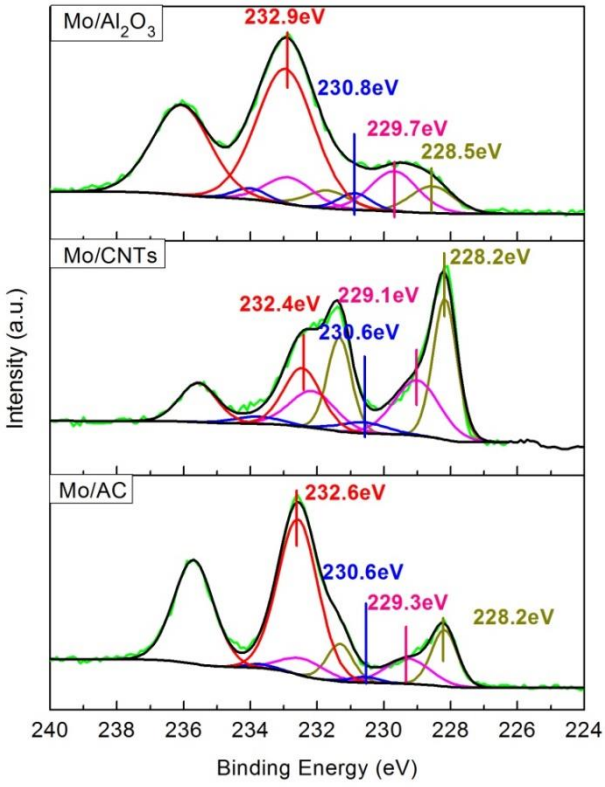

Figure 5-4: Mo 3d XPS spectra of carburized Mo on different support.

The broad envelop of the Mo 3d signal can be deconvoluted into four separate overlapping doublets indicating the presence of different Mo oxidation states. According to the literature, the peak at binding energy (BE) of 228.5 eV can be attributed to the Mo^{2+} species in the Mo carbide phase [14, 25, 37, 38]. The peak at binding energy of 229.3 eV can be attributed to Mo^{4+} species which involves in MoO_2 phase[39, 40]. The peak at 230.6 eV can be attributed to $Mo^{\delta+}$ ($4 < \delta < 6$) which may be involved in Mo oxycarbide species and the one at 232.6 eV can be assigned to Mo^{6+} species corresponding to MoO_3 phase [39, 41]. The presence of those two later species can be explained by the passivation step which oxidizes the surface Mo carbide species. It cannot be however completely excluded that the presence of Mo^{6+}, $Mo^{\delta+}$ and Mo^{4+} species can be due to incomplete catalyst carburization.

As it is clearly shown in the Figure 5-4, all the catalysts display peaks of Mo^{2+}, $Mo^{\delta+}$, Mo^{4+} and Mo^{6+} species. Interestingly, no characteristic peak of metallic molybdenum was detected. The molybdenum species distribution from XPS results (Table 5-4) reveals that the molybdenum carbide supported on carbon materials (AC and CNTs) exhibits obviously concentration of Mo^{2+} species when compared to the alumina support counterpart. This may due to the reducing property of the carbon material support.

Table 5-4: Mo^{X+}/Mo ratio of the carburized different Mo on different support.

Catalysts	**Mo species distribution of Mo 3d 5/2 (%)**			
	Mo^{2+}	**Mo^{4+}**	**$Mo^{\delta+}$**	**Mo^{6+}**
Mo/Al_2O_3	10.3	16.8	4.8	68.1
Mo/CNTs	39.0	29.4	6.1	25.5
Mo/AC	17.9	9.0	4.7	68.4

The XPS results confirm the results obtained in XRD concerning the carburization process. Indeed the alumina supported molybdenum carbides catalyst exhibited small molybdenum species crystallite size along with high concentration of weak and moderate basic sites. Besides, higher olefins selectivity was obtained over this catalyst. Thus, alumina will be particularly used for the further study.

5.3 Impact of different promoters on the Mo/Al_2O_3 catalysts

5.3.1 Catalytic performance in Fischer-Tropsch synthesis

The alumina supported molybdenum carbides were promoted with Na, K, Fe and Ni. Carbon monoxide hydrogenation was conducted at 300 ℃ with a H_2/CO ratio of 2 at 10 bar. The CO conversion and product selectivities were obtained at the steady state and at iso-GHSV (12000 $cm^3.g^{-1}.h^{-1}$). Similarly, for the sake of clarity, carbon dioxide was included in the total selectivity calculations, but is excluded from the hydrocarbon selectivity. The catalytic performance and stability are displayed in Table 5-5 and Figure 5-5.

Table 5-5: Catalytic performances of different promoted Mo carbide catalysts in Fischer-Tropsch synthesis.

Catalysts	X_{CO} (%)	CH distribution (% C mol)					CO_2 selec. (%)
		CH_4	$C_2^=$-$C_4^=$	C_2-C_4	C_5^+	C-OH	
$10Mo/Al_2O_3$	14.4	40.0	9.0	41.7	6.7	2.5	45.8
$NaMo/Al_2O_3$-(1:5)	12.2	31.9	8.5	35.7	21.3	2.6	41.1
$FeMo/Al_2O_3$-(1:5)	12.4	32.2	9.7	37.4	17.9	2.8	42.0
$K(Mo/Al_2O_3$-1:5)	10.7	34.4	10.4	37.1	16.7	1.4	43.3
$NiMo/Al_2O_3$-(1:5)	44.9	47.2	0.5	27.8	23.4	1.1	40.8

As is shown in the Table 5-5 and Figure 5-5, a decrease in CO conversion from 14.4% to 12.2%, 12.4% and 10.7% were obtained after addition of Na, Fe and K, respectively. Similarly, a decrease in CH_4, CO_2, and light paraffin selectivities was also observed compared to $10Mo/Al_2O_3$. At the same time, an increase in C_5^+ selectivity (from 6.7 % to 21.3%, 17.9% and 16.7% for Na, Fe and K promotion, respectively) was observed under these conditions. A slight increase in light olefin selectivity was observed for the potassium and iron promoted catalysts (from 9.0% to 10.4% and 9.7%, respectively). The Ni promoter led to an increase in CO conversion but mainly CO_2, methane and C_5^+ are produced. Low selectivity in light olefins (0.5%) as well as in alcohols (1.1%) is observed.

Significant enhancement of CO hydrogenation activity was observed over the nickel promoted Mo/Al_2O_3 catalyst, which may due to the high hydrogenation activity of nickel (high selectivity in CH_4). The promotion of nickel seems to restrict the activity of reverse

water gas shift reaction and to increase the carbon chain growth. The CO_2 selectivity was lower while the Ni promoted catalyst showed higher C_5^+ selectivity.

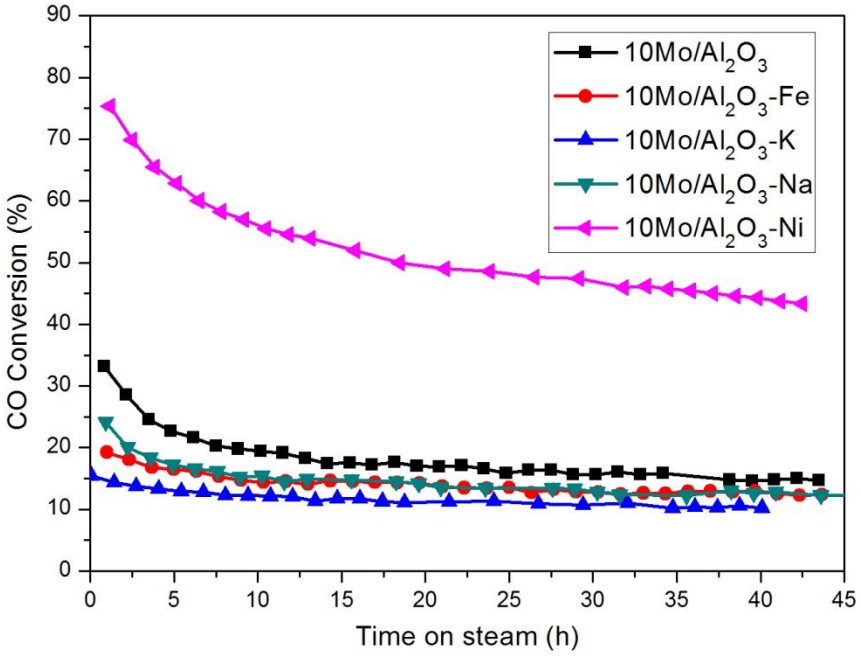

Figure 5-5: Lifetime of different promoted Mo/Al_2O_3 catalysts over Fischer-Tropsch synthesis.

Besides, the Mo carbide catalyst activity is stable with the promotion of Na, Fe and K. After a slight decrease in CO conversion within the first 5 h of test, the catalysts remained stable during at least 40 h.

The nickel promoted catalyst presents a better CO conversion but a not a good stability compared to the non-promoted Mo/Al_2O_3 carbide catalyst. A slow decrease in CO conversion can be still observed during 40 hours of time on stream.

5.3.2 XRD patterns for different promoted Mo/Al_2O_3 catalysts

X-ray diffraction patterns of the different calcined promoted Mo/Al_2O_3 catalysts are shown in Figure 5-6. The diffraction peaks at $2\theta = 23.3°$, 25.7 ° and 27.3 ° were observed over the Mo/Al_2O_3, $NaMo/Al_2O_3$-1:5 and KMo/Al_2O_3-1:5 catalyst and are attributed to the crystallographic planes of the orthorhombic MoO_3 phase (JCPDS 35-0609). The XRD peaks broadening indicate the presence of small molybdenum oxide crystallites on the alumina support [31]. However, after nickel or iron promotion, no characteristic peaks of MoO_2 or MoO_3 were detected in the XRD patterns. This suggests that the molybdenum species could

be well dispersed on the alumina support [32], the crystallite sizes should be below the detection limits of the X-ray diffraction equipment. Thus, the addition of nickel or iron promotes the dispersion of molybdenum species on the alumina support. Besides, no new characteristic peak was observed after the promotion, which implies that the addition of Na, K, Fe or Ni did not lead to new crystalline phases

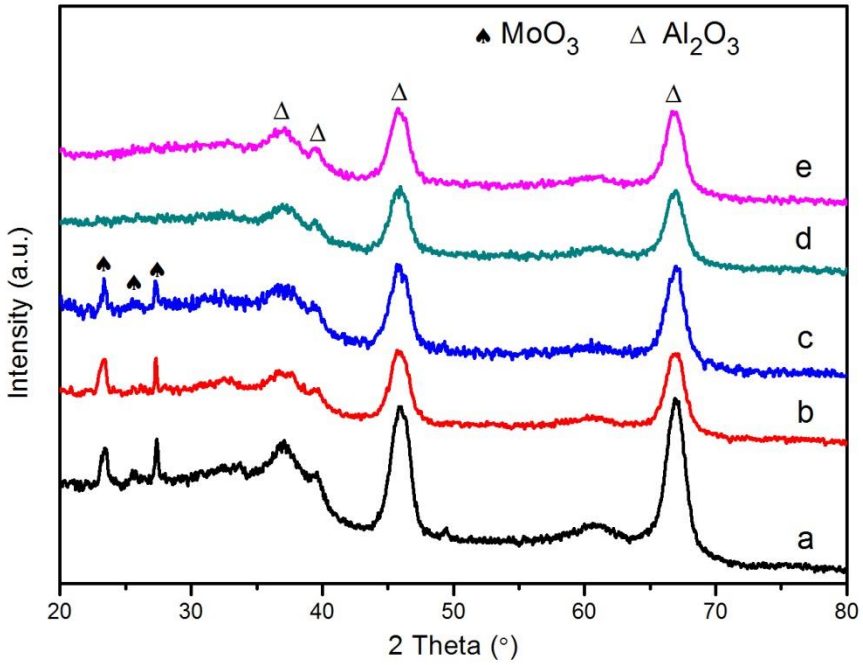

Figure 5-6: The XRD patterns for (a): calcined Mo/Al_2O_3; (b): calcined $NaMo/Al_2O_3$-1:5; (c): calcined KMo/Al_2O_3-1:5; (d): calcined $FeMo/Al_2O_3$-1:5; (e): calcined $NiMo/Al_2O_3$-1:5.

The same samples have been carburized then characterized by XRD. No characteristic peaks of MoO_2 or MoO_3 were detected in the XRD patterns of non-promoted and promoted Mo carbide catalysts. Note, however, that it is not obvious to confirm the presence of carbide in the Mo/Al_2O_3 catalysts by X-ray diffraction as some of the β-Mo_2C XRD peaks ($2\theta = 52.3°$, 61.9 ° and 75.0 °) are overlapped with the characteristic peaks of alumina. They could be also finely dispersed on alumina, the crystallite sizes of molybdenum carbide should be below the detection limits of X-ray diffraction because of peak broadening [32].

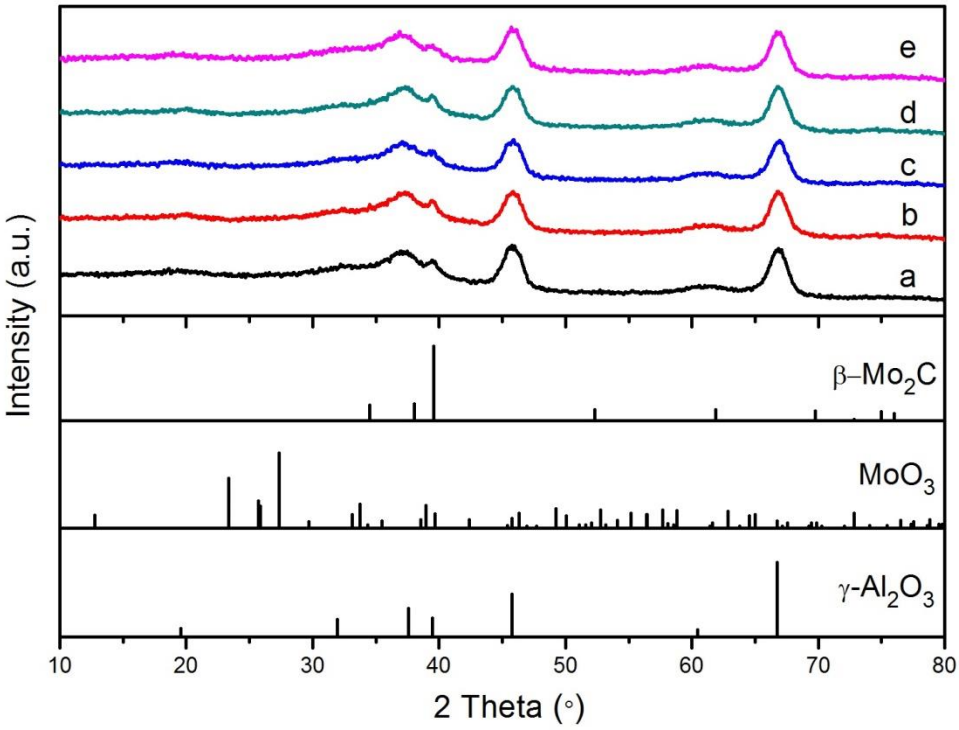

Figure 5-7: The XRD patterns for (a): carburized Mo/Al_2O_3; (b): carburized $NaMo/Al_2O_3$-1:5; (c): carburized KMo/Al_2O_3-1:5; (d): carburized $FeMo/Al_2O_3$-1:5; (e): carburized $NiMo/Al_2O_3$-1:5.

5.3.3 TPR curves for different promoted Mo/Al_2O_3 catalysts

The H_2-TPR curves of the carburized catalysts are shown in Figure 5-8. The TCD signal indicated the presence of an intense hydrogen consumption peak between 250-450 ℃, a smaller hydrogen consumption peak between 475-600 ℃ and a broad hydrogen consumption peak between 650-1000 ℃. Previous reports [42-45] suggested that several layers of carbon could be formed on the surface of an ideal Mo_2C phase. The first peak can be attributed to the reduction of surface carbidic layer. We have to mention that the catalysts have been passivated before TPR experiment. The second peak can be attributed to the reduction of a sublayer of carbon, producing methane. The third board H_2 consumption peak can be attributed to the reduction of Mo_2C phase [42, 44].

A slight shift to higher temperature was observed after potassium promotion and it is more obvious after iron addition. The promotion of iron seems to restrict the reducibility of molybdenum species. A slight shift to lower temperature is observed for the nickel promoted catalyst which suggests the increase in molybdenum reducibility in presence of nickel particles [44, 46]. The presence of the promoters does not have an influence on the reducibility of the bulk Mo_2C phase.

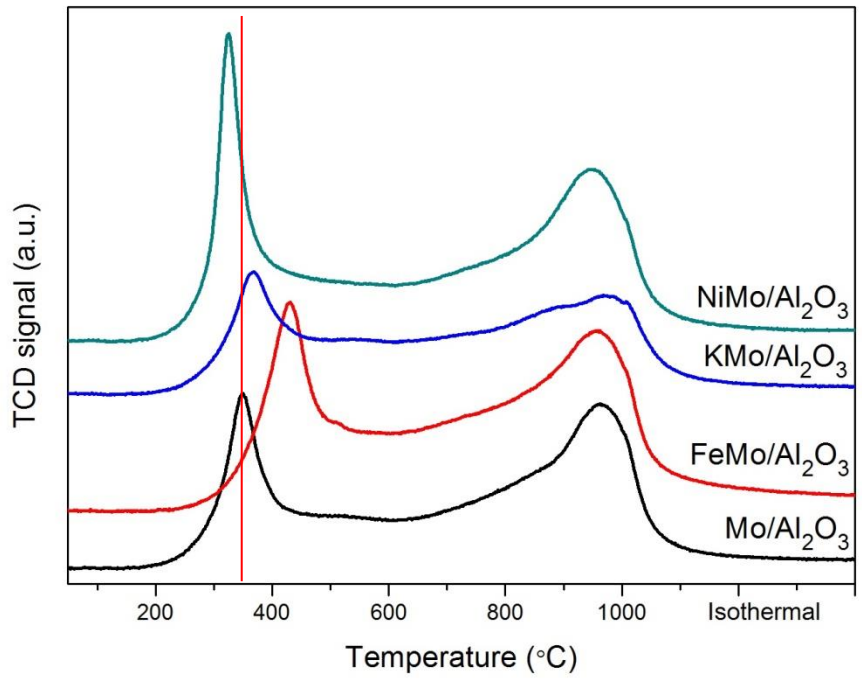

Figure 5-8: H_2-TPR curves for carburized different promoted Mo/Al_2O_3 catalyst.

The H_2 consumption measured from the TPR profiles are shown in Table 5-6. The H_2 consumption measured from the TPR profiles decrease with the addition of potassium while it increased with the promotion of Ni or Fe. The nickel and the iron are two reducible species. So this increase in hydrogen consumption could be due partially to their reduction. The formation of carbon layers and molybdenum reducibility seems to be hindered by the presence of potassium.

Table 5-6: H_2 consumption for the different carburized promoted catalysts ($mmolH_2/g_{catalyst}$).

Catalysts	H_2 consumption (mmol/g)
Mo/Al_2O_3	1.36
$K/Mo/Al_2O_3$-1:5	1.13
$Ni/Mo/Al_2O_3$-1:5	1.56
$FeMo/Al_2O_3$-1:5	1.70

5.3.4 XPS for different promoted Mo/Al_2O_3 catalysts

XPS spectra for carburized catalysts have been recorded. The Mo 3d XPS spectra and element distribution are displayed Figure 5-9 and Table 5-7.

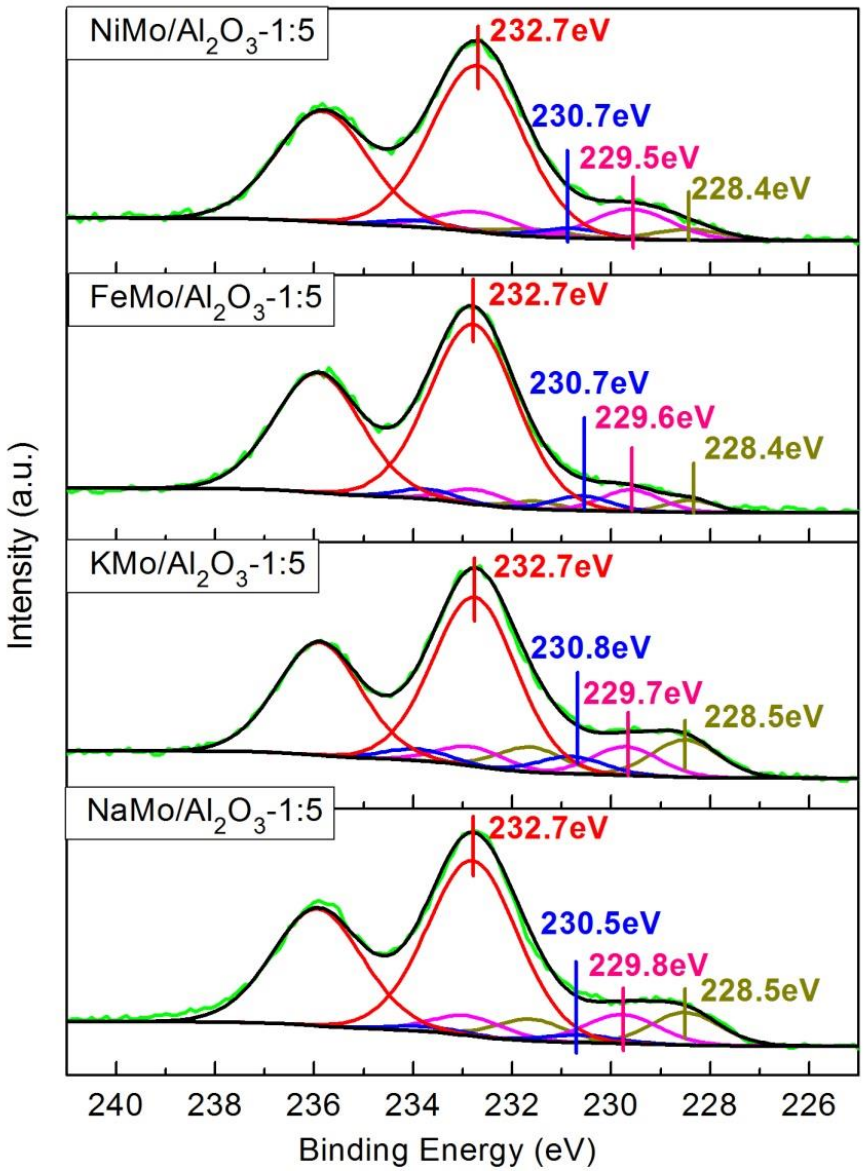

Figure 5-9: Mo 3d XPS spectra of different carburized promoted Mo/Al_2O_3 catalysts.

As is clearly shown in Figure 5-9, after the addition of promoters, the catalysts display similar Mo 3d spectra compared with the non-promoted Mo/Al_2O_3 catalyst. All the catalysts exhibit peaks of Mo^{2+} (228.5 eV), Mo^{4+} (229.8 eV), $Mo^{\delta+}$ (230.5 eV) and Mo^{6+} (232.6 eV) species. Similarly, no characteristic peak of metallic molybdenum was detected.

The surface compositions of catalysts and the Mo^{x+}/Mo total ratio measured by XPS are listed in Table 5-7.

Table 5-7: Element distribution (wt%) and Mo^{X+}/Mo ratio of different promoted Mo/Al_2O_3 catalysts.

Catalysts	Element distribution (wt%)					Mo 3d 5/2 (at%)			
	C 1s	Al 2p	O 1s	Promoters 2p (K, Na, Fe or Ni)	Mo 3d	Mo^{2+}	Mo^{4+}	$Mo^{\delta+}$	Mo^{6+}
Mo/Al_2O_3	9.6	35.8	38.8	0	15.8	10.3	16.8	4.8	68.1
KMo/Al_2O_3-1:5	6.2	40.1	39.9	0.9	12.9	11.9	10.3	2.7	75.2
$NaMo/Al_2O_3$-1:5	6.5	40.6	40.0	0.7	12.2	12.6	9.8	5.9	71.7
$FeMo/Al_2O_3$-1:5	5.7	41.0	40.5	1.1	11.6	3.3	7.0	4.7	85.0
$NiMo/Al_2O_3$-1:5	6.7	40.1	40.5	1.9	10.9	4.2	12.6	3.0	80.1

As is estimated using the simple close-packed monolayer model (A close-packed monolayer capacity of 0.12 g MoO_3/100 m^2) [8,9], the monolayer capacity of molybdenum on alumina support is as low as 10.1 wt%, which is close to the theory concentration of molybdenum in the catalyst(10wt%), suggests the presence of molybdenum monolayer on alumina. Hence, Mo is highly dispersed on the alumina surface. Note that no big crystalline particle of molybdenum species was detected by XRD for the carburized catalysts. The presence of potassium seems to slightly decrease the dispersion of molybdenum (Mo/Al = 0.44 for Mo/Al_2O_3 and 0.32, 0.30, 0.28 and 0.27 for KMo/Al_2O_3-1:5, $NaMo/Al_2O_3$-1:5, $FeMo/Al_2O_3$-1:5, and $NiMo/Al_2O_3$-1:5, respectively).

The Mo^{6+} specie is attributed to passivation layers and is dominant among the Mo species distribution. The relative concentration of Mo^{2+} species attributed to Mo_2C is higher for the alkali promoted catalysts KMo/Al_2O_3-1:5 and $NaMo/Al_2O_3$-1:5. For the metallic promoters such as Fe or Ni, lower concentration of Mo^{2+} species is obtained, even compared to the non-promoted Mo/Al_2O_3 catalyst.

Compared with non-promoted Mo/Al_2O_3 and Na-, Fe-, and Ni-promoted Mo/Al_2O_3 catalysts, the K promoted Mo/Al_2O_3 catalyst exhibits higher light olefins selectivity and better stability from oxidation (higher Mo^{2+} percentage on the surface even after passivation). Thus, different potassium content promotion over Mo/Al_2O_3 catalyst was investigated in the following paragraphs.

5.3.5 Catalytic performance of Mo/Al_2O_3 catalysts with different content of potassium

Carbon monoxide hydrogenation was conducted at 300 ℃ under a total pressure of 10 bar and with H_2/CO ratio of 2. The CO conversion and products selectivities were obtained at the steady state and iso-GHSV (12000 $cm^3.g^{-1}.h^{-1}$). Methane, light olefins and paraffins, alcohols, heavy hydrocarbons and carbon dioxide were the major reaction products detected. For the sake of clarity, carbon dioxide was included in the total selectivity calculations, but is excluded from the hydrocarbon selectivity. Furthermore, in order to avoid relative error due to low conversion, the KMo/Al_2O_3-1:1 catalyst has been evaluated at a lower GHSV (6000 $cm^3.g^{-1}.h^{-1}$). The catalytic results obtained with non-promoted and potassium promoted molybdenum carbide catalysts are given in Table 5-8.

Table 5-8: Fischer-Tropsch performance over non-promoted and potassium promoted Mo/Al_2O_3 catalysts at 300 ℃, 10 bar, H_2/CO = 2.

Catalysts	GHSV $cm^3.g^{-1}h^{-1}$	**X_{CO} (%)**	CH selectivity (% C mol)					CO_2 selec. (%)
			CH_4	**$C_2^=$-$C_4^=$**	C_2-C_4	**C_{5+}**	C-OH	
$10Mo_2C/Al_2O_3$	12000	**14.4**	40.0	**9.0**	41.5	**6.9**	2.6	45.4
$10Mo_2C$-K(1/5)/Al_2O_3	12000	**10.7**	34.4	**10.4**	37.1	**16.7**	1.4	43.3
$10Mo_2C$-K(1/2)/Al_2O_3	12000	**5.2**	23.5	**17.3**	22.9	**36.0**	0.3	39.1
$10Mo_2C$-K(1/1)/Al_2O_3	12000	**< 0.2**	-	**-**	-	**-**	-	-
$10Mo_2C$-K(1/2)/Al_2O_3	6000	**20.1**	32.5	**13.6**	36.5	**12.5**	4.9	46.6
$10Mo_2C$-K(1/1)/Al_2O_3	6000	**4.2**	15.4	**21.8**	6.8	**55.4**	0.6	34.5
$10Mo_2C$-K(1/2)/Al_2O_3	4000	**23.5**	32.2	**13.0**	37,1	**14.1**	3.6	48.9
$10Mo_2C$-K(1/1)/Al_2O_3	4000	**8.2**	19.6	**15.7**	23.2	**33.1**	8.4	39.1

In agreement with previous reports [47, 48], addition of potassium significantly influences the catalytic performance of the $10Mo_2C/Al_2O_3$ catalyst. The CO conversion at GHSV=12 000 $cm^3.g^{-1}.h^{-1}$ decreased from 14.4 % to less than 0.2 % with the increase in K/Mo ratio. Similarly, a decrease in the CH_4, CO_2, light paraffin and alcohol selectivities was observed. At the same time, an increase in light olefin selectivity (from 9 % to 17.3 %) and C_{5+} hydrocarbon selectivity (from 6.9 % to 36.3 %) was observed under these conditions.

The same trends were observed when comparing the catalytic performances at different GHSV. The decrease in GHSV led to an increase in the CO conversion over the same catalyst (from 5.2% at 12000 $cm^3.g^{-1}.h^{-1}$ up to 23.5% at 4000 $cm^3.g^{-1}.h^{-1}$ for the $10Mo_2C$-K(1/2)/Al_2O_3 catalyst and from less than 0.2 % at 12000 $cm^3.g^{-1}.h^{-1}$ up to 8.2% at 4000 $cm^3.g^{-1}.h^{-1}$ for the $10Mo_2C$-K(1/1)/Al_2O_3 catalyst). The selectivity to different products is also affected by the conversion. At high CO conversion, the methane, light paraffin and CO_2 selectivities increased at the expense of the olefin and C_{5+} hydrocarbon selectivities.

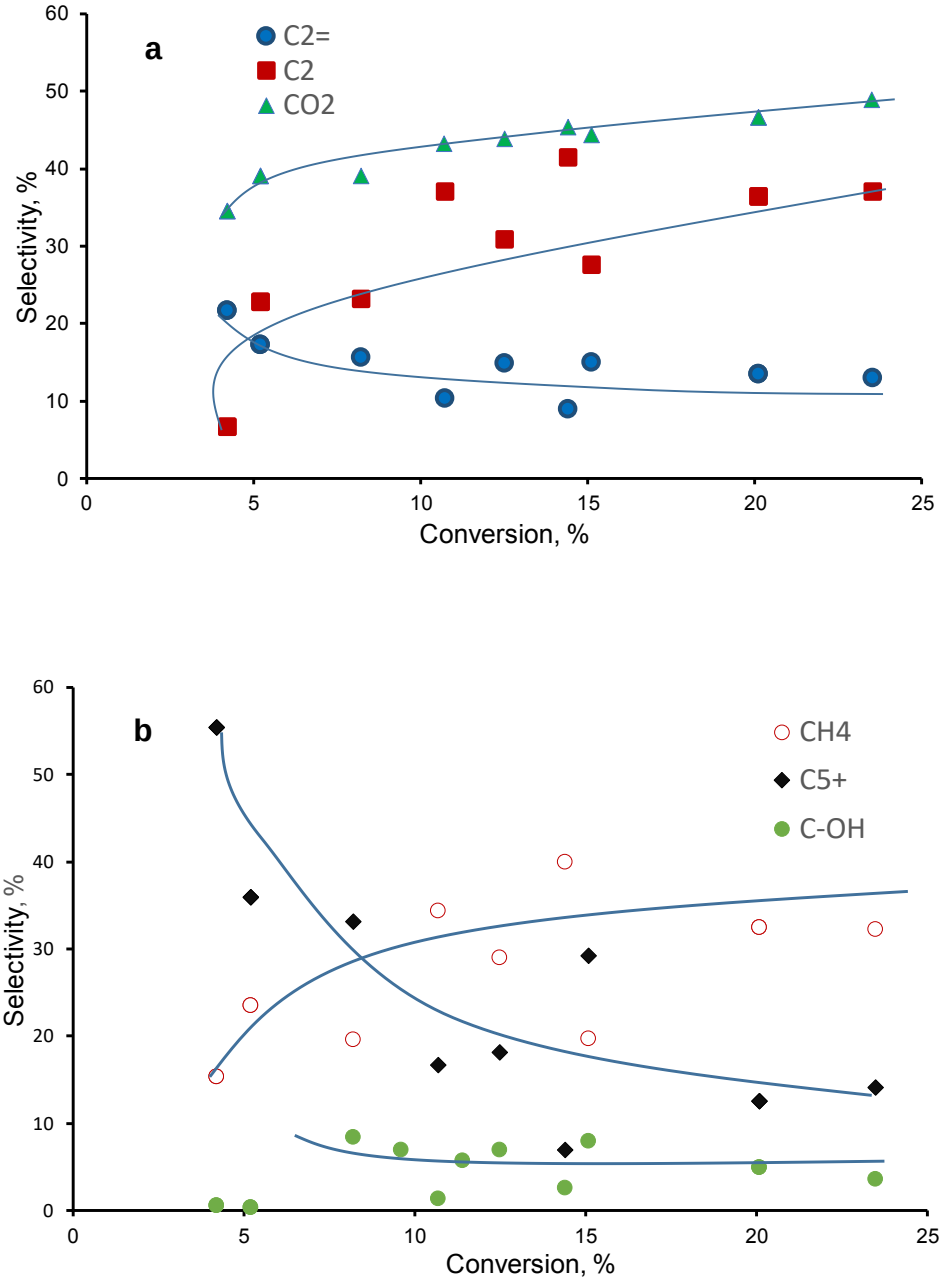

Figure 5-10: Selectivities as functions of CO conversion on different potassium content promoted molybdenum carbide catalysts (P=10 bar, T= 300 ℃, H_2/CO=2).

At similar conversion value (5.4% at 12000 $cm^3.g^{-1}.h^{-1}$ for $10Mo_2C$-K(1/2)/Al_2O_3 and 4.2% at 6000 $cm^3.g^{-1}.h^{-1}$ for $10Mo_2C$-K(1/1)/Al_2O_3), higher light olefins and C_5^+ selectivities along with lower methane and light paraffin selectivities were obtained with the catalysts containing a higher amount of potassium. As reported in the literature [49], high potassium content is favorable for synthesis of light olefins and heavy hydrocarbons.

Figure 5-10 (a and b) presents the relations between product selectivities and carbon monoxide conversion for all studied catalysts. The selectivities to light olefins (C2=) and C_{5+} hydrocarbons decrease with an increase in CO conversion, while light paraffins (C2), methane and carbon dioxide selectivities increase. Lower selectivity to light olefins at higher conversion can be due to their secondary hydrogenation, while higher CH_4 selectivity at high CO conversion can be probably due to hydrogenolysis of higher hydrocarbons. The increase in CO_2 selectivity (Figure 5-10 a) can be assigned to the WGS reaction ($CO + H_2O \leftrightarrows CO_2 + H_2$). The alcohol selectivity reached a maximum value for $10Mo_2C$-K(1/1)/Al_2O_3 catalyst at 4000 $cm^{-3}.g^{-1}.h^{-1}$, at CO conversion of 8.2%. The observed relatively low alcohol selectivities on the molybdenum carbide based catalysts can be explained by the reaction pressure. Commonly higher alcohol selectivity is obtained under high pressure reaction conditions (P>30 bar).

H_2/CO ratio also significantly affects the product selectivity. Table 5-9 presents the steady-state activity and selectivity in the CO hydrogenation on the $10Mo_2C$-K(1/2)/Al_2O_3 catalyst and $10Mo_2C$-K(1/1)/Al_2O_3 catalyst at 300 ℃, 10 bar, and H_2/CO ratio of 1 and 2. Once the H_2/CO ratio decreased from 2 to 1, the CO conversion decreased from 20.1% to 11.4% for $10Mo_2C$-K(1/2)/Al_2O_3 catalyst and from 15.1% to 9.6% for $10Mo_2C$-K(1/1)/Al_2O_3 catalyst. The light olefin and C_{5+} selectivities increase, while methane, light paraffin and alcohol selectivities decrease. Interestingly, the selectivity to CO_2 also decreases at lower H_2/CO ratio.

At similar CO conversion (around 10.5%) for the different K promoted catalysts at different H_2/CO ratios (10,7% for the catalyst with K/Mo = 1/5 (Table 5-8); 11.4% for the catalyst with K/Mo = 1/2; 9.6% for the catalyst with K/Mo = 1/1 at H_2/CO = 1 (Table 5-9)), the light olefin, alcohol, C_{5+} hydrocarbon selectivities increase with the increase in the potassium content and with the decrease in the H_2/CO ratio. Correspondingly, at similar CO conversion, methane and light paraffin selectivities are lower when a potassium amount is higher and the H_2/CO ratio is lower. In agreement with previous reports [49], low H_2/CO ratio is favorable for production of high hydrocarbons.

Table 5-9: Fischer-Tropsch performance over potassium promoted $10Mo/Al_2O_3$ catalysts at 300 ℃, 10 bar at various GHSV and ratio H_2/CO

Catalysts	H_2/CO	GHSV $cm^3.g^{-1}h^{-1}$	X_{CO} (%)	CH selectivity (% C mol)					CO_2 selec. (%)
				CH_4	$C_2^=$-$C_4^=$	C_2-C_4	C_{5+}	C-OH	
$10Mo_2C$-K(1/2)/Al_2O_3	2	6000	**20.1**	32.5	**13.6**	36,5	**12.5**	4.9	46.6
	1	6000	**11.4**	16.1	**15.5**	16.2	**46.5**	5.7	40.6
$10Mo_2C$-K(1/1)/Al_2O_3	2	2000	**15.1**	19.7	**15.1**	27.7	**29.2**	8.0	44.4
	1	2000	**9.6**	13.9	**17.1**	16.4	**45.6**	7.0	37.2

5.3.6 Textural properties for different K content promoted Mo based catalysts

The specific surface area is an important catalyst characteristics. The textural properties of the alumina support, calcined and carburized Mo-based catalysts are displayed in Table 5-10. The surface area, the average pore volume and diameter decreased after alumina impregnation with molybdenum. This decrease should due to the partial blockage of alumina pores by molybdenum species. In addition, the promotion by potassium resulted in a further slight decrease in the catalyst surface area while the average pore volume and diameter remained constant.

Table 5-10: Physical properties of Mo-based catalysts.

Sample		S_{BET} m^2/g	V_{total} cm^3/g	D_{meso} nm
Calcined catalysts	Al_2O_3	138.7	0.42	6.0
	Mo/Al_2O_3	123.4	0.33	5.4
	KMo/Al_2O_3-1:5	117.6	0.32	5.4
	KMo/Al_2O_3-1:2	115.3	0.32	5.3
	KMo/Al_2O_3-1:1	112.7	0.31	5.4
Carburized catalysts	Mo/Al_2O_3	119.7	0.34	5.7
	KMo/Al_2O_3-1:1	104.4	0.31	5.1

The BET surface area also decreased after carburization (123.4 m^2/g before and 119.7 m^2/g after carburization for $10Mo/Al_2O_3$ catalyst; 112.7 m^2/g before and 104.4 m^2/g after carburization for KMo/Al_2O_3-1:1 catalyst). The average pore volume and diameter are not influenced by the carburization process. However, after calcination or carburization, the K promoted Mo/Al_2O_3 catalysts surface area remains relatively high.

5.3.7 Raman spectra for different K content promoted Mo based catalysts

The Raman spectra of the calcined KMo/Al_2O_3-(X) catalysts are reported in Figure 5-11. The spectra exhibit the presence of MoO_3, $Al_2(MoO_4)_3$ and polymolybdates phases.

The presence of MoO_3 phase in $10Mo/Al_2O_3$ and all the KMo/Al_2O_3-(X) catalysts is evidenced by the characteristic peaks of MoO_3 at the Raman wavenumber of 288, 335, 664, 818 and 995 cm^{-1} [50-54]. The Raman spectra also exhibit a band at 377 cm^{-1} corresponding to the $Al_2(MoO_4)_3$ phase resulting from the interaction of molybdenum with the alumina support [47, 55]. The relative intensity of this later band increases slightly with the increase in K content.

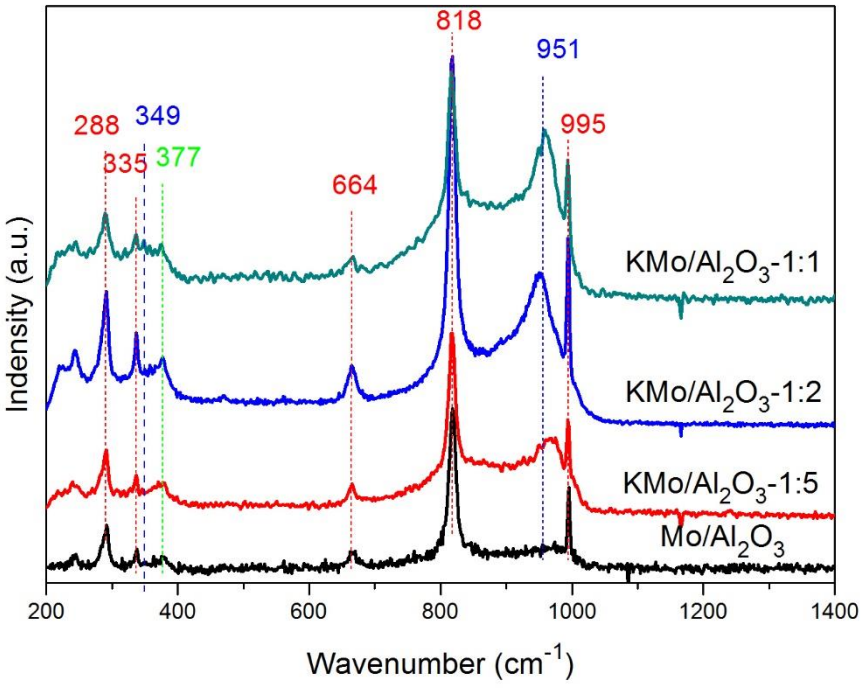

Figure 5-11: Raman spectra of the different calcined K promoted Mo/Al_2O_3 catalysts.

After potassium promotion, the spectra of calcined KMo/Al_2O_3-(X) catalysts revealed a dominant asymmetric feature at 951 cm^{-1} and a small band at 349 cm^{-1}, which can be assigned to symmetric stretching of the Mo=O bond in octahedrally coordinated Mo^{6+} species such as $Mo_4O_6^{2-}$ and $Mo_7O_{24}^{2-}$ [50, 56] . These two molybdenum species can be associated to the K-Mo mixed phases as the relative intensity of these peaks increases along with the potassium amount.

The Raman data suggest that K promotion of Mo/Al_2O_3 catalyst results in a stronger interaction between molybdenum, potassium and alumina and may lead to the formation of mixed K-Mo, Mo-Al and K-Mo-Al oxides.

5.3.8 XRD patterns for K promoted Mo based catalysts

X-ray diffraction patterns for the calcined Mo/Al_2O_3, carburized Mo/Al_2O_3 catalysts and non-supported Mo_2C are shown in Figure 5-12. The diffraction peaks at $2\theta = 23.3°$, 25.7 ° and 27.3 ° for the Mo/Al_2O_3 and KMo/Al_2O_3-1:1 catalyst are attributed to the crystallographic planes of the orthorhombic MoO_3 phase (JCPDS 35-0609). The XRD peaks broadening indicates high dispersion of molybdenum species on the alumina support [31]. Interestingly, no new diffraction peaks are observed in the potassium promoted catalysts corresponding to K-containing crystalline phases. However, the Raman spectra imply the existence of K-Mo and K-Mo-Al mixed phase after K promotion. The K-containing phases could be located in small crystalline particles, which sizes are below the detection limits of X-ray diffraction.

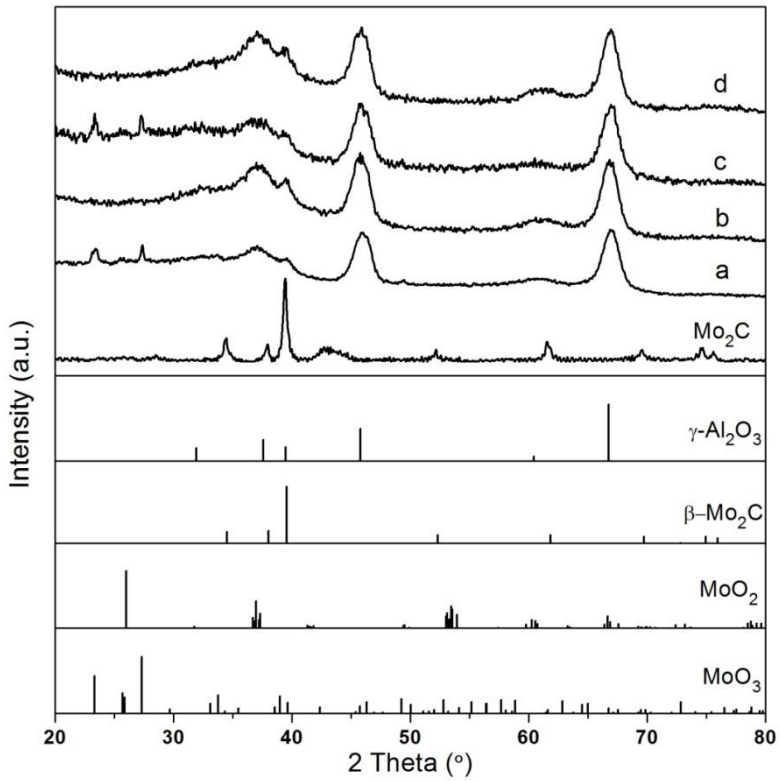

Figure 5-12: XRD patterns for **(a)** calcined Mo/Al_2O_3; **(b)** carburized Mo/Al_2O_3; **(c)** calcined KMo/Al_2O_3-1:1; **(d)** carburized KMo/Al_2O_3-1:1 and β-Mo_2C (JCPDS #65-8766), γ-Al_2O_3 (JCPDS#29-0063), MoO_2 (JCPDS #65-5787), MoO_3 (JCPDS #35-0609).

After the carburization, no characteristic peaks of MoO_2 or MoO_3 were detected in the XRD patterns of the unpromoted and promoted Mo_2C/Al_2O_3 catalysts indicating successful molybdenum oxide conversion into the oxycarbide and/or carbides phases. Note, however, that some of the β-Mo_2C XRD peaks may overlap with the characteristic peaks of alumina. This could be a reason why Mo_2C is not easily identified by XRD in the alumina supported catalysts. Note however that even the β-Mo_2C characteristic peaks at $2\theta = 52.3°$, $61.9°$ and $75.0°$ which are clearly distinguishable from XRD patterns of Al_2O_3 were not detected in the carburized catalysts. This could be indicative of very high dispersion of supported molybdenum carbide on alumina, its crystallite sizes should be below the detection limits of X-ray diffraction [32].

5.3.9 CO_2-TPD for different K content promoted Mo based catalysts

The basicity of the molybdenum carbide catalysts was measured by CO_2-TPD and the results are shown in Figure 5-13. Similarly, all the samples exhibited weak basic sites at range of 150 - 350 ℃, moderate basic sites at range of 200 - 550 ℃ and strong basic sites at range

of 400 - 700 ℃, after fitting by the Gauss function from the broad CO_2 desorption peak. The intensity of the strong basic sites is slightly higher after the addition of potassium, resulting in a slight shifted to higher temperature. However, the peaks positions are not influenced by the increase in K content.

The intensity of the weaker and the moderate basic site peaks increases with the increase in potassium content, resulting to a slight shift of the weaker basic site to lower temperature.

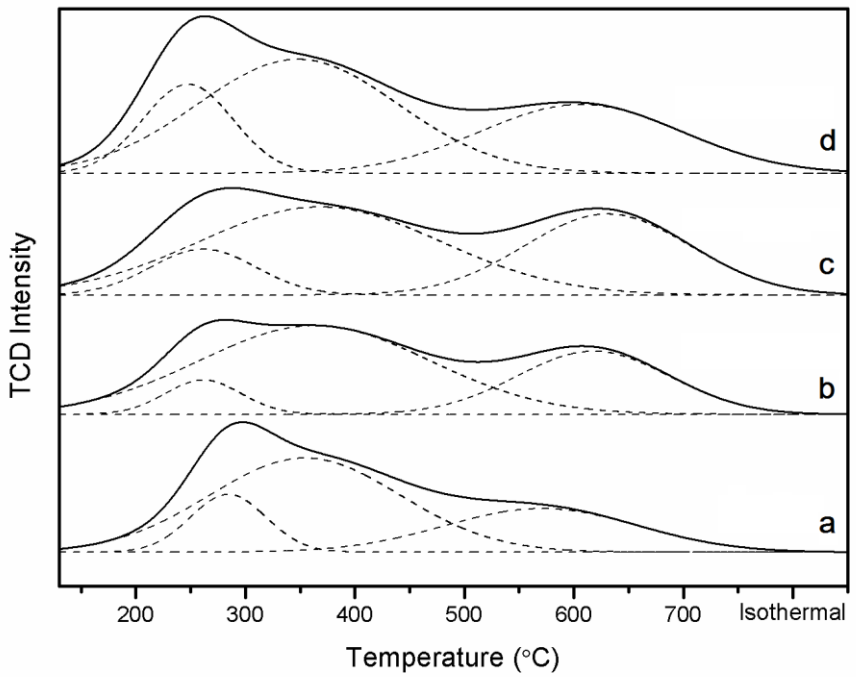

Figure 5-13: CO_2-TPD curves of **(a)** Mo/Al_2O_3; **(b)** KMo/Al_2O_3-(1:5); **(c)** KMo/Al_2O_3-(1:2); **(d)** KMo/Al_2O_3-(1:1).

Note that the presence of basic sites was detected on the alumina support itself. The total amount of CO_2 adsorption measured from the CO_2-TPD (Table 5-11) confirmed that potassium contributed to the increase in the number of the catalyst basic sites. In comparison to the non-promoted Mo/Al_2O_3 catalyst, the concentration of weak (150-350 ℃) and strong (200-600 ℃) basic sites increased significantly with the addition of potassium. Interestingly the concentration of the moderate basic sites did not change with the increase in K content (0.08 mmol/g).

Table 5-11: CO_2 desorption amount of carburized K promoted Mo/Al_2O_3 catalysts in mmol/g.

Samples	CO_2 desorption (mmol/g)			
	Weak basic site	Moderate basic site	Strong basic site	total
Mo/Al_2O_3	0.01	0.06	0.03	0.11
KMo/Al_2O_3-(1:5)	0.01	0.08	0.04	0.13
KMo/Al_2O_3-(1:2)	0.02	0.08	0.05	0.15
KMo/Al_2O_3-(1:1)	0.03	0.08	0.05	0.16

5.3.10 H_2-TPR for carburized different K content promoted Mo based catalysts

The H_2-TPR curves of Mo/Al_2O_3 and KMo/Al_2O_3-(X) catalysts with X = 1:5 and 1:1 are shown in Figure 5-14. The TCD signal indicated the presence of an intense hydrogen consumption peak between 250 - 450 ℃ and a smaller hydrogen consumption peak between 475 - 600 ℃. Previous reports suggest [42-45] that several layers of carbon can be formed on the surface of an ideal Mo_2C phase. Note that. some molybdenum species can be oxidized during the passivation. The hydrogen consumption of the first peak can be therefore attributed to the reduction of oxidized molybdenum species. The second peak can be attributed to the hydrogenation of carbidic carbon and/or hydrogenolysis of polymeric carbon. Note however that the bulk Mo2C phase is stable in the presence of hydrogen. Lee [42] and Leclercq [44] showed that the Mo_2C structure can be maintained even after 10 h of reduction in hydrogen at 700 ℃.

The TPR profiles of $10Mo_2C/Al_2O_3$ and $10Mo_2C$-K(1/5)/Al_2O_3 are similar. Interestingly, the first reduction peak slightly shifts to higher temperature with the increase in K content. This behavior may be due to the change in the interaction between active Mo components and support, and the presence of mixed K-Mo phases.

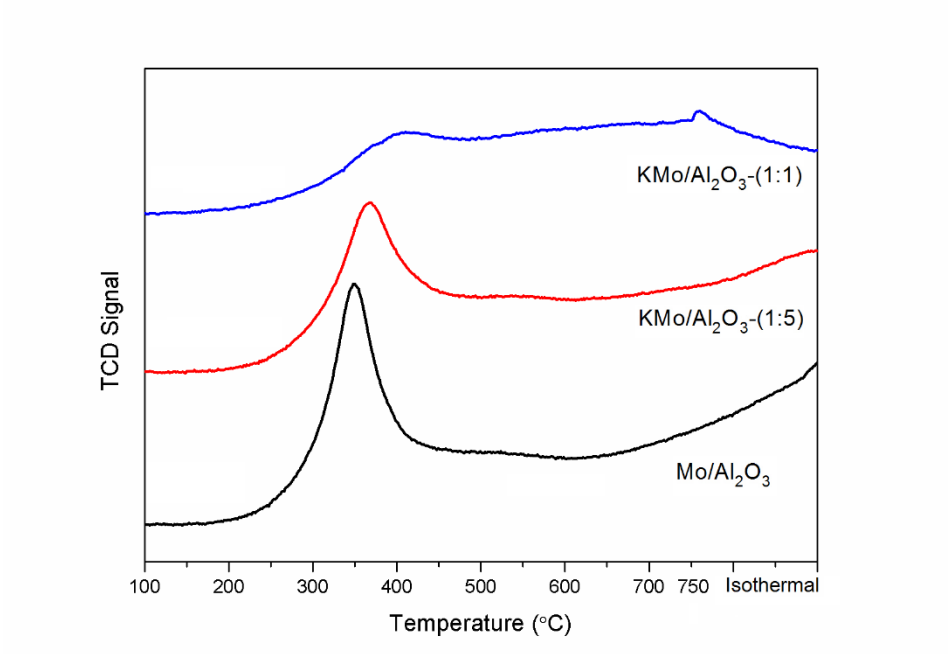

Figure 5-14: H_2-TPR curves of carburized Mo/Al_2O_3, carburized KMo/Al_2O_3-(1:5) and carburized KMo/Al_2O_3-(1:1) catalysts.

The potassium promotion influences both the position of the TPR peaks and H_2 consumptions measured from the TPR profiles (Table 5-12). The hydrogen consumption is almost 50% smaller with the $10Mo_2C$-K(1/1)/Al_2O_3 catalyst compared to the $10Mo_2C/Al_2O_3$ counterpart. Molybdenum reducibility seems to be hindered by the presence of potassium. This may be due to the formation of mixed K-Mo phases seen by Raman spectroscopy, but also to the Mo_2C surface covered, at least partially, by potassium.

Table 5-12 H_2 consumption from TPR experiments over the different catalysts ($mmolH_2/g_{catalyst}$)

Catalysts	H_2 consumption (mmol/g)
Mo/Al_2O_3	0.31
$K/Mo/Al_2O_3$-1:5	0.26
$K/Mo/Al_2O_3$-1:1	0.17

5.3.11 TEM for different K content promoted Mo based catalysts

Figure 5-15 shows the bright field TEM images of Mo/Al_2O_3 and KMo/Al_2O_3-(1:5) catalysts. The presence of highly dispersed molybdenum carbide nanoparticles on an amorphous material (possibly carbon) can be easily detected. The average particle size of molybdenum carbide is ~1 nm, which is consistent with previous reports by Shou et al. [57]

or of Stellwagenand et al.[58]. Very small sizes of molybdenum carbide nanoparticles can explain the absence of X-ray diffraction peaks of the Mo carbide phases.

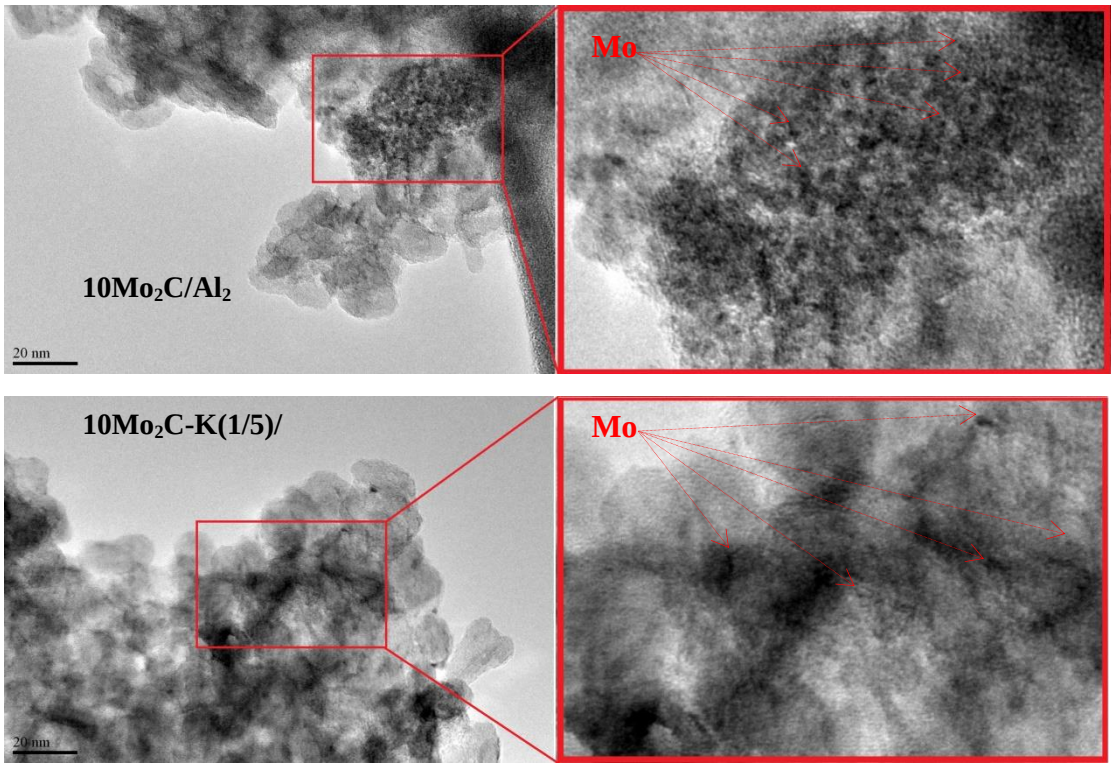

Figure 5-15: TEM images of carburized Mo/Al_2O_3 and KMo/Al_2O_3-1:5 catalysts.

5.4 Impact of the presence of CH_4 or CO_2 in FTS

During the dry methane reforming, the produced syngas can contains some amount of unreacted CH_4 and CO_2. Taking into account a conversion of 90% and the flow of CH_4 and CO_2 at the outlet of the DMR reactor, the Fischer-Tropsch synthesis was conducted in the presence of 5% CO_2 or 5% CH_4, under a total pressure of 10 bar and with syngas of H_2/CO ratio of 1. The CO conversion and products selectivities were obtained at the steady state and iso-GHSV (6000 $cm^3.g^{-1}.h^{-1}$). For the sake of clarity, carbon dioxide was included in the total selectivity calculations, but is excluded from the hydrocarbon selectivity. In order to avoid low conversion after the addition of CH_4 or CO_2, the reaction temperature was increased to 380 ℃. Particularly, the selectivity of CH_4 and CO_2 is excluded the CH_4 or CO_2 which was added in syngas. The catalytic results over the KMo/Al_2O_3-1:2 catalyst are given in Table 5-13.

As expected, the increase in reaction temperature led to a significant increase in CO conversion (from 11.4 % at 300 ℃ up to 26.3% at 380 ℃). The products selectivities are also affected by the conversion. At high CO conversion, the methane, light paraffin and CO_2

selectivities increased at the expense of the olefins and C_5^+ hydrocarbon selectivities (from 15.5 % to 13.5 % for olefins and from 51.7 % to 18.6 % for C_5^+ at temperature of 300 ℃ to 350 ℃, respectively). The increase in CH_4 selectivity at high CO conversion can be due to hydrogenolysis of higher hydrocarbons or methanol hydrogenation. The increase in CO_2 selectivity may be due to the WGS reaction which is more significant at higher CO conversion.

Table 5-13: CO hydrogenation catalytic perofrmance over KMo/Al_2O_3-1:2 catalyst at the presence of CH_4 and CO_2.

Condition	T/ ℃	X_{CO} (%)	CH selectivity (% mol)					CO_2 selec. (%)
			CH_4	$\mathbf{C_2^=\text{-}C_4^=}$	C_2-C_4	C_5^+	C-OH	
Syngas	300	11.4	16.1	**15.5**	16.2	**51.7**	0.47	40.6
	380	26.3	36.1	**13.5**	31.8	**18.6**	0	47.1
5% CH_4	380	15.9	42.4	**15.7**	26.8	**15.0**	0	22.5
5% CO_2	380	8.9	26.9	**17.5**	19.0	**36. 6**	0	47.5

The presence of CH_4 or CO_2 in the syngas affects significantly activity and products selectivity. With the addition of 5% CH_4, the CO conversion decreased from 26.3% to 15.9% along with an increase in methane selectivity. CO_2 selectivity decreased significantly from 47.1% to 22.5%. Light olefins increased while C_5^+ selectivity decreased. Hence, the addition of CH_4 in the syngas restricts the WGS reaction and the chain growth rate and promotes the generation light olefins.

With the addition of CO_2, a significant decrease in the CO conversion was observed (from 26.3% to 8.9%). The selectivity of CO_2 remains constant (47.1% with pure syngas and 47.5% with syngas + CO_2). In presence of additional CO_2 in the flux, light olefins and C_5^+ selectivity increased while methane reforming decreased. The result implies that the addition of CO_2 is inclined to promote the generation of light and heavy hydrocarbons.

5.5 Discussion

Let us first discuss the effect of different supports on the structure and the catalytic performances of molybdenum carbide catalysts. The BET results are indicative of the different surface area and pore size of the different materials used as support. The XRD patterns of the calcined samples indicate a good dispersion of molybdenum species on the

alumina surface, the others four catalysts exhibited relative larger molybdenum species crystallite size. After carburization process, the absence of XRD characteristic peaks of molybdenum oxide revealed the complete conversion of Mo oxide phase to Mo carbides phase. As well, the presence of carbides has been pointed out by XPS. The CO_2-TPD results prove the presence of stronger basic site for the carburized Mo/Al_2O_3 catalysts. The catalytic data of carbon monoxide hydrogenation indicated that the non-promoted Mo_2C catalysts produce mainly C_1-C_4 light hydrocarbons and negligible amounts of heavy hydrocarbons in Fischer-Tropsch synthesis, which is in agreement with previous reports [26, 27]. Due to the strong water gas shift reaction activity of molybdenum carbides, considerable CO_2 selectivity was obtained over all the samples. Note that Mo supported on alumina catalyst exhibited higher light olefins selectivity compared to the other counterparts. It may be due to the higher concentration of basic sites of alumina support, which is beneficial for the generation of light olefins.

The addition of promoter has an obvious influence on the structure of the molybdenum carbide species supported on alumina and on their catalytic performance in carbon monoxide hydrogenation. The XRD patterns for calcined samples suggest that addition of nickel and iron seems to increase the dispersion of molybdenum species on the alumina. Despite the presence of promoters, the XRD of the carburized sample also indicated the completed conversion of Mo oxide phase to Mo carbide phase and a good dispersion of carbide species. XPS spectra showed that the addition of promoters contributed to the increase in the interaction between the molybdenum species and the alumina support. The promotion of iron and nickel seems to promote formation of sensitive carbide species as the less molybdenum carbides phase over the catalysts surface measured from XPS. The catalytic data showed that the promotion of Na, Fe and K decreased the CO hydrogenation activity and increased the carbon chain growth. Particularly, the addition of potassium increased the light olefin selectivity. The excellent hydrogenation capacity of nickel leads to a significant enhancement of the CO conversion while mainly methane was produced.

Effect of promotion with different potassium content on molybdenum carbide species supported on alumina and their catalytic performance in carbon monoxide hydrogenation have been particularly investigated.

There are obvious interactions between K and Mo species and alumina support. The $Al_2(MoO_4)_3$ phase is observed in the calcined K-promoted samples by Raman spectroscopy. The addition of potassium enhances the interaction of molybdenum phase with alumina

support and results in mixed K-Mo, Mo-Al and K-Mo-Al oxides, which were detected by Raman and H_2-TPR.

XPS indicates formation of the molybdenum carbide species. TEM images indicated that molybdenum carbide was present as very small particles highly dispersed on the alumina support, which was also confirmed by XRD patterns due to the peak broadening for molybdenum carbide phase. Molybdenum dispersion however remained relatively high after the carburization. The BET results indicate that K-promoted molybdenum carbide catalysts keep the same physical properties. However, some potassium atoms can be dissolved in alumina matrix with the formation of potassium aluminate. The potassium incorporation also inhibits the reduction of the carbide catalyst, resulting in a lower CO hydrogenation rate with the increase in K content. The addition of potassium led to the increase in weak and moderate basic sites which affects the catalytic behavior for CO hydrogenation. Liu et al. [47] have reported that the increase in K content in a Mo catalyst contributes to increase the catalyst basicity, thus leading to higher C_5^+ selectivity. This observation is consistent with our work.

It seems that moderate basicity is indispensable for the maximum olefins selectivity. The non-promoted molybdenum carbide catalyst mainly generates methane, light paraffins and carbon dioxide. The chain growth probability can be increased by addition of potassium and optimization of the operating conditions.

5.6 Conclusion

Molybdenum carbide catalysts supported by different materials and promoted by different promoters have been synthesized by temperature programmed carburization using a mixture of H_2/CH_4 and tested in Fischer-Tropsch synthesis. The carbon monoxide hydrogenation catalytic data indicate all the non-promoted Mo_2C catalysts produce mainly C_1-C_4 light hydrocarbons and negligible amounts of heavy hydrocarbons in Fischer-Tropsch synthesis. Due to the strong water gas shift reaction activity of molybdenum carbides, considerable CO_2 selectivity was obtained over all the samples. Particularly, the alumina supported catalyst, which has higher concentration of basic sites, exhibits obvious higher light olefins selectivity compared to other counterparts.

The catalytic data suggest that the promotion with Na, Fe and K decreases the CO hydrogenation activity while increases carbon chain growth and leads to an increase in C_5^+ selectivity. Particularly, the promotion of potassium increases the light olefin selectivity. The

promotion with nickel leads to a significant enhancement of the CO hydrogenation activity while a negligible light olefin selectivity.

The characterization and catalytic data of different potassium content promoted Mo/Al_2O_3 suggest that the addition of potassium promoter results in a decrease in the FT reaction rate most probably because of the formation of more difficultly carburized potassium-molybdenum and molybdenum-aluminum mixed oxides and electronic effects due to the promoter. Potassium promotion leads however to higher light olefin and C_{5+} hydrocarbon selectivities. Higher light olefin and C_{5+} hydrocarbon selectivities can be possibly attributed to the lower hydrogenation activity of the promoted catalysts. The decrease in the selectivity to light olefins and C_{5+} hydrocarbons at higher carbon monoxide conversions was attributed to secondary hydrogenation and hydrocarbon hydrogenolysis leading to light paraffins and methane.

The addition of CH_4 in the syngas restricts the WGS reaction and chain growth while promotes the generation methane and light olefins. Furthermore, the presence of CO_2 in the syngas seems to promote the generation light hydrocarbons and leads to an increase in CO_2, light olefins and paraffin selectivities.

5.7 Reference

[1] X. Wang, C. Zhang, The impacts of global oil price shocks on China′s fundamental industries, Energy Policy, 68 (2014) 394-402.

[2] K. Cheng, V.V. Ordomsky, M. Virginie, B. Legras, P.A. Chernavskii, V.O. Kazak, C. Cordier, S. Paul, Y. Wang, A.Y. Khodakov, Support effects in high temperature Fischer-Tropsch synthesis on iron catalysts, Applied Catalysis A: General, 488 (2014) 66-77.

[3] A.Y. Khodakov, W. Chu, P. Fongarland, Advances in the development of novel cobalt Fischer-Tropsch catalysts for synthesis of long-chain hydrocarbons and clean fuels, Chemical Reviews, 107 (2007) 1692-1744.

[4] Q. Wu, J.M. Christensen, G.L. Chiarello, L.D. Duchstein, J.B. Wagner, B. Temel, J.-D. Grunwaldt, A.D. Jensen, Supported molybdenum carbide for higher alcohol synthesis from syngas, Catalysis today, 215 (2013) 162-168.

[5] H.M. Torres Galvis, K.P. de Jong, Catalysts for Production of Lower Olefins from Synthesis Gas: A Review, ACS Catalysis, 3 (2013) 2130-2149.

[6] A.C.L. Gomes, M.H.O. Nunes, V.T. da Silva, J.L.F. Monteiro, Thiophene hydrodesulfurization using β-MO2C/MCM-41 as catalyst, in: M.C. E. van Steen, L.H. Callanan (Eds.) Studies in Surface Science and Catalysis, Elsevier, 2004, pp. 2432-2440.

[7] E. Puello-Polo, M. Ayala-G, J.L. Brito, Sulfidability and thiophene hydrodesulfurization activity of supported NiMo carbides, Catalysis Communications, 53 (2014) 9-14.

[8] W. Piskorz, G. Adamski, A. Kotarba, Z. Sojka, C. Sayag, G. Djéga-Mariadassou, Hydrodenitrogenation of indole over Mo2C catalyst: Insights into mechanistic events through DFT modeling, Catalysis Today, 119 (2007) 39-43.

[9] K. Fang, D. Li, M. Lin, M. Xiang, W. Wei, Y. Sun, A short review of heterogeneous catalytic process for mixed alcohols synthesis via syngas, Catalysis Today, 147 (2009) 133-138.

[10] M. Xiang, D. Li, H. Xiao, J. Zhang, W. Li, B. Zhong, Y. Sun, K/Ni/β-Mo2C: A highly active and selective catalyst for higher alcohols synthesis from CO hydrogenation, Catalysis Today, 131 (2008) 489-495.

[11] M. Xiang, J. Zou, CO Hydrogenation over Transition Metals (Fe, Co, or Ni) Modified K/Mo 2 C Catalysts, Journal of Catalysts, 2013 (2013).

[12] M. Nagai, K. Matsuda, Low-temperature water–gas shift reaction over cobalt–molybdenum carbide catalyst, Journal of Catalysis, 238 (2006) 489-496.

[13] P.M. Patterson, T.K. Das, B.H. Davis, Carbon monoxide hydrogenation over molybdenum and tungsten carbides, Applied Catalysis A: General, 251 (2003) 449-455.

[14] A. Griboval-Constant, J.-M. Giraudon, G. Leclercq, L. Leclercq, Catalytic behaviour of cobalt or ruthenium supported molybdenum carbide catalysts for FT reaction, Applied Catalysis A: General, 260 (2004) 35-45.

[15] E.T. Liakakou, E. Heracleous, Transition metal promoted K/Mo2C as efficient catalysts for CO hydrogenation to higher alcohols, Catalysis Science & Technology, 6 (2016) 1106-1119.

[16] H.C. Woo, K.Y. Park, Y.G. Kim, J.S. Lee, Mixed alcohol synthesis from carbon monoxide and dihydrogen over potassium-promoted molybdenum carbide catalysts, Applied catalysis, 75 (1991) 267-280.

[17] M. Xiang, D. Li, H. Xiao, J. Zhang, H. Qi, W. Li, B. Zhong, Y. Sun, Synthesis of higher alcohols from syngas over Fischer–Tropsch elements modified K/β-Mo2C catalysts, Fuel, 87 (2008) 599-603.

[18] M. Xiang, D. Li, W. Li, B. Zhong, Y. Sun, Performances of mixed alcohols synthesis over potassium promoted molybdenum carbides, Fuel, 85 (2006) 2662-2665.

[19] M. Xiang, D. Li, W. Li, B. Zhong, Y. Sun, Potassium and nickel doped β-Mo2C catalysts for mixed alcohols synthesis via syngas, Catalysis Communications, 8 (2007) 513-518.

[20] H. Shou, R.J. Davis, Reactivity and in situ X-ray absorption spectroscopy of Rb-promoted Mo2C/MgO catalysts for higher alcohol synthesis, Journal of Catalysis, 282 (2011) 83-93.

[21] K. Yin, H. Shou, D. Ferrari, C.W. Jones, R.J. Davis, Influence of Cobalt on Rubidium-Promoted Alumina-Supported Molybdenum Carbide Catalysts for Higher Alcohol Synthesis from Syngas, Topics in Catalysis, 56 (2013) 1740-1751.

[22] D.V.N. Vo, V. Arcotumapathy, B. Abdullah, A.A. Adesina, Evaluation of Ba‐promoted Mo carbide catalyst for Fischer‐Tropsch synthesis, Journal of Chemical Technology and Biotechnology, 88 (2013) 1358-1363.

[23] Y. Aoki, H. Tominaga, M. Nagai, Hydrogenation of CO on molybdenum and cobalt molybdenum carbide catalysts—Mass and infrared spectroscopy studies, Catalysis Today, 215 (2013) 169-175.

[24] M. Xiang, D. Li, W. Li, B. Zhong, Y. Sun, K/Fe/β-Mo2C: A novel catalyst for mixed alcohols synthesis from carbon monoxide hydrogenation, Catalysis Communications, 8 (2007) 88-90.

[25] M. Xiang, D. Li, W. Li, B. Zhong, Y. Sun, Synthesis of higher alcohols from syngas over K/Co/β-Mo2C catalysts, Catalysis Communications, 8 (2007) 503-507.

[26] D.-V.N. Vo, A.A. Adesina, Fischer–Tropsch synthesis over alumina-supported molybdenum carbide catalyst, Applied Catalysis A: General, 399 (2011) 221-232.

[27] D.-V.N. Vo, V. Arcotumapathy, B. Abdullah, A.A. Adesina, Non-linear ASF product distribution over alkaline-earth promoted molybdenum carbide catalysts for hydrocarbon synthesis, Catalysis Today, 214 (2013) 42-49.

[28] A.Y. Khodakov, A. Griboval-Constant, R. Bechara, V.L. Zholobenko, Pore Size Effects in Fischer Tropsch Synthesis over Cobalt-Supported Mesoporous Silicas, Journal of Catalysis, 206 (2002) 230-241.

[29] V.K. Saini, M. Andrade, M.L. Pinto, A.P. Carvalho, J. Pires, How the adsorption properties get changed when going from SBA-15 to its CMK-3 carbon replica, Separation and Purification Technology, 75 (2010) 366-376.

[30] W. Dai, M. Zheng, Y. Zhao, S. Liao, G. Ji, J. Cao, Template synthesis of three-dimensional cubic ordered mesoporous carbon with tunable pore sizes, Nanoscale research letters, 5 (2010) 103-107.

[31] F. El Kady, S. Shaban, A.A. El Naga, Catalytic dehydrogenation of cyclohexene over MoO3/γ-Al2O3 catalysts, Transition Metal Chemistry, 36 (2011) 237-244.

[32] G. Wang, J.A. Schaidle, M.B. Katz, Y. Li, X. Pan, L.T. Thompson, Alumina supported Pt–Mo2C catalysts for the water–gas shift reaction, Journal of Catalysis, 304 (2013) 92-99.

[33] J.-H. Zhou, Z.-J. Sui, J. Zhu, P. Li, D. Chen, Y.-C. Dai, W.-K. Yuan, Characterization of surface oxygen complexes on carbon nanofibers by TPD, XPS and FT-IR, Carbon, 45 (2007) 785-796.

[34] R.S. Ribeiro, A.M.T. Silva, M.T. Pinho, J.L. Figueiredo, J.L. Faria, H.T. Gomes, Development of glycerol-based metal-free carbon materials for environmental catalytic applications, Catalysis Today, 240, Part A (2015) 61-66.

[35] G. De la Puente, J. Pis, J. Menendez, P. Grange, Thermal stability of oxygenated functions in activated carbons, Journal of Analytical and Applied Pyrolysis, 43 (1997) 125-138.

[36] W. Ngantsoue-Hoc, Y. Zhang, R.J. O'Brien, M. Luo, B.H. Davis, Fischer−Tropsch synthesis: activity and selectivity for Group I alkali promoted iron-based catalysts, Applied Catalysis A: General, 236 (2002) 77-89.

[37] G. Vitale, H. Guzmán, M.L. Frauwallner, C.E. Scott, P. Pereira-Almao, Synthesis of nanocrystalline molybdenum carbide materials and their characterization, Catalysis Today, 250 (2015) 123-133.

[38] N. Perret, X. Wang, L. Delannoy, C. Potvin, C. Louis, M.A. Keane, Enhanced selective nitroarene hydrogenation over Au supported on β-Mo2C and β-Mo2C/Al2O3, Journal of Catalysis, 286 (2012) 172-183.

[39] Z. Yao, J. Jiang, Y. Zhao, F. Luan, J. Zhu, Y. Shi, H. Gao, H. Wang, Insights into the deactivation mechanism of metal carbide catalysts for dry reforming of methane via comparison of nickel-modified molybdenum and tungsten carbides, RSC Advances, 6 (2016) 19944-19951.

[40] Y. Zhao, Z. Yao, Y. Shi, X. Qiao, G. Wang, H. Wang, J. Yin, F. Peng, A novel approach to the synthesis of bulk and supported [small beta]-Mo2C using dimethyl ether as a carbon source, New Journal of Chemistry, 39 (2015) 4901-4908.

[41] C. Shi, S. Zhang, X. Li, A. Zhang, M. Shi, Y. Zhu, J. Qiu, C. Au, Synergism in NiMoOx precursors essential for CH4/CO2 dry reforming, Catalysis Today, 233 (2014) 46-52.

[42] J.S. Lee, S.T. Oyama, M. Boudart, Molybdenum carbide catalysts, Journal of Catalysis, 106 (1987) 125-133.

[43] K.J. Leary, J.N. Michaels, A.M. Stacy, Carbon and oxygen atom mobility during activation of Mo2C catalysts, Journal of Catalysis, 101 (1986) 301-313.

[44] G. Leclercq, M. Kamal, J.F. Lamonier, L. Feigenbaum, P. Malfoy, L. Leclercq, Treatment of bulk group VI transition metal carbides with hydrogen and oxygen, Applied Catalysis A: General, 121 (1995) 169-190.

[45] W. Wu, Z. Wu, C. Liang, X. Chen, P. Ying, C. Li, In situ FT-IR spectroscopic studies of CO adsorption on fresh Mo2C/Al2O3 catalyst, The Journal of Physical Chemistry B, 107

(2003) 7088-7094.

[46] A. Zhang, A. Zhu, B. Chen, S. Zhang, C. Au, C. Shi, In-situ synthesis of nickel modified molybdenum carbide catalyst for dry reforming of methane, Catalysis Communications, 12 (2011) 803-807.

[47] C. Liu, M. Virginie, A. Griboval-Constant, A. Khodakov, Impact of potassium content on the structure of molybdenum nanophases in alumina supported catalysts and their performance in carbon monoxide hydrogenation, Applied Catalysis A: General, 504 (2015) 565-575.

[48] J.S. Lee, S. Kim, Y.G. Kim, Electronic and geometric effects of alkali promoters in CO hydrogenation over K/Mo2C catalysts, Topics in Catalysis, 2 (1995) 127-140.

[49] M.E. Dry, The Fischer–Tropsch process: 1950–2000, Catalysis today, 71 (2002) 227-241.

[50] Z.-r. Li, Y.-l. Fu, M. Jiang, Structures and performance of Rh–Mo–K/Al2O3 catalysts used for mixed alcohol synthesis from synthesis gas, Applied Catalysis A: General, 187 (1999) 187-198.

[51] B.C. Windom, W. Sawyer, D.W. Hahn, A Raman spectroscopic study of MoS2 and MoO3: applications to tribological systems, Tribology Letters, 42 (2011) 301-310.

[52] M.Z. Ahmad, Investigation of nanostructured metal oxide based H2, NOx & C2H5OH conductometric and optical sensors, in, RMIT University Melbourne, Australia, 2013.

[53] W. Li, G.D. Meitzner, R.W. Borry Iii, E. Iglesia, Raman and X-Ray Absorption Studies of Mo Species in Mo/H-ZSM5 Catalysts for Non-Oxidative CH4 Reactions, Journal of Catalysis, 191 (2000) 373-383.

[54] A. Arfaoui, S. Touihri, A. Mhamdi, A. Labidi, T. Manoubi, Structural, morphological, gas sensing and photocatalytic characterization of MoO3 and WO3 thin films prepared by the thermal vacuum evaporation technique, Applied Surface Science, 357, Part A (2015) 1089-1096.

[55] A. Tavasoli, S. Karimi, M. Davari, N. Nasrollahi, T. Nematian, Enhancement of MoO3–K2O/CNTs nanocatalyst activity and selectivity in higher alcohols synthesis using microemulsion technique, Journal of Industrial and Engineering Chemistry, 20 (2014) 674-681.

[56] S.L. González-Cortés, T.-C. Xiao, T.-W. Lin, M.L.H. Green, Influence of double promotion on HDS catalysts prepared by urea-matrix combustion synthesis, Applied Catalysis A: General, 302 (2006) 264-273.

[57] H. Shou, D. Ferrari, D.G. Barton, C.W. Jones, R.J. Davis, Influence of Passivation on the Reactivity of Unpromoted and Rb-Promoted Mo2C Nanoparticles for CO Hydrogenation, ACS Catalysis, 2 (2012) 1408-1416.

[58] D.R. Stellwagen, J.H. Bitter, Structure–performance relations of molybdenum-and tungsten carbide catalysts for deoxygenation, Green Chemistry, 17 (2015) 582-593.

Chapter 6 General conclusion

6.1 General conclusion

Valorisation of renewable resources to fuels and chemicals is currently one of the major societal and industrial challenges. Biogas is a product of anaerobic digestion of biomass and organic waste and is principally composed by methane and carbon dioxide. Both methane and carbon dioxide are relatively inert molecules. In addition, they largely contribute to the greenhouse effect. Dry methane reforming represents one of the unique opportunities to convert simultaneously methane and carbon dioxide into syngas which is an important intermediate for synthesis of valuable products using Fischer-Tropsch reaction. This thesis explored a possibility of combining dry method reforming and Fischer-Tropsch synthesis into a single process using the same or similar catalysts on the basis of supported molybdenum carbide.

The following catalysts were synthetized and characterized using different techniques:

- Nickel promoted Mo_2C/Al_2O_3 catalysts for dry methane reforming;

- Different Mo_2C promoters on various supports for Fischer-Tropsch synthesis.

The catalysts were tested in dry methane reforming and Fischer-Tropsch synthesis in a wide range of operating conditions. In order to understand and to optimise their performances in these reactions, the catalysts were characterized at different steps: after preparation, activation and reaction. The obtained conclusions are summarized below.

6.1.1 Promoted Mo_2C catalysts for dry methane reforming

Non-promoted Mo_2C/Al_2O_3 catalyst showed low activity for dry methane reforming, the activity decreased rapidly due to the oxidation of molybdenum carbide during the reaction. The addition of nickel significantly enhanced both the activity and the stability of Mo_2C/Al_2O_3 catalyst. Particularly, a rapid increase in activity and H_2 selectivities was observed during dry methane reforming over $NiMo/Al_2O_3$-1:1 catalyst. Excellent reaction results were obtained (96.5% of CH_4 conversion, 93.4% of CO_2 conversion, and ratio H_2/CO = 0.89 at 850 ℃). The characterization results indicated that the addition of nickel and sintering of Ni species resulted in the re-carburization of the Mo to carbide phase and the activity increases during dry methane reforming. Besides, Ni-Mo mixing phase, which has been generated during the dry methane reforming, has a positive influence on the stability.

The preparation methods played an important role in the catalytic performances. In the case of Ni/Mo=1:2, the catalyst prepared by mechanical mixture exhibited particularly good catalytic performance (96.5% and 94.7% of CH_4 and CO_2 conversion respectively, H_2/CO = 0.88 and steady state more than 20 h) in comparison to the catalysts prepared by incipient wetness impregnation and impregnation & precipitation method. The order of activity and stability were followed by mechanical mixture method > impregnation & precipitation method > incipient wetness impregnation method.

Beside, in the case of equimolar nickel: molybdenum content (Ni:Mo=1:1), the amount of carbon deposition particularly coincide with the metallic nickel crystallite size (mechanical mixture method > impregnation & precipitation method > incipient wetness impregnation method). It suggests that the crystallite size of nickel strongly affects the catalytic performances and the carbon formation.

At low nickel content (Ni:Mo= 1:2), larger nickel crystallite size results in better oxidation-recarburization balance, which leads to better stability over dry methane reforming. Nevertheless, the large nickel crystallite size also leads to high amount of carbon deposition on the catalysts surface at high nickel content (Ni:Mo= 1:1).

6.1.2 Mo_2C catalysts for Fischer-Tropsch synthesis

The non-promoted Mo_2C catalysts produce mainly C_1-C_4 light hydrocarbons over Fischer-Tropsch synthesis while the selectivity of heavy hydrocarbons was negligible. Due to the strong water gas shift reaction activity of molybdenum carbide, considerable CO_2 selectivity was obtained over all samples. Particularly, Mo_2C supported on alumina leads to better molybdenum species dispersion and stronger basic sites. This catalyst exhibited higher light olefins selectivity compared to its other counterparts.

The addition of different promoters was investigated for Fischer-Tropsch synthesis. Molybdenum species were well dispersed on the alumina surface. The catalytic data suggested that the promotion with nickel led to a significant enhancement of the CO hydrogenation activity while a negligible light olefin selectivity. However, the promotion with Na, Fe and K contributed to the decrease in the CO hydrogenation activity while the carbon chain growth (high C_5^+ selectivity) was enhanced. Particularly, the KMo/Al_2O_3 catalyst exhibited better stability from oxidation (higher Mo^{2+} percentage on the surface even after passivation). Due to excellent hydrogenation capacity of nickel, the promotion led to a

significant enhancement of the CO hydrogenation activity while a negligible light olefin is produced.

The characterizations of different potassium content suggested that addition of potassium enhanced the interaction between molybdenum and alumina support, did not affect the particles size and dispersion, and increased the weak and moderate basic sites. The increasing of potassium content decreased the activities of CO hydrogenation and also inhibited the water gas shift reaction. However, the catalytic results showed that the further increase in K content increased the olefins selectivity and carbon chain growth properties. The better selectivity in olefins has been obtained with KMo/Al_2O_3-(1:1) catalyst.

6.1.3 When combining dry methane reforming and Fischer-Tropsch process can be realistic?

Catalyst stability and sufficient selectivity are the most important challenges for the design of sequential dry methane reforming and Fischer-Tropsch process.

In this process, dry methane reforming should be conducted at elevated pressure. The catalytic results of dry methane reforming under pressure showed that the increase of pressure decreased the DMR activity and led to significant carbon deposition on $NiMo/Al_2O_3$-1:2-M catalyst.

Insufficient selectivity is a major problem of Fischer-Tropsch synthesis. The catalytic data of FTS in presence of CH_4 or CO_2 showed that the addition of CH_4 in the syngas restricted the WGS reaction and the chain growth while promoted the generation of methane and light olefins. Furthermore, the presence of CO_2 in the syngas seemed to promote the generation of light olefins and long-chain hydrocarbons. Note that considerable C_2^+ (C_2-C_4 and C_5^+) hydrocarbon selectivity can be obtained in the presence of CH_4 or CO_2.

To summarize, carbon deposition in dry methane reforming at elevated pressure and insufficient selectivity to valuable products in FTS are two main problems for the combination of dry methane reforming and Fischer-Tropsch synthesis in a single process.

Hence, the research work must continue in order to establish a catalyst formulation that should resist to carbon deposition at elevated pressure in dry methane reforming and to optimize a catalyst formulation and the operating conditions to improve the selectivity of Fischer-Tropsch to value-added products (e.g. olefins, oxygenates, long-chain hydrocarbons).

This thesis contributes in a first approach to the concept of a combination direct process to produce value-added products from biogas.

6.2 Perspectives

Based on the obtained results in this thesis, some perspectives can be proposed for further investigation on this project.

1. As the presence of CH_4 or CO_2 in syngas influences activity and products selectivity on Fischer-Tropsch synthesis, impact of CH_4 and CO_2 in syngas will be interesting to investigate.

2. Combination of dry methane reforming and Fischer-Tropsch synthesis in a single process will be necessary for the valorization of biogas.

3. Biogas generated from anaerobic digestion always contains moisture, thus, the influence of the presence of H_2O on the stability of Mo_2C in dry methane reforming should be necessary.

4. The investigation of sulfur tolerance for molybdenum carbide catalysts in dry methane reforming and Fischer-Tropsch synthesis will be interesting as the biogas always contains trace of H_2S.

Acknowledgement

Firstly, I would like to express my sincere gratitude to my advisors Dr. Andrei Khodakov and Dr Mirella Virginie for the continuous support of my PhD study and related research, for their patience, motivation, and immense knowledge. Their guidance helped me in all the time of research and writing of this thesis. I could not have imagined having a better advisor and mentor for my PhD study.

Besides my advisor, I would like to thank the rest of my thesis committee: Prof. Pascal Fongarland, Prof. Dominique Begin, and Prof. Jean-Marc Giraudon, for their insightful comments and encouragement, but also for the hard question which incented me to widen my research from various perspectives.

Special thanks to our technicians Johann Jezequel, Gérard Cambien, Pascale Dewalle in UCCS-ECL and our secretary Zohra Gueroui for their help during this research. I am grateful to Pardis Simon, Martine Trentesaux, and Olivier Gardoll for characterization analysis.

I would like to thank my colleagues Dr. Mengdie Cai, Dr Kang Cheng, Dr Mengnan Lu, Dr. Chang Liu, Dr. Fangli Jing, Dr. Jorge Beiramar, Xiaofeng, Zhiping, Marine, Ruinian, Yaqian, Haiqin, Xuemei, Jin and all the PhD students who has shared unforgettable years for their support and help during my PhD study. And thanks to Qian, Bing, Qi, Zaidao, Xingyu, Xiaokun, Jian, Yue and all my friends for their support and friendship.

Specially, I am grateful to my motherland and the China Scholarship Council (CSC) to offer the financial support and opportunity for my study in France.

Last but not the least, I would like to thank my family: my parents, uncles, aunts and to my brothers and sisters for supporting me spiritually throughout writing this thesis and my life in general. Particularly, thank you very much for my wife Wenwen Dong for her consideration and support.